Western Graduate&PostdoctoralStudies

Western University
Scholarship@Western

Electronic Thesis and Dissertation Repository

12-12-2013 12:00 AM

New Technology and Techniques for Needle-Based Magnetic Resonance Image-Guided Prostate Focal Therapy

Jeremy Cepek
The University of Western Ontario

Supervisor
Dr. Aaron Fenster
The University of Western Ontario

Graduate Program in Biomedical Engineering
A thesis submitted in partial fulfillment of the requirements for the degree in Doctor of Philosophy
© Jeremy Cepek 2013

Follow this and additional works at: https://ir.lib.uwo.ca/etd

Part of the Biomedical Devices and Instrumentation Commons

Recommended Citation

Cepek, Jeremy, "New Technology and Techniques for Needle-Based Magnetic Resonance Image-Guided Prostate Focal Therapy" (2013). *Electronic Thesis and Dissertation Repository*. 1821.
https://ir.lib.uwo.ca/etd/1821

This Dissertation/Thesis is brought to you for free and open access by Scholarship@Western. It has been accepted for inclusion in Electronic Thesis and Dissertation Repository by an authorized administrator of Scholarship@Western. For more information, please contact wlswadmin@uwo.ca.

www.manaraa.com

NEW TECHNOLOGY AND TECHNIQUES FOR NEEDLE-BASED MAGNETIC RESONANCE IMAGE-GUIDED PROSTATE FOCAL THERAPY

(Thesis format: Integrated Article)

by

Jeremy Cepek

Graduate Program in Biomedical Engineering

A thesis submitted in partial fulfillment
of the requirements for the degree of
Doctor of Philosophy

The School of Graduate and Postdoctoral Studies
The University of Western Ontario
London, Ontario, Canada

© Jeremy Cepek 2014

www.manaraa.com

Abstract

The most common diagnosis of prostate cancer is that of localized disease, and unfortunately the optimal type of treatment for these men is not yet certain. This uncertainty has led to the overtreatment of prostate cancer, leaving men with side effects from the treatment of disease that may not have been lethal. MRI-guided focal laser ablation (FLA) therapy is a promising potential treatment option for select men with localized prostate cancer, and may result in fewer side effects than whole-gland therapies, while still achieving oncologic control. However, while MRI provides excellent visualization tools for this procedure, it presents several technical challenges for needle guidance. These challenges result from the unique MRI environment and the limited access to the prostate within clinical scanners. The objective of this thesis was to develop new technology and techniques for accurately guiding needles to the prostate within the bore of a clinical MRI scanner for MRI-guided FLA therapy.

To achieve this goal, a method of accurately tracking devices in MRI using a passive tracking frame was developed. The new design of tracking frame can localize devices with less sensitivity to image distortions than previous methods. Next, a mechatronic needle guidance system was developed. The system, which uses the newly developed tracking frame design, enables precise targeting of prostate tumours through angulated trajectories and insertion of needles with the patient remaining in the bore of a clinical MRI scanner. The system was rigorously tested for accuracy and repeatability of needle guidance, and MRI-compatibility. After confirming the system was capable of accurately guiding needles in tissue-mimicking phantoms, and that MRI-compatibility was acceptable, it was used to guide needles for MRI-guided FLA therapy in eight

www.manaraa.com

patients. Results from this case series demonstrated an improvement in the time required to guide needles to their target and ease of needle delivery, as compared to conventional approaches. Methods of more reliable treatment planning and quantification of the effect of needle placement uncertainty on treatment outcome were sought, leading to the development of a systematic treatment planning method, and Monte Carlo simulations of needle placement uncertainty. The result was an estimate of the maximum size of focal target that can be confidently ablated using the mechatronic needle guidance system, leading to better guidelines for patient eligibility. These results also quantified the benefit that could be gained with improved techniques for needle guidance.

Further technological and methodological improvements, including the incorporation of 3D finite-element modeling into a treatment plan optimization framework, real-time monitoring of steerable needles, and real-time monitoring and compensation of prostate motion will enable confident focal target ablation in men with larger tumours that what is currently achievable. If the clinical efficacy of focal therapy for men with localized prostate cancer is proven, these methods could have an enormous impact on the clinical management of these men.

Keywords

Magnetic resonance imaging, MRI, prostate cancer, focal therapy, laser ablation, treatment planning, MRI-guided interventions, image-guided interventions, transperineal, needle guidance, passive tracking

www.manaraa.com

Co-Authorship Statement

This thesis is presented in an integrated article format, the chapters of which are based on the following journal publications that are either published, in press, in revision, or in preparation for submission:

Chapter 2: Cepek, J., Chronik, B., Fenster, A.: The Effects of Magnetic Field Distortion on the Accuracy of Passive Device Localization Frames in MR. Med. Phys. (2013, In Revision)

My contributions to this chapter included conceptual design of the experiments, design of the tracking frames for testing and preparation of working drawings for their manufacture, MRI scanning, image processing for computation of error, preparation of graphs, and preparation of the manuscript in its entirety. B. Chronik provided assistance in performing MRI scans and played a supervisory role. The work was performed under the supervision of A. Fenster.

Chapter 3: Cepek, J., Chronik, B., Lindner, U., Trachtenberg, J., Davidson, S., Bax, J., Fenster, A.: A system for MRI-guided transperineal delivery of needles to the prostate for focal therapy. Med. Phys. 40, 012304-1-15 (2013)

My contributions to the work in this chapter were many and will be listed categorically. Mechanical design: I designed the needle guidance device and targeting interface and prepared detailed manufacturing drawings for all components of each. Manufacturing: I manufactured several prototypes of MRI-compatible subsystems for the needle guidance device including some that are present in the final version of the device, and designed the targeting interface in its entirety. Electrical design: I designed the system's electronics, which included the system's main controller and the targeting interface's circuit board. This involved electrical schematic preparation and printed circuit board design. Electrical

www.manaraa.com

system manufacturing: I soldered all components to the circuit boards, prepared all necessary cables and connectors, and tested the electrical systems. Software: I wrote the microcontroller software for both the system's main controller and alignment interface controller, and wrote a C++ library for interfacing the device with existing user interface software. System testing: I brought the system to Attica manufacturing for measurement of its "open-air accuracy" using a coordinate measurement machine, wrote the software for recording encoder positions for this test, and assisted a technologist with recording positions of the device using the CMM. I acquired the MRI scans for the MR-compatibility tests, and processed the data for assessment of distortion and SNR reduction. I acquired MRI scans for the remaining two accuracy tests, and prepared the phantoms for the phantom tests. System integration: I worked with S. Davidson to integrate the system's software library into his existing software, and performed extensive debugging to ensure the system's reliability. Through consultation with U. Lindner, I redesigned many of the system's components, enabling integration with the existing clinical workflow. I also prepared the manuscript in its entirety. B. Chronik provided assistance in performing MRI scans and assessing MRI-compatibility of the system. U. Lindner was a clinical collaborator, providing guidance on how to modify the needle guidance device for clinical use, and performing focal laser ablation procedures using the system. J. Trachtenberg was a clinical collaborator, providing funding, facilities, and various other essential resources for the project. S. Davidson integrated the device control software into the existing image guidance software program used for template procedures. J. Bax provided consultation on device design. The work was performed under the supervision of A. Fenster.

www.manaraa.com

Chapter 4: Cepek, J., Lindner, U., Louis, AS., Ghai, S., Davidson, SRH., Gertner, M., Hlasny, E., Sussman, MS., Trachtenberg, J., Fenster, A.: A Mechatronic System for In-Bore MR-Guided Insertion of Needles to the Prostate: Experiences Using the System for Prostate Focal Laser Ablation in Eight Patients. J. Magn. Reson. Im. (2013, In Preparation)

My contributions to this chapter include setting up the system for each procedure, providing technical support and operating the software during each procedure, directing the acquisition of images for the measurement of needle placement error, processing of images for computing error, taking detailed notes to quantify the time consumed by each component of the procedure, preparation of custom trocars and catheters for each procedure, statistics, and preparation of a large proportion of the manuscript, including four of the five figures. U. Lindner was a clinical collaborator, providing guidance on how to modify the needle guidance device for clinical use, and performing focal laser ablation procedures using the system. A.S. Louis assisted in the literature review and manuscript preparation. S. Ghai was a clinical collaborator, and performed focal laser ablation procedures using the system. S.R.H. Davidson integrated the device control software into the existing image guidance software program used for template procedures. M. Gertner provided consultation on development of custom needles, and the design of components for sterilizability. E. Hlasny performed the MRI scans during the procedures, and assisted in the development of the procedural workflow. M.S. Sussman contributed to the development of MRI sequences for needle tracking. J. Trachtenberg was a clinical collaborator, providing funding, facilities, and various other essential resources for the project. The work was performed under the supervision of A. Fenster.

www.manaraa.com

Chapter 5: Cepek, J., Lindner, U., Davidson, S., Haider, M., Ghai, S., Trachtenberg, J., Fenster, A.: Treatment Planning for Prostate Focal Laser Ablation in the Face of Needle Placement Uncertainty. Med. Phys. (2014, In Press)

My contributions to this chapter included development of the simplified model of treatment planning and the method of performing the simulations, implementation of the simulation in software, processing of the results and preparation of graphs and tables, and preparation of the entire manuscript. U. Lindner was a clinical collaborator, providing the images and valuable experience from the many focal laser ablation procedures he performed. S. Davidson provided the software used for generating figures, and assisted in data collection. M. Haider performed segmentations of suspicious regions on prostate MR images. S. Ghai also performed segmentations on MRI, and assisted in editing the manuscript. J. Trachtenberg was a clinical collaborator, providing funding, facilities, and various other essential resources for the project. The work was performed under the supervision of A. Fenster.

www.manaraa.com

Acknowledgments

There are many people to whom I am extremely grateful for supporting me over the past four years. This support has come in the form of guidance, mentorship, companionship, comradery, inspiration, and financial assistance.

First I would like to thank my supervisor Dr. Aaron Fenster who, by consistently challenging my stubborn ways of thinking and communicating, has instilled in me the attitudes required to approach problems with a scientific mind, and effectively communicate my work. He has given me his unwavering support, while offering me the freedom to pursue my own approach to solving problems.

I would like to thank Dr. Blaine Chronik for offering so much of his expertise in the design of MRI-compatible devices, and devoting his time teaching me how to perform scans and device testing. His enthusiasm for his work is inspiring.

The team in Toronto has contributed enormously to what is described in this thesis, and quite honestly, I don't know where I would be without them. Dr. Uri Lindner recognized the potential of MR PING (an endearing name given to the device described in this work) early on, and his confidence in my abilities was extremely motivating. Even as an extremely busy urological fellow, Uri found the time to personally involve himself in much of the technical details of device development, and the refinement of MR PING into something valuable would not have been possible without his perseverance through the many design iterations. I believe this process may have also taught Uri a valuable lesson: that Velcro is not always the solution. Sean Davidson was instrumental in integrating the system into the existing clinical workflow, devoting much time to modifying his software, and provided valuable feedback on several manuscripts. Mark

www.manaraa.com

Gertner provided valuable contributions in development of custom needles, the design of sterilizable components, and editing of manuscripts. Dr. Sangeet Ghai has been a pleasure to work with, and has provided unique insight into how this procedure can be improved in the future. Alyssa Louis has been extremely helpful in preparing manuscripts. It has also been a great pleasure working with the rest of the team: Eugen Hlasny, Michael Nesbitt, Kateri Corr, and Marshall Sussman. Last, but certainly not least, I would like to thank Dr. John Trachtenberg for making this project possible, and his creative vision of the future of prostate focal therapy.

There are many people in Dr. Fenster's lab who deserve a great deal of gratitude. Jacques Montreuil taught me a great deal about manufacturing, enabling me to personally build some of the early prototypes of the components of MR PING. In addition, whenever I needed something built, Jacques would push everything else aside and make sure it was done on time. I can't thank him enough for his devotion to seeing me succeed. Kevin Barker was also instrumental in this process and his talent for designing and building the most cleverly intricate devices will always amaze me. Dr. Jeff Bax contributed greatly to my approach to mechanical design, and he was always available and willing to share his experiences and expertise. Several other members of Dr. Fenster's and adjacent labs must also be recognized for countless intelligent discussions, support, and contributions: Dr. David Tessier, Igor Gyackov, Lori Gardi, Chandima Edirisinghe, Eranga Ukwatta, Tharindu De Silva, Eli Gibson, Hamid Neshat, Bon Ryu, Shi Sherebrin, Dr. Derek Cool, Amila Samarabandu, Jenna Zaleski, Matt Gravett, Kimberley Booth, Trevor Szekeres, Cyndi Harper Little, Andrew Alejski, and Janos Bartha.

www.manaraa.com

I must also recognize two people in particular who have been invaluable mentors during my career in graduate school: Dr. Anthony Straatman, my Masters supervisor, who instilled in me a great passion for research early on; and Dr. Aaron Ward, who provided me with an immeasurable amount of support and guidance throughout the course of my PhD. I am also extremely grateful for the amount of time and effort that each of my examiners dedicated to evaluating this work: Dr. Glenn Bauman, Dr. Terry Peters, Dr. Robert Bartha, and Dr. Tim Salcudean. Having the opportunity to spend the morning with these gentlemen was an honor and a pleasure.

Finally, there are so many people in my life outside the lab I must acknowledge for their support and friendship. My parents, Paulette and Les, have supported me from the start, and instilled in me the attitudes of hard work that got me where I am today. My brother Justin and his wife Jessie have shared the joy of their family with me as it grew over the last few years. I would also like to thank the following people with whom I've shared many good times, and who have generally helped me keep my sanity: Jessica Kishimoto, Tom Kurowski, Chris Fischer, Steve Jenniskens, David Del Rey Fernandez, Jennifer Collis, Jesse Tanguay, Amy Khan, Matt Kramers, Martin Rajchl, Kamyar Abhari, Peter Martin, Kathryn Manning, Dave Edey, Bob Thomson, Eric Sadowski, Ryan DeForge, Mallory Downie, and my favourite cousin in the whole wide world, Jenna Simpson.

Sources of funding that have supported me personally include the National Sciences and Engineering Research Council of Canada, the Queen Elizabeth II Graduate Scholarship in Science and Technology (partially made possible by a generous

www.manaraa.com

contribution from the T.R. Meighen Family Foundation), the Computer Assisted Medical Interventions CREATE Award, and the Western Graduate Research Scholarship.

www.manaraa.com

Table of Contents

Abstract ii

Co-Authorship Statement iv

Acknowledgments viii

Table of Contents xii

List of Tables xvi

List of Figures xvii

List of Abbreviations xxiii

Chapter 1. Introduction 1
1.1 Prostate Cancer ... 1
1.1.1 Prostate Cancer Epidemiology ... 1
1.1.2 The Impact of Prostate Cancer ... 2
1.2 Prostate Cancer Diagnosis ... 3
1.2.1 The Prostate Specific Antigen Test ... 3
1.2.2 Digital Rectal Examination ... 5
1.2.3 Biopsy ... 5
1.2.4 Imaging ... 11
1.3 Prostate Cancer Treatment ... 19
1.3.1 Conventional Approaches and the Focal Therapy Concept ... 20
1.3.2 Focal Laser Ablation Therapy ... 21
1.4 Challenges in MRI-Guided Needle-Based Prostate Interventions ... 23
1.4.1 The MRI Environment ... 24
1.5 Existing MRI-Guided Prostate Needle Guidance Devices & Techniques ... 26
1.5.1 The Conventional Approach ... 27
1.5.2 Mechatronic or Robotic Devices ... 28
1.6 Thesis Hypothesis and Objectives ... 30
1.6.1 Specific Objectives ... 31
1.7 Outline of this Thesis ... 32
1.7.1 Chapter 2: The Effects of Magnetic Field Distortion on the Accuracy of Passive Device Localization Frames in MR ... 32
1.7.2 Chapter 3: A System for MRI-Guided Transperineal Delivery of Needles to the Prostate for Focal Therapy ... 33
1.7.3 Chapter 4: A Mechatronic System for In-Bore MR-Guided Insertion of Needles to the Prostate: Experiences Using the System for Prostate Focal Laser Ablation in Eight Patients ... 34
1.7.4 Chapter 5: Treatment Planning for Prostate Focal Laser Ablation in the Face of Needle Placement Uncertainty ... 35
1.7.5 Chapter 6: Conclusions and Future Work ... 36

www.manaraa.com

References 37

Chapter 2. The Effects of Magnetic Field Distortion on the Accuracy of Passive Device Localization Frames in MR[†] **47**
2.1 Introduction 47
2.2 Methods 50
2.2.1 2D Gradient Echo Imaging of Ellipsoids 50
2.2.2 In-Plane Centroid Measurement 51
2.2.3 Localization Frames 52
2.2.4 Z-Frame 54
2.2.5 + Frame 56
2.2.6 Spherical Marker Frame 58
2.2.7 Model Parameters 59
2.2.8 Error Measurement in MR 60
2.3 Results 61
2.4 Discussion 68
2.5 Conclusions 71
References 72

Chapter 3. A System for MRI-Guided Transperineal Delivery of Needles to the Prostate for Focal Therapy[†] **75**
3.1 Introduction 75
3.2 Methods 80
3.2.1 System Design 80
3.2.2 Mechanical Design and Kinematics 82
3.2.3 Registration of Device and MRI Coordinate Systems 86
3.2.4 Electrical Systems 90
3.2.5 User Interface and Procedure Workflow 90
3.2.6 MR-Compatibility 95
3.2.7 Image Distortion and Signal-to-Noise Ratio 95
3.2.8 Effects of MRI on the Device 96
3.2.9 Targeting Accuracy 97
3.2.10 Clinical Evaluation 102
3.2.11 MR Imaging Parameters 103
3.3 Results 103
3.3.1 MR-Compatibility 103
3.3.2 Targeting Accuracy 105
3.3.3 Clinical Evaluation 108
3.4 Discussion 109
3.5 Conclusions 113
References 114

Chapter 4. A Mechatronic System for In-Bore MR-Guided Insertion of Needles to the Prostate: Experiences Using the System for Prostate Focal Laser Ablation in Eight Patients[†] **119**
4.1 Introduction 119
4.2 Materials and Methods 121

www.manaraa.com

4.2.1 System Design 121
4.2.2 Integration with Clinical Workflow 122
4.2.3 Intra-Procedure Performance Assessment 123
4.2.4 Data analysis 125
4.3 Results 125
4.4 Discussion 128
4.5 Conclusions 132
References 133

Chapter 5. Treatment Planning for Prostate Focal Laser Ablation in the Face of Needle Placement Uncertainty[†] **136**
5.1 Introduction 136
5.2 Methods 140
5.2.1 Treatment Planning 140
5.2.2 3D Ablation Volume Model 140
5.2.3 2D Approximation 141
5.2.4 Specification of Planned Laser Fiber Locations 145
5.2.5 Estimation of Treatment Overlap 148
5.2.6 Mathematical Description of Treatment Overlap 149
5.2.7 Statistical Model of Needle Placement Error 151
5.2.8 Numerical Implementation Considerations 153
5.2.9 Treatment Simulation Parameters 155
5.2.10 Treatment Target Shapes 155
5.2.11 Ablation Sizes 157
5.3 Results 158
5.3.1 Idealized Treatment Simulations 158
5.4 Discussion 164
5.5 Conclusions 167
References 169

Chapter 6. Conclusions and Suggestions for Future Work **174**
6.1 Conclusions 174
6.2 Suggestions for Future Work 176
6.2.1 Procedure Time 176
6.2.2 Improved Treatment Planning 179
6.2.3 Real-Time Control of Needle Trajectories 180
References 183

Appendix A. 2D Gradient Echo Imaging of Ellipsoids **184**
A.1 Cylinder 184
A.2 Sphere 187

Appendix B. Trajectory Alignment Device Kinematics Solutions **189**
B.1 Forward Kinematics 190
B.2 Reverse Kinematics 192

Appendix C. Health Canada Application **193**

www.manaraa.com

Appendix D. Patent Application: System and Method for Guiding a Medical Device to a Target Region **205**

Appendix E. Permissions **245**
E.1 Permission to reproduce previously published material in Chapters 2, 3, and 5 245
E.2 Permission to reproduce Figure 1.3 246
E.3 Permission to reproduce Figure 1.4**.** 248

Curriculum Vitae **249**

www.manaraa.com

List of Tables

Table 2.1: Line parameters for each cylinder in the z-frame. $v_z = 0$, and $s_z = 1$ for all segments. 55

Table 2.2: Line parameters for each cylinder in the + frame. **s** = 0 for both segments.... 57

Table 2.3: Parameters used in the model of localization frame imaging in MR. The gradient strengths are chosen to be representative of values typically used in clinical sequences. 60

Table 2.4: Sources of static field distortion and their effects on frame localization error 69

Table 3.1: MR imaging parameters used for all images acquired in this chapter. 103

Table 3.2: Summary of SNR measurements. 104

Table 3.3: Summary of device accuracy tests in MR. Needle guidance error, NGE [Eq. (3.7)], needle guidance human error, NGHE [Eq. (3.10)], and needle trajectory error [Eq. (3.12)] quantify the system accuracy for both the intra-MR trajectory alignment, and tissue-mimicking phantom targeting tests. 95% CI is the confidence interval on the mean. 95% PI is the prediction interval for each error. All values are reported as mean ± STD. Values in bold are those mentioned in the discussion. 106

Table 3.4: *In vivo* needle targeting errors in two patients. Patient 1 had four needles inserted, while patient 2 had five. Needle deflection error in patient 2 was less than half that in patient 1, demonstrating how much tissue properties can vary between patients. 109

Table 4.1: Needle guidance error and needle guidance time for each of six patients. Data are shown as median (interquartile range). 126

Table 5.1: Minimum required ratio of ablation diameter to target length R_A for varying target aspect ratio and number of planned laser fibers. 148

Table 5.2: Ranges of the parameters varied for simulations of the fraction of target treated. 155

Table 5.3: Maximum allowable target length (in mm) to maintain a minimum probability of complete target ablation (P_{100}) of at least 90%. 163

www.manaraa.com

List of Figures

Figure 1.1: Age standardized incidence rates of prostate cancer in Canada. (Image taken from [2].) 4

Figure 1.2: Light micrograph of a sample of prostate tissue, stained with hematoxylin and eosin (H&E). At this level of magnification, the individual prostate glands and the cells comprising them can be seen. (Image © 2010 Nephron / Wikimedia Commons)..... 6

Figure 1.3: Zonal anatomy of the prostate: a) young, healthy male, b) older male with benign prostatic hypertrophy (BPH), causing enlargement of the transition zone (TZ). (Reproduced with permission from Ref. [15])..... 8

Figure 1.4: Multiparametric MR images of a prostate with histologically-proven prostate cancer: a) T2-weighted image correctly demonstrates the presence of cancer, as indicated by the region of hypointensity, b) a map of K^{trans} (a DCE MRI PK parameter) showing sensitivity to the presence of the tumour, but a lack of specificity in this case, since several other benign areas within the prostate show enhanced areas, c) ADC map which also correctly identified the cancerous region, as shown by the region of hypointensity (restricted diffusion), and d) the region of histologically-proven prostate cancer. (Figure reproduced with permission from Ref. [42]) 19

Figure 2.1: Illustration of the various components that contribute to needle placement error. This chapter considers the sensitivity of error in device localization to the presence of static magnetic field distortions in MR..... 48

Figure 2.2: Accurate in-plane measurement of an object's position in MR in the presence of static field distortion by acquiring two images with the frequency-encoded (F.E.) direction alternated: a) frequency-encoding in the left-right (horizontal) direction, b) frequency-encoding in the anterior-posterior (vertical) direction, c) sum of images in a) and b), showing how measurements of the object's position in the phase-encoded direction in separate acquisitions can be combined to find the true position. 51

Figure 2.3: The z-frame: a) coordinate system and image intersection points, b) MR image showing the seven ellipses. 55

Figure 2.4: The + localization frame: a) coordinate system and localization points for the + frame, b) MR images showing the four points used for localization..... 57

Figure 2.5: The spherical marker localization frame: a) localization points and coordinate system, b) MR image of the frame. Note that, without acquiring multiple contiguous slices, accurate sphere localization requires the acquisition of additional images in at least one other plane perpendicular to the one shown. 58

Figure 2.6: The three localization frames constructed for error sensitivity tests in MR: a) z-frame, b) + frame, c) spherical marker frame..... 61

Figure 2.7: Error in pose estimation of the z-frame: a) rotational error, represented by the three Euler angles, b) translational error. Solid and dashed lines (denoted "Th." in

www.manaraa.com

the legends) indicate theoretical results, while the markers (denoted "Exp." in the legends) indicate results from the MR imaging experiments. 63

Figure 2.8: Error in pose estimation of the + frame: a) rotational error, represented by the three Euler angles, b) translational error. Solid and dashed lines (denoted "Th." in the legends) indicate theoretical results, while the markers (denoted "Exp." in the legends) indicate results from the MR imaging experiments. Note the lack of translational error with frequency encoding in the x-direction (Figure b, first column). This result is due to the polarity of the frequency-encoding gradient in the x-direction being reversed in axial and coronal scans, thereby cancelling out the translational error. 64

Figure 2.9: Error in pose estimation of the spherical marker frame: a) rotational error, represented by the three Euler angles, b) translational error. Solid and dashed lines (denoted "Th." in the legends) indicate theoretical results, while the markers (denoted "Exp." in the legends) indicate results from the MR imaging experiments. 65

Figure 2.10: The magnetic field distortion field created by the presence of a 10 mm radius austenitic stainless steel sphere located 150 mm from the center of a localization frame. The white circles represent the points at which the frame is imaged. For the purposes of estimating the effects of the distortion on frame localization error, a linear representation of the distortion field over the frame's geometry is used. 68

Figure 3.1: Computer-aided design drawing showing the trajectory alignment device in position with a patient in the bore of an MRI scanner. a) View from above, b) Side view with patient sectioned to show internal anatomy. The device is designed to allow oblique needle trajectories to reduce pubic arch interference while avoiding interference with the endorectal (ER) coil. 80

Figure 3.2: Manual alignment of the trajectory alignment device using the targeting interface. a) The handle is misaligned and must be moved to the right and downward, as indicated by the 'right' grid display, b) the device has been successfully aligned with the selected target. 81

Figure 3.3: The trajectory alignment device in position with a patient in the bore of a 1.5T clinical MRI scanner (Signa HDxt, GE Healthcare, Milwaukee, WI). Access to the lock handles, alignment handle, and rear template are maintained with the patient still in the bore. Two catheters have been successfully inserted, and the physician is preparing a laser fiber for ablation. 82

Figure 3.4: The trajectory alignment device. The pose of the needle templates is uniquely defined by the positions of the front and rear linear stages. Positioning of each set of stages can be independently achieved by unlocking the corresponding set using the locking handles and manipulating the alignment handle. The spring counterbalances maintain the position of each set of stages during positioning. The two rear needle templates allow the physician to insert a long catheter from outside the MRI bore and guide it into the front template, which is located adjacent to the patient's skin. 83

www.manaraa.com

Figure 3.5: Schematic of the spring counterbalance system. The leaf springs provide a force F_s that opposes the force of gravity F_g acting on the components with a vertical degree of freedom. The cam assembly ensures that F_s is constant throughout the entire range of angle θ 84

Figure 3.6: Device coordinate system and kinematics variables. Specification of all four linear stages positions e_{1x}, e_{1y}, e_{2x}, and e_{2y} uniquely defines the intended needle trajectory, defined by $\hat{v}_n$ and p_t in a closed kinematic chain (forward kinematics). Likewise, a given needle trajectory corresponds to a unique set of linear stage positions (reverse kinematics). 86

Figure 3.7: Detachable registration fiducial component. The component is imaged in both axial and coronal planes for the localization of four points, necessary for registration of the device's coordinate system to that of the MRI. 87

Figure 3.8: Localization of registration fiducials in MR images. a) Original fiducial image, b) filtered & thresholded fiducial image. The red cross indicates the centroid. ... 88

Figure 3.9: Intra-treatment prostate registration. a) Pre-treatment image with prostate boundary (thin blue contour) and suspicious region (red contour) segmented, b) intra-treatment image showing both the manual intra-treatment contour (thick green contour) and registered pre-treatment contours (thin blue contour). The registration process locates the suspicious region in intra-treatment MR space. 91

Figure 3.10: Live 3D needle trajectory display overlaid on a coronal image of the prostate and surrounding anatomy. a) Device misaligned, b) device aligned to target and entry point, c) device aligned only to target point (target only mode). Orange line: expected needle trajectory, computed from device kinematics equations and displayed in real-time. Red line: desired needle trajectory, specified by the user. Green contour: prostate boundary. 92

Figure 3.11: Device alignment interface. a) Front and rear stages misaligned, b) front aligned, rear misaligned, c) device fully aligned with desired trajectory. 92

Figure 3.12: Custom tungsten trocar and polyetheretherketone catheter. The assembly is 55 cm in length to allow for needle insertion with the patient in the MRI bore. The tungsten trocars feature a 3-sided symmetrical bevel tip. Standard Luer-Lok fittings mate the trocar to the catheter during insertion. 93

Figure 3.13: MR thermometry and tissue thermal damage estimation. a) Temperature image showing the ablation zone and prostate and tumour boundaries, b) thermal damage map superimposed on an MR image of the prostate. Regions in red correspond to $\Omega >= 1$ from Eq. (3.6) and are considered ablated. Note that in this case the ablated region did not reach the anterior edge of the tumour boundary, requiring the insertion of an additional needle. 95

Figure 3.14: Illustration of the components of needle placement error measured in each of the three accuracy tests. Red box: errors measured in the open-air targeting test. Blue box: errors measured in the intra-MR targeting test. Green box: errors

www.manaraa.com

measured in the intra-MR phantom needle guidance test. Evaluation of target localization error was not performed, as it was beyond the scope of this chapter. 98

Figure 3.15: Images from distortion test: a) baseline. Difference images: b) device only, c) device connected, d) device powered. 104

Figure 3.16: Illustration of each of the components of needle guidance error that were measured: needle trajectory error (NTE), which includes errors due to needle deflection and device localization; needle guidance human error (NGHE), which measures the user's ability to align the device with the desired needle trajectory; and needle guidance error (NGE), which includes contributions from NTE and NGHE. 107

Figure 3.17: MR images of needles in a patient's prostate. a) Axial image showing needles, b) sagittal image of needles showing how inserting a needle into a posterior template hole allowed the physician to reach the original, more anterior target. 112

Figure 4.1: Needle guidance device setup and components. a) Device in place on MR table prior to patient positioning. LED grid panel indicates position of the needle guide relative to target position. b) Sterilizable components including (from top to bottom): guidance arm, mounting pin, alignment handle and needle guides. c) Device in operating position before moving the patient into the MR bore. d) Placement of laser fibers with the patient remaining inside the bore. 123

Figure 4.2: Images showing final catheter placement in two different prostates. a) Patient 7, sagittal FSPGR image showing 3D prostate (blue) and target region (red) surfaces, target point (red arrow) and needle at its final position (white arrow) in the left posterior peripheral zone. b) Patient 3, axial FSPGR image showing excellent visualization of the catheter, but poor contrast between prostatic and surrounding tissue. c) Patient 3, bSSFP image showing excellent visualization of the same catheter in *(b)*, clear contrast between prostatic and surrounding tissue, and internal prostate anatomical detail. 126

Figure 4.3: Needle guidance error for each of the 29 insertions. a) Components of needle guidance error in the anterior-posterior and medial-lateral directions. Positive values correspond to the posterior and lateral directions. The point (0,0) corresponds to the target point for each insertion. Needles tended to deflect in the lateral and posterior directions. b) Fraction of needles within a given level of error e_{max} using the system described in this chapter. 127

Figure 4.4: Box plot showing the time required to guide each needle to its target using either a brachytherapy-like grid template, or the mechatronic system described in this work. Red line: median, blue box: interquartile range (IQR), black bars: extremum. The median time was statistically significantly different between the two methods ($p < 0.0001$). 128

Figure 4.5: Two cases for which the needle guidance system proved extremely valuable. a), b) Patient 7, with a prostate volume of 268 cm^3. The use of an angulated needle trajectory allowed the tumour in the far lateral posterior peripheral zone to be reached while avoiding pubic arch interference. c), d) Patient 8, with an anterior tumour that would have been inaccessible using a parallel needle trajectory due to

www.manaraa.com

interference with the urethra. The target was reached while avoiding damage to the urethra using the angulated trajectory shown. 130

Figure 5.1: Estimated regions of ablated tissue in four patient's prostates, as seen on immediate post-treatment dynamic contrast-enhanced MR images (coronal slices): a), b) single fiber insertion with laser application at only one axial position; c), d) single fiber insertion with multiple laser applications at multiple axial positions, which created a region of ablated tissue that is elongated in the direction of the laser fiber (needle) axis. In all cases the insertion direction was approximately superior-inferior, with case d) showing a slight lateral angulation. 143

Figure 5.2: Idealized ablation volume. A set of confluent regions of ablated tissue in the direction of the needle insertion is modeled as a cylinder of maximum diameter that can be enclosed by the actual ablated region. As the axial spacing between laser applications is reduced, the amount of under-prediction of ablated tissue around the periphery of the ablation region decreases, and it increases at each end. 144

Figure 5.3: Effect of laser fiber axial positioning on the validity of the cylindrical ablation region model. a), c), view from "needle's eye view"; b), d), view perpendicular to needle axis. The cylindrical ablation region model is valid if the axial extent of the planned ablation region is chosen such that $m_p = m_{min}$. In a) & b), the planned ablation region is not long enough ($m_p > m_{min}$), in c) & d), $m_p = m_{min}$ and therefore the 2D model would reliably predict when needle placement error results in untreated target tissue. 145

Figure 5.4: The two patterns considered for the ideal placement of laser fibers: a) Pattern A (linear pattern), b) Pattern B (concentric ellipse pattern). Solid black contour: idealized target boundary, red contours: idealized ablation region boundaries, dashed contour: concentric planning ellipse. For a given target width, target aspect ratio, and number of laser fibers, the ideal pattern of the two is that which requires the smallest ablation diameter. 146

Figure 5.5: Minimum treatment plan required to achieve complete target coverage for varying target aspect ratio and number of laser fibers used. Either Pattern A (fibers equally distributed along the major axis of the target) or Pattern B (fibers distributed around an ellipse concentric to the target boundary) is employed, based on whichever pattern gives the minimum required size of ablation region. Black contour: idealized target boundary, red circle: idealized ablation region boundary..... 147

Figure 5.6: Examples showing how the planned number of laser fibers can be increased. Pattern A (the linear pattern) is used when the diameter of the ablation is large relative to the target width. Pattern B (concentric ellipse pattern) is used when the ablation diameter is small relative to the target width, in which case it becomes necessary to distribute laser fibers around the periphery of the target. As the number of laser fibers increases, Pattern B can be employed to increase the treatment margin around the periphery of the target. 148

Figure 5.7: Distribution of the sizes and aspect ratios of the ellipses enclosing the MR-identified targets in 47 men included in a Phase I/II clinical trial of FLA for

www.manaraa.com

prostate cancer: a) histogram of ellipse lengths, b) histogram of ellipse aspect ratios, c) lengths vs. widths, d) aspect ratios vs. lengths. 156

Figure 5.8: Examples of ellipses of minimum area fitted to target shapes, as seen from the "needle's eye view". Gray regions: actual volumes of suspected tumours, as contoured on multi-parametric MR images; black contours: fitted ellipses. The aspect ratio AR is defined as AR = length/width. 157

Figure 5.9: Probability of achieving complete focal target ablation (P_{100}) for a given target aspect ratio, target length, standard deviation of needle placement error and various diameters of ablation regions: a) 10 mm, b) 15 mm, c) 20 mm. For a given set of: minimum desired P_{100}, target size and shape, size of ablation achievable, and estimated level of needle placement uncertainty, this figure can be used to estimate the number of laser fibers that should be used for the treatment. Cases for which target coverage cannot be achieved using 8 fibers or less are omitted. 162

Figure 5.10: Immediate post-treatment axial dynamic contrast-enhanced MR images showing variation in ablation region symmetry: a) more tissue was ablated medial to the laser fiber than lateral, b) the region of ablated tissue was much more axisymmetric about the laser fiber axis. 166

Figure 6.1: Time taken to complete various components of the MRI-guided prostate FLA procedure, as recorded over seven cases. Red line = median, blue box = IQR, black T's = extrema, red crosses = outliers. 177

www.manaraa.com

List of Abbreviations

2D	Two-Dimensional
3D	Three-Dimensional
ADC	Apparent Diffusion Coefficient
AR	Aspect Ratio
ASAP	Atypical Small Acinar Proliferation
ASTM	American Society for Testing and Materials
BPH	Benign Prostatic Hyperplasia
bSSFP	Balanced Steady State Free Precession
BW	Bandwidth
CCDF	Complementary Cumulative Distribution Function
CDF	Cumulative Distribution Function
CEUS	Contrast-Enhanced Ultrasound
CI	Confidence Interval
CMM	Coordinate Measurement Machine
CT	Computed Tomography
CZ	Central Zone
DCE	Dynamic Contrast-Enhanced
DICOM	Digital Image and Communications in Medicine
DRE	Digital Rectal Examination
DW	Diffusion-Weighted
EBRT	External Beam Radiotherapy
ER	Endorectal
FA	Flip Angle
FIESTA	Fast Imaging Employing Steady State Acquisition
FLA	Focal Laser Ablation
FSPGR	Fast Spoiled Gradient Echo
Gd-DTPA	Gadolinium Diethylenetriaminepentaacetic Acid
HG-PIN	High-Grade Prostatic Intraepithelial Neoplasia
HIFU	High-Intensity Focused Ultrasound

www.manaraa.com

HRQOL	Health-Related Quality of Life
IQR	Interquartile Range
LED	Light-Emitting Diode
mpMRI	Multi-Parametric Magnetic Resonance Imaging
MR	Magnetic Resonance
MR PING	Magnetic Resonance Prostate Imaging Needle Guidance System
MRE	Magnetic Resonance Elastography
MRI	Magnetic Resonance Imaging
MRSI	Magnetic Resonance Spectroscopic Imaging
Nd-YAG	Neodymium-Doped Yttrium Aluminum Garnet
NDE	Needle Deflection Error
NGE	Needle Guidance Error
NGHE	Needle Guidance Human Error
NTE	Needle Trajectory Error
PDF	Probability Density Function
PDT	Photodynamic Therapy
PET	Positron Emission Topography
PK	Pharmacokinetic
PIVOT	Prostate Cancer Intervention Versus Observation Trial
PPV	Positive Predictive Value
PSA	Prostate-Specific Antigen
PYLL	Potential Years of Life Lost
PZ	Peripheral Zone
RF	Radiofrequency
ROI	Region of Interest
RP	Radical Prostatectomy
SD	Standard Deviation
SNR	Signal-to-Noise Ratio
SPECT	Single Positron Emission Computed Tomography
TE	Echo Time
TR	Repetition Time

www.manaraa.com

TRUS	Transrectal Ultrasound
TRUS-GB	Transrectal Ultrasound-Guided Biopsy
TTL	Transistor-Transistor Logic
TZ	Transition Zone
US	Ultrasound

www.manaraa.com

Chapter 1.

Introduction

The work in this thesis is concerned with advances in technology and techniques for the treatment of clinically localized prostate cancer. The need for less invasive prostate cancer treatments that cause fewer treatment-related side effects than traditional approaches has been widely recognized, resulting in the emergence of a wide variety of new ablative modalities for focal therapy. As a result, there is continued debate in the urologic community regarding which modality holds the most promise for achieving the goals of focal therapy. The answer depends not only on which energy modality is employed, but strongly on the specific technologies and techniques employed by the interventionalist delivering the therapy. To this end, the work described in this thesis is aimed at improving the technology and techniques used for the delivery of prostate focal laser ablation (FLA) therapy under magnetic resonance image guidance. Such improvements will allow a more accurate evaluation of the true potential of FLA for achieving the goals of focal therapy as clinical trials progress.

1.1 Prostate Cancer

1.1.1 Prostate Cancer Epidemiology

Prostate cancer remains the most commonly diagnosed solid organ malignancy in North American men.[1] In Canada, this amounts to an estimated 23,600 new cases of prostate cancer in 2013, and a lifetime probability of developing prostate cancer of 14.3%.[2] In

www.manaraa.com

other words, approximately 1 in 7 men will develop this disease during their lifetime, and it is estimated that 3,900 men will die of it in 2013 (approximately 1 in 6 diagnosed).

1.1.2 The Impact of Prostate Cancer

Cancer continues to be the biggest killer of Canadians, causing over a million potential years of life lost (PYLL) in 2009.[2] Having caused 35,600 PYLL in Canadian men in 2009, prostate cancer is the third largest contributor to PYLL, next to colorectal (65,100 PYLL) and lung (152,200 PYLL) cancers.

While premature death is arguably the highest cost of prostate cancer, there are significant costs to health-related quality of life (HRQOL) for patients living with the disease. A recent study by Reeve *et al.*[3] prospectively compared HRQOL of patients diagnosed with prostate cancer before and after the diagnosis to a control group. Their results showed a significant decline in physical and mental health, and social aspects of the patient's lives as compared to the control group, and that the largest declines were observed within the first 6 months of diagnosis. This finding, along with the observation that HRQOL before diagnosis of men diagnosed with prostate cancer was similar to that of the control group, suggests that the process of undergoing treatment as well as the diagnosis itself both carry a heavy burden. While the study by Reeve *et al.* is the only such study (to the authors of the study's knowledge) incorporating HRQOL data taken *before* a diagnosis, the patient population studied was limited to American Medicare beneficiaries ≥ 65 years old. However, it is not difficult to imagine how a prostate cancer diagnosis could just as substantially affect a younger man, and evidence from other studies supports this theory.[4] In fact, some treatment-related effects have actually been shown to be worse in younger men.[5] Irrespective of age, the anatomical location of the

www.manaraa.com

prostate gland relative to the rectum, bladder, urethra and delicate neurovascular bundles (NVBs) means that any treatment to the prostate is likely to result in a decrease in urinary, bowel, and sexual health.[4] This problem of challenging anatomy is reflected in the types of treatment-related side effects associated with common types of prostate cancer therapies. Pertinent examples include an association of radical prostatectomy with adverse urinary function, and external-beam radiation therapy with adverse bowel function.[6]

1.2 Prostate Cancer Diagnosis

The four most common methods by which prostate cancer is diagnosed are the prostate specific antigen (PSA) test, the digital rectal examination (DRE), biopsy, and imaging. This section highlights the benefits and shortcomings of each of these types of tests for detecting prostate cancer.

1.2.1 The Prostate Specific Antigen Test

Prostate specific antigen (PSA) is a glycoprotein produced by the prostate gland. In the early 1980s, researchers discovered that PSA could be detected in the blood, and shortly thereafter a landmark study by Stamey *et al.*[7] showed that PSA levels in the blood correlated with the stage of prostate cancer, and were proportional to the estimated volume of the tumour.[8] It is thought that the increase of PSA in the bloodstream is caused by the disturbance of the normal prostate glandular structure due to invasion by cancer.[9] Following this discovery, the use of PSA as a screening tool for prostate cancer became widespread, and the number of prostate cancer diagnoses in Canada saw a substantial increase, reaching a sharp peak in 1993 (see Figure 1.1).[2, 10]

www.manaraa.com

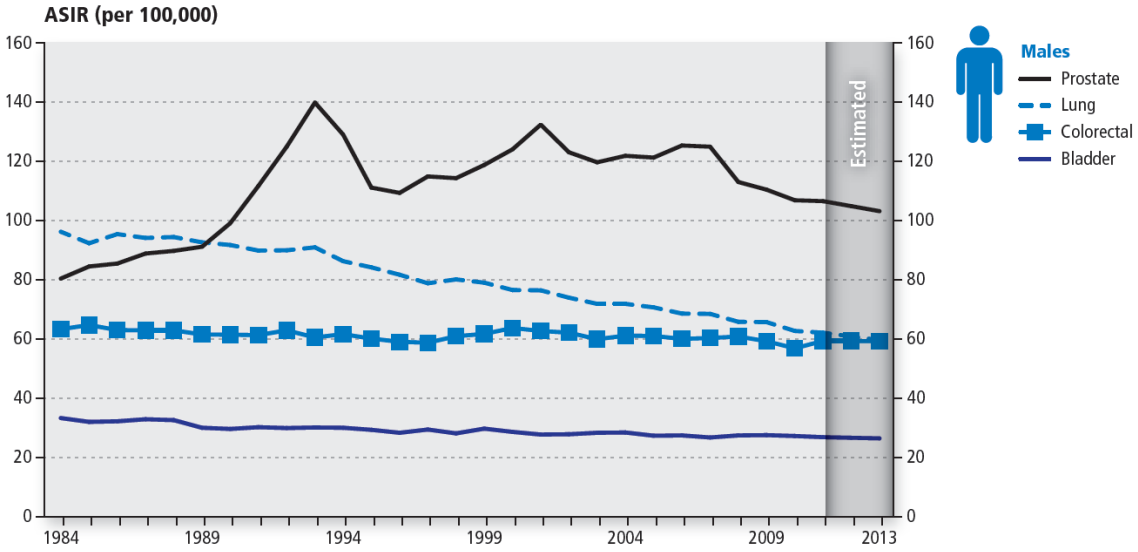

Figure 1.1: Age standardized incidence rates of prostate cancer in Canada. (Image taken from [2].)

The age-standardized mortality rate of prostate cancer in Canada since 1979 reached a maximum of 31.2 deaths per 100,000 men in 1991 and is estimated to be 17.8 deaths per 100,000 men in 2013. This 43% decrease in mortality rate in the last two decades is impressive; however, it is generally attributed more to advances in treatment than to the increased rate of early detection attributed to PSA screening.[2] For the same reasons, there is currently much debate regarding the true value of PSA screening, as it is now understood that PSA screening leads to overdiagnosis and overtreatment in some men whose cancer may not have ever progressed enough to alter their HRQOL if left undetected.

The PSA test also suffers from several sources of inaccuracy. Most notably, factors other than prostate cancer may cause an increase in serum PSA, including benign prostatic hyperplasia (BPH), prostatitis, and prostate biopsy.[9] Any one of these factors can contribute to a false positive test result, causing a patient to receive an unnecessary biopsy, or, if the biopsy is positive, an overestimation of the aggressiveness of treatment required.[11] Despite these issues, and not being recommended as a population-based

www.manaraa.com

screening tool in Canada, PSA testing is still available to men who have been well-informed of the risks of overdiagnosis, and remains the most common method by which prostate cancer is initially diagnosed.

1.2.2 Digital Rectal Examination

The digital rectal examination (DRE) is a basic test for detecting prostate cancer in which the physician palpates the prostate through the patient's rectum using a gloved finger. The DRE is sensitive to the presence of prostate cancer in the peripheral zone (PZ) of the prostate, as the PZ is adjacent to the rectal wall. In these cases, the physician may detect a hardening of the tissue that is especially suspicious if it is asymmetric with respect to the left and right lobes of the prostate. Generally, the result of a DRE is considered along with PSA level in determining the risk of prostate cancer. It has been shown that the positive predictive value (PPV) of DRE is low in patients with a low PSA (< 4.0 ng/ml), and it is therefore not a reliable independent predictor of prostate cancer in such patients.[12] In addition, DRE can miss prostate cancer in regions of the prostate other than the PZ, and it therefore must be used in conjunction with other tests that are sensitive to the presence of the disease in other regions in order to exclude its presence.

1.2.3 Biopsy

Biopsy of the prostate results in the collection of small tissue samples obtained by the insertion of specialized needles, usually through the patient's rectum under transrectal ultrasound (TRUS) guidance. The small tissue samples (biopsy cores) obtained during biopsy are then prepared for examination under a microscope for analysis by a pathologist. By examining the appearance of the structure of the glands and the individual

www.manaraa.com

cells comprising them, a pathologist is not only able to determine if cancerous tissue is present in the tissue sample, but is also able to grade the cancer, giving an indication of the aggressiveness of the disease. Figure 1.2 shows an example of a sample of cancerous tissue, as seen under a light microscope. The figure shows how the glands of the prostate, as well at the individual cells comprising them, are visible.

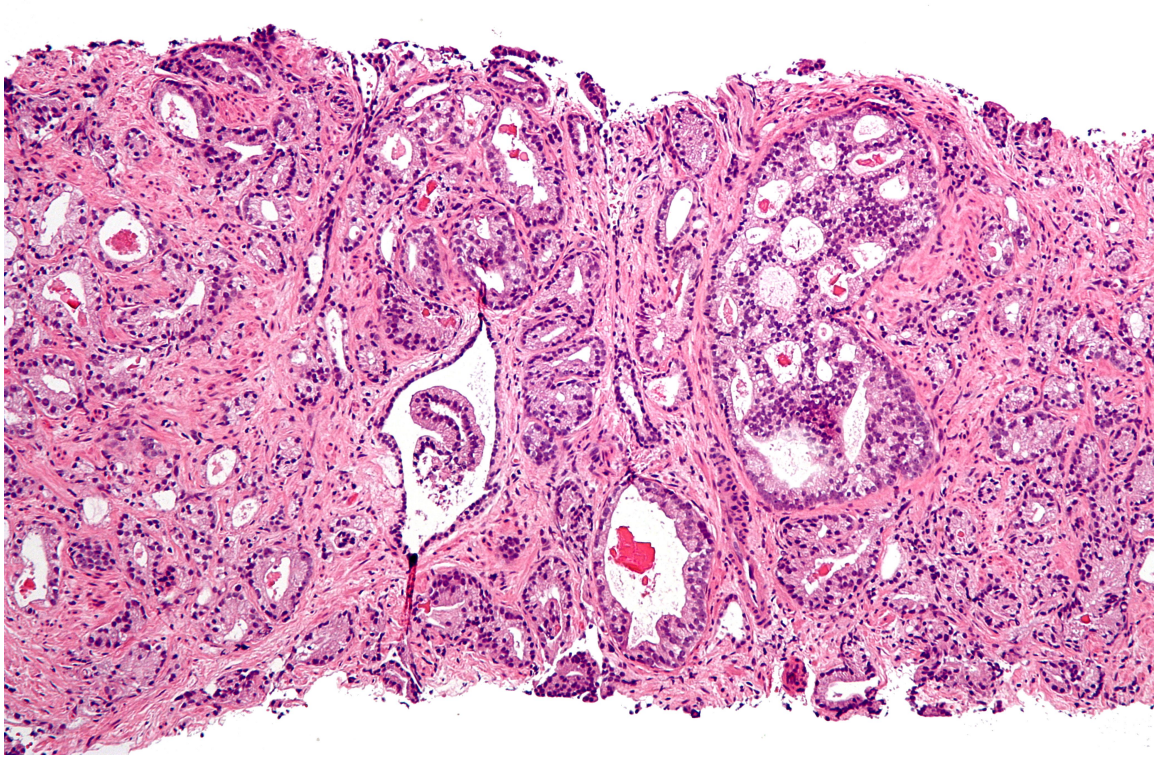

Figure 1.2: Light micrograph of a sample of prostate tissue, stained with hematoxylin and eosin (H&E). At this level of magnification, the individual prostate glands and the cells comprising them can be seen. (Image © 2010 Nephron / Wikimedia Commons)

If cancer is found in the biopsy cores, it is graded according to the Gleason grading system, which assigns the sample a number ranging from 1 (least aggressive) to 5 (most aggressive). The Gleason score is calculated as the sum of the two most frequently occurring Gleason grades present in all biopsy samples. Note that, for example, a Gleason score of 4 + 3 = 7 differs from one of 3 + 4 = 7, in that pattern 4 occurs more frequently than pattern 3, making 4 + 3 a potentially more aggressive cancer than 3 + 4.

www.manaraa.com

The Gleason score from biopsy samples has become a very important tool for estimating the prognosis of prostate cancer in each individual patient, and is a key tool for guiding the selection of the appropriate treatment. However, while an experienced pathologist's grading of cancer within each biopsy core is generally considered to be very accurate (and is therefore considered the gold standard method of grading),[13] sampling errors inherent in the biopsy procedure can lead to unreliable estimates of the total gland's burden and/or aggressiveness (*i.e.* Gleason score) of prostate cancer.[14]

1.2.3.1 Transrectal Ultrasound (TRUS)-Guided Biopsy

Transrectal ultrasound-guided biopsy (TRUS-GB) remains the most common method of obtaining tissue samples for the diagnosis of prostate cancer. In the TRUS-GB approach, the patient is placed in a lateral decubitus position, and an ultrasound probe is inserted through the anus to visualize the prostate and biopsy needles through the rectal wall. Biopsy needles are then directed through a needle guide mounted to the ultrasound probe, and biopsy cores are taken from regions in the prostate known to have a high probability of developing cancer. Figure 1.3 shows the zonal anatomy of the prostate.

www.manaraa.com

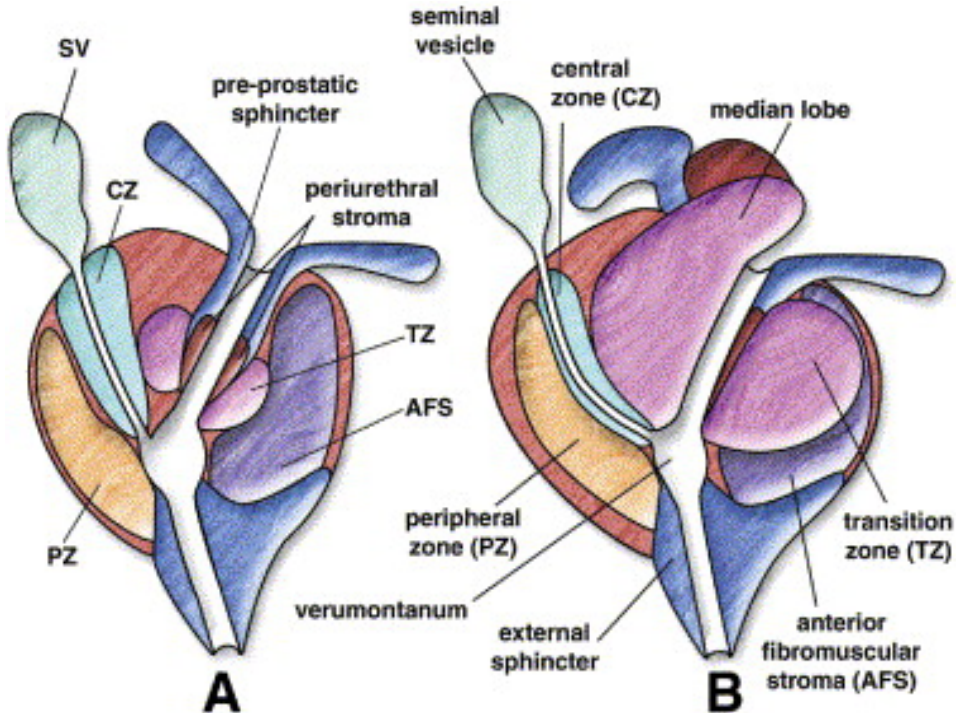

Figure 1.3: Zonal anatomy of the prostate: a) young, healthy male, b) older male with benign prostatic hypertrophy (BPH), causing enlargement of the transition zone (TZ). (Reproduced with permission from Ref. [15])

70 - 80% of prostate cancers are found in the peripheral zone (PZ), and therefore the first round of systematic biopsies usually aims to exclusively or mostly sample this region. The accepted standard for several years was an initial sextant (6 core) biopsy scheme, but the standard number of cores has increased to 10 - 12, as it has been demonstrated that, in up to 1 in 3 cases, the sextant biopsy method will underestimate the underlying Gleason grade present in the gland.[16] Increasing the number of biopsy cores taken will increase the probability of sampling cancerous tissue, if it is present, but also results in an increase in symptoms including urinary retention, sepsis and dysuria.[17] In addition, the systematic TRUS-GB approach has difficulty sampling the anterior, midline, and apex of the prostate.[18] For these reasons, and with recent advances in imaging of prostate cancer, a targeted biopsy approach is receiving increased attention.

www.manaraa.com

1.2.3.2 Targeted Biopsy

If the presence of prostate cancer is still suspected after a negative biopsy, the common practice is to perform a repeat biopsy, perhaps increasing the number of cores taken. Not only is it undesirable to continue repeating a biopsy procedure due to the associated discomfort and side effects, but a repeat systematic biopsy may suffer from the same sampling error issues as the initial biopsy, making the test no more sensitive to the presence of cancer than the first biopsy.[19] Under TRUS guidance, the physician will attempt to sample previously unsampled areas in the prostate; however, there is no guarantee that previously sampled regions aren't resampled. In addition, if high-grade prostatic intraepithelial neoplasia (HG-PIN) or atypical small acinar proliferation (ASAP) histopathological patterns are found on the initial biopsy, the area surrounding where these patterns were found should be resampled, as they are often markers for prostate cancer.[20, 21] The detection rate of a second systematic biopsy after an initial negative one has been demonstrated to range from 10% - 20%, clearly demonstrating the poor sensitivity of the initial biopsy for detecting prostate cancer in some patients.[19, 22]

In an attempt to remedy some of the aforementioned issues, the concept of targeted biopsy, in which regions of the prostate that appear suspicious on imaging are sampled, has recently developed growing interest.[18] This approach has been made possible by advances in imaging techniques, particularly those of magnetic resonance imaging (MRI), resulting in promising accuracy for detecting, localizing, and potentially grading prostate cancer using imaging.[23] By ensuring that regions suspicious on imaging are sampled during subsequent biopsy sessions, the goal is to increase the probability of detecting clinically significant cancer, thereby reducing the number of

www.manaraa.com

subsequent biopsies required, and increasing the accuracy of the Gleason score obtained by biopsy.[18] Obtaining an accurate Gleason score is crucial in directing the optimal therapy for each patient, as an error as small as one point on the scale could substantially alter the type of treatment received.[16]

The performance and potential clinical utility of the targeted biopsy approach has been studied by several researchers. The prevalence of a lesion deemed suspicious for prostate cancer on MRI among men with a clinical suspicion of prostate cancer has been estimated as 63%, when combining the results of two studies in which MRI was performed prior to biopsy.[24, 25] This relatively high prevalence suggests that there may be a role for MRI in guiding the biopsies of a substantial proportion of men with suspicion of prostate cancer. Pooled data from several studies comparing the systematic biopsy approach to targeted biopsy in either the same man or between randomized groups showed a cancer detection rate of 36% for systematic biopsy and 48% for targeted biopsy.[18] In addition, these studies found that cancer was detected in 30% of targeted cores, compared to 7% of cores from systematic biopsies, indicating that the number of cores required to detect cancer is less when using targeted biopsy (*i.e.* it is more efficient). One group studied the detection rate of MRI-guided targeted biopsy for clinically significant cancer in men with a previous negative TRUS-GB, and found a 52% detection rate.[26] This result is impressive, considering the 10% - 20% detection rate associated with subsequent systematic biopsies after an initial negative one. At least one group has studied the effect of augmenting systematic biopsy with targeted biopsy, and found that doing so increased the rate of detection of clinically significant cancer from 14% to 19%.[18]

www.manaraa.com

There are several issues with many of the studies on targeted biopsy performed to date, including variations in the definition of clinically significant disease, limited sample sizes, selection biases, and confounding effects such as the accuracy of the techniques employed. Because of these issues, and in light of the fact that the concept of targeted biopsy has shown promise for more accurately and efficiently providing estimates of the histopathological grade of prostate cancer, large multi-institutional prospective studies have been recommended in order to quantify the technique's true clinical benefit.[18]

1.2.4 Imaging

This section gives a brief overview of the current state-of-the-art of the most common modalities of prostate cancer imaging. The discussion is limited to ultrasound and MRI, as these are the most common modalities used for imaging the gland itself. Other modalities, such as computed tomography (CT), positron emission tomography (PET), single positron emission computed tomography (SPECT), and PET/CT are more commonly used for evaluation of lymph node and/or distant metastases, and their use in imaging the gland itself is either limited (*e.g* CT), or the development of techniques for prostate gland imaging are premature (*e.g.* PET or PET/CT). As this work in this thesis is concerned with the imaging of the prostate gland in patients with localized prostate cancer, a discussion of these imaging modalities was excluded.

1.2.4.1 Ultrasound

Owing to its real-time nature, portability, and low cost compared to MRI, TRUS is the most commonly used modality for imaging the prostate. TRUS has the ability to visualize the zonal anatomy, and does have some ability to visualize prostate cancer in the

www.manaraa.com

peripheral zone. TRUS is also an important tool for obtaining the prostate volume, which is used in some predictive nomograms, and is necessary for computing PSA density.[27] However, TRUS is generally only sensitive to the presence of higher grade, larger tumours,[28] and is not sensitive to tumours in the transition zone, the site of ~20% of prostate cancer.[29] Despite these pitfalls, TRUS is still regarded as an essential tool for guiding prostate biopsies and needles for brachytherapy.[27, 30]

Because prostate tumours often exhibit hypervascularity, techniques such as Doppler and contrast-enhanced US (CEUS) have been developed for potentially increasing the sensitivity of US to prostate cancer. Dopper US is capable of measuring the amplitude of blood flow in the direction perpendicular to the transducer, and displaying this information as colour-coded regions on the screen. Similarly, CEUS employs the use of an injected contrast agent containing highly echogenic microbubbles to enhance visualization of hypervascularized regions. Findings of asymmetric or irregular flow may indicate the presence of prostate cancer.[31] Several studies of the potential utility of CEUS for detecting prostate cancer have been performed, with most of them concluding that the addition of CEUS for targeted biopsy increased the sensitivity of the biopsy procedure for detecting cancer. Results from these studies also generally agreed that biopsies targeted to areas suspicious on CEUS images could not replace systematic biopsy, as ~20% of patients with a positive systematic biopsy were negative on the targeted biopsy.[31, 32] Similar results have been found using Doppler US.[31]

Another emerging technique receiving increased attention for improving the sensitivity of TRUS is US elastography (also called strain imaging). Similar to the age-old technique of DRE, elastography aims to detect regions of prostate tissue with

www.manaraa.com

increased stiffness, which may result from the loss of architecture, disordered growth, and increase in cell density that is typically associated with prostate cancer.[32] Elastography requires mechanical forcing of the tissue combined with real-time imaging to measure the induced tissue motion. The tissue motion data is then processed to provide estimates of tissue mechanical properties at various spatial locations, generating an image of estimated tissue stiffness.[33] Several studies have evaluated the sensitivity of US elastography for detecting prostate cancer and guiding targeted biopsies, with similar results as those for Doppler and CEUS.[31, 32, 34, 35] A recent study on the interpretation of US elastography images of the prostate found that US elastography images were superior to traditional b-mode images for visualizing prostate anatomy, suggesting that this technique could have particular utility in guiding interventional procedures such as brachytherapy and robot-assisted laparoscopic radical prostatectomy.[36, 37] In an attempt to exploit the superior contrast-to-noise ratio of US elastography images, fusion of US b-mode and elastography images has been performed for improving 3D segmentation of the prostate.[38] Research on improved techniques for performing US elastography is ongoing, and more potential applications are being explored.[39]

1.2.4.2 Magnetic Resonance Imaging

Magnetic resonance imaging (MRI) has demonstrated promising performance in detecting and localizing prostate cancer.[27] As a result, MRI has recently seen increased use in clinical practice, most commonly for detecting cancer or for providing targets for a targeted biopsy in men with a previous negative biopsy and continued suspicion of prostate cancer.[40] The sensitivity of MRI for detecting prostate cancer has been

www.manaraa.com

estimated in several studies, and varies greatly depending on the criteria selected for a positive result (which sometimes only includes tumours considered clinically significant), the zone in which the cancer is found in the gland, the type of MRI hardware used (*e.g.* field strength, type of rf coil used), and the sequence or combination of MR sequences employed.[41]

Since the first publication of low-resolution T2-weighted prostate MR images in the 1980s, the technology of MR imaging, through advancements such as increased static field and gradient strengths and the introduction of endorectal (ER) receive coils, has developed to the point of providing high-resolution (*i.e.* ~3 mm slice thickness and sub-millimeter in-plane resolution), high-contrast images of the prostate with fast acquisition times.[23] Modern T2-weighted prostate MR images provide detailed maps of prostate zonal anatomy, demonstrating clear differentiation between peripheral zone (PZ), central zone (CZ), and transition zone (TZ) tissues, though the CZ may not be discernable in men with substantial benign prostatic hyperplasia (BPH).[42] For prostate cancer detection, T2-weighted images demonstrate the best performance in the PZ, where cancer appears as a region of hypointensity compared to adjacent healthy PZ tissue, with the contrast between the two increasing in cancerous tissue of higher Gleason grade.[42] The use of T2-weighted images alone for detecting prostate cancer has demonstrated promising sensitivity, but it suffers from poor specificity in some patients, since the presence of prostatitis, scars, and post-biopsy hemorrhage can also cause regions of hypointensity on T2.[42] Despite this, T2-weighted images have found particular utility in assessing the extent of extra-glandular disease, including extra-capsular extension, neurovascular bundle and seminal vesicle invasion, and local lymphadenopathy and bone

www.manaraa.com

metastases, especially when tri-planar images are used.[23, 27] In addition, T2-weighted images can be used to detect TZ tumours, and may be more sensitive to the presence of anterior PZ tumours than biopsy, since this is a region that is often difficult to sample with TRUS-guided biopsy.[27] Though there is substantial variability in the reported values of sensitivity of T2-weighted images (from 37% - 96%)[41] due to major differences in the definition of cancer, criteria chosen for a positive MRI result, and exclusion of TZ cancers in some studies, intensive work is currently being undertaken to accurately compare MR images of the prostate to whole-mount histopathology.[41, 43-46]

A functional MR imaging technique that has proved useful in identifying prostate cancer is dynamic contrast-enhanced (DCE) MRI. In a typical DCE MRI scan, the patient is injected with a contrast agent and imaged using a 3D T1-weighted MR sequence with high temporal resolution (~ 3 - 10 s), starting before the contrast agent reaches the prostate, and ending after it has completely washed out.[27, 47] Prostate cancer is associated with increased angiogenesis, with new blood vessels exhibiting higher permeability than those of healthy prostate tissue. This effect is thought to be the cause of earlier enhancement and washout of the contrast agent observed in regions of prostate cancer compared to that in healthy tissue.[27] Analysis of DCE MRI images can be performed qualitatively, but quantitative methods that measure pharmacokinetic (PK) parameters are becoming more popular, as they have the potential to reduce the inter-observer and inter-patient variability in the analysis of DCE MR images.[23] As with T2-weighted images, DCE MR images suffer from similar specificity issues, since prostatitis in the PZ and BPH nodules in the TZ appear as cancer, but the reported sensitivity of

www.manaraa.com

DCE MRI is similar to that of T2-weighted images.[42] Current challenges in the clinical adoption of DCE MRI for prostate cancer detection include the limited availability of standardized analysis tools, a lack of consensus regarding optimal acquisition protocols, and limited spatial resolution due to the requirement for high temporal resolution and the inherent trade-off that exists between the two.[40]

Another functional MR imaging technique that is seeing increased use for prostate cancer imaging is diffusion-weighted (DW) imaging. Unlike DCE MRI, DW imaging does not require the injection of a contrast agent, and instead employs the use of motion-encoding gradients to produce image contrast that is related to the diffusion properties of protons in water.[42] By acquiring multiple DW images with different b-values (a setting that quantifies the level of diffusion-weighting in each image), it is possible to compute a quantitative image of apparent diffusion coefficient (ADC).[42] Areas with relatively low ADC values have been shown to correlate with regions of prostate cancer, a result that may be related to a decrease in the volume of fluid-filled ducts that is associated with cancerous prostate tissue.[42, 48] When combined with T2-weighted imaging, DW imaging has demonstrated a sensitivity of 81% and specificity of 84% for detecting prostate tumours larger than 4 mm diameter and Gleason score ≥ 6, though the specificity of T2-weighted and DW images combined was less than that of T2-weighted images alone.[48] Limitations of DW imaging include a high susceptibility to artifacts from magnetic field inhomogeneity, and low in-plane resolution. However, DW imaging can be performed in less time than DCE MR and does not require the injection of a contrast agent, making it potentially more practical for clinical use.[42]

www.manaraa.com

Magnetic resonance spectroscopic imaging (MRSI) is a molecular imaging technique that has also seen use in the prostate. MRSI is unique in that it provides a 3D image of spectral profiles of tissue, and is therefore able to quantify the relative amount of the metabolites citrate, creatine, and choline within the prostate. Since levels of citrate tend to decrease, and those of choline increase in cancerous prostate tissue, a measurement of the relative concentrations of these two can be a marker for prostate cancer.[42] Though MRSI scans can be acquired within a reasonable timeframe (~ 10 - 15 minutes), their interpretation requires special expertise and is very time-consuming, currently limiting the clinical applicability of this technique.[42] Other limitations include a sensitivity to static magnetic field inhomogeneity, limited spatial resolution, and limited specificity, since prostatitis in the PZ also lowers citrate and raises choline concentrations.[23, 42] However, MRSI has shown use in evaluating high-risk cancers, has demonstrated a good sensitivity for TZ tumours (~80%), and may be better than biopsy at detecting recurrent disease after radiotherapy.[27, 41] As such, continued research into improved methods of MRSI is ongoing.[49, 50]

Emerging new techniques for prostate cancer MR imaging include sodium imaging and MR elastography (MRE). Cancerous prostate tissue may contain a higher concentration of sodium than healthy tissue, making sodium concentration a potential marker for the disease. The technique has been previously used to detect other pathologies including stroke, and breast and brain cancer, and a technique for producing quantitative sodium images of mouse prostate has recently been developed.[51] Sodium imaging, like MRSI, is a molecular imaging technique, but has the potential for producing higher resolution images, since there is a lack of other dominant resonances

www.manaraa.com

near that of sodium.[51] As in US elastography, MRE produces images of the mechanical properties of prostate tissue, and has found use in improving registration between *in vivo* and *ex vivo* MRI of the prostate, and may hold promise for improved prostate cancer detection and localization.[52, 53]

With so many available techniques for achieving different contrast in MRI, it is difficult to identify which technique provides the most clinical benefit for imaging prostate cancer. There seems to be a general consensus in the imaging and urologic communities that optimal detection and localization of prostate cancer using MRI will require some combination of T2-weighted images with one or more functional or molecular MR imaging sequences,[42, 54, 55] and the results from various studies have consistently shown that such combinations perform better than T2-weighted imaging alone, quite often improving the specificity over that of each individual technique.[27, 41, 42] Figure 1.4 shows a series of multiparametric MR images of a prostate with histologically-proven prostate cancer, demonstrated how complementary MR images can improve the specificity of MR imaging for prostate cancer detection and localization.

www.manaraa.com

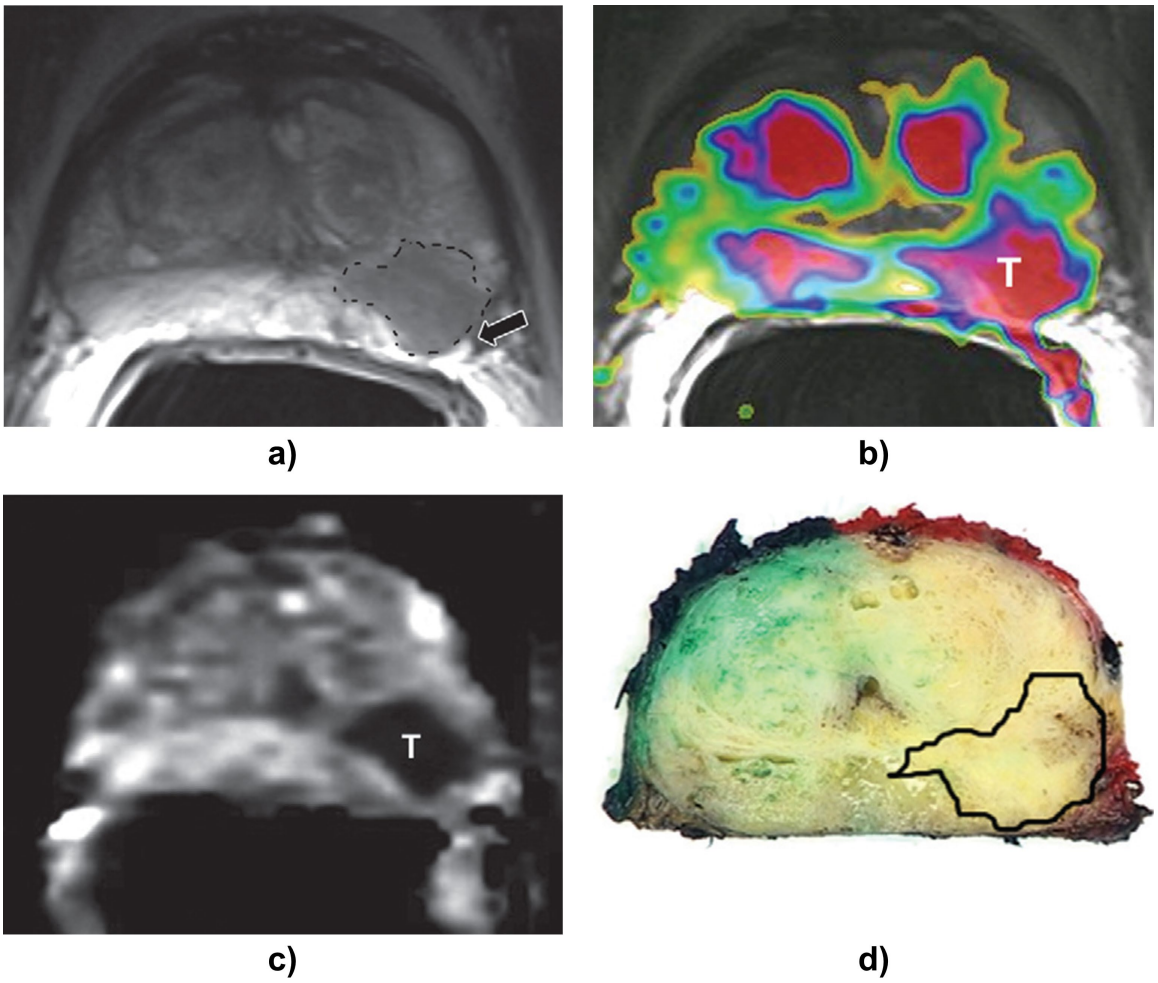

Figure 1.4: Multiparametric MR images of a prostate with histologically-proven prostate cancer: a) T2-weighted image correctly demonstrates the presence of cancer, as indicated by the region of hypointensity, b) a map of K^{trans} (a DCE MRI PK parameter) showing sensitivity to the presence of the tumour, but a lack of specificity in this case, since several other benign areas within the prostate show enhanced areas, c) ADC map which also correctly identified the cancerous region, as shown by the region of hypointensity (restricted diffusion), and d) the region of histologically-proven prostate cancer. (Figure reproduced with permission from Ref. [42])

1.3 Prostate Cancer Treatment

In this section, the prostate cancer treatments most commonly used in clinical practice are discussed in terms of their ability to control prostate cancer at various stages, and rates of treatment-related side effects. Following this, some of the most promising emerging modalities for delivering focal therapy are introduced, with particular attention to focal laser ablation (FLA) therapy, which is of relevance to the rest of the work in this thesis.

www.manaraa.com

1.3.1 Conventional Approaches and the Focal Therapy Concept

The three most common interventional procedures for localized prostate cancer are radical prostatectomy (RP), external beam radiation therapy (EBRT) and brachytherapy. Each of these treatments act on the whole prostate gland, and, since the prostate is in close contact with several sensitive structures (*e.g.* urethra, rectum, neurovascular bundles and bladder), each is associated with similar rates of long-term urinary incontinence, bowel toxicity and sexual dysfunction.[6, 56]. Studies have shown that, while whole-gland treatments such as RP can provide excellent control of disease in men with low- to intermediate-risk prostate cancer, men with this stage of the disease are currently over-treated.[57] In the PIVOT trial (Prostate Cancer Intervention versus Observation Trial), 731 men with localized prostate cancer were randomized to either RP or observation and followed for a median of 10.0 years. Results from the PIVOT trial showed no significant difference in the rates of prostate cancer-specific mortality between groups of patients treated with RP or observation, but patient-reported rates of urinary incontinence and erectile dysfunction were significantly different (17.1% vs. 6.3% and 81.1% vs. 44.1%, respectively).[58] In a similar trial, RP was show to have an absolute reduction in risk of prostate cancer death of 5.4% over watchful waiting at 12 years follow-up. However, it was also found that nearly all men in the RP group who died from prostate cancer had tumour growth outside the prostate capsule, suggesting that men with truly organ-confined disease may not require whole-gland therapy.[59] In addition, patients in the low-risk category have been shown to receive equal benefit from treatment with RP, EBRT, or brachytherapy.[60, 61]

www.manaraa.com

While it may be agreed upon that men with low- and intermediate-risk prostate cancer are being over-treated, the optimal type of treatment for these men is not yet clear. Evidence in the literature suggests that watchful waiting may constitute under-treatment, and men who choose active surveillance often either suffer a decreased HRQOL knowing that the disease is left untreated, or eventually opt for definitive treatment even with a lack of evidence of progression.[62-64] In an attempt to provide a more optimal treatment option for men with low- to intermediate-risk prostate cancer, the concept of focal therapy is currently being investigated. The hypothesis of focal therapy is that treatment of the dominant prostate tumour, while leaving the rest of the gland intact, may provide sufficient control of the disease, while causing a minimal amount of treatment-related side effects.[65] There is currently much debate regarding the definition of a "dominant lesion", which patients could benefit most from this approach, and which modality of treatment delivery is best suited to this approach.[66] However, several energy-delivery modalities, including high-intensity focused ultrasound (HIFU), cryotherapy, photodynamic therapy (PDT), and laser ablation have demonstrated an ability to create focal regions of ablated tissue within the prostate with limited morbidity.[67]

1.3.2 Focal Laser Ablation Therapy

Focal laser ablation (FLA) is an attractive modality for the controlled ablation of focal regions within the prostate. The first reported use of laser ablation for the treatment of localized prostate cancer was in 1984, in which Beisland *et al.* used a neodymium-doped yttrium aluminum garnet (Nd-YAG) laser at 1,064 nm to ablate prostate tissue using a combined transurethral and suprapubic approach in 47 patients.[68] Results from

www.manaraa.com

this case series showed that it was possible to ablate focal regions within the prostate while avoiding damage to the rectal wall.

Following the work of Beisland *et al.*, in which the only method of temperature monitoring was via a single temperature probe attached to a palpating finger in the rectum, Amin *et al.* reported laser ablation (referred to the authors as interstitial laser photocoagulation) of a focal lesion in one patient by inserting needles transperineally, and monitoring the region of ablation in real-time using b-mode and colour Doppler US.[69] Post-treatment biopsy of this patient revealed some remaining cancer, but the technique allowed re-treatment in this region without additive side effects. As more cases of prostate FLA were performed, the technique used for image-guidance advanced, with Lindner *et al.* completing a Phase I trial studying the safety of MRI-targeted, US-guided FLA therapy using CEUS to monitor treatment progression.[70, 71] In this trial, the authors found no significant decrease in erectile or urinary function due to the treatment, but unfortunately 50% of the 12 patients treated had positive post-treatment biopsies. The authors attributed the inaccuracy in the treatment delivery to registration accuracy between the pre-treatment MR and intra-treatment US images, as well as limitations in the ability of MRI to accurately visualize small tumours.[71]

In an attempt to circumvent some of these issues, Raz *et al*. performed MRI-guided FLA therapy in 2 patients, taking advantage of the ability of MRI to provide real-time guidance of both needle insertion and temperature monitoring during laser application.[72] Following the treatments, a DCE MRI scan was performed to compare the estimated region of ablation to the pre-treatment region, as defined on combined T2-weighted and DW MR images used for planning. They found that the DCE MR images,

www.manaraa.com

which have been shown by Lindner *et al.* to correlate well with the region of ablated tissue on whole-mount histopathology, also correlated well with the region predicted by MRI thermometry.[72, 73]

Over the last three decades, the technique of performing FLA therapy for localized prostate cancer evolved from using a 1,064 nm laser with only a single point of temperature monitoring, to a minimally-invasive transperineal procedure that is targeted and monitored using MRI, and delivered with a 980 nm laser at lower power and for shorter laser application times than previously achieved.[74] However, despite these technical advances, each case series or clinical trial studying FLA therapy has consistently demonstrated a high rate of detection of residual or recurrent cancer on post-treatment biopsy. For this reason, it is part of the overarching hypothesis of this thesis that advances in the technology and techniques used to deliver MRI-guided prostate FLA therapy could enable this technique to consistently provide a high level of control of localized prostate cancer. The first proposed improvement is the development of an MRI-compatible mechatronic system for the accurate guidance of needles for prostate FLA.

1.4 Challenges in MRI-Guided Needle-Based Prostate Interventions

The unique electromagnetic environment and physics of image encoding in MRI present several challenges to the development of mechatronic devices that must operate in the bore of an MRI scanner. The nature of each of these challenges will be described in this section.

www.manaraa.com

1.4.1 The MRI Environment

1.4.1.1 Effects of MRI on Devices

The strong static (*i.e.* constant in time) magnetic field present in the bore of a clinical MRI scanner (usually 1.5 T - 3.0 T) places restrictions on the use of any magnetic materials. When placed near the bore of an MRI scanner, magnetic materials will experience a force that is proportional to magnitude of the spatial gradient of the magnetic field. This force has the potential to accelerate objects, turning them into deadly projectiles that could easily cause injury.[75] At the center of the MRI bore, where the static magnetic field is nearly spatially uniform, no force will be induced on an object; however, any non-spherical object will still experience a torque.[76] Unfortunately, this means that the use of some standard engineering materials such as martensitic stainless steel is prohibited. Since these materials have particular utility in the construction of precision devices, alternate custom solutions must be sought.[75, 77]

Spatial encoding of the MR signal in tissue is performed by applying fast-switching magnetic field gradients. Depending on their size, shape, and orientation, electrically conductive materials placed in the MRI bore during image acquisition may experience vibration or heating due to currents induced by these switching gradients.[77, 78] This effect places further limitations on the materials available for use in an MRI-guided device. For example, aluminum is an extremely versatile (non-magnetic) material, but its high electrical conductivity places restrictions on its use in MR. The use of large plates or loops of conductive materials should be avoided, especially if they are positioned near the gradient coils.[77] In addition to vibration and heating, the switching magnetic field gradients have the potential to induce currents in the electrical circuits of a

www.manaraa.com

mechatronic device, thereby introducing noise into the signals from sensors, or causing erratic behavior of actuators.

The third type of effect that an MRI scanner can have on a device is due to the transmitted rf field, which can induce currents in conductive materials. Objects with the greatest potential for rf heating are those with an elongated shape, or structures that form a loop.[76] In the context of the work in this thesis, rf heating presents the biggest challenge in terms of selection of MRI compatible needles.

1.4.1.2 Effects of Devices on MRI

In addition to avoiding negative effects to the device from the MRI, the presence of a device operating within an MRI scanner must not degrade the quality of the images being acquired. The primary mechanisms by which a device may degrade image quality are through the introduction of magnetic field inhomogeneity or rf noise.

A magnetic object placed within an MRI scanner will cause a spatial distortion of the static magnetic field (inhomogeneity), an effect that can also be caused by eddy currents induced in a conductive material by the switching gradient fields.[75] Any deviation of the static field in the image field-of-view (FOV) from uniform will result in spatial distortions of the image that is generated.[79] Spatial distortions take the form of slice-select error, which is incorrect placement of the out-of-plane position of an image slice, and in-plane distortions, which cause the shape of objects (*i.e.* the patient's anatomy) to contain error.[80] The magnitude of these errors is proportional to the magnetic susceptibility of the foreign material, inversely proportional to the strength of the gradient fields used to encode position, and inversely proportional to the cube of the distance from the image to the foreign object. The amount of image distortion can

www.manaraa.com

therefore be proportionately reduced by increasing the strength of the gradients. However, for all other imaging parameters remaining the same, doing so requires an increase in rf receiver bandwidth (*i.e.* the range of frequencies to which the rf receive system is sensitive), thereby increasing the amount of noise in the image. In addition, the strength of the slice-select gradient is generally not user-controllable.[79] In regions where the magnetic material has caused a substantial gradient in magnetic field across image voxels, the resulting signal in the image in these voxels will be decreased unless a spin echo sequence is used.[79]

Mechatronic devices may also emit rf signals (noise) that affect the quality of images acquired.[80] If the rf noise is concentrated at a particular frequency, it may result in a so-called "zipper artifact" in the images, appearing as a bright line. rf noise across a wide frequency range will result in uniform noise in the image, resulting in a decrease in the signal-to-noise ratio (SNR), and a decreased ability to visualize the anatomy being imaged.[80] SNR can be improved by decreasing the receiver bandwidth, but this comes at the expense of decreased gradient strength (with all other parameters the same), thereby increasing any distortions due to static field inhomogeneity. Therefore, attempts to shield all electrical components present in the mechatronic device should be made, and cables entering the MR scanner room should be connected through low-pass filters.[77, 80]

1.5 Existing MRI-Guided Prostate Needle Guidance Devices & Techniques

The past decade has seen a substantial increase in the number of new devices developed for MRI-guided prostate interventions. Most of these devices have been developed for

www.manaraa.com

biopsy, brachytherapy, or focal therapy of the prostate, and have taken either the transrectal, transperineal, or even transgluteal access approaches. This section will focus on a review of the current devices and techniques previously employed for transperineal delivery of needles to the prostate under MRI-guidance.

1.5.1 The Conventional Approach

The most commonly used approach for transperineal prostate needle guidance is with the use of a fixed grid template. The template consists of a regular grid of holes, with the rows identified by number, and columns identified alphabetically. In a TRUS-guided transperineal procedure such as brachytherapy, the grid template is fixed to a stabilizer on which the US probe is also mounted. This fixed relationship between the US probe and template allows the template holes to be superimposed onto the US image of the prostate, thereby allowing the physician to target specific regions in the prostate by using the appropriate template hole. Since this technique is so widely-used for brachytherapy, it should come as no surprise that the first attempts at MRI-guided transperineal prostate interventions were also performed using a fixed template. In 1998, D'Amico *et al.* reported MRI-guided prostate interstitial prostate brachytherapy in 9 patients. The authors performed the procedure in a 0.5 T interventional MRI unit, and inserted needles under real-time MR imaging guidance using a perineal template.[81] Two years later, the same group reported a similar case of transperineal MRI-guided prostate biopsy in which the prostate was imaged at the start of the procedure for identification of suspicious region(s). A random sextant biopsy was then performed, followed by targeted biopsy of the suspicious region(s). In this case, the MRI-guided approach proved especially valuable, since the patient had previously undergone a proctocolectomy, and was

www.manaraa.com

therefore ineligible for TRUS-guided biopsy. In addition, the two targeted biopsy cores were positive for cancer, whereas the sextant samples were negative. This publication therefore made an excellent case for the advantages of performing prostate interventions under MRI-guidance.[82] Hata *et al.* followed a similar approach, performing MR-guided prostate biopsy in an open MRI using a grid template that was registered to the MRI using an optical tracking system. Similar to the case done by D'Amico *et al.*, they visualized suspected tumours during the procedure, and in one of the two cases performed, found positive targeted biopsy samples and negative samples from the sextant cores. In the other case, while all biopsy cores were found to be negative, the use of MRI-guidance proved valuable in ensuring biopsy needles reached the peripheral zone, which was very thin in this patient due to the presence of BPH.[83]

1.5.2 Mechatronic or Robotic Devices

As the technique of MRI-guided prostate interventions became more popular, the need for improvements in guidance technology became evident. While the technique of using a grid template to guide needles in an open-bore MRI had proved feasible, most clinical centers only have access to closed-bore MRI scanners intended for diagnostic use. In addition, closed-bore scanners have the potential for producing much higher quality images due to increased field strengths and higher gradient performance, making them more attractive.[84] However, closed-bore MRI scanners present a challenge in the available workspace for an MRI-guided prostate procedure: the patient, along with all interventional devices, must fit within a bore of ~55 - 60 cm diameter that is generally ~1.5 - 2 m in length, while leaving enough room for physician access.[77]

www.manaraa.com

In spite of these workspace constraints, Susil *et al.* and Menard *et al.* presented the results of 10 MRI-guided prostate HDR brachytherapy procedures performed on 5 patients within the bore of a 1.5 T clinical closed bore MRI scanner. Their approach employed the use of a custom-made integrated grid template and endorectal (ER) receive coil device with the patient placed in a lateral decubitus position. The authors reported good dosimetric results with their technique, which they partially attributed to the advantage of having high-field intra-treatment MR images at their disposal for needle guidance and target delineation. However, they reported a long overall procedure time (> 5 hours), and anticipated possible issues with having the patient in the lateral decubitus position, as well as instability of the prostate gland as compared to the standard lithotomy position used for brachytherapy.[84, 85]

In attempts to overcome the issue of limited physician access in a clinical MRI scanner, several researchers developed novel custom needle guidance robots. One of the first reported robotic systems for an MRI-guided prostate procedure was designed for use in an open MRI scanner, and consisted of a 5 axis linear motion module located above the MRI bore that actuated the motions of two rigid arms reaching into the bore of the scanner. The authors suggested their device could be used for the navigation of needles for prostate brachytherapy.[86] Other seminal works included a pneumatic cylinder-actuated robot presented by DiMaio *et al.*, and a unique parallel robot called "MRI Stealth" employing the use of newly developed pneumatic stepper motors by Muntener *et al*. in 2006.[87-89] The pneumatic device originally reported by DiMaio *et al*., which was intended for biopsy and brachytherapy, demonstrated good MRI compatibility and accurate targeting abilities.[90, 91] The MRI Stealth robot saw extensive preclinical

www.manaraa.com

evaluation in terms of positioning accuracy and repeatability, seed placement accuracy in tissue-mimicking phantoms, and tests in a canine model.[92, 93] Though clinical tests of the MRI Stealth robot (AKA MRBot) have yet to be reported, the same group indicated a possible clinical trial using the device, and development of a commercial system for brachytherapy.[94] Various devices employing novel MRI-compatible actuation techniques were developed, including a binary robot employing a parallel arrangement of dielectric elastomer actuators, a similar concept employing newly developed "air muscle" actuators, and a concept of a wire-driven manipulator for MRI-guided prostate cryoablation.[95-97] Fully-actuated robots that have seen use in humans include a device employing hydraulic actuation for positioning and a pneumatic needle-tapping system described by van den Bosch *et al.*, and an ultrasonic motor-driven robot reported by Goldenberg *et al*.[98-101] Su *et al.* presented a unique design of a master-slave user-controlled robot featuring a custom-made optical force sensor for haptic feedback.[102] Recently developed systems still in the preclinical phase include a 4 degree-of-freedom (DOF) pneumatically-actuated parallel robot, first presented by Song *et al.*, and a piezoelectric motor-driven robot designed for the guidance of needles and adapted for the guidance of a concentric tube manipulator, demonstrated by Su *et al.*[103, 104]

1.6 Thesis Hypothesis and Objectives

The central hypothesis of this thesis is that an MRI-compatible mechatronic needle-guidance system, combined with a treatment planning strategy that recognizes and compensates for the uncertainties in system performance, can provide an accurate and reliable method for completely ablating focal prostate cancer targets identified on imaging. Such a method would allow an accurate appraisal of the clinical efficacy of

www.manaraa.com

focal laser ablation therapy for controlling cancer in men with localized prostate cancer, and the level of treatment-related side effects associated with this technique.

1.6.1 Specific Objectives

The four primary objectives of this thesis, described respectively in each of the four main chapters, are to:

I. Develop and validate a method of accurately registering the coordinate system of an MRI-guided interventional device to that of a clinical MRI scanner under the unfavourable conditions generally found in the interventional MRI environment.

II. Develop a mechatronic system for accurately guiding needles within the bore of an MRI scanner. Verify the system's safety and MRI-compatibility, and quantify the achievable accuracy to which it can guide needles to the prostate.

III. Use the system to perform focal laser ablation therapy in men who have consented to participate in an ongoing Phase I/II clinical trial. Quantify improvements gained in usability and clinical workflow, and quantify the achievable accuracy in needle placement.

IV. Develop a method of treatment planning for MRI-guided focal laser ablation therapy that compensates for a given level of uncertainty in needle placement error. Combined with results from the previous objective, this will lead to more precise, evidence-based patient selection criteria for focal laser ablation eligibility, and improved treatment plans to ensure a high probability of complete focal target ablation in each case.

www.manaraa.com

1.7 Outline of this Thesis

The following four chapters form the body of this thesis, and are summarized here:

1.7.1 Chapter 2: The Effects of Magnetic Field Distortion on the Accuracy of Passive Device Localization Frames in MR

The intra-treatment magnetic resonance (MR) imaging environment presents many challenges for the accurate localization of interventional devices. In particular, geometric distortion of the static magnetic field may be both appreciable and unpredictable. This chapter aims to quantify the sensitivity of localization error of various passive device localization frames to static magnetic field distortion in MR.

Three localization frames were considered based on having distinctly different methods of encoding pose in MR images. For each frame, the effects of static field distortion were modeled, allowing errors in rotational and translational pose estimation to be computed as functions of the level of distortion, which was modeled using a first order approximation. Validation of the model was performed by imaging the localization frames in a 3T clinical MR scanner, and simulating the effects of static field distortion by varying the scanner's center frequency and gradient shim values.

Plots of both rotational and translational error in localization frame pose estimates are provided for ranges of uniform static field distortions of 1 – 100 μT and static field distortion gradients of 0.01 – 1 mT/m in all three directions. The theoretical estimates are in good agreement with the results obtained by imaging.

The error in pose estimation of passive localization frames in MR can be sensitive to static magnetic field distortion. The level of sensitivity, the type of error (*i.e.* rotational

www.manaraa.com

or translational), and the direction of error are dependent on the frame's design and the method used to image it. If 2D gradient echo imaging is employed, frames with pose estimate sensitivity to slice-select error (such as the z-frame) should be avoided, since this source of error is not easily correctable. Accurate frame pose estimates that are insensitive to static field distortion can be achieved using 2D gradient echo imaging if: a) the method of determining pose only uses in-plane measurements of marker positions, b) the in-plane marker positions in images are not sensitive to slice-select error, and c) methods of correcting in-plane error in the readout direction are employed. Results from the work in this chapter were critical to the development of the needle guidance system described in Chapter 3.

1.7.2 Chapter 3: A System for MRI-Guided Transperineal Delivery of Needles to the Prostate for Focal Therapy

The purpose of this chapter is to demonstrate the technical capabilities of a new magnetic resonance imaging (MRI)-guided system for delivering needles to the prostate for focal therapy. Included is a presentation of the design of the system and its user interface, evaluation of MR-compatibility, and quantitative evaluation of guidance accuracy and repeatability within the bore of a clinical MRI scanner. The system consists of a manually-actuated trajectory alignment device that allows a physician to precisely align a set of needle guides with an intended target in the prostate within the bore of a clinical closed-bore MRI scanner. Needle insertion is then performed transperineally, with the patient in the bore of the MRI, and custom software provides monitoring of thermal ablative procedures.

www.manaraa.com

The system is shown to have a minimal effect on image distortion, and only a 6% decrease in image signal-to-noise ratio. Through needle insertion tests in tissue-mimicking phantoms, the system's potential for reliably guiding needles to intra-MR targets within 2.64 mm has been demonstrated. Use of the system to deliver focal laser ablation therapy to two patients showed that it can be used to deliver needles with minimal disruption of workflow, and in less time than when insertions are performed freehand or with a fixed grid template.

Results from needle insertion tests in phantoms suggest that the system has the potential to provide accurate delivery of focal therapy to prostate tumours of the smallest clinically significant size. Initial tests in two patients showed that needle deflection was larger than in phantoms, but methods of manually compensating for this effect were employed and needles were delivered to treatment sites with sufficient accuracy to deliver effective treatment. In addition, the treatment was delivered in less time than with a fixed grid template or freehand insertions. Despite this success, methods of reducing or compensating for needle deflection are needed in order to fully utilize the potential of this system, and further reduce total procedure time.

1.7.3 Chapter 4: A Mechatronic System for In-Bore MR-Guided Insertion of Needles to the Prostate: Experiences Using the System for Prostate Focal Laser Ablation in Eight Patients

The purpose of this chapter is to present our experiences in development and initial clinical evaluation of a novel mechatronic system for in-bore guidance of needles to the prostate for magnetic resonance (MR)-guided prostate interventions. We report feasibility of use and accuracy of this device in the context of focal laser thermal ablation therapy

www.manaraa.com

for localized prostate cancer. Patients underwent MR-guided focal laser thermal ablation with device-mediated laser fiber delivery. We recorded targeting error and needle delivery time and compared device performance to a fixed grid template approach.

Eight patients, requiring a total of 29 needle insertions, were treated with use of the system. Median needle guidance error was 3.4 mm (IQR 2.1 – 5.2 mm) and median needle guidance time was 8 min (IQR 6.5 - 10.5 min). The median time required to guide each needle to its target using this device was significantly less than with use of the template: 8 vs. 18 min ($p < 0.0001$, 95% CI of difference: 5 – 13 min).

Needle guidance time was significantly decreased compared to a fixed grid template approach, and the needle guidance error was within the acceptable range for clinically significant prostate tumours. This system provides a reliable method of accurately aligning needle guides for in-bore needle delivery to the prostate, and an improved workflow for an in-bore procedure.

1.7.4 Chapter 5: Treatment Planning for Prostate Focal Laser Ablation in the Face of Needle Placement Uncertainty

The purpose of this chapter is to study the effect of needle placement uncertainty on the expected probability of achieving complete focal target destruction in focal laser ablation (FLA) of prostate cancer. Using a simplified model of prostate cancer focal target, and focal laser ablation region shapes, Monte Carlo simulations of needle placement error were performed to estimate the probability of completely ablating a region of target tissue.

Graphs of the probability of complete focal target ablation are presented over clinically relevant ranges of focal target sizes and shapes, ablation region sizes, and levels

www.manaraa.com

of needle placement uncertainty. In addition, a table is provided for estimating the maximum target size that is treatable. The results predict that targets whose length is at least 5 mm smaller than the diameter of each ablation region can be confidently ablated using, at most, 4 laser fibers if the standard deviation in each component of needle placement error is less than 3 mm. However, targets larger than this (i.e. near to or exceeding the diameter of each ablation region) require more careful planning. This process is facilitated by using the table provided.

The probability of completely ablating a focal target using FLA is sensitive to the level of needle placement uncertainty, especially as the target length approaches and becomes greater than the diameter of ablated tissue that each individual laser fiber can achieve. The results of this work can be used to help determine individual patient eligibility for prostate FLA, to guide the planning of prostate FLA, and to quantify the clinical benefit of using advanced systems for accurate needle delivery for this treatment modality.

1.7.5 Chapter 6: Conclusions and Future Work

This chapter describes the overall conclusions of all major chapters in the thesis, and provides recommendations for future work that could address some of the remaining challenges.

www.manaraa.com

References

1. R. Siegel, D. Naishadham and A. Jemal, "Cancer statistics, 2013," CA. Cancer J. Clin. **63**, 11-30 (2013).

2. Canadian Cancer Society's Advisory Committee on Cancer Statistics, "Canadian Cancer Statistics 2013", Toronto, ON: Canadian Cancer Society; 2013

3. B. B. Reeve, A. M. Stover, R. E. Jensen, R. C. Chen, K. L. Taylor, S. B. Clauser, S. P. Collins and A. L. Potosky, "Impact of diagnosis and treatment of clinically localized prostate cancer on health-related quality of life for older Americans," Cancer **118**, 5679-5687 (2012).

4. D. T. Eton and S. J. Lepore, "Prostate cancer and health-related quality of life: a review of the literature," Psycho-Oncology **11**, 307-326 (2002).

5. A. L. Potosky, J. Legler, P. C. Albertsen, J. L. Stanford, F. D. Gilliland, A. S. Hamilton, J. W. Eley, R. A. Stephenson and L. C. Harlan, "Health outcomes after prostatectomy or radiotherapy for prostate cancer: results from the Prostate Cancer Outcomes Study," J. Natl. Cancer Inst. **92**, 1582-1592 (2000).

6. J. T. Wei, R. L. Dunn, H. M. Sandler, P. W. McLaughlin, J. E. Montie, M. S. Litwin, L. Nyquist and M. G. Sanda, "Comprehensive comparison of health-related quality of life after contemporary therapies for localized prostate cancer," J. Clin. Oncol. **20**, 557-566 (2002).

7. T. A. Stamey, N. Yang, A. R. Hay, J. E. McNeal, F. S. Freiha and E. Redwine, "Prostate-specific antigen as a serum marker for adenocarcinoma of the prostate," N. Engl. J. Med. **317**, 909-916 (1987).

8. A. R. Rao, H. G. Motiwala and O. Karim, "The discovery of prostate-specific antigen," BJU Int. **101**, 5-10 (2008).

9. J. I. Izawa, L. Klotz, D. R. Siemens, W. Kassouf, A. So, J. Jordan, M. Chetner and A. E. Iansavichene, "Prostate cancer screening: Canadian guidelines 2011," Can. Urol. Assoc. J. **5**, 235 (2011).

10. Y. Fradet, L. Klotz, J. Trachtenberg and A. Zlotta, "The burden of prostate cancer in Canada," Can. Urol. Assoc. J. **3**, S92 (2009).

11. J. B. Eifler, Z. Feng, B. M. Lin, M. T. Partin, E. B. Humphreys, M. Han, J. I. Epstein, P. C. Walsh, B. J. Trock and A. W. Partin, "An updated prostate cancer staging nomogram (Partin tables) based on cases from 2006 to 2011," BJU Int. **111**, 22-29 (2013).

www.manaraa.com

12. F. H. Schröder, A. B. Kruger, J. Rietbergen, R. Kranse, P. van der Maas, P. Beemsterboer and R. Hoedemaeker, "Evaluation of the digital rectal examination as a screening test for prostate cancer," J. Natl. Cancer Inst. **90**, 1817-1823 (1998).

13. M. B. Amin, *Gleason grading of prostate cancer: a contemporary approach*. (Wolters Kluwer Health, 2004).

14. G. L. Andriole, "Pathology: the lottery of conventional prostate biopsy," Nat. Rev. Urol. **6**, 188-189 (2009).

15. P. W. McLaughlin, S. Troyer, S. Berri, V. Narayana, A. Meirowitz, P. L. Roberson and J. Montie, "Functional anatomy of the prostate: implications for treatment planning," Int. J. Radiat. Oncol. Biol. Phys. **63**, 479-491 (2005).

16. C. R. King, J. E. McNeal, H. Gill and J. C. Presti Jr, "Extended prostate biopsy scheme improves reliability of Gleason grading: implications for radiotherapy patients," Int. J. Radiat. Oncol. Biol. Phys. **59**, 386-391 (2004).

17. U. Patel and D. Rickards, *Handbook of transrectal ultrasound and biopsy of the prostate*. (Martin Dunitz, 2002).

18. C. M. Moore, N. L. Robertson, N. Arsanious, T. Middleton, A. Villers, L. Klotz, S. S. Taneja and M. Emberton, "Image-guided prostate biopsy using magnetic resonance imaging–derived targets: a systematic review," Eur. Urol. **63**, 125-140 (2013).

19. J. Bax, D. Cool, L. Gardi, K. Knight, D. Smith, J. Montreuil, S. Sherebrin, C. Romagnoli and A. Fenster, "Mechanically assisted 3D ultrasound guided prostate biopsy system," Med. Phys. **35**, 5397-5410 (2008).

20. D. G. Bostwick, "High grade prostatic intraepithelial neoplasia. The most likely precursor of prostate cancer," Cancer **75**, 1823-1836 (1995).

21. K. A. Iczkowski, T. J. Bassler, V. S. Schwob, I. C. Bassler, B. S. Kunnel, R. E. Orozco and D. G. Bostwick, "Diagnosis of "suspicious for malignancy" in prostate biopsies: predictive value for cancer," Urology **51**, 749-758 (1998).

22. D. Keetch, W. Catalona and D. Smith, "Serial prostatic biopsies in men with persistently elevated serum prostate specific antigen values," J. Urol. **151**, 1571-1574 (1994).

23. J. V. Hegde, R. V. Mulkern, L. P. Panych, F. M. Fennessy, A. Fedorov, S. E. Maier and C. Tempany, "Multiparametric MRI of prostate cancer: An update on state-of-the-art techniques and their performance in detecting and localizing prostate cancer," J. Magn. Reson. Imaging **37**, 1035-1054 (2013).

www.manaraa.com

24. J. Haffner, L. Lemaitre, P. Puech, G. P. Haber, X. Leroy, J. S. Jones and A. Villers, "Role of magnetic resonance imaging before initial biopsy: comparison of magnetic resonance imaging-targeted and systematic biopsy for significant prostate cancer detection," BJU Int. **108**, E171-E178 (2011).

25. B. K. Park, J. W. Park, S. Y. Park, C. K. Kim, H. M. Lee, S. S. Jeon, S. I. Seo, B. C. Jeong and H. Y. Choi, "Prospective Evaluation of 3-T MRI Performed Before Initial Transrectal Ultrasound–Guided Prostate Biopsy in Patients With High Prostate-Specific Antigen and No Previous Biopsy," Am. J. Roentgenol. **197**, W876-W881 (2011).

26. M. Roethke, A. Anastasiadis, M. Lichy, M. Werner, P. Wagner, S. Kruck, C. D. Claussen, A. Stenzl, H. Schlemmer and D. Schilling, "MRI-guided prostate biopsy detects clinically significant cancer: analysis of a cohort of 100 patients after previous negative TRUS biopsy," World J. Urol. **30**, 213-218 (2012).

27. H. Hricak, P. L. Choyke, S. C. Eberhardt, S. A. Leibel and P. T. Scardino, "Imaging prostate cancer: A multidisciplinary perspective," Radiology **243**, 28-53 (2007).

28. E. K. Outwater and J. L. Montilla-Soler, "Imaging of prostate carcinoma," Cancer Control **20**, 161-176 (2013).

29. R. Clements, "Ultrasonography of prostate cancer," Eur. Radiol. **11**, 2119-2125 (2001).

30. S. Ghai and A. Toi, "Role of Transrectal Ultrasonography in Prostate Cancer," Radiol. Clin. North Am. **50**, 1061-1073 (2012).

31. R. A. Linden and E. J. Halpern, Seminars in Ultrasound, CT, and MRI, 2007.

32. E. J. Trabulsi, D. Sackett, L. G. Gomella and E. J. Halpern, "Enhanced transrectal ultrasound modalities in the diagnosis of prostate cancer," Urology **76**, 1025-1033 (2010).

33. R. Z. Azar, A. Baghani, S. E. Salcudean and R. Rohling, "2-D high-frame-rate dynamic elastography using delay compensated and angularly compounded motion vectors: preliminary results," IEEE Trans. Ultrason. Ferr. **57**, 2421-2436 (2010).

34. F. Aigner, L. Pallwein, D. Junker, G. Schäfer, G. Mikuz, F. Pedross, M. J. Mitterberger, W. Jaschke, E. J. Halpern and F. Frauscher, "Value of real-time elastography targeted biopsy for prostate cancer detection in men with prostate specific antigen 1.25 ng/ml or greater and 4.00 ng/ml or less," J. Urol. **184**, 913-917 (2010).

35. G. Salomon, J. Köllerman, I. Thederan, F. K. Chun, L. Budäus, T. Schlomm, H. Isbarn, H. Heinzer, H. Huland and M. Graefen, "Evaluation of prostate cancer

www.manaraa.com

detection with ultrasound real-time elastography: a comparison with step section pathological analysis after radical prostatectomy," Eur. Urol. **54**, 1354-1362 (2008).

36. S. Sara Mahdavi, M. Moradi, X. Wen, W. J. Morris and S. E. Salcudean, "Evaluation of visualization of the prostate gland in vibro-elastography images," Med. Image Anal. **15**, 589-600 (2011).

37. T. Adebar, S. Salcudean, S. Mahdavi, M. Moradi, C. Nguan and L. Goldenberg, "A robotic system for intra-operative trans-rectal ultrasound and ultrasound elastography in radical prostatectomy," in *Information Processing in Computer-Assisted Interventions,* (Springer, 2011), pp. 79-89.

38. S. Mahdavi, M. Moradi, W. Morris, S. Goldenberg and S. Salcudean, "Fusion of ultrasound B-mode and vibro-elastography images for automatic 3D segmentation of the prostate," (2012).

39. A. Baghani, H. Eskandari, W. Wang, D. Da Costa, M. N. Lathiff, R. Sahebjavaher, S. Salcudean and R. Rohling, "Real-time quantitative elasticity imaging of deep tissue using free-hand conventional ultrasound," in *Med. Image Comput. Comput. Assist. Interv.,* edited by N. Ayache, H. Delingette, P. Golland and K. Mori (Springer, 2012), pp. 617-624.

40. Y. Mazaheri, A. Shukla-Dave, A. Muellner and H. Hricak, "MR imaging of the prostate in clinical practice," Magn. Reson. Mater. Phys., Biol. Med. **21**, 379-392 (2008).

41. A. P. Kirkham, M. Emberton and C. Allen, "How good is MRI at detecting and characterising cancer within the prostate?," Eur. Urol. **50**, 1163-1175 (2006).

42. C. M. Hoeks, J. O. Barentsz, T. Hambrock, D. Yakar, D. M. Somford, S. W. Heijmink, T. W. Scheenen, P. C. Vos, H. Huisman and I. M. van Oort, "Prostate cancer: multiparametric MR imaging for detection, localization, and staging," Radiology **261**, 46-66 (2011).

43. A. Ward, C. Crukley, C. McKenzie, J. Montreuil, E. Gibson, J. Gomez, M. Moussa, G. Bauman and A. Fenster, "Registration of in vivo prostate magnetic resonance images to digital histopathology images," Prostate Cancer Imaging. Computer-Aided Diagnosis, Prognosis, and Intervention, 66-76 (2010).

44. A. D. Ward, C. Crukley, C. A. McKenzie, J. Montreuil, E. Gibson, C. Romagnoli, J. A. Gomez, M. Moussa, J. Chin and G. Bauman, "Prostate: Registration of Digital Histopathologic Images to in Vivo MR Images Acquired by Using Endorectal Receive Coil," Radiology (2012).

www.manaraa.com

45. E. Gibson, C. Crukley, J. Gomez, M. Moussa, J. Chin, G. Bauman, A. Fenster and A. Ward, "Fiducial-Based Registration of Digital Histopathology to Ex Vivo Prostate MRI," Med. Phys. **38**, 3761 (2011).

46. E. Gibson, C. Crukley, M. Gaed, J. A. Gómez, M. Moussa, J. L. Chin, G. S. Bauman, A. Fenster and A. D. Ward, "Registration of prostate histology images to ex vivo MR images via strand-shaped fiducials," J. Magn. Reson. Imaging **36**, 1402-1412 (2012).

47. S. Verma, B. Turkbey, N. Muradyan, A. Rajesh, F. Cornud, M. A. Haider, P. L. Choyke and M. Harisinghani, "Overview of dynamic contrast-enhanced MRI in prostate cancer diagnosis and management," Am. J. Roentgenol. **198**, 1277-1288 (2012).

48. M. A. Haider, T. H. van der Kwast, J. Tanguay, A. J. Evans, A. T. Hashmi, G. Lockwood and J. Trachtenberg, "Combined T2-weighted and diffusion-weighted MRI for localization of prostate cancer," Am. J. Roentgenol. **189**, 323-328 (2007).

49. J. Near, C. Romagnoli, A. T. Curtis, L. M. Klassen, J. Izawa, J. Chin and R. Bartha, "High-field MRSI of the prostate using a transmit/receive endorectal coil and gradient modulated adiabatic localization," J. Magn. Reson. Imaging **30**, 335-343 (2009).

50. J. Near, C. Romagnoli and R. Bartha, "Reduced power magnetic resonance spectroscopic imaging of the prostate at 4.0 Tesla," Magn. Reson. Med. **61**, 273-281 (2009).

51. J. Near and R. Bartha, "Quantitative sodium MRI of the mouse prostate," Magn. Reson. Med. **63**, 822-827 (2010).

52. G. Nir, R. S. Sahebjavaher, P. Kozlowski, S. D. Chang and R. Sinkus, "Model-based registration of ex vivo and in vivo MRI of the prostate using elastography," IEEE Trans. Med. Imaging **32**, 1068-1080 (2013).

53. R. S. Sahebjavaher, A. Baghani, M. Honarvar, R. Sinkus and S. E. Salcudean, "Transperineal prostate MR elastography: initial in vivo results," Magn. Reson. Med. (2012).

54. L. Dickinson, H. U. Ahmed, C. Allen, J. O. Barentsz, B. Carey, J. J. Futterer, S. W. Heijmink, P. J. Hoskin, A. Kirkham and A. R. Padhani, "Magnetic resonance imaging for the detection, localisation, and characterisation of prostate cancer: recommendations from a European consensus meeting," Eur. Urol. **59**, 477-494 (2011).

55. J. O. Barentsz, J. Richenberg, R. Clements, P. Choyke, S. Verma, G. Villeirs, O. Rouviere, V. Logager and J. J. Fütterer, "ESUR prostate MR guidelines 2012," Eur. Radiol. **22**, 746-757 (2012).

www.manaraa.com

56. M. G. Sanda, R. L. Dunn, J. Michalski, H. M. Sandler, L. Northouse, L. Hembroff, X. Lin, T. K. Greenfield, M. S. Litwin and C. S. Saigal, "Quality of life and satisfaction with outcome among prostate-cancer survivors," N. Engl. J. Med. **358**, 1250-1261 (2008).

57. M. Djulbegovic, R. J. Beyth, M. M. Neuberger, T. L. Stoffs, J. Vieweg, B. Djulbegovic and P. Dahm, "Screening for prostate cancer: systematic review and meta-analysis of randomised controlled trials," Br. Med. J. **341** (2010).

58. T. J. Wilt, M. K. Brawer, K. M. Jones, M. J. Barry, W. J. Aronson, S. Fox, J. R. Gingrich, J. T. Wei, P. Gilhooly and B. M. Grob, "Radical prostatectomy versus observation for localized prostate cancer," N. Engl. J. Med. **367**, 203-213 (2012).

59. A. Bill-Axelson, L. Holmberg, F. Filén, M. Ruutu, H. Garmo, C. Busch, S. Nordling, M. Häggman, S. O. Andersson and S. Bratell, "Radical prostatectomy versus watchful waiting in localized prostate cancer: the Scandinavian prostate cancer group-4 randomized trial," J. Natl. Cancer Inst. **100**, 1144-1154 (2008).

60. A. V. D'Amico, R. Whittington, S. B. Malkowicz, D. Schultz, K. Blank, G. A. Broderick, J. E. Tomaszewski, A. A. Renshaw, I. Kaplan and C. J. Beard, "Biochemical outcome after radical prostatectomy, external beam radiation therapy, or interstitial radiation therapy for clinically localized prostate cancer," JAMA: The Journal of the American Medical Association **280**, 969-974 (1998).

61. I. Thompson, J. B. Thrasher, G. Aus, A. L. Burnett, E. D. Canby-Hagino, M. S. Cookson, A. V. D'Amico, R. R. Dmochowski, D. T. Eton, J. D. Forman, S. L. Goldenberg, J. Hernandez, C. S. Higano, S. R. Kraus, J. W. Moul and C. M. Tangen, "Guideline for the management of clinically localized prostate cancer: 2007 update," J. Urol. **177**, 2106-2131 (2007).

62. F. Fang, N. L. Keating, L. A. Mucci, H. O. Adami, M. J. Stampfer, U. Valdimarsdóttir and K. Fall, "Immediate risk of suicide and cardiovascular death after a prostate cancer diagnosis: cohort study in the United States," J. Natl. Cancer Inst. **102**, 307-314 (2010).

63. B. J. Davison and S. L. Goldenberg, "Patient acceptance of active surveillance as a treatment option for low-risk prostate cancer," BJU Int. **108**, 1787-1793 (2011).

64. R. Choo, L. Klotz, C. Danjoux, G. C. Morton, G. DeBoer, E. Szumacher, N. Fleshner, P. Bunting and G. Hruby, "Feasibility study: watchful waiting for localized low to intermediate grade prostate carcinoma with selective delayed intervention based on prostate specific antigen, histological and/or clinical progression," J. Urol. **167**, 1664-1669 (2002).

www.manaraa.com

65. M. R. Abern, M. Tsivian and T. J. Polascik, "Focal therapy of prostate cancer: evidence-based analysis for modern selection criteria," Curr. Urol. Rep. **13**, 160-169 (2012).

66. S. Eggener, G. Salomon, P. T. Scardino, J. De la Rosette, T. J. Polascik and S. Brewster, "Focal therapy for prostate cancer: possibilities and limitations," Eur. Urol. **58**, 57-64 (2010).

67. G. Bozzini, P. Colin, P. Nevoux, A. Villers, S. Mordon and N. Betrouni, "Focal therapy of prostate cancer: energies and procedures," Urol. Oncol.-Semin. Ori. **31**, 155-167 (2012).

68. H. Beisland and E. Stranden, "Rectal temperature monitoring during neodymion-YAG laser irradiation for prostatic carcinoma," Urol. Res. **12**, 257-259 (1984).

69. Z. Amin, W. Lees and S. Bown, "Interstitial laser photocoagulation for the treatment of prostatic cancer," Br. J. Radiol. **66**, 1044-1047 (1993).

70. M. Atri, M. R. Gertner, M. A. Haider, R. A. Weersink and J. Trachtenberg, "Contrast-enhanced ultrasonography for real-time monitoring of interstitial laser thermal therapy in the focal treatment of prostate cancer," Can. Urol. Assoc. J. **3**, 125-130 (2009).

71. U. Lindner, R. Weersink, M. Haider, M. Gertner, S. Davidson, M. Atri, B. Wilson, A. Fenster and J. Trachtenberg, "Image guided photothermal focal therapy for localized prostate cancer: phase I trial," J. Urol. **182**, 1371-1377 (2009).

72. O. Raz, M. A. Haider, S. R. H. Davidson, U. Lindner, E. Hlasny, R. Weersink, M. R. Gertner, W. Kucharcyzk, S. A. McCluskey and J. Trachtenberg, "Real-time magnetic resonance imaging-guided focal laser therapy in patients with low-risk prostate cancer," Eur. Urol. **58**, 173-177 (2010).

73. U. Lindner, N. Lawrentschuk, R. A. Weersink, S. R. H. Davidson, O. Raz, E. Hlasny, D. L. Langer, M. R. Gertner, T. Van der Kwast and M. A. Haider, "Focal laser ablation for prostate cancer followed by radical prostatectomy: validation of focal therapy and imaging accuracy," Eur. Urol. **57**, 1111-1114 (2010).

74. R. J. McNichols, A. Gowda, M. Kangasniemi, J. A. Bankson, R. E. Price and J. D. Hazle, "MR thermometry-based feedback control of laser interstitial thermal therapy at 980 nm," Lasers Surg. Med. **34**, 48-55 (2004).

75. N. V. Tsekos, A. Khanicheh, E. Christoforou and C. Mavroidis, "Magnetic resonance-compatible robotic and mechatronics systems for image-guided interventions and rehabilitation: a review study," Annu. Rev. Biomed. Eng. **9**, 351-387 (2007).

www.manaraa.com

76. J. A. Nyenhuis, S.-M. Park, R. Kamondetdacha, A. Amjad, F. G. Shellock and A. R. Rezai, "MRI and implanted medical devices: basic interactions with an emphasis on heating," IEEE Trans. Dev. Mat. Rel. **5**, 467-480 (2005).

77. R. Gassert, E. Burdet and K. Chinzei, "Opportunities and challenges in MR-compatible robotics," Engineering in Medicine and Biology Magazine, IEEE **27**, 15-22 (2008).

78. K. El Bannan, W. Handler, B. Chronik and S. P. Salisbury, "Heating of metallic rods induced by time-varying gradient fields in MRI," J. Magn. Reson. Imaging (2013).

79. J. F. Schenck, "The role of magnetic susceptibility in magnetic resonance imaging: MRI magnetic compatibility of the first and second kinds," Med. Phys. **23**, 815 (1996).

80. K. Chinzei, R. Kikinis and F. A. Jolesz, "MR compatibility of mechatronic devices: design criteria," in *Med. Image Comput. Comput. Assist. Interv.,* edited by C. Taylor and A. Colchester (Springer, 1999), pp. 1020-1030.

81. A. D'Amico, R. Cormack, C. Tempany, S. Kumar, G. Topulos, H. Kooy and C. N. Coleman, "Real-time magnetic resonance image-guided interstitial brachytherapy in the treatment of select patients with clinically localized prostate cancer," Int. J. Radiat. Oncol. Biol. Phys. **42**, 507-515 (1998).

82. A. D'Amico, C. Tempany, R. Cormack, N. Hata, M. Jinzaki, K. Tuncali, M. Weinstein and J. Richie, "Transperineal magnetic resonance image guided prostate biopsy," J. Urol. **164**, 385-387 (2000).

83. N. Hata, M. Jinzaki, D. Kacher, R. Cormak, D. Gering, A. Nabavi, S. G. Silverman, A. V. D'Amico, R. Kikinis and F. A. Jolesz, "MR imaging-guided prostate biopsy with surgical navigation software: Device validation and feasibility1," Radiology **220**, 263-268 (2001).

84. C. Ménard, R. C. Susil, P. Choyke, G. S. Gustafson, W. Kammerer, H. Ning, R. W. Miller, K. L. Ullman, N. Sears Crouse and S. Smith, "MRI-guided HDR prostate brachytherapy in standard 1.5 T scanner," Int. J. Radiat. Oncol. Biol. Phys. **59**, 1414-1423 (2004).

85. R. C. Susil, K. Camphausen, P. Choyke, E. R. McVeigh, G. S. Gustafson, H. Ning, R. W. Miller, E. Atalar, C. N. Coleman and C. Ménard, "System for prostate brachytherapy and biopsy in a standard 1.5 T MRI scanner," Magn. Reson. Med. **52**, 683-687 (2004).

86. K. Chinzei, N. Hata, F. Jolesz and R. Kikinis, "MR compatible surgical assist robot: System integration and preliminary feasibility study," in *Med. Image Comput.*

www.manaraa.com

Comput. Assist. Interv., edited by S. Delp, A. DiGioia and B. Jaramaz (Springer, 2000), pp. 921-930.

87. S. DiMaio, G. Fischer, S. Maker, N. Hata, I. Iordachita, C. Tempany, R. Kikinis and G. Fichtinger, IEEE Conference on Biomedical Robotics and Biomechatronics, 2006.

88. M. Muntener, A. Patriciu, D. Petrisor, D. Mazilu, H. Bagga, L. Kavoussi, K. Cleary and D. Stoianovici, "Magnetic resonance imaging compatible robotic system for fully automated brachytherapy seed placement," Urology **68**, 1313-1317 (2006).

89. D. Stoianovici, A. Patriciu, D. Petrisor, D. Mazilu and L. Kavoussi, "A new type of motor: pneumatic step motor," IEEE Trans. Mech. **12**, 98-106 (2007).

90. G. S. Fischer, I. Iordachita, C. Csoma, J. Tokuda, S. P. DiMaio, C. M. Tempany, N. Hata and G. Fichtinger, "MRI-compatible pneumatic robot for transperineal prostate needle placement," IEEE Trans. Mech. **13**, 295-305 (2008).

91. P. W. Mewes, J. Tokuda, S. P. DiMaio, G. S. Fischer, C. Csoma, D. G. Gobbi, C. M. Tempany, G. Fichtinger and N. Hata, IEEE International Conference on Robotics and Automation, 2008.

92. D. Stoianovici, D. Song, D. Petrisor, D. Ursu, D. Mazilu, M. Muntener, M. Schar and A. Patriciu, ""MRI Stealth" robot for prostate interventions," Minim. Invasive Ther. Allied Tech. **16**, 241-248 (2007).

93. A. Patriciu, D. Petrisor, M. Muntener, D. Mazilu, M. Schar and D. Stoianovici, "Automatic brachytherapy seed placement under MRI guidance," IEEE Trans. Biomed. Eng. **54**, 1499-1506 (2007).

94. J. A. Cunha, I.-C. Hsu, J. Pouliot, M. Roach III, K. Shinohara, J. Kurhanewicz, G. Reed and D. Stoianovici, "Toward adaptive stereotactic robotic brachytherapy for prostate cancer: demonstration of an adaptive workflow incorporating inverse planning and an MR stealth robot," Minim. Invasive Ther. Allied Tech. **19**, 189-202 (2010).

95. K. Tadakuma, L. M. DeVita, J.-S. Plante, Y. Shaoze and S. Dubowsky, IEEE International Conference on Robotics and Automation, 2008.

96. G. Miron, A. Girard, J.-S. Plante and M. Lepage, "Design and Manufacturing of Embedded Air-Muscles for a Magnetic Resonance Imaging Compatible Prostate Cancer Binary Manipulator," J. Mech. Des. **135**, 011003 (2013).

97. S. Abdelaziz, L. Esteveny, P. Renaud, B. Bayle, L. Barbé, M. De Mathelin and A. Gangi, "Design considerations for a novel MRI compatible manipulator for prostate cryoablation," Int. J. Comput. Assist. Radiol. Surg. **6**, 811-819 (2011).

www.manaraa.com

98. M. R. van den Bosch, M. R. Moman, M. van Vulpen, J. J. Battermann, E. Duiveman, L. J. van Schelven, H. de Leeuw, J. J. Lagendijk and M. A. Moerland, "MRI-guided robotic system for transperineal prostate interventions: proof of principle," Phys. Med. Biol. **55**, N133 (2010).

99. A. A. Goldenberg, J. Trachtenberg, W. Kucharczyk, Y. Yi, M. Haider, L. Ma, R. Weersink and C. Raoufi, "Robotic system for closed-bore MRI-guided prostatic interventions," IEEE Trans. Mech. **13**, 374-379 (2008).

100. A. A. Goldenberg, J. Trachtenberg, Y. Yi, R. Weersink, M. S. Sussman, M. Haider, L. Ma and W. Kucharczyk, "Robot-assisted MRI-guided prostatic interventions," Robotica **28**, 215 (2010).

101. U. Lindner, A. Louis, A. Colquhoun, P. Boström, S. Davidson and O. Raz, "First robotic magnetic resonance-guided laser focal therapy for prostate cancer: a case report and review of the literature," Interven. Oncol. Soc. J. **1**, 69-77 (2011).

102. H. Su, W. Shang, G. A. Cole, K. Harrington and G. S. Fischer, IEEE Haptics Symposium, 2010.

103. H. Su, A. Camilo, G. A. Cole, N. Hata, C. M. Tempany and G. S. Fischer, MMVR, 2011.

104. H. Su, D. C. Cardona, W. Shang, A. Camilo, G. A. Cole, D. C. Rucker, R. Webster and G. S. Fischer, "A MRI-guided concentric tube continuum robot with piezoelectric actuation: A feasibility study," IEEE Int. Conf. Rob. Autom., 1939-1945 (2012).

www.manaraa.com

Chapter 2.

The Effects of Magnetic Field Distortion on the Accuracy of Passive Device Localization Frames in MR†

2.1 Introduction

Magnetic resonance (MR) imaging is an attractive modality for guiding minimally-invasive procedures. This is due to several features that MR offers: high soft tissue contrast, true 3D acquisition capability, multiparametric imaging capability, and a lack of ionizing radiation.[1] For these reasons, MR-guided procedures have been explored for applications such as prostate biopsy and therapy,[2-10] breast biopsy,[11] liver ablation,[12, 13] and neurologic intervention,[14-16] to name a few. In an attempt to provide a solution that can guide needles, catheters or surgical tools with high accuracy, MR-compatible robotic, mechatronic, or mechanically-assistive devices are often employed for these applications. Some salient examples of devices that have seen use in clinical procedures include: Neuroarm, an MR-compatible image-guided robot for neurosurgery;[17] DynaTRIM, a commercially available device for MR-guided transrectal prostate biopsy (Invivo Corporation, Gainesville, Florida, USA);[18] and Innomotion, a commercially available general purpose robot for percutaneous MR-guided interventions (Innomedic, Herxheim, Germany).[19] Successful implementation of these

†. A version of this chapter has been submitted for publication: Cepek, J., Chronik, B., Fenster, A., "The Effects of Magnetic Field Distortion on the Accuracy of Passive Device Localization Frames in MR." Med. Phys. (2013, In Revision).

www.manaraa.com

systems for an MR-guided procedure requires accurate localization of the device within the MR image space.[20] This process allows MR-identified targets to be transformed to the interventional device's coordinate system for device alignment and manipulation, and the device's position in MR to be known for visualization or alignment verification purposes. Any error in localizing a device in MR image space will result in systematic errors in subsequent targeting tasks, and they should therefore be minimized. In the context of this thesis, the relevant metric of error is needle placement error, which is defined as the distance between a needle's final position in tissue and the point in the tissue at which the needle was planned to be placed. This chapter aims to study the sensitivity of but one component of needle placement error, as illustrated in Figure 2.1**.** Specifically, this chapter will study the *sensitivity* of device localization error to static magnetic field distortions in MR. In Chapter 3, additional components of error will be evaluated, and the absolute value of localization error will be considered.

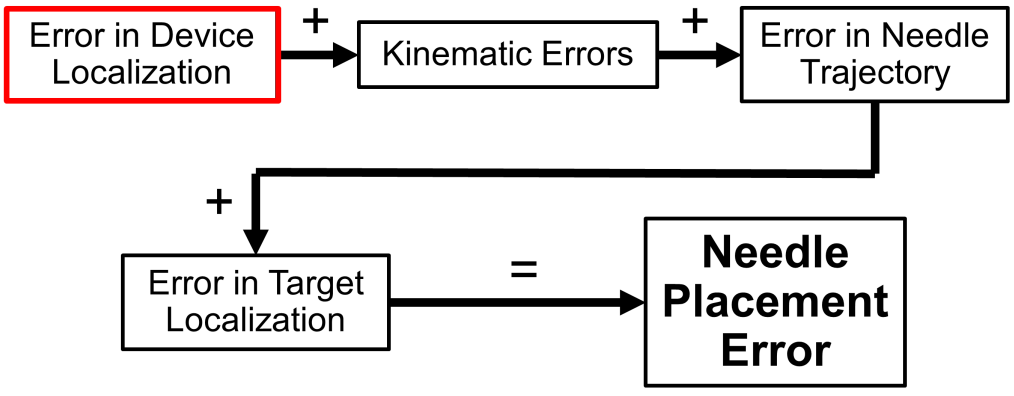

Figure 2.1: Illustration of the various components that contribute to needle placement error. This chapter considers the sensitivity of error in device localization to the presence of static magnetic field distortions in MR.

Three methods are commonly used to locate interventional devices in MR image space: positional encoding of the joints of the device,[2] active tracking,[21, 22] and

www.manaraa.com

passive markers.[3, 23-25] The sole use of joint encoding requires that the device be fixed to the MR scanner and accurately calibrated to its coordinate system. As many interventional devices are designed for use in clinical diagnostic scanners, they are usually removable and portable, and are generally not placed at the same precise position for each procedure, making this approach impractical. For these reasons, active and passive tracking markers are used much more commonly, as these methods allow for localization of the device in the MR workspace for each procedure.

Active tracking in MR involves the placement of small radiofrequency (rf) receive coils on the object to be tracked.[21] A minimum of three projection images are then acquired, providing 3D localization of the coil. While this method can provide high-accuracy localization of interventional devices, it requires integration with the scanner's software and connection of each coil to the scanner through wires, adding complexity. As well, each coil must be surrounded by an MR-visible material, a requirement that is trivially satisfied for applications such as endovascular catheter tracking, but can be cumbersome for tracking devices external to the body. In addition, as high-field scanners are commonly used for interventional procedures, sufficient signal-to-noise ratio in images of small tracking markers can be achieved using a body coil, making active tracking coils potentially unnecessary for tracking devices external to the body.[10]

Passive localization frames employ MR-visible markers arranged in a known geometric configuration. Once imaged, a relationship between the device's and MR's coordinate systems can be established; allowing any point in MR space to be targeted by the interventional device. Common localization frames, such as the Brown-Roberts-Wells frame (hereafter referred to as the z-frame), developed for CT-guided neurosurgical

www.manaraa.com

interventions, have recently seen use in MR.[3] However, since the nature of geometric distortion in MR images is much different from that in CT, it is important to consider the sources of localization error in the MR environment. This is especially true because geometric distortion in MR images is dependent on the level of magnetic field distortion, which can be both substantial and unpredictable in the region surrounding a patient's body and near devices containing magnetic materials.

In this work, a simplified mathematical description of MR imaging of ellipsoids in the presence of static field distortion is presented. Next, this formulation is applied to three characteristic MR device localization frames found in the literature to compare each of their sensitivities to static field distortion. Finally, each of the three localization frames were constructed and imaged in a clinical MR scanner to validate the simplified theoretical model.

2.2 Methods

2.2.1 2D Gradient Echo Imaging of Ellipsoids

Any object placed in an external magnetic field will experience an induced magnetization, leading to a shift in the net magnetic field both inside and outside of the object. For a general shape, finding the spatial distribution of the magnetic field shift requires the solution of a partial differential equation in three dimensions. Fortunately, however, for the case of ellipsoids in a uniform external field, analytic solutions are readily available. Details of these solutions and the resulting location at which cylinders and spheres would appear in a 2D gradient echo image in the presence of static field distortion are provided in Appendix A. In the remainder of this section, a simple method of correcting in-plane distortion in 2D gradient echo images is described.

www.manaraa.com

2.2.2 In-Plane Centroid Measurement

In imaging cylinders or spheres using MR, three methods are considered: 1) a single image of each object is acquired with frequency-encoding along rows of image pixels, 2) a single image of each object is acquired with frequency-encoding along columns of image pixels, and 3) two images of each object are acquired, with the frequency-encoded direction switched in each acquisition, and measurements only made in the phase-encoded direction of each image. Figure 2.2 demonstrates method 3.

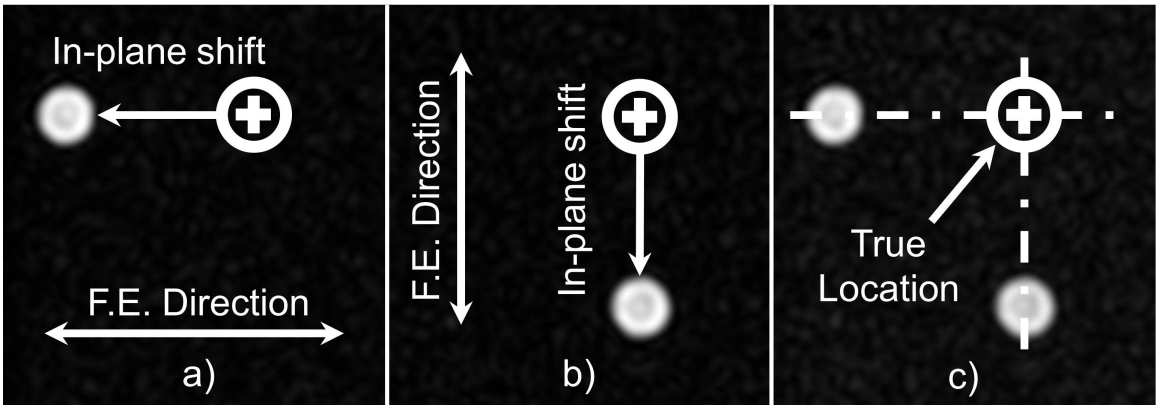

Figure 2.2: Accurate in-plane measurement of an object's position in MR in the presence of static field distortion by acquiring two images with the frequency-encoded (F.E.) direction alternated: a) frequency-encoding in the left-right (horizontal) direction, b) frequency-encoding in the anterior-posterior (vertical) direction, c) sum of images in a) and b), showing how measurements of the object's position in the phase-encoded direction in separate acquisitions can be combined to find the true position.

The first two methods represent the simplest and quickest method of in-plane object localization, since they only require a single 2D image acquisition. Comparison of results using these two methods will show the sensitivity of each frame's accuracy to the direction of frequency-encoding. By using the third method, in-plane measurements are insensitive to static field distortion, allowing error in frame localization to be studied independently of this source of in-plane error. Correction of out-of-plane error due to static field distortion in 2D gradient echo imaging requires more complex methods, and the ability to control the slice-select gradient strength or polarity.[26] Such techniques

www.manaraa.com

were not considered in this work since they are not generally at the operator's disposal on a standard clinical scanner.

Practically, computation of the centroid of each ellipse is performed by first filtering the images using a circular averaging (pill-box) filter of radius 2 pixels to remove noise. A binary mask is then created by thresholding the filtered image such that the area of the resultant mask is equal to the known area of the elliptical cross section. Finally, the filtered image is masked to remove background information, and an intensity-weighted centroid is computed.

2.2.3 Localization Frames

Three localization frame designs are considered: the z-frame, first developed for use in CT-guided neurosurgical procedures;[27] the + frame, developed for an MR-guided prostate needle delivery device;[10] and an arrangement of spherical fiducials.[19] Each frame is characteristic in the way in which it encodes pose (*i.e.* position and orientation) in images. The effect of static field distortion is therefore expected to affect each frame's accuracy differently. Each of these localization frames consists of a fixed arrangement of either cylinders or spheres, enabling a theoretical analysis of pose estimation error using the expressions in Appendix A. For each frame, it is desired to find a rigid transformation that relates any point in the frame coordinate system to that in the MR scanner's coordinate system. This transformation can be formulated using a 4x4 transformation matrix $\mathbf{A}$, as follows

$$\begin{bmatrix} \mathbf{p}_{MR} \\ 1 \end{bmatrix} = \mathbf{A} \begin{bmatrix} \mathbf{p}_{f} \\ 1 \end{bmatrix}, \tag{2.1}$$

www.manaraa.com

where $\mathbf{p}_{MR}$ is the point in the MR coordinate system, and $\mathbf{p}_f$ is the point in the frame's coordinate system (column vectors). The transformation matrix can be decomposed as

$$\mathbf{A} = \begin{bmatrix} \mathbf{R} & \mathbf{t} \\ \mathbf{0}^T & 1 \end{bmatrix}, \tag{2.2}$$

where

$$\mathbf{R} = \begin{bmatrix} R_{11} & R_{12} & R_{13} \\ R_{21} & R_{22} & R_{23} \\ R_{31} & R_{32} & R_{33} \end{bmatrix} \tag{2.3}$$

is a rigid rotation matrix, and

$$\mathbf{t} = \begin{bmatrix} t_x \\ t_y \\ t_z \end{bmatrix} \tag{2.4}$$

is a translation vector. Inversion of $\mathbf{A}$ allows points defined in the MR coordinate system to be found in frame coordinates

$$\begin{bmatrix} \mathbf{p}_f \\ 1 \end{bmatrix} = \mathbf{A}^{-1} \begin{bmatrix} \mathbf{p}_{MR} \\ 1 \end{bmatrix}. \tag{2.5}$$

Furthermore, since this work aims to study the *sensitivity* of localization frame error to static field distortion alone, the transformation relative to a reference pose is of interest

$$\mathbf{A}_{rel} = \mathbf{A}_0^{-1}\mathbf{A}_i, \tag{2.6}$$

where $\mathbf{A}_0$ is the transformation matrix for the frame at a reference pose (*i.e.* in the absence of static field distortion), and $\mathbf{A}_i$ is that for the frame at its current pose. $\mathbf{A}_0$ is obtained by imaging the frame in the absence of static field distortion, and using the third method of centroiding, as described in section 2.2.2. $\mathbf{A}_{rel}$ quantifies the relative error.

www.manaraa.com

In this chapter, error is represented by each of the three Euler angles and translational components of error in localizing each frame, represented by the rotation matrix $\mathbf{R}_{\mathbf{rel}}$ and translation vector $\mathbf{t}_{\mathbf{rel}}$, respectively. In defining the Euler angles, the rotation matrix is decomposed into rotations about the x, y, and z axes

$$\mathbf{R}_{\mathbf{rel}} = \mathbf{R}_z(\theta_z)\mathbf{R}_y(\theta_y)\mathbf{R}_x(\theta_x), \tag{2.7}$$

where θ_x, θ_y and θ_z are the angles of rotation about the x, y and z axes, respectively, and the three rotation matrices are defined as

$$\mathbf{R}_{\mathbf{x}}(\theta_x) = \begin{bmatrix} 1 & 0 & 0 \\ 0 & \cos(\theta_x) & -\sin(\theta_x) \\ 0 & \sin(\theta_x) & \cos(\theta_x) \end{bmatrix}, \mathbf{R}_{\mathbf{y}}(\theta_y) = \begin{bmatrix} \cos(\theta_y) & 0 & \sin(\theta_y) \\ 0 & 1 & 0 \\ -\sin(\theta_y) & 0 & \cos(\theta_y) \end{bmatrix},$$
$$\mathbf{R}_{\mathbf{z}}(\theta_z) = \begin{bmatrix} \cos(\theta_z) & -\sin(\theta_z) & 0 \\ \sin(\theta_z) & \cos(\theta_z) & 0 \\ 0 & 0 & 1 \end{bmatrix}. \tag{2.8}$$

Using this definition, rotational and translational errors in localization of each frame in each axis can be studied independently.

2.2.4 Z-Frame

The z-frame consists of an arrangement of seven MR-visible cylinders. A single image slice will show seven ellipses, the centroids of which are used for localizing the frame. The z-frame is shown in Figure 2.3.

www.manaraa.com

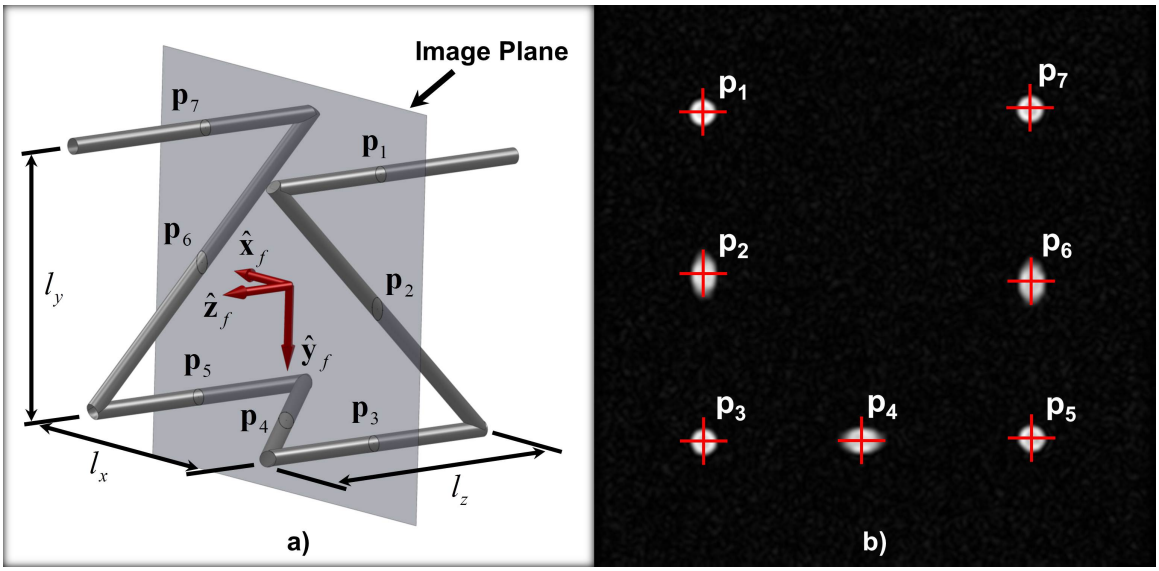

Figure 2.3: The z-frame: a) coordinate system and image intersection points, b) MR image showing the seven ellipses.

Table 2.1 gives the values of the parameters for the equation of each cylinder in the MR coordinate system, with the frame aligned with the MR axes and centered at the scanner's isocenter. Each cylinder's axis is described by the parametric equation

$$\mathbf{l} = \mathbf{s} + \mathbf{v}t \,. \tag{2.9}$$

Table 2.1: Line parameters for each cylinder in the z-frame. $v_z = 0$, and $s_z = 1$ for all segments.

Segment	v_x	v_y	s_z	s_y	α*
1	0	0	$-l_x/2$	$-l_y/2$	0
2	0	$-l_y/l_z$	$-l_x/2$	0	$\pi/4$
3	0	0	$-l_x/2$	$l_y/2$	0
4	$-l_x/l_z$	0	0	$l_y/2$	$\pi/4$
5	0	0	$l_x/2$	$l_y/2$	0
6	0	l_y/l_z	$l_x/2$	0	$\pi/4$
7	0	0	$l_x/2$	$-l_y/2$	0

*the angle that each cylinder's axis makes with the longitudinal component of the static magnetic field

The three corresponding points in the frame coordinate system can be found as

www.manaraa.com

$$\begin{bmatrix} \mathbf{p}_{2_f} & \mathbf{p}_{4_f} & \mathbf{p}_{6_f} \end{bmatrix} = \begin{bmatrix} l_x\{ & -½ & ½ - f_4 & ½ & \} \\ l_y\{ & ½ - f_2 & ½ & -½ + f_6 & \} \\ l_z\{ & -½ + f_2 & -½ + f_4 & -½ + f_6 & \} \end{bmatrix}, \tag{2.10}$$

where f_i is a function that measures the fraction along the length of the frame at which each diagonal cylinder is imaged

$$f_i = \frac{\left| \mathbf{p}_{(i+1)_{MR}} - \mathbf{p}_{i_{MR}} \right|}{\left| \mathbf{p}_{(i+1)_{MR}} - \mathbf{p}_{(i-1)_{MR}} \right|}, \tag{2.11}$$

and $\mathbf{p}_{i_{MR}}$ is the centroid of ellipse *i* identified in an MR image. The transformation matrix for the z-frame can be defined as that which minimizes the l^2-norm of the error between the three points in the MR coordinate system, and the corresponding transformed set of points.[28] That is:

$$\mathbf{A}_Z = \arg\min_{\mathbf{A}} (D), \tag{2.12}$$

where D is the sum of the squared error between the two sets of points

$$D = \sum_i \left| \mathbf{p}_{i_{MR}} - \mathbf{A}\mathbf{p}_{i_f} \right|^2, \; i = 2,4,6 \tag{2.13}$$

$\mathbf{A}_Z$ was computed in MATLAB using the *procrustes* function without scaling or reflection.

2.2.5 + Frame

The + frame consists of two perpendicular MR-visible cylinders.[10] Localization of four points on the frame is achieved by imaging each cylinder in two image planes perpendicular to its axis. The frame is shown in Figure 2.4.

www.manaraa.com

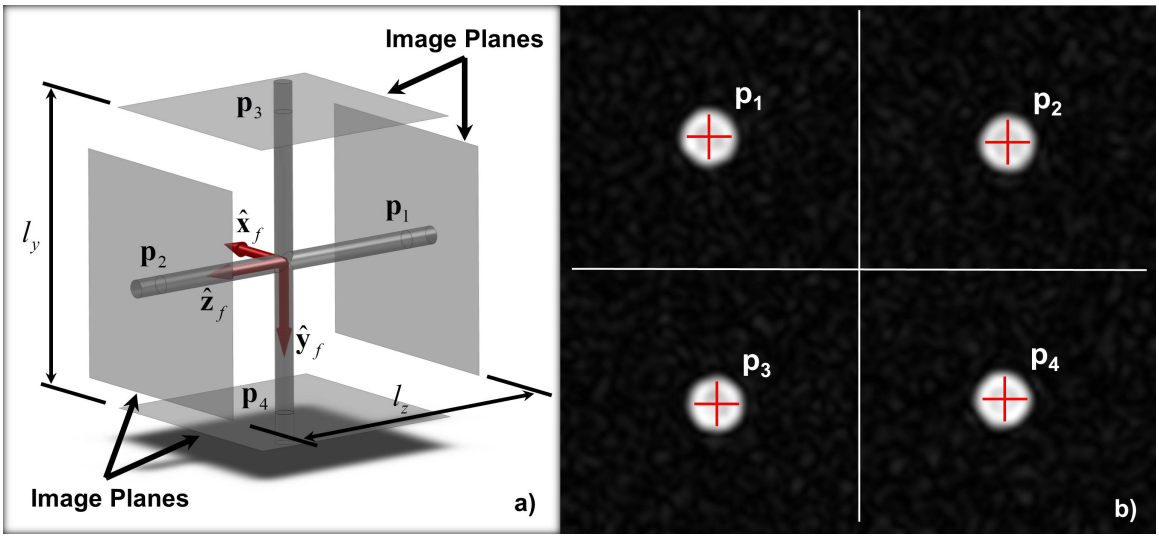

Figure 2.4: The + localization frame: a) coordinate system and localization points for the + frame, b) MR images showing the four points used for localization.

Table 2.2 gives the parameters of each cylinder's axis, in the MR coordinate system, with the frame centered at the MR isocenter and aligned with the MR axes.

Table 2.2: Line parameters for each cylinder in the + frame. **s** = 0 for both segments.

Segment	v_x	v_y	v_z	α
1	0	0	1	0
2	0	1	0	π/2

With the frame in this orientation, points $\mathbf{p}_{1_{MR}}$ and $\mathbf{p}_{2_{MR}}$ are localized in axial (*x-y* plane) MR images, while $\mathbf{p}_{3_{MR}}$ and $\mathbf{p}_{4_{MR}}$ are localized in coronal (*x-z* plane) images. Unit vectors in the direction of the axes of the frame can then be defined as

$$\hat{\mathbf{z}}_{f_{MR}} = \frac{\mathbf{p}_{2_{MR}} - \mathbf{p}_{1_{MR}}}{\left|\mathbf{p}_{2_{MR}} - \mathbf{p}_{1_{MR}}\right|}, \quad \hat{\mathbf{x}}_{f_{MR}} = \frac{-\left(\mathbf{p}_{2_{MR}} - \mathbf{p}_{1_{MR}}\right)\times\left(\mathbf{p}_{4_{MR}} - \mathbf{p}_{3_{MR}}\right)}{\left|\left(\mathbf{p}_{2_{MR}} - \mathbf{p}_{1_{MR}}\right)\times\left(\mathbf{p}_{4_{MR}} - \mathbf{p}_{3_{MR}}\right)\right|}, \text{ and}$$

$$\hat{\mathbf{y}}_{f_{MR}} = \hat{\mathbf{z}}_{f_{MR}} \times \hat{\mathbf{x}}_{f_{MR}}, \tag{2.14}$$

with the origin of the frame defined as

$$\mathbf{o}_{f_{MR}} = \mathbf{M}\left(\mathbf{l}_1, \mathbf{l}_2\right), \tag{2.15}$$

www.manaraa.com

where $\mathbf{M}(\mathbf{l}_1, \mathbf{l}_2)$ is a point midway between a point on line $\mathbf{l}_1$ and a point on line $\mathbf{l}_2$ that are a minimum distance from each other. Using Equations (2.14) and (2.15), the transformation matrix for the + frame can be written as

$$\mathbf{A}_+ = \begin{bmatrix} \hat{\mathbf{x}}_{f_{MR}} & \hat{\mathbf{y}}_{f_{MR}} & \hat{\mathbf{z}}_{f_{MR}} & \mathbf{o}_{f_{MR}} \\ 0 & 0 & 0 & 1 \end{bmatrix}. \tag{2.16}$$

2.2.6 Spherical Marker Frame

The third localization frame design considered in this work is an arrangement of MR-visible spheres. Since the correspondence between spheres in the images and on the frame is known, a minimum of only three spheres is required. This arrangement is shown in Figure 2.5.

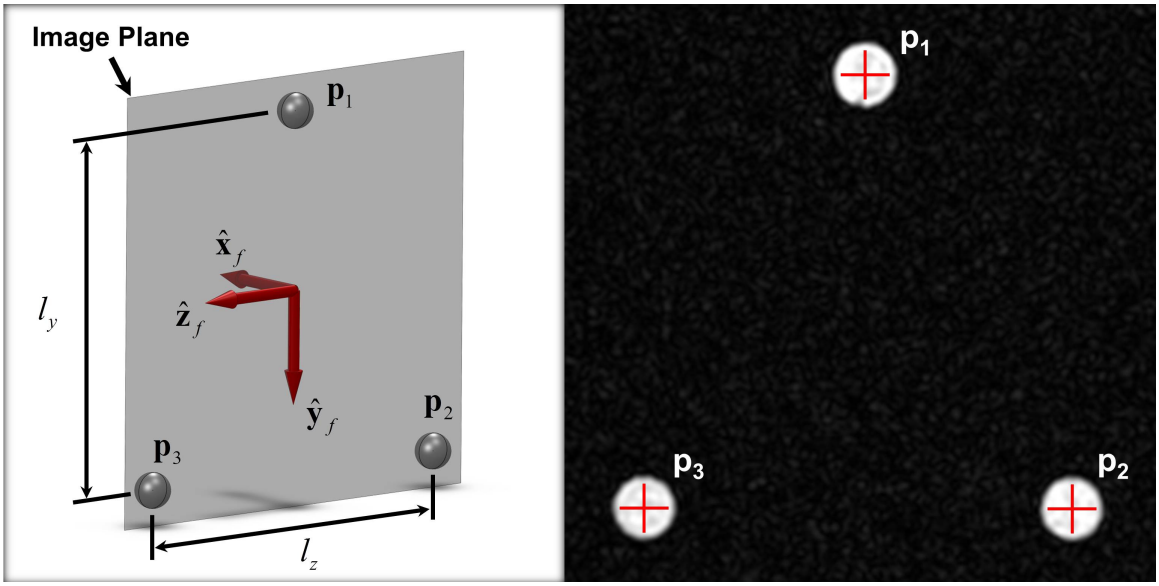

Figure 2.5: The spherical marker localization frame: a) localization points and coordinate system, b) MR image of the frame. Note that, without acquiring multiple contiguous slices, accurate sphere localization requires the acquisition of additional images in at least one other plane perpendicular to the one shown.

As for the z-frame, imaging the spherical fiducial frame provides three corresponding points in both the MR and frame coordinate system, and the frame's

www.manaraa.com

transformation matrix can be defined by the rigid transformation that minimizes the l^2-norm of the error between the corresponding points.

2.2.7 Model Parameters

Accurate tuning of a clinical MR scanner's calibration values (*e.g.* rf center frequency, gradient shim values, transmit gain) to the object being imaged requires an object of sufficient volume to provide adequate signal for measurement. Since localization frames generally contain a relatively small volume of fluid, this process may not always be performed successfully on a clinical scanner. A common approach is to obtain calibration values using a large object (human body or a phantom) and save these parameters for imaging of the frame. Assuming that the scanner is tuned to a spherical volume of tissue with uniform magnetic field equal to[29]

$$B_{tiss} = B_0\left(1+\frac{1}{3}\chi_{air}\right), \tag{2.17}$$

the center frequency will be equal to

$$\omega_c = \gamma B_0\left(1+\frac{1}{3}\chi_{air}\right). \tag{2.18}$$

Table 2.3 summarizes the rest of the MR parameters used in the model, selected to be representative of a typical MR sequence used for localization frames, and the localization frame physical properties.

www.manaraa.com

Table 2.3: Parameters used in the model of localization frame imaging in MR. The gradient strengths are chosen to be representative of values typically used in clinical sequences.

Parameter	Value	Units
B_0	3	T
G_{ss}	25	mT/m
G_{fe}	9.2	mT/m
Repetition Time	150	ms
Echo Time	4	ms
Flip Angle	60	degrees
Slice Thickness	3	mm
Field-of-view	128 x 128	mm
Acquisition Matrix	128 x 128	-
$\chi_{water}, \chi_{tiss}$ *	-9.05 x 10^{-6}	unitless
χ_e †	-9.05 x 10^{-6}	unitless
χ_{air}	0.36 x 10^{-6}	unitless
ΔB_d	[10^{-6}, 10^{-4}]	T
G'_x, G'_y, G'_z	[0.01, 1]	mT/m
l_x, l_y, l_z	76.2	mm

*Susceptibility defined as $\chi = M/H$

†Estimate of susceptibility for acetyl homopolymer[30]

2.2.8 Error Measurement in MR

Each of the three passive localization frames was constructed for validation of the theoretical model of error in a 3T clinical MR scanner (MR750, GE Healthcare, Milwaukee, WI). All cylindrical sections were manufactured as 6 mm drilled holes in plastic (acetal homopolymer), and spherical markers were manufactured from an Acrylic resin in a 3D rapid manufacturing system (Perfactory Mini, EnvisionTEC, Dearborn, MI) with a resolution of 25 μm. The cylindrical sections and spherical markers were filled with a 1% solution of gadolinium diethylenetriaminepentaacetic acid (Gd-DTPA,

www.manaraa.com

Magnevist, Bayer Healthcare, Berlin, Germany) by volume. Figure 2.6 shows each of the three frames constructed for tests in MR.

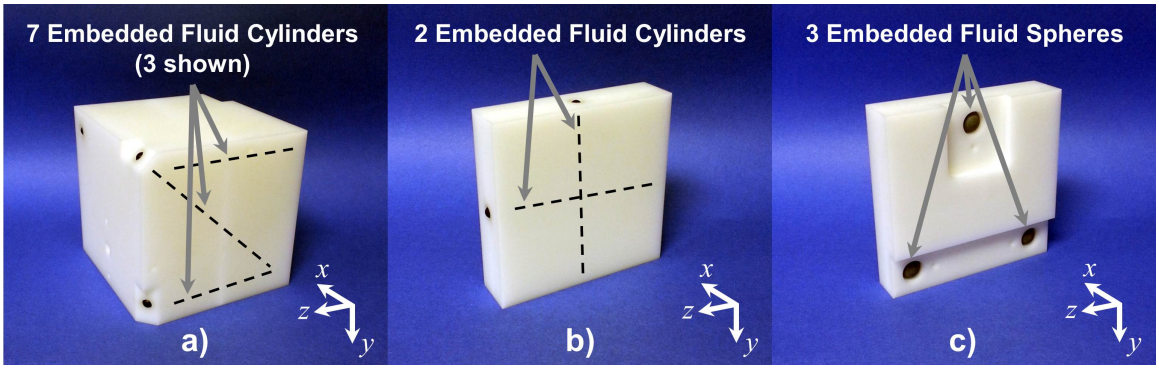

Figure 2.6: The three localization frames constructed for error sensitivity tests in MR: a) z-frame, b) + frame, c) spherical marker frame.

Simulation of the effects of a magnetic field distortion on each localization frame was performed by varying the MR scanner's center frequency and gradient shim values over several localization frame image acquisitions. Before imaging any of the frames, a spherical phantom (3T Head TLT Sphere Phantom, General Electric Company, Milwaukee, WI) was placed at the scanner's isocenter and imaged to provide calibration values similar to what would be obtained for a human head. All center frequency and gradient shim offsets were relative to the initial values obtained by imaging the phantom. Error was defined relative to the pose of each frame, as estimated using images without simulated distortion, and with in-plane measurements only made in the phase-encoded direction. Localization of the centroid of ellipses and spheres in each image was performed semi-automatically using the method described in Section 2.2.2.

2.3 Results

Figures 2.7 - 2.9 show the localization error of each frame in the presence of a uniform magnetic field distortion ranging from 1 – 100 μT and static field distortion gradients of

www.manaraa.com

0.01 – 1 mT/m in each direction. In the figures, theoretical results are shown using lines, and experimental results using point markers. Note that the range of gradient distortion values tested experimentally was limited to the maximum value available for manual adjustment on the scanner.

www.manaraa.com

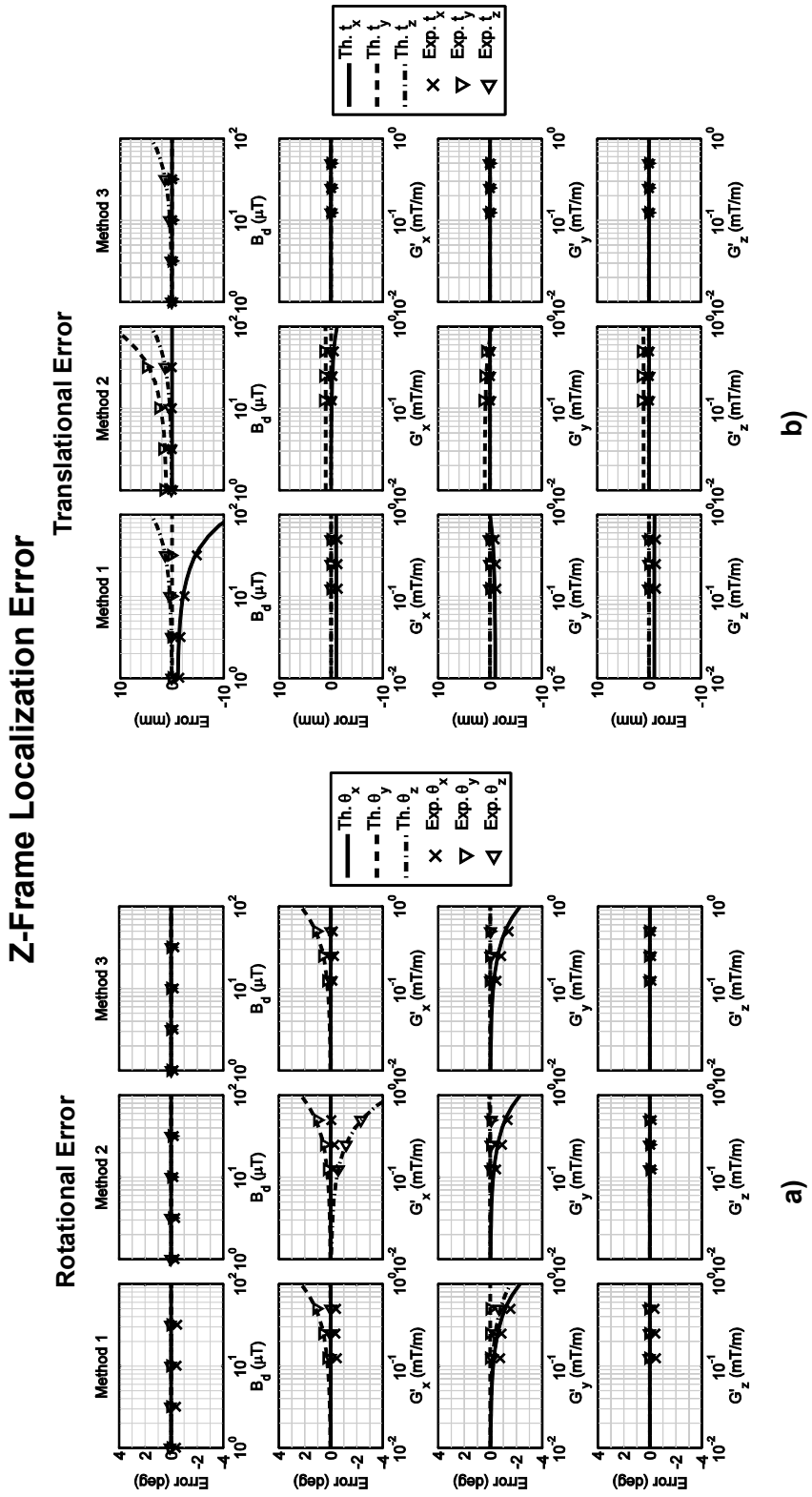

Figure 2.7: Error in pose estimation of the z-frame: a) rotational error, represented by the three Euler angles, b) translational error. Solid and dashed lines (denoted "Th." in the legends) indicate theoretical results, while the markers (denoted "Exp." in the legends) indicate results from the MR imaging experiments.

www.manaraa.com

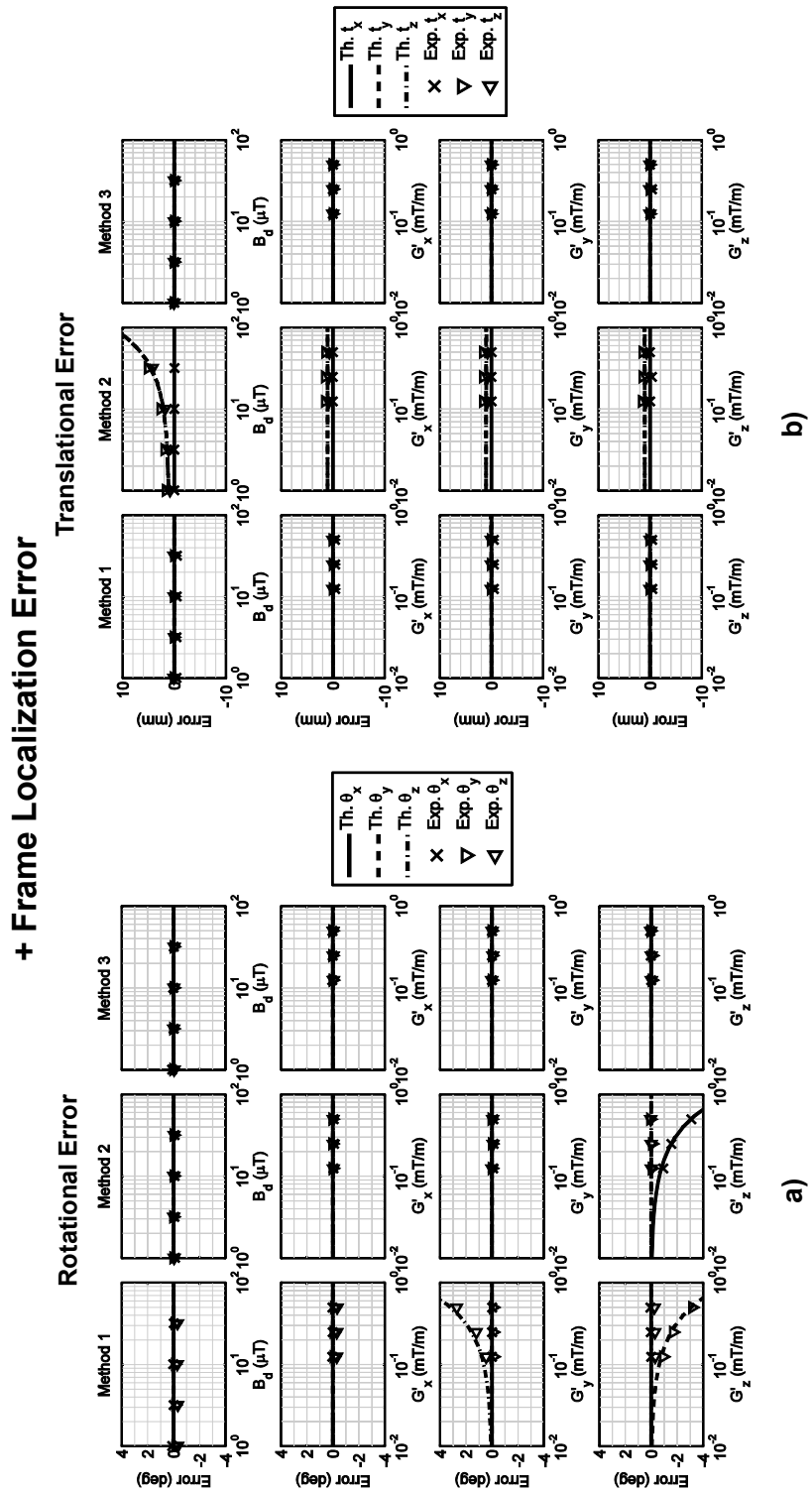

Figure 2.8: Error in pose estimation of the + frame: a) rotational error, represented by the three Euler angles, b) translational error. Solid and dashed lines (denoted "Th." in the legends) indicate theoretical results, while the markers (denoted "Exp." in the legends) indicate results from the MR imaging experiments. Note the lack of translational error with frequency encoding in the x-direction (Figure b, first column). This result is due to the polarity of the frequency-encoding gradient in the x-direction being reversed in axial and coronal scans, thereby cancelling out the translational error.

www.manaraa.com

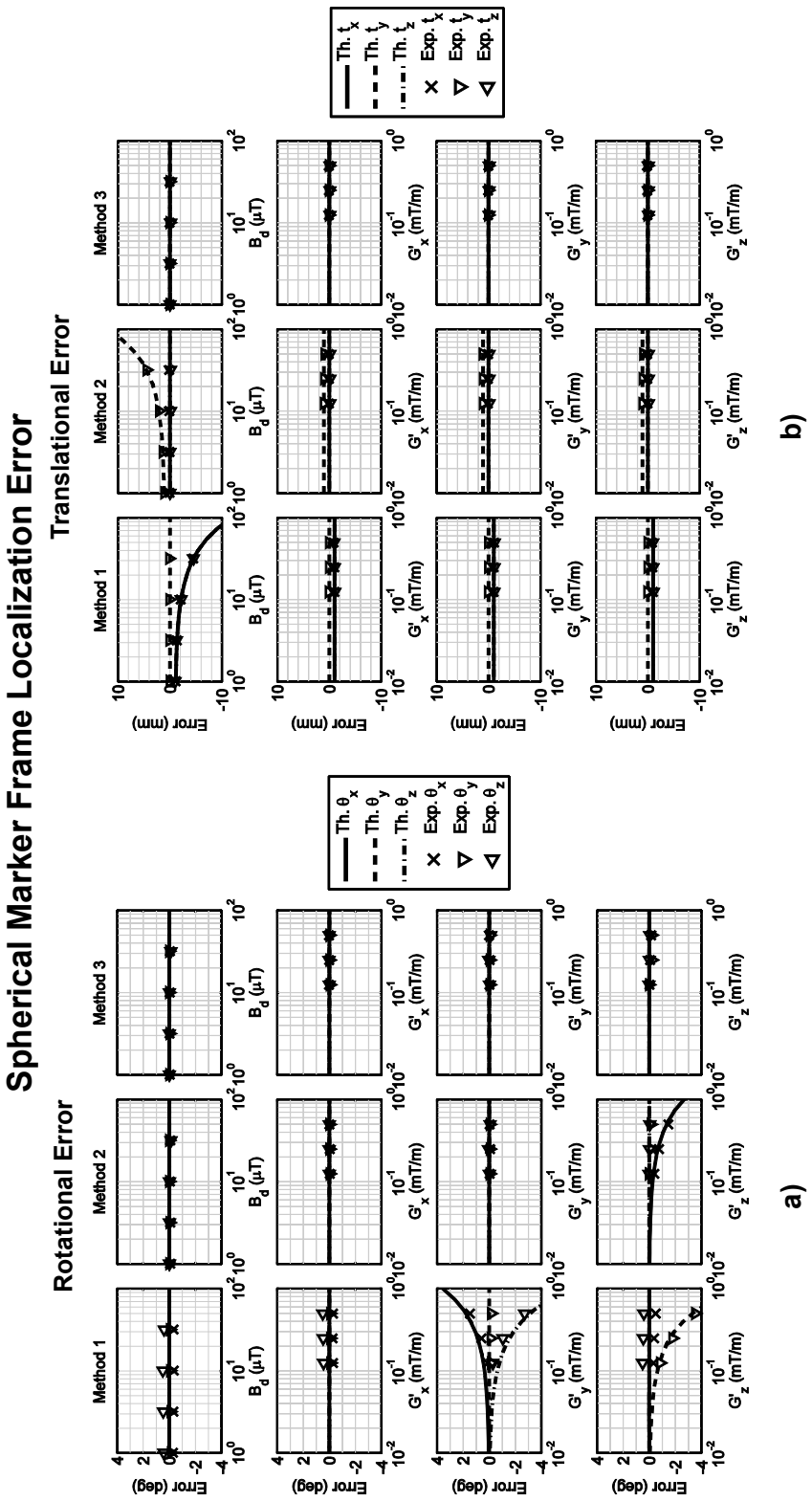

Figure 2.9: Error in pose estimation of the spherical marker frame: a) rotational error, represented by the three Euler angles, b) translational error. Solid and dashed lines (denoted "Th." in the legends) indicate theoretical results, while the markers (denoted "Exp." in the legends) indicate results from the MR imaging experiments.

www.manaraa.com

In the presence of a uniform static field distortion, each frame exhibits components of translational error that are proportional to the magnitude of the distortion (Figure 2.7b - Figure 2.9b, first row). In cases where sensitivity was observed, the translational errors range from nearly zero at 1 μT of distortion to greater than 10 mm at 100 μT. For the + and spherical marker frames, these components of error are eliminated if a method of correcting in-plane distortion is used (Figure 2.7b - Figure 2.9b, first row, third column). However, errors using the z-frame were not eliminated using the in-plane distortion method, since some components are due to slice-select error. For all three frames considered, the translational error is not sensitive to static field distortion gradients. A constant level of translational error of ~ 1 mm is also observed for each of the three frames. This is due to the transmit rf frequency not being properly matched to the fluid in each frame.

Static magnetic field distortion gradients result in rotational errors in frame pose estimates. For the frames tested, rotational errors ranged from zero to greater than 4 degrees over a range of distortion gradients of 0.01 – 1 mT/m. As with translational error, a method of correcting in-plane distortion can eliminate this sensitivity for both the + and spherical marker frames, but not the z-frame. Note also the presence of constant components of rotational error of ~ 0.5 degrees (most notable in Figure 2.7a - Figure 2.9a, first column) when in-plane distortion was not corrected. This trend is only observed in the experimental results, and is likely due to the presence of a baseline gradient shim from the spherical head phantom scan.

A practical example is now presented to aid in interpreting the results. Consider a sphere of radius *a* placed within the bore of an MR scanner. The expression for the

www.manaraa.com

external magnetic field distortion caused by the presence of this object in the bore of an MR scanner is given in Schenck *et al.*[30] as

$$\Delta B_d = \frac{\Delta\chi B_0 a^3}{3} \frac{2z_s^{\,2} - x_s^{\,2}}{\left(x_s^{\,2} + z_s^{\,2}\right)^{5/2}} \tag{2.19}$$

where z_s and y_s are parallel and perpendicular to the main field direction, respectively. Consider such a sphere consisting of austenitic stainless steel, for which the magnetic susceptibility is estimated from Schenck *et al.*[30] as 5110×10^{-6}, having a radius of 10 mm, and placed in a 3T scanner 150 mm from the center of a + frame. Figure 2.10 shows the resulting external magnetic field surrounding the sphere and frame, with the value of magnetic field distortion at each sampling point shown. In this case, the distortion field can be modeled as

$$\Delta B_d \approx 4.4 \times 10^{-6} - 0.07 \times 10^{-3} z\,, \tag{2.20}$$

giving $B_{d_0} = 4.4\mu\mathrm{T}$, $G_x' = 0$, $G_y' = 0$, and $G_z' = -0.07m\mathrm{T}/m$. Referring to Figure 2.8, these values can be used to estimate the resulting translational and rotational errors in pose estimate using each of the three imaging methods.

www.manaraa.com

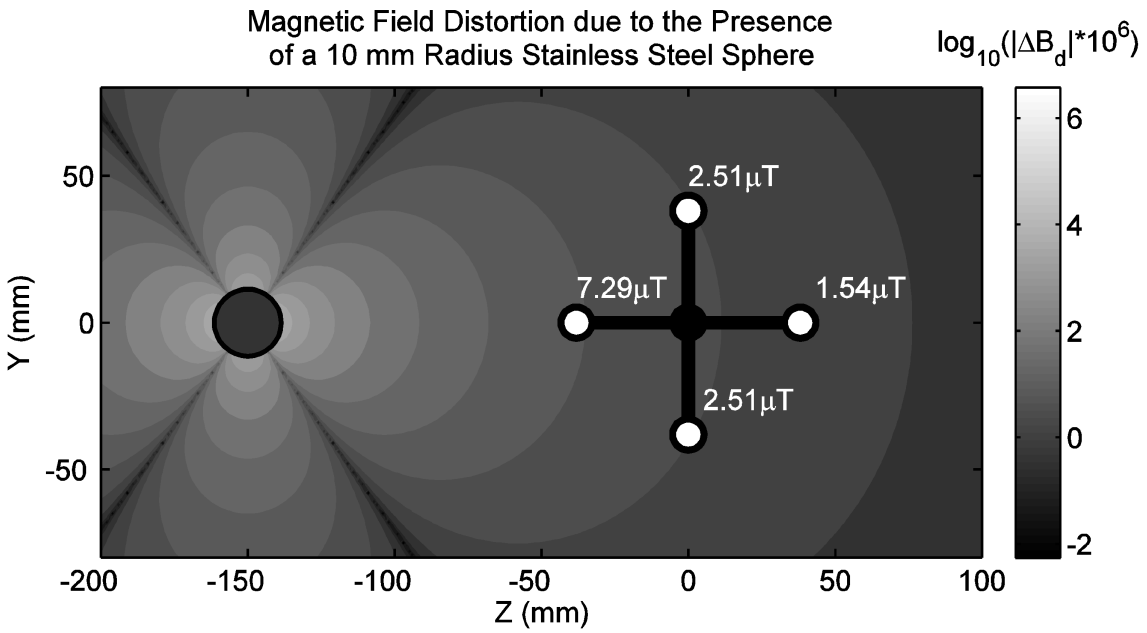

Figure 2.10: The magnetic field distortion field created by the presence of a 10 mm radius austenitic stainless steel sphere located 150 mm from the center of a localization frame. The white circles represent the points at which the frame is imaged. For the purposes of estimating the effects of the distortion on frame localization error, a linear representation of the distortion field over the frame's geometry is used.

2.4 Discussion

This work quantifies the effects of static field distortion on the accuracy of three types of passive localization frames in MR. The geometric nature of static field distortion across the geometry of each frame was modeled as the sum of uniform and linearly-varying components (*i.e.* magnetic field distortion gradients). 2D fast spoiled gradient echo sequences were used, as these represent the types of scans appropriate for quickly localizing objects in MR, and are readily available on any clinical MR scanner.

The pose of each frame considered is encoded in MR images in a characteristic manner: by using diagonal cylinders, the z-frame encodes the out-of-plane position of the frame in the in-plane position of ellipses in a 2D image; the + frame employs 2D bi-planar imaging to estimate frame position using only in-plane measurements of cylinder positions; and the spherical marker frame uses 2D tri-planar imaging to estimate frame

www.manaraa.com

position using in-plane measurements of sphere positions. As a result, the sensitivity of localization error to field distortion is characteristic of each type of frame. Most notably, the behavior of the z-frame is quite different from that of the other two. This is due to the fact that the z-frame's pose estimate from imaging is sensitive to slice-select error, resulting in components of rotational and translational error that are not eliminated by correcting in-plane error due to field distortion. Correction of the out-of-plane error would be possible by estimating the level of distortion based on the in-plane error, but this method requires knowledge of the slice-select gradient strength and polarity, which is not generally available on clinical scanner consoles or in DICOM files. Another notable trend in the results was the presence of error components that are (nearly) independent of the level of distortion. This source of error results from the transmit center frequency not being matched to the fluid in the frames. Table 2.4 summarizes typical sources of static field distortion and the types of localization error they cause in the absence of proper correction techniques. Sensitivity to all of these sources of error is eliminated using 2D gradient echo imaging if: a) the method of determining pose only uses in-plane measurements of marker positions, b) the in-plane marker positions in images are not sensitive to slice-select error, and c) methods of correcting in-plane error in the readout direction are employed.

Table 2.4: Sources of static field distortion and their effects on frame localization error

Source of distortion	Geometric nature of the distortion	Resulting error
Magnetic materials	Uniform + gradient	Translation + rotation
Center frequency offset	Uniform	Translation
Frame susceptibility	Uniform	Translation
Gradient shims	Gradient	Rotation

www.manaraa.com

Some practical considerations must be made when interpreting the results of this work. The magnitude of the distortion-sensitive components of rotational and translational error is inversely proportional to the readout gradient strength (and slice-select gradient strength, for the z-frame only). Therefore, a decrease in error could be achieved by increasing the readout gradient strength. However, doing so would result in a decrease in signal-to-noise ratio (SNR), and possibly an increase in localization error due to decreased accuracy in centroiding each marker. This effect was not explored in this work, and a fixed value of readout gradient strength of 9.2 mT/m was used for all images to maintain a reasonable SNR. Another important practical consideration is the location of the frame relative to the scanner's isocenter. Since this work aimed to quantify the sensitivity of localization error to static field distortion alone, the frames were imaged at the isocenter. At a distance from the isocenter, the effects of gradient field nonlinearity become an important factor. However, this effect is scanner hardware dependent, requiring experiments to be performed on each scanner individually in order to quantify it. The methods used in this work are general; the trends in error as a function of uniform or gradient static field distortion level are valid for any scanner, but they are only valid for frames located near the isocenter.

www.manaraa.com

2.5 Conclusions

The error in pose estimation of passive localization frames in MR can be sensitive to static magnetic field distortion. The level of sensitivity, the type of error (*i.e.* rotational or translational), and the direction of error are dependent on the frame's design and the method used to image it. If 2D gradient echo imaging is employed, frames whose pose estimate is sensitive to slice-select error (such as the z-frame) should be avoided, since this source of error is not easily correctable. Accurate frame pose estimates that are insensitive to static field distortion can be achieved using 2D gradient echo imaging if: a) the method of determining pose only uses in-plane measurements of marker positions, b) the in-plane marker positions in images are not sensitive to slice-select error, and c) methods of correcting in-plane error in the readout direction are employed.

For the work in this thesis, the error characteristics of each tracking frame were considered along with practical considerations. The z-frame was rejected due to its sensitivity to slice-select error that is difficult to correct using only 2D imaging sequences, and its relatively larger size than the other two frames considered. Between the + and spherical marker frames, the + frame was chosen for practical reasons, since spherical markers are difficult to keep filled with fluid and free of air bubbles, and they also require more precise positioning of image slice locations to ensure the bulk of the marker appears in the image. In addition, the + frame is simpler to manufacture than either of the alternatives, as it only requires two perpendicular holes to be drilled.

www.manaraa.com

References

1. A. Melzer, E. Immel, R. Toomey and F. Fernandez-Gutierrez, "MR-Guided Interventions and Surgery," in *Springer Handbook of Medical Technology,* (Springer, 2012), pp. 477-501.

2. K. Chinzei, N. Hata, F. Jolesz and R. Kikinis, "MR compatible surgical assist robot: System integration and preliminary feasibility study," in *Med. Image Comput. Comput. Assist. Interv.,* edited by S. Delp, A. DiGioia and B. Jaramaz (Springer, 2000), pp. 921-930.

3. G. Fischer, S. DiMaio, I. Iordachita and G. Fichtinger, Med. Image Comput. Comput. Assist. Interv., 2007.

4. A. A. Goldenberg, J. Trachtenberg, Y. Yi, R. Weersink, M. S. Sussman, M. Haider, L. Ma and W. Kucharczyk, "Robot-assisted MRI-guided prostatic interventions," Robotica **28**, 215 (2010).

5. A. Krieger, I. Iordachita, S. E. Song, N. B. Cho, P. Guion, G. Fichtinger and L. L. Whitcomb, Proc. IEEE International Conference on Robotics and Automation, Anchorage, Alaska, 2010.

6. C. Ménard, R. C. Susil, P. Choyke, G. S. Gustafson, W. Kammerer, H. Ning, R. W. Miller, K. L. Ullman, N. Sears Crouse and S. Smith, "MRI-guided HDR prostate brachytherapy in standard 1.5 T scanner," Int. J. Radiat. Oncol. Biol. Phys. **59**, 1414-1423 (2004).

7. M. G. Schouten, J. Ansems, W. K. Renema, D. Bosboom, T. W. Scheenen and J. J. Futterer, "The accuracy and safety aspects of a novel robotic needle guide manipulator to perform transrectal prostate biopsies," Med. Phys. **37**, 4744-4750 (2010).

8. S. Song, J. Tokuda, K. Tuncali, C. Tempany, E. Zhang and N. Hata, "Development and Preliminary Evaluation of a Motorized Needle Guide Template for MRI-guided Targeted Prostate Biopsy," IEEE Trans. Biomed. Eng. (2013).

9. H. Su, D. C. Cardona, W. Shang, A. Camilo, G. A. Cole, D. C. Rucker, R. Webster and G. S. Fischer, "A MRI-guided concentric tube continuum robot with piezoelectric actuation: A feasibility study," IEEE Int. Conf. Rob. Autom., 1939-1945 (2012).

10. J. Cepek, B. Chronik, U. Lindner, J. Trachtenberg, S. Davidson, J. Bax and A. Fenster, "A system for MRI-guided transperineal delivery of needles to the prostate for focal therapy," Med. Phys. **40**, 012304 (2013).

www.manaraa.com

11. B. E. Dogan, C. H. Le-Petross, J. R. Stafford, N. Atkinson and G. J. Whitman, "MRI-Guided Vacuum-Assisted Breast Biopsy Performed at 3 T With a 9-Gauge Needle: Preliminary Experience," Am. J. Roentgenol. **199**, W651-W653 (2012).

12. V. U. Fiedler, H. J. Schwarzmaier, F. Eickmeyer, F. P. Müller, C. Schoepp and P. R. Verreet, "Laser-induced interstitial thermotherapy of liver metastases in an interventional 0.5 Tesla MRI system: Technique and first clinical experiences," J. Magn. Reson. Imaging **13**, 729-737 (2001).

13. T. J. Vogl, R. Straub, K. Eichler, D. Woitaschek and M. G. Mack, "Malignant Liver Tumors Treated with MR Imaging–guided Laser-induced Thermotherapy: Experience with Complications in 899 Patients (2,520 lesions)," Radiology **225**, 367-377 (2002).

14. G. Bourgeois, M. Magnin, A. Morel, S. Sartoretti, T. Huisman, E. Tuncdogan, D. Meier and D. Jeanmonod, "Accuracy of MRI-guided stereotactic thalamic functional neurosurgery," Neuroradiology **41**, 636-645 (1999).

15. G. Cole, J. Pilitsis and G. S. Fischer, IEEE International Conference on Robotics and Automation, 2009.

16. W. A. Hall, W. Galicich, T. Bergman and C. L. Truwit, "3-Tesla intraoperative MR imaging for neurosurgery," J. Neurooncol. **77**, 297-303 (2006).

17. G. R. Sutherland, S. Lama, L. S. Gan, S. Wolfsberger and K. Zareinia, "Merging machines with microsurgery: clinical experience with neuroArm: Clinical article," J. Neurosurg. **118**, 521-529 (2013).

18. V. Mouraviev, S. Verma, B. Kalyanaraman, Q. J. Zhai, K. Gaitonde, M. Pugnale and J. F. Donovan, "The Feasibility of Multiparametric Magnetic Resonance Imaging for Targeted Biopsy Using Novel Navigation Systems to Detect Early Stage Prostate Cancer: The Preliminary Experience," J. Endourol. (2012).

19. A. Melzer, B. Gutmann, T. Remmele, R. Wolf, A. Lukoscheck, M. Bock, H. Bardenheuer and H. Fischer, "Innomotion for percutaneous image-guided interventions," Engineering in Medicine and Biology Magazine, IEEE **27**, 66-73 (2008).

20. A. B. Wolbarst, A. Karellas, E. A. Krupinski and W. R. Hendee, "Advances in Medical Physics: 2010," Med. Phys. **38**, 4468 (2011).

21. C. Dumoulin, S. Souza and R. Darrow, "Real-time position monitoring of invasive devices using magnetic resonance," Magn. Reson. Med. **29**, 411-415 (1993).

22. J. Anders, P. SanGiorgio, X. Deligianni, F. Santini, K. Scheffler and G. Boero, "Integrated active tracking detector for MRI-guided interventions," Magn. Reson. Med. **67**, 290-296 (2012).

www.manaraa.com

23. A. de Oliveira, J. Rauschenberg, D. Beyersdorff, W. Semmler and M. Bock, "Automatic passive tracking of an endorectal prostate biopsy device using phase-only cross-correlation," Magn. Reson. Med. **59**, 1043-1050 (2008).

24. S. DiMaio, E. Samset, G. Fischer, I. Iordachita, G. Fichtinger, F. Jolesz and C. Tempany, Med. Image Comput. Comput. Assist. Interv., 2007.

25. I. Bricault, N. Zemiti, E. Jouniaux, C. Fouard, E. Taillant, F. Dorandeu and P. Cinquin, "Light puncture robot for CT and MRI interventions," Engineering in Medicine and Biology Magazine, IEEE **27**, 42-50 (2008).

26. H. Chang and J. M. Fitzpatrick, "A technique for accurate magnetic resonance imaging in the presence of field inhomogeneities," IEEE Trans. Med. Imaging **11**, 319-329 (1992).

27. R. A. Brown, "A stereotactic head frame for use with CT body scanners," Invest. Radiol. **14**, 300 (1979).

28. S. Lee, G. Fichtinger and G. S. Chirikjian, "Numerical algorithms for spatial registration of line fiducials from cross-sectional images," Med. Phys. **29**, 1881 (2002).

29. E. M. Haacke, R. Brown, M. Thompson and R. Venkatesan, *Magnetic resonance imaging: physical principles and sequence design*. (Wiley-Liss, 1999).

30. J. F. Schenck, "The role of magnetic susceptibility in magnetic resonance imaging: MRI magnetic compatibility of the first and second kinds," Med. Phys. **23**, 815 (1996).

www.manaraa.com

Chapter 3.

A System for MRI-Guided Transperineal Delivery of Needles to the Prostate for Focal Therapy†

3.1 Introduction

Though the worldwide prevalence of prostate cancer is third only to lung and skin cancers,[1] evidence has shown that the key to survival may be early detection and treatment.[2] As a result, the use of prostate specific antigen testing as a screening tool has increased, and more prostate cancer is being detected at earlier stages.[3] Early detection often results in the diagnosis of a localized cancer that is confined within the prostate capsule. Recent studies have demonstrated a reduction in prostate-cancer-specific mortality for patients with localized cancer treated with radical prostatectomy.[4, 5] While early detection and radical treatments may decrease mortality rates, there is growing belief that localized disease is being over-treated, resulting in unnecessary morbidities such as permanent sexual dysfunction and incontinence.[6, 7] As an alternative, many patients with low-grade localized disease may be candidates for active surveillance. However, though groups followed under active surveillance have shown low rates of prostate-cancer-specific mortality,[8] patients often choose to elect for definitive therapy due to the psychological burden that accompanies the diagnosis.[9]

†. A version of this chapter has been published: Cepek, J., Chronik, B., Lindner, U., Trachtenberg, J., Davidson, S., Bax, J., Fenster, A., "A system for MRI-guided transperineal delivery of needles to the prostate for focal therapy." Med. Phys. 40, 012304-1-15 (2013).

www.manaraa.com

The great discrepancy between prostate cancer prevalence and mortality rates[10] indicates that many patients are being over-treated with radical prostatectomy; however, results of following men on active surveillance have also indicated that some are under-treated.[11] Although localized prostate cancer is currently the most common diagnosis,[12] there is unfortunately no unified agreement regarding the optimal treatment of patients with this stage of the disease.

An emerging treatment for the management of localized prostate cancer is focal therapy.[13] The potential efficacy of focal therapies is based on the hypothesis that there is an 'index' tumour, that is the most likely cause of extension of disease outside of the prostate and ultimately, metastases leading to death.[14] If methods of accurately identifying index lesions were available, focal therapies could potentially offer definitive treatment to patients with localized prostate cancer without the excessive morbidity associated with radical prostatectomy, and without the stress caused by leaving the disease untreated.[15, 16] Much work is currently being done to achieve this goal including: methods of accurately recording the locations of biopsy samples from the prostate,[17] advanced imaging techniques for visualization of tumours,[18-20] and the correlation of *in vivo* images of prostate cancer from multiple modalities to ground truth grading through registration of histopathologic sections to *in vivo* images.[21] Such techniques have the potential to provide accurate localization of aggressive prostate tumours as the primary targets for focal therapy.

The most common emerging modalities for focal therapy include cryotherapy, high-intensity focused ultrasound, focal laser ablation and photodynamic therapy. While clinical trials investigating the efficacy of these techniques are ongoing, most have

www.manaraa.com

reached phase I trials, and their safety has been proven.[15] In particular, focal laser ablation has shown promise with regards to its ability to completely ablate a targeted volume of prostate tissue, and the use of contrast-enhanced MRI for accurate identification of the ablated tissue volume has been demonstrated.[22] Focal laser ablation is performed by inserting either an open-ended or translucent catheter into the prostate through the patient's perineum. An optical fiber with a diffusing tip is then inserted through the catheter to the tumour site, and is attached to a laser for thermal ablation.[23] MRI-guided focal laser ablation of prostate cancer has also been tested and it was found that MRI provided excellent visualization of the needle for guidance, thermal monitoring and damage estimation during the ablation using MR thermometry, and intra-treatment visualization of the ablated region.[23] While MRI appears to provide a full suite of tools for image-guided focal laser ablation, a method of accurately guiding the therapy to the tumour site in a time frame that would make the procedure economically feasible in the clinic has yet to be demonstrated. This is likely due to the greater operating cost of MRI compared to other imaging tools conventionally used for guiding prostate interventions (namely ultrasound). In addition, the accuracy of focal laser ablation methods must be evaluated *in vivo* to enable evaluation of the potential clinical efficacy of MR-guided prostate cancer focal therapies. Only once the clinical benefit of MR-guided prostate focal therapies is proven to exceed that of their cost will such procedures become economically feasible in the clinic.

The advantages of using MRI for guiding therapy or biopsies to the prostate have previously been recognized, and various research devices have been developed for needle guidance to the prostate in MRI scanners.[24-30] While several of these devices have

www.manaraa.com

shown promise with respect to targeting accuracy, issues remain regarding reductions in image signal-to-noise ratio (SNR), procedure workflow, and patient safety. SNR reduction is generally caused by the use of electromechanical actuators that increase noise in the MR scanner's rf receive coils, especially if the actuators are moved during imaging.[25, 27, 31] The main obstacle with regards to procedure workflow appears to be the limited space around the patient in the MR scanner bore, and the fact that the prostate is generally about 1 m into the bore (at the scanner's isocenter). The general solution to this problem has been to remove the patient from the MR scanner bore for needle insertion, and then move him back into the scanner for verification of needle depth with imaging.[26-28, 30] Since the needle cannot be visualized while it is being inserted, this method requires incremental insertions, with multiple translations of the patient in and out of the MRI bore. Doing so results in excessive movement - reducing potential accuracy, and longer procedure time. Finally, some existing devices have been fully automated, compromising patient safety since there is generally no haptic feedback or redundant safety systems in place.[25, 27]

In this work, we hypothesize that a manually-actuated, MRI-guided needle trajectory alignment device could enable accurate and time-effective delivery of needles to the prostate for focal therapy while maintaining image SNR and patient safety, and allowing for real-time monitoring of needle guidance with the patient in-bore. We present the design and prototype of such a device, results from MR-compatibility tests, demonstration of its potential to accurately target tumours of the smallest clinically significant size (~10 mm diameter)[32], and preliminary results from clinical testing.

www.manaraa.com

Preliminary results from this work have been previously described in a conference paper.[33] In this previous publication, the trajectory alignment device was briefly described and only one simple test of needle guidance accuracy was performed. This chapter includes rigorous testing of needle guidance accuracy and repeatability using a more realistic prostate phantom, demonstration of a user interface that is integrated with the MRI scanner and trajectory alignment device, and results from initial experiences using the system to deliver focal laser ablation therapy to two patients. In addition, the trajectory alignment device features an improved method of registration to the MRI scanner that has resulted in decreased needle guidance error. In the previous work, the registration component was placed nearly 20 cm inferior to the prostate. When the imaging field-of-view is this far from the isocenter, most clinical scanners will automatically translate the bed to place the center of the field-of-view at the isocenter, and output image positions relative to the isocenter. It was found that the scanners we used (GE Discovery MR750, and GE Signa HDxt 1.5T) could not accurately estimate the scanner bed movements, and therefore could not reliably give an accurate location of the device's fiducials.

The rest of this chapter will be organized as follows: Section 3.2 will describe the design of the trajectory alignment device and the system's user interface, methods of evaluation of the system's MR-compatibility, methods of quantifying the system's targeting error, and the setup and workflow of the system for tests in patients; Section 3.3 includes results from the MR-compatibility tests, targeting error tests, and experience using the system to deliver focal laser ablation therapy to two patients; followed by a

www.manaraa.com

discussion of the results and recommendations for future work in Section 3.4; and conclusions in Section 3.5.

3.2 Methods

3.2.1 System Design

The primary component of the system is the needle trajectory alignment device. The device is placed between the legs of the patient within the bore of an MRI scanner, and is used to precisely align a set of needle guides with a target in the prostate.

Figure 3.1 shows a computer-aided design rendering of the device in position with a patient in an MRI bore.

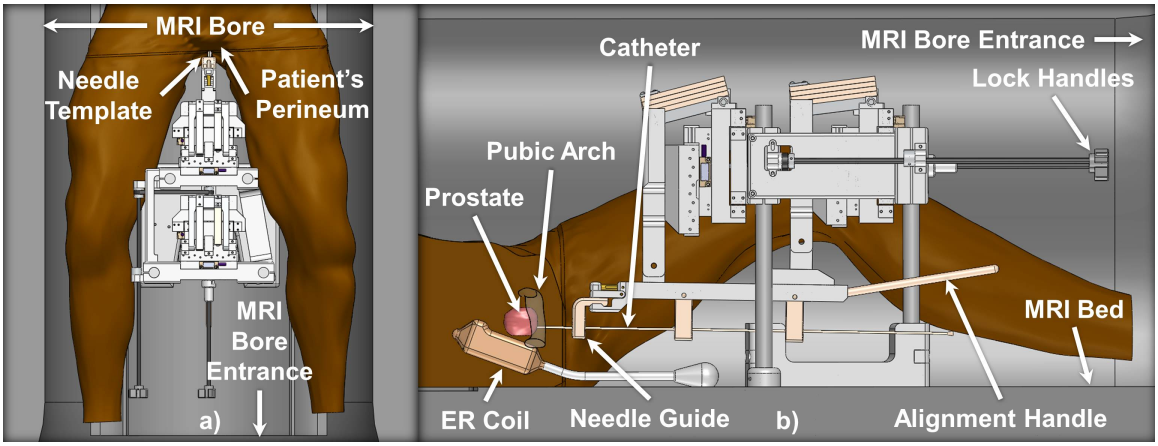

Figure 3.1: Computer-aided design drawing showing the trajectory alignment device in position with a patient in the bore of an MRI scanner. a) View from above, b) Side view with patient sectioned to show internal anatomy. The device is designed to allow oblique needle trajectories to reduce pubic arch interference while avoiding interference with the endorectal (ER) coil.

The entire system consists of the trajectory alignment device and its supporting components: a laptop computer, embedded controller electronics, and an MR-compatible alignment interface. Custom focal laser ablation guidance software on the laptop communicates with the MRI scanner via the File Transfer Protocol for acquisition of images. The images are used to register the pose of the needle targeting device to the

www.manaraa.com

scanner, select target points in the prostate, and monitor needles during insertion. The controller compares the device's position to that required to reach the specified target and indicates to the physician, via the alignment interface, in which direction the device should be moved to be aligned with the target.

Figure 3.2 shows how manual device alignment is achieved by the physician, and Figure 3.3 shows the device in position with a patient during a focal laser ablation procedure.

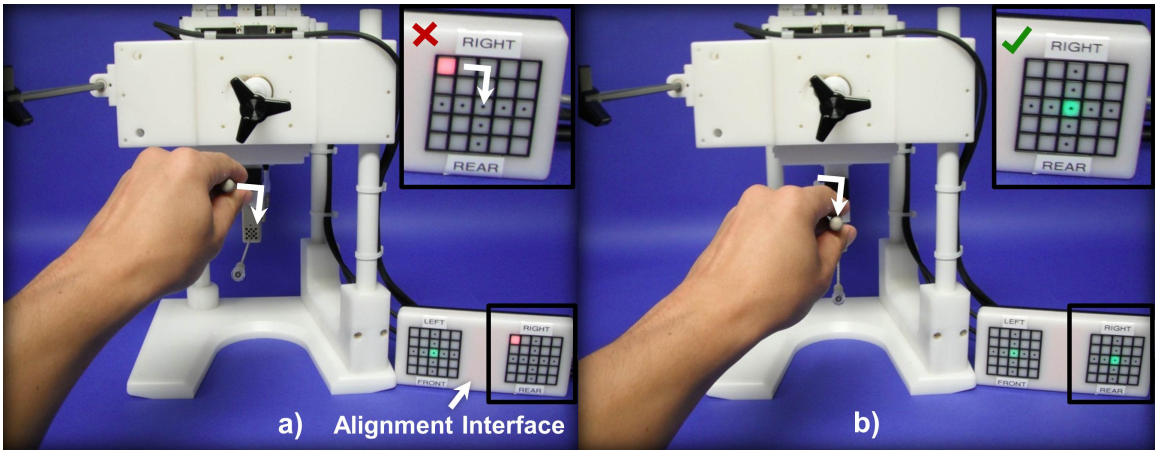

Figure 3.2: Manual alignment of the trajectory alignment device using the targeting interface. a) The handle is misaligned and must be moved to the right and downward, as indicated by the 'right' grid display, b) the device has been successfully aligned with the selected target.

www.manaraa.com

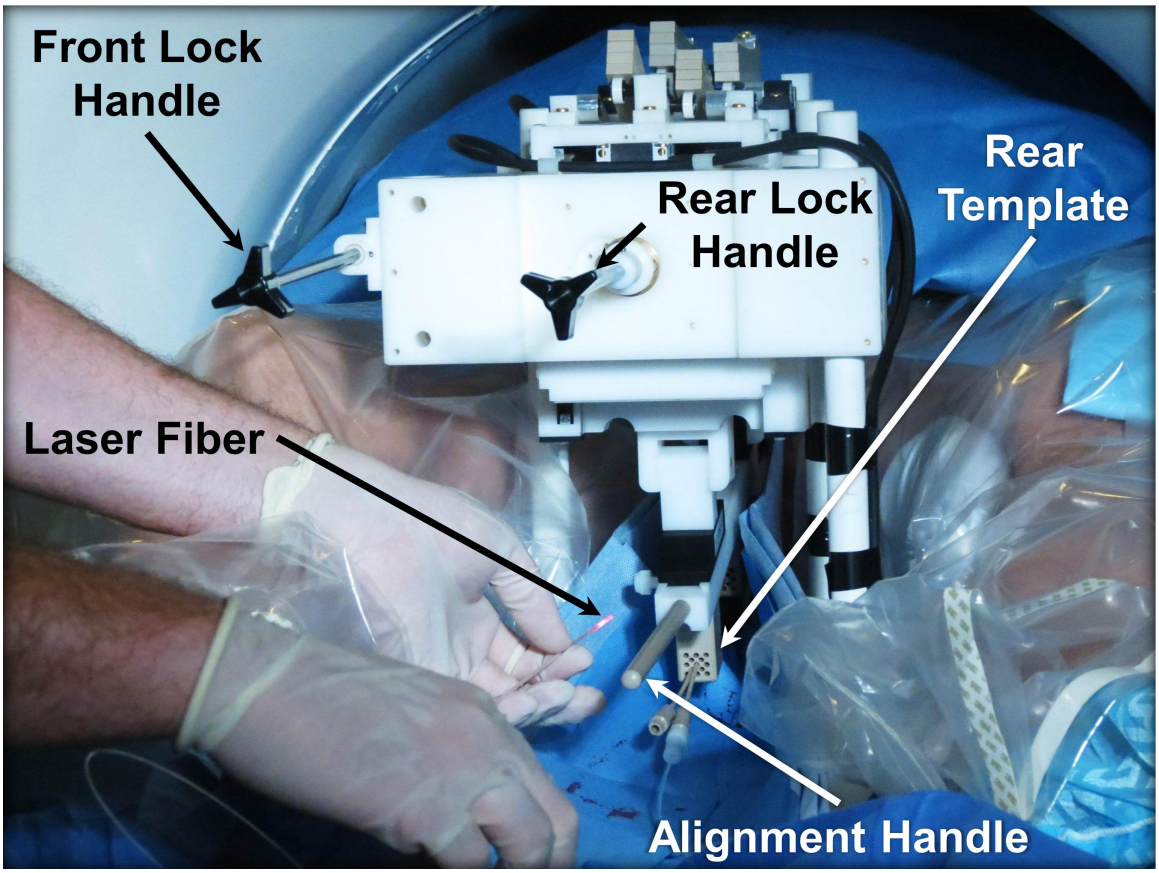

Figure 3.3: The trajectory alignment device in position with a patient in the bore of a 1.5T clinical MRI scanner (Signa HDxt, GE Healthcare, Milwaukee, WI). Access to the lock handles, alignment handle, and rear template are maintained with the patient still in the bore. Two catheters have been successfully inserted, and the physician is preparing a laser fiber for ablation.

3.2.2 Mechanical Design and Kinematics

Figure 3.4 shows the trajectory alignment device and its major components. The device consists of three needle guide templates mounted to a movable arm. The orientation and position of the arm is manually controlled by the physician, and it is supported by two sets of custom-built dual-axis linear stages through rotational joints. The position of each linear stage is encoded with MR-compatible linear optical encoders (LIA-20, Numerik Jena, Jena) and, through the use of forward kinematics equations, the precise position and pose of the needle trajectory is known. These encoders were selected over purely optical sensors because they are readily available off-the-shelf, and come in a compact linear

www.manaraa.com

form factor that integrated well with our design. As well, our tests indicated that they cause a minimal reduction in image quality. The position of each set of the linear stages can be independently manipulated by locking the opposite set (with manual locking handles), and moving the alignment handle. In this way, the physician can control four degrees of freedom of the needle trajectory using three simple controls with the device in-bore. Manipulation of the 'front' set of linear stages sets the approximate needle insertion point on the patient's skin, while that of the 'rear' set modifies the angle of needle insertion.

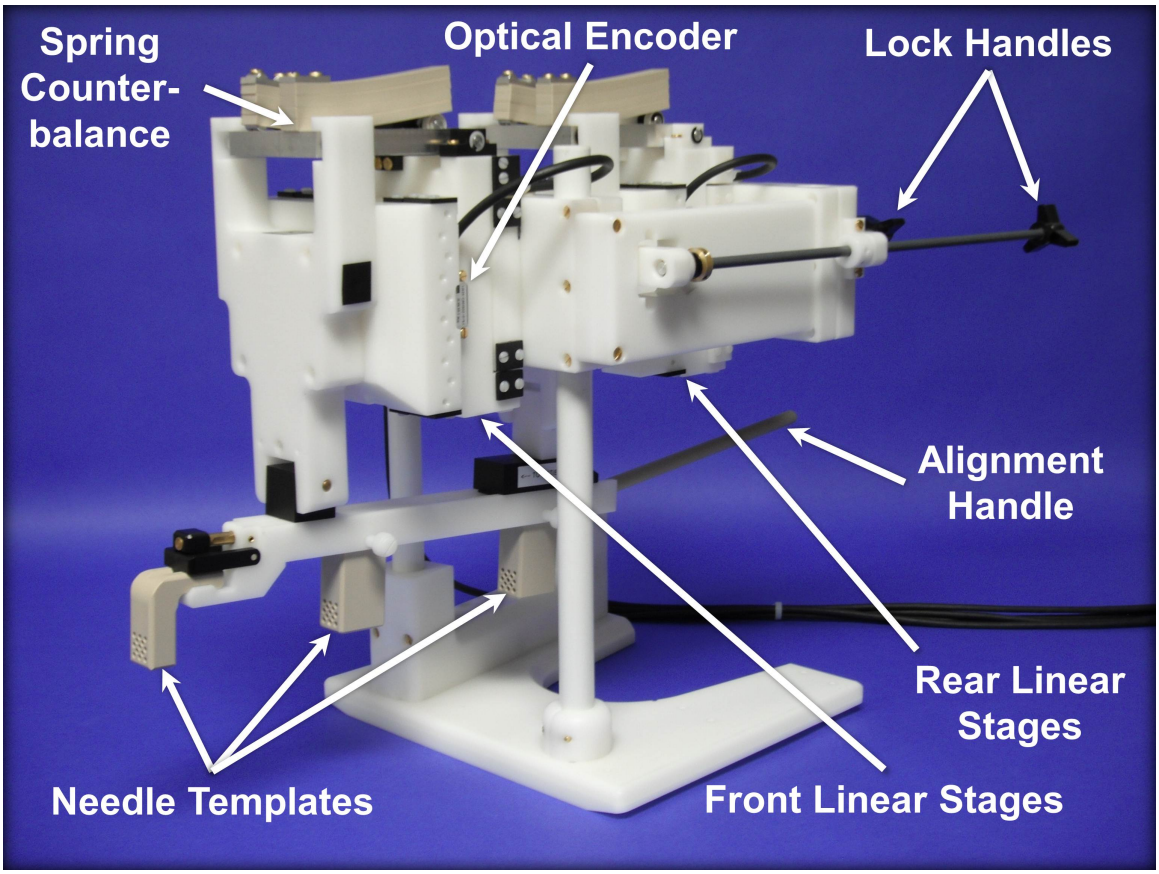

Figure 3.4: The trajectory alignment device. The pose of the needle templates is uniquely defined by the positions of the front and rear linear stages. Positioning of each set of stages can be independently achieved by unlocking the corresponding set using the locking handles and manipulating the alignment handle. The spring counterbalances maintain the position of each set of stages during positioning. The two rear needle templates allow the physician to insert a long catheter from outside the MRI bore and guide it into the front template, which is located adjacent to the patient's skin.

www.manaraa.com

When the stages are unlocked, the trajectory is maintained by spring-loaded counterbalances that oppose the force of gravity.[34] The counterbalances supply a force to the device's vertical stages that are equal to their weight and constant throughout the device's entire range of motion. MR-compatibility of the counterbalance assembly is maintained through the use of leaf springs made from plastic (polyetheretherketone), as opposed to conventional steel coil springs. Figure 3.5 shows the spring counterbalance system.

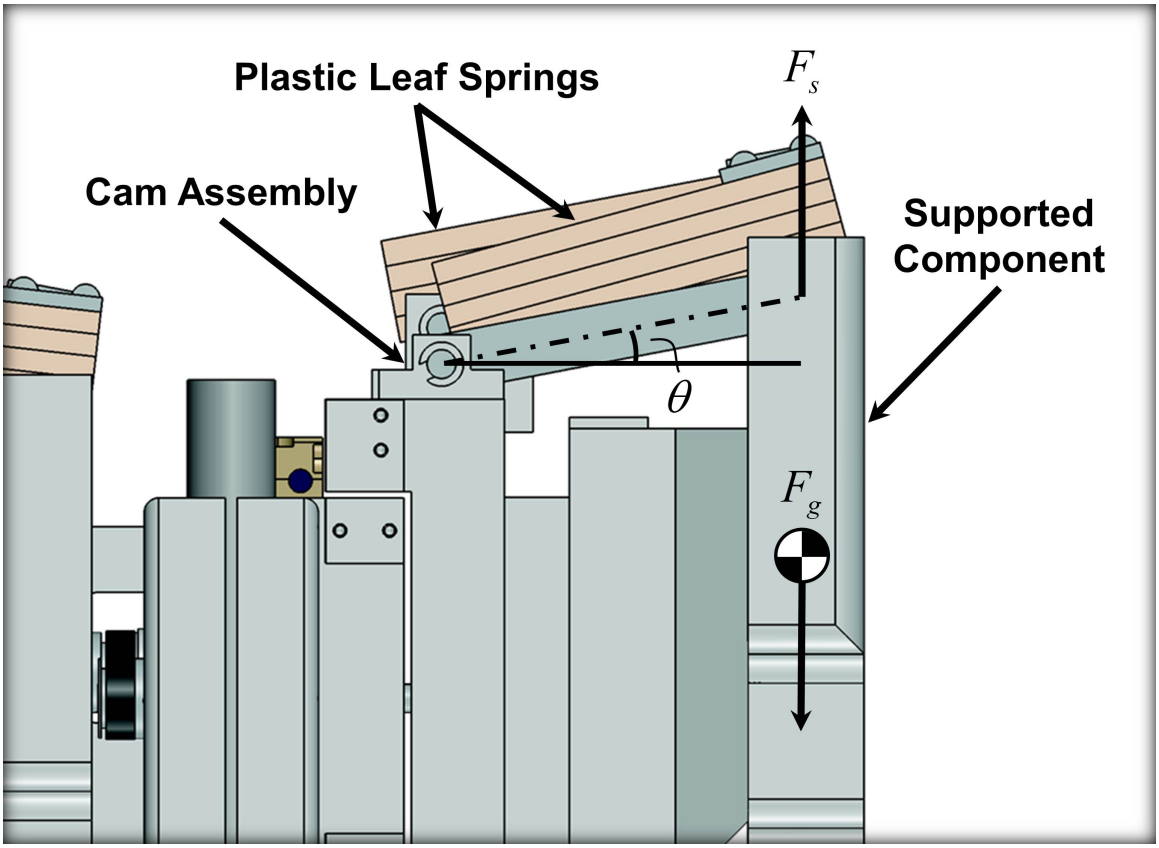

Figure 3.5: Schematic of the spring counterbalance system. The leaf springs provide a force F_s that opposes the force of gravity F_g acting on the components with a vertical degree of freedom. The cam assembly ensures that F_s is constant throughout the entire range of angle θ.

Figure 3.6 illustrates the variables used in the kinematics equations and the device's coordinate system. The forward kinematics equations serve to compute the pose

www.manaraa.com

of the needle guide (represented by p_t and $\hat{v}_n$), given positions of the linear stages (as measured by the linear encoder values: e_{1x}, e_{1y}, e_{2x} and e_{2y}). Reverse kinematics equations compute the linear stage positions required for the device to be aligned with a given needle trajectory. Detailed kinematics solutions can be found in Appendix B. The device can be operated in two modes: "target only mode" and "target and entry mode". In the former, the physician is allowed to reach a given target from any angle, and the forward kinematics solution is used to compare the selected target point with the intersection of the needle with an axial plane that contains the target point. In the latter, the reverse kinematics solutions are used to guide the physician to constrain all four degrees-of-freedom of the device to ensure the needle will pass through two given points: the target point and the entry point.

www.manaraa.com

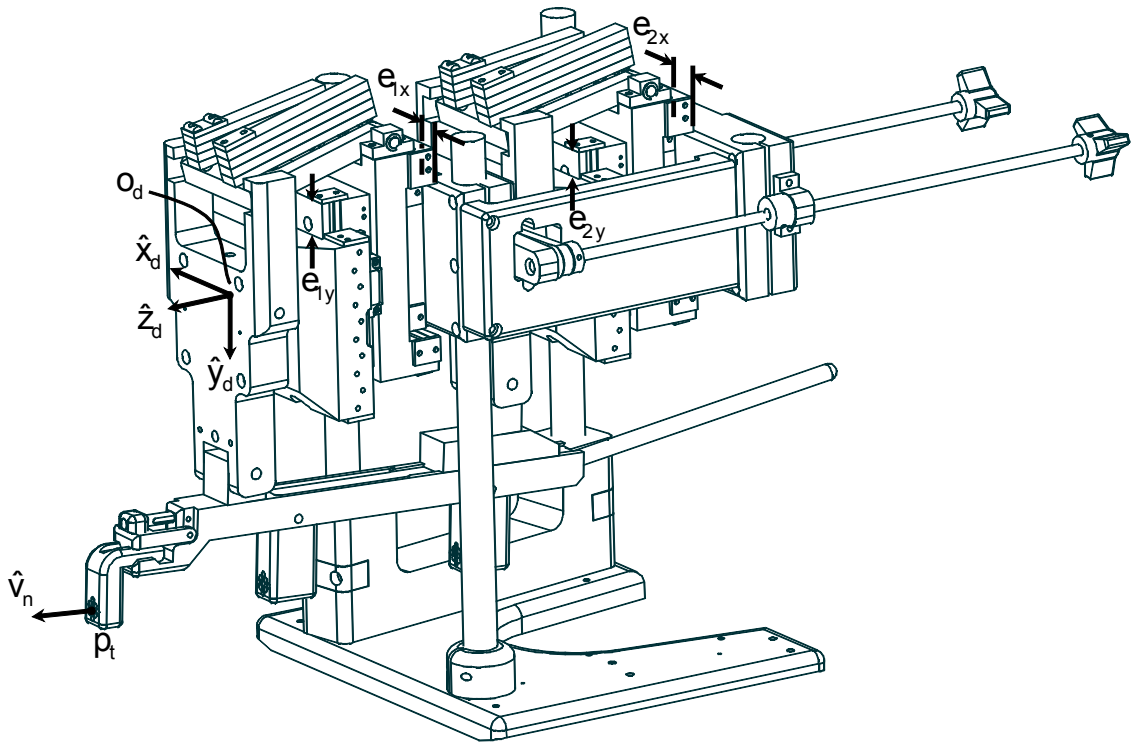

Figure 3.6: Device coordinate system and kinematics variables. Specification of all four linear stages positions e_{1x}, e_{1y}, e_{2x}, and e_{2y} uniquely defines the intended needle trajectory, defined by $\hat{v}_n$ and p_t in a closed kinematic chain (forward kinematics). Likewise, a given needle trajectory corresponds to a unique set of linear stage positions (reverse kinematics).

3.2.3 Registration of Device and MRI Coordinate Systems

The precise position of the device in MRI coordinate space will differ in each procedure because: a) optimal device placement differs between cases depending on individual patient size and placement, b) each new MRI study requires a new landmark position, and the position of each image is given relative to that landmark position, and c) since the device is designed for use in a clinical MR scanner, it is likely that the scanner would be used for diagnostic scanning in between focal therapy procedures; requiring removal of the device. It is therefore necessary to register the device's coordinate system to that of the MRI at the beginning of each procedure to ensure accurate guidance. This is achieved with the use of a detachable MR-visible fiducial component. The removable component

www.manaraa.com

consists of two perpendicular drilled holes in the shape of a +, filled with an aqueous solution of 1% gadolinium by volume (Magnevist, 469 mg/ml). The fiducial arrangement is embedded in a plastic component that is mounted to the front of the device. The fiducial component is shown in Figure 3.7, along with a sagittal MR image showing the four points that must be localized for registration. The dashed lines indicate the image planes in which each point is localized. The points p_0 and p_1 are localized in axial images, and p_2 and p_3 in coronal images. Figure 3.8 shows an axial image of the registration fiducials.

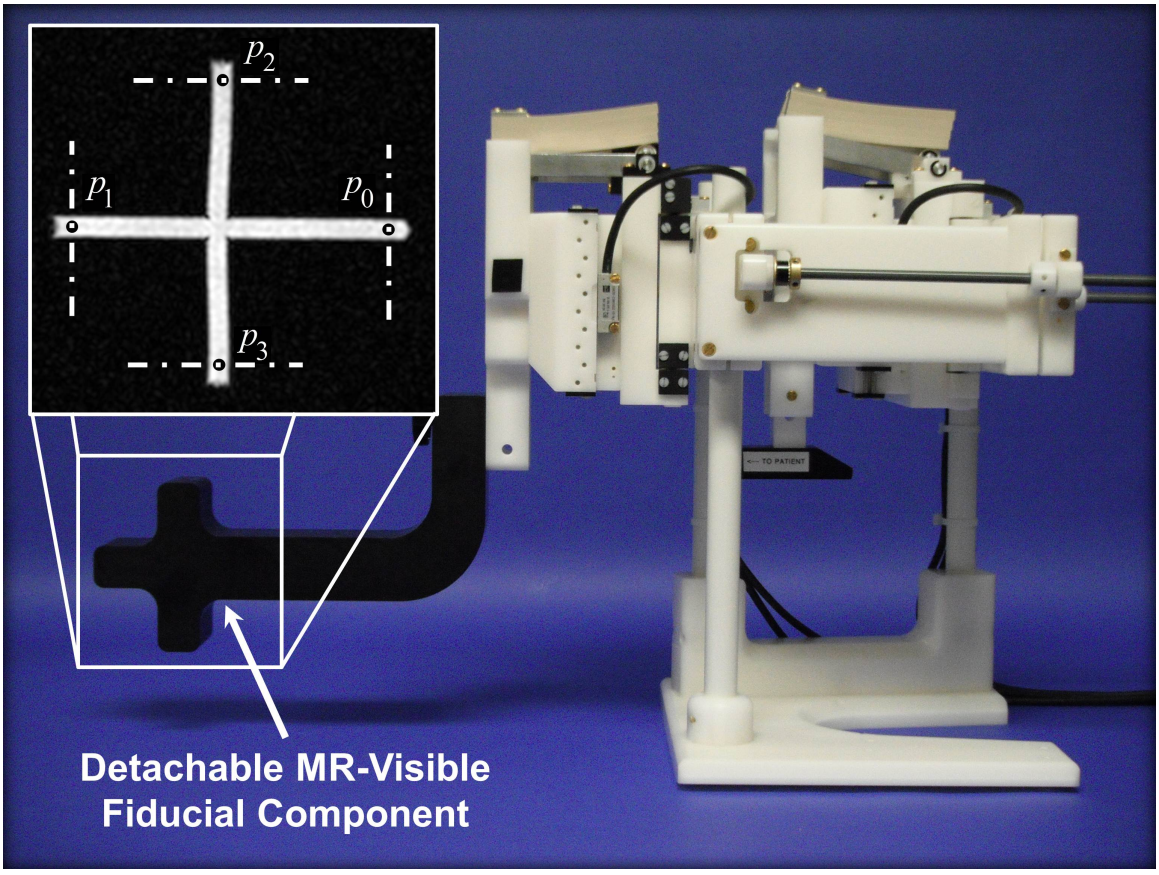

Figure 3.7: Detachable registration fiducial component. The component is imaged in both axial and coronal planes for the localization of four points, necessary for registration of the device's coordinate system to that of the MRI.

www.manaraa.com

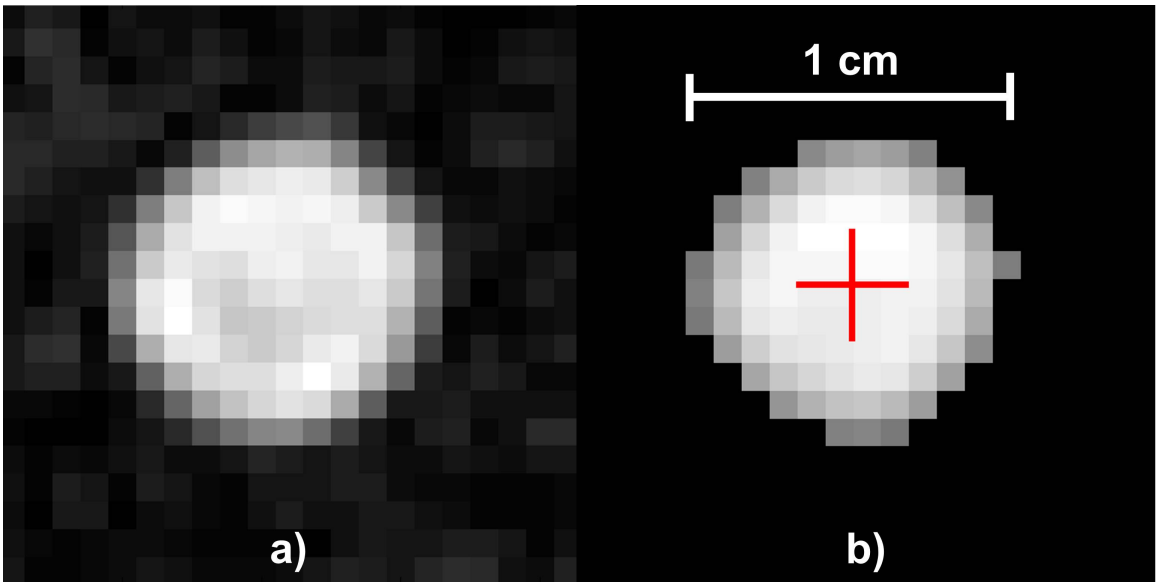

Figure 3.8: Localization of registration fiducials in MR images. a) Original fiducial image, b) filtered & thresholded fiducial image. The red cross indicates the centroid.

The images are filtered to reduce noise using a circular averaging filter (pill-box) of radius 2 pixels, then thresholded. The size of each fiducial tube is known, so the threshold is chosen such that the total area of the thresholded image is equal to the known area of a section of a fiducial tube. Fiducial localization is then performed by computing an intensity-weighted centroid of the filtered, thresholded image

$$\bar{x}_i = \frac{\sum_{j=1}^{m}\sum_{k=1}^{n} I(j,k)\,x_i(j,k)}{\sum_{j=1}^{m}\sum_{k=1}^{n} I(j,k)}, \tag{3.1}$$

where $x_i(j,k)$ is the i^{th} coordinate of the pixel at index (j,k), $I(j,k)$ is the corresponding pixel intensity, and $\bar{x}_i$ is the i^{th} coordinate of the centroid of the image of size $m \times n$.

Sensitivity of fiducial localization to main field inhomogeneity is reduced by only measuring coordinates in the phase encode direction of each image.[35] Accordingly, two

www.manaraa.com

sets of images of each fiducial are acquired, with the phase encode direction swapped in each acquisition. Since the device axes are generally nearly aligned with those of the MRI system, error in pose estimation of the fiducial arrangement due to slice-select error is minimal.[35] The four points are used to compute the unit vectors in the direction of each of the device's axes, in MR coordinates, as:

$$\hat{z}_d = \frac{p_1 - p_0}{|p_1 - p_0|},\ \hat{x}_d = \frac{-(p_1 - p_0)\times(p_3 - p_2)}{|(p_1 - p_0)\times(p_3 - p_2)|}, \text{ and } \hat{y}_d = \hat{z}_d \times \hat{x}_d, \tag{3.2}$$

and the origin as the closest point to the line that passes through p_0 and p_1, and that which passes through p_2 and p_3. Points in the device coordinate system can be converted to the MRI's coordinate system using:

$$(p_{mr})_i = (p_d)_1(\hat{x}_d)_i + (p_d)_2(\hat{y}_d)_i + (p_d)_3(\hat{z}_d)_i + (o_d)_i, \tag{3.3}$$

where p_d is a point in the device coordinate system, and p_{mr} is the point in the coordinate system of the MRI. Points in the MRI's coordinate system can be converted to device coordinates by solving the linear system:

$$\begin{bmatrix} (\hat{x}_d)_1 & (\hat{y}_d)_1 & (\hat{z}_d)_1 \\ (\hat{x}_d)_2 & (\hat{y}_d)_2 & (\hat{z}_d)_2 \\ (\hat{x}_d)_3 & (\hat{y}_d)_3 & (\hat{z}_d)_3 \end{bmatrix} \begin{bmatrix} (p_d)_1 \\ (p_d)_2 \\ (p_d)_3 \end{bmatrix} = \begin{bmatrix} (p_{mr})_1 - (o_d)_1 \\ (p_{mr})_2 - (o_d)_2 \\ (p_{mr})_3 - (o_d)_3 \end{bmatrix}. \tag{3.4}$$

The registration fiducials are placed at the MRI isocenter, scanned before the patient is positioned, and removed from the device before the patient arrives; a process that generally takes less than ten minutes to complete. This approach reduces the amount of time the patient must be anesthetized.

www.manaraa.com

3.2.4 Electrical Systems

Measurement of the position of each of the device's linear stages is achieved with LIA-20 optical encoders (Numerik Jena, Jena, Germany). The encoders are constructed from non-magnetic materials and output a sine-cosine signal in the kHz range. Since the rf system of the MRI operates in the MHz range, the encoders do not introduce an appreciable level of noise to the images. The encoder cables are connected through rf filters on the scanner room's penetration panel to the console room, where the signals are converted to digital TTL levels and are read by the controller. The targeting interface was manufactured from non-magnetic surface-mount electrical components in a shielded enclosure and was connected to the controller through rf filters in the penetration panel. Though the targeting interface uses digital signals, it was not found to appreciably degrade image quality, and an alternative solution such as a fiber optic display was not deemed necessary.

3.2.5 User Interface and Procedure Workflow

The focal laser ablation guidance software is the hub of the procedure workflow. At the start of the procedure, pre-treatment T2-weighted MR images of the prostate, and the prostate and tumour boundaries (as identified on multi-parametric MR images), are imported into the visualization software. Intra-treatment T2-weighted MR images of the prostate are then acquired, transferred to the software, manually segmented, and registered to the pre-treatment prostate image using an iterative closest point method that compares the pre- and intra-treatment prostate boundaries. This process provides localization of predefined targets in the intra-treatment workspace for targeting.

www.manaraa.com

Figure 3.9 shows the result of a registration between pre- and intra-treatment prostate images.

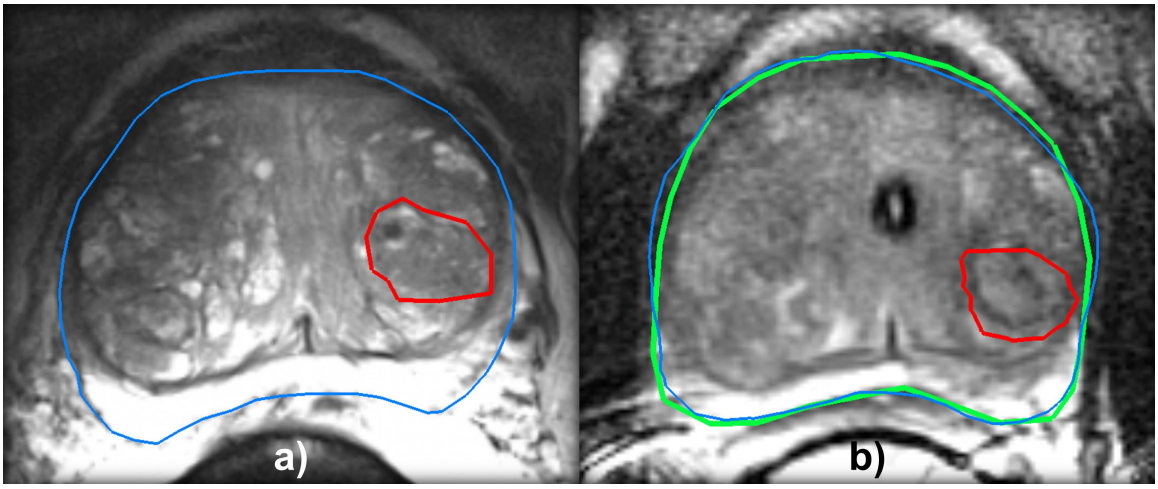

Figure 3.9: Intra-treatment prostate registration. a) Pre-treatment image with prostate boundary (thin blue contour) and suspicious region (red contour) segmented, b) intra-treatment image showing both the manual intra-treatment contour (thick green contour) and registered pre-treatment contours (thin blue contour). The registration process locates the suspicious region in intra-treatment MR space.

Images of the targeting device's fiducials are imported and localized for computation of the device's origin and coordinate axes in the intra-treatment coordinate space. Once the device registration transform has been sent to the controller, the needle pose is continually retrieved and the needle's projected trajectory is visualized in real-time (at approximately 10 frames per second) for verification of device positioning. Figure 3.10 shows the needle trajectory display.

www.manaraa.com

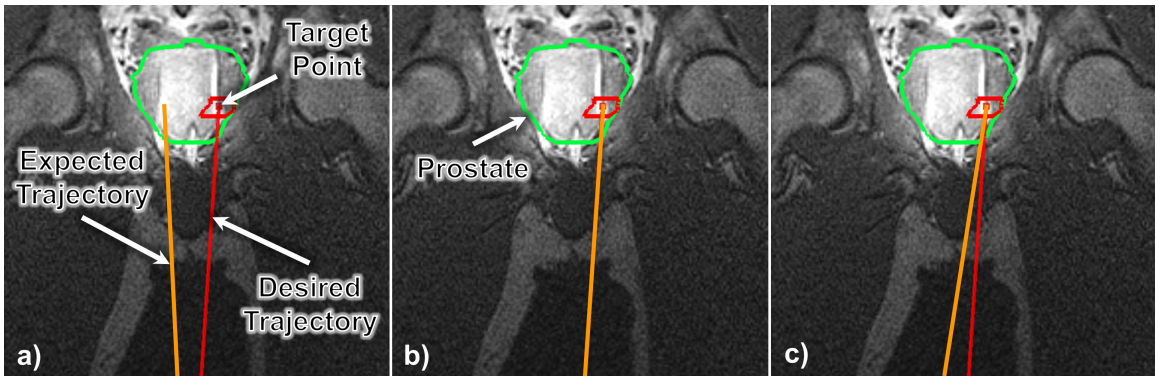

Figure 3.10: Live 3D needle trajectory display overlaid on a coronal image of the prostate and surrounding anatomy. a) Device misaligned, b) device aligned to target and entry point, c) device aligned only to target point (target only mode). Orange line: expected needle trajectory, computed from device kinematics equations and displayed in real-time. Red line: desired needle trajectory, specified by the user. Green contour: prostate boundary.

After device registration to the MR coordinate system is complete, targets within the prostate can be selected and the targeting interface guides the physician to align the device. The guidance interface consists of two grids of multi-coloured lights, shown in Figure 3.11.[33]

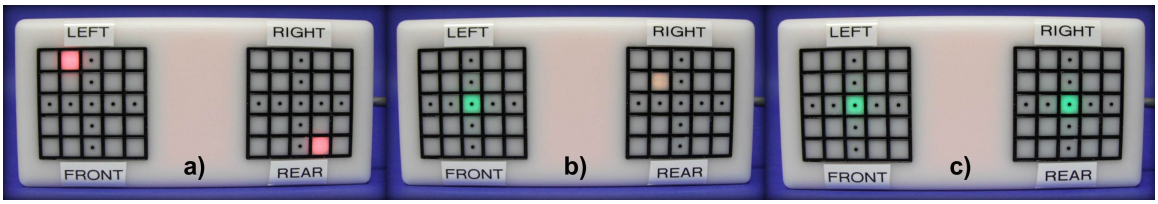

Figure 3.11: Device alignment interface. a) Front and rear stages misaligned, b) front aligned, rear misaligned, c) device fully aligned with desired trajectory.

The illuminated light on each grid indicates to the physician the direction in which the alignment handle must be moved. The device is aligned with its target trajectory only once the center lights of the grids are illuminated. In this way, the physician must always move the handle in the direction in which he/she wants to move the light, regardless of which set of stages is being moved, or which targeting mode is being used. In 'target and entry mode', one grid is used to align the front set of stages, and the other is used for the rear set. In 'target only mode', only one grid is used for

www.manaraa.com

alignment. In this case, the physician is free to position the front set of stages as they see fit, and then adjust the rear set using the targeting interface.

Custom needles, consisting of a tungsten trocar inside of an open-ended polyetheretherketone catheter, were used for all experiments and tests in patients, as shown in Figure 3.12. The use of custom needles was necessary as it was not possible to find an existing commercially available nonmagnetic needle with an optimal combination of stiffness, sufficient length, and sharpness, in a gauge that would accommodate the laser ablation equipment used for this procedure.

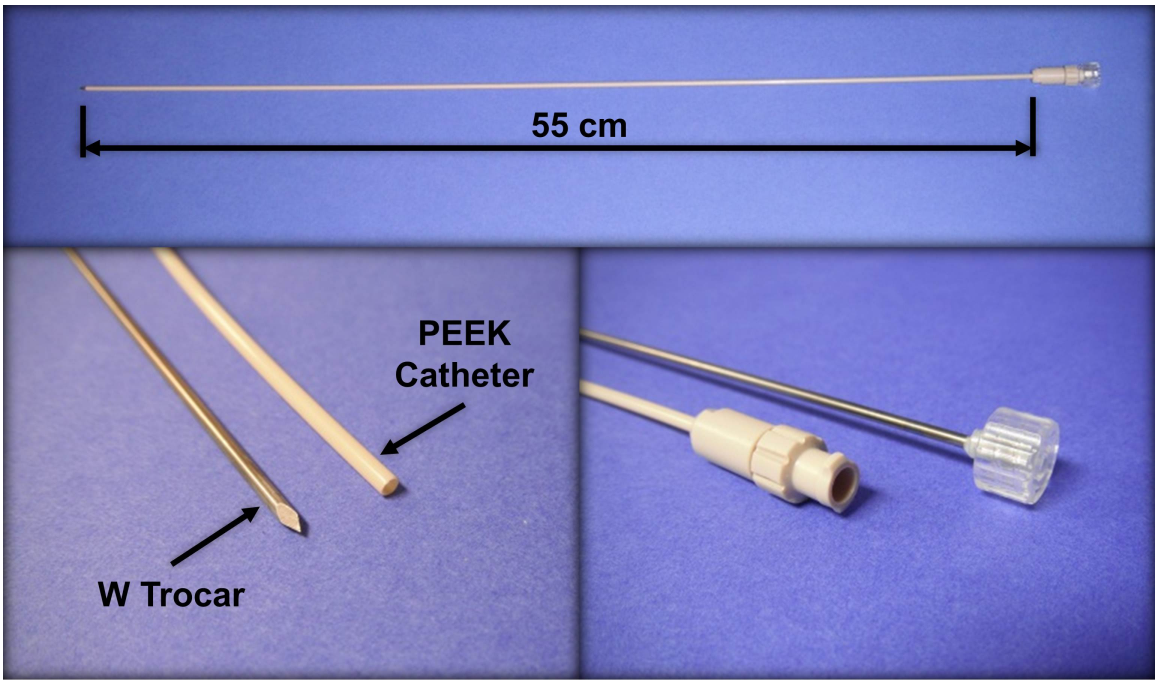

Figure 3.12: Custom tungsten trocar and polyetheretherketone catheter. The assembly is 55 cm in length to allow for needle insertion with the patient in the MRI bore. The tungsten trocars feature a 3-sided symmetrical bevel tip. Standard Luer-Lok fittings mate the trocar to the catheter during insertion.

Enhancement of needle MR images is achieved by periodically replacing the tungsten trocar with a gadolinium solution-filled tube during imaging. This method provides a well-delineated, bright image of the needle for localization. MR images of metal needles in a patient show a large susceptibility artifact at the needle tip, making

www.manaraa.com

localization difficult, especially since the size and orientation of the artifact varies with scan parameters.[36] The software provides tools for measuring the remaining insertion depth required to reach the target. Once the target is reached, a laser fiber, housed in a plastic coaxial cooling sheath, is inserted to the end of the catheter. Verification of the position of the end of the laser fiber is achieved by imaging the cooling sheath, which is flushed with a 1% solution of gadolinium in water. The laser is then activated and tissue heating begins while the tissue temperature is monitored using the proton resonant frequency shift method.[37] Using this method, a temperature map can be computed relative to that of a baseline image. The change in temperature in each voxel is computed as

$$\Delta T(t) = \frac{\Delta\phi(t)}{\alpha\gamma B_0 TE}, \tag{3.5}$$

where $\Delta\phi(t)$ is the difference in phase between the image at time t and the baseline image, α is the proton resonant frequency temperature dependence coefficient of water (-0.01 ppm/°C), γ is the gyromagnetic ratio for a ^1H nucleus (2.68 × 10^8 rad/s/T), B_0 is the main magnetic field strength, and TE is the echo time.

From the temperature map, tissue damage is estimated using an Arrhenius formulation wherein the tissue damage is quantified using a single parameter

$$\Omega(t) = \int_0^t A\exp\left(\frac{-E_a}{RT(\tau)}\right)d\tau, \tag{3.6}$$

where R is the universal gas constant, E_a is the activation energy, T is the temperature, and A is the frequency factor. The parameter $\Omega(t)$ varies from zero to positive infinity, and the tissue is considered to be ablated once it reaches a value of unity.[38]

www.manaraa.com

Figure 3.13 shows thermal and damage mapping in the prostate during a focal laser ablation procedure.

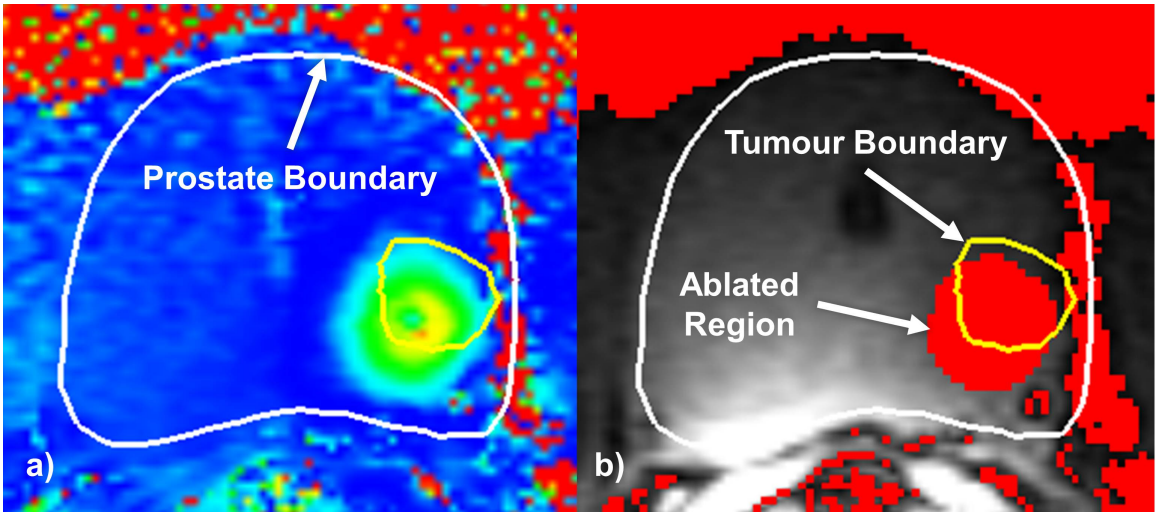

Figure 3.13: MR thermometry and tissue thermal damage estimation. a) Temperature image showing the ablation zone and prostate and tumour boundaries, b) thermal damage map superimposed on an MR image of the prostate. Regions in red correspond to $\Omega >= 1$ from Eq. (3.6) and are considered ablated. Note that in this case the ablated region did not reach the anterior edge of the tumour boundary, requiring the insertion of an additional needle.

3.2.6 MR-Compatibility

To enable an accurate delivery of needles to the prostate, the guidance system must not degrade the quality of MR images, and the MRI system must not affect the operation of the guidance system.[39, 40] Specifically, the presence of the device in the scanner must not cause detrimental image artifacts due to magnetic field distortions or a substantial reduction in SNR, and the scanner must not induce notable force, torque, vibration or heating effects on the device or affect operation of the device's electronics.

3.2.7 Image Distortion and Signal-to-Noise Ratio

Our methods for evaluation of image distortion and SNR effects in MRI were based on the American Society for Testing and Materials "Standard Test Method for Evaluation of MR Image Artifacts from Passive Implants",[41] and the National Electrical

www.manaraa.com

Manufacturers Association standard for "Determination of Signal-to-Noise Ratio (SNR) in Diagnostic Magnetic Resonance Imaging",[42] as these are the most relevant existing standards for such tests. Image distortion and SNR reduction effects were measured by acquiring images of a fluid-filled grid phantom adjacent to the device. The center of the phantom was placed a distance from the device equivalent to that expected for a patient's prostate (~10 cm). Axial images of the phantom were acquired for each of the following cases: 1) device not present (baseline), 2) device in position, not connected, 3) device in position, cables connected, not powered, and 4) device in position, cables connected, powered. Axial gradient echo images were acquired on a 3T MR scanner (MR750, GE Healthcare, Milwaukee, WI) with the parameters: field-of-view: 400 mm x 400 mm, matrix: 256 x 256, repetition time: 270 ms, echo time: 4 ms, flip angle: 25°. Each set of images was acquired with bandwidths of both 195 and 977 Hz/pixel. The low bandwidth image set was used to evaluate image distortion, while the higher bandwidth set was used for SNR calculations. Doing so ensures that the test is sensitive to any distortions or SNR reductions due to the device presence. SNR was calculated using a mean signal in a 30 x 60 voxel region near the middle of the field-of-view, and the standard deviation of the signal in a region of the same size outside the phantom. The SNR was calculated in image slices that contained only fluid.

3.2.8 Effects of MRI on the Device

The MRI system may induce effects on the device that compromise patient safety or the fidelity of its operation. These effects include induced force and torque, and rf-induced heating. In addition, the MRI must not cause enough interference in the device's encoder electronics to introduce an error in the device's encoded position. The American Society

www.manaraa.com

for Testing and Materials (ASTM) has developed methods for evaluating the force and torque effects on passive implants.[43, 44] The ASTM methods are deemed appropriate for these evaluations since the targeting device will, at most, only make contact with the surface of a patient's skin. The ASTM tests for induced force and torque evaluate whether the induced force is "less than the force on the device due to gravity"[43] and whether the induced torque is "less than the product of the longest dimension of the medical device and its weight".[44] These conditions were tested qualitatively by holding the device in the MRI bore and observing the induced force / torque. rf-induced heating of the device was also judged qualitatively. Finally, errors in encoder operation can be detected by continually checking that the incremental encoder counts are equal to zero each time an index pulse is received.

3.2.9 Targeting Accuracy

Three tests were performed to quantify the system's targeting abilities. The first measured the system's ability to accurately position its needle guides throughout its usable workspace in free space. The second evaluated its ability to aim the needle guides at virtual targets in MRI space under MRI guidance. The third experiment quantified the system's overall performance in guiding a needle to a target in a tissue-mimicking phantom under MRI guidance. Figure 3.14 illustrates each of the components of needle placement error that were measured in each of the three tests. Evaluation of target localization error was beyond the scope of this chapter. The components of error within the green box in Figure 3.14 represent an estimate of needle guidance error (NGE), which is equal to needle placement error in the absence of target localization error, which may

www.manaraa.com

result from inaccurate registration of pre-treatment targets to the intra-treatment image space and target motion.

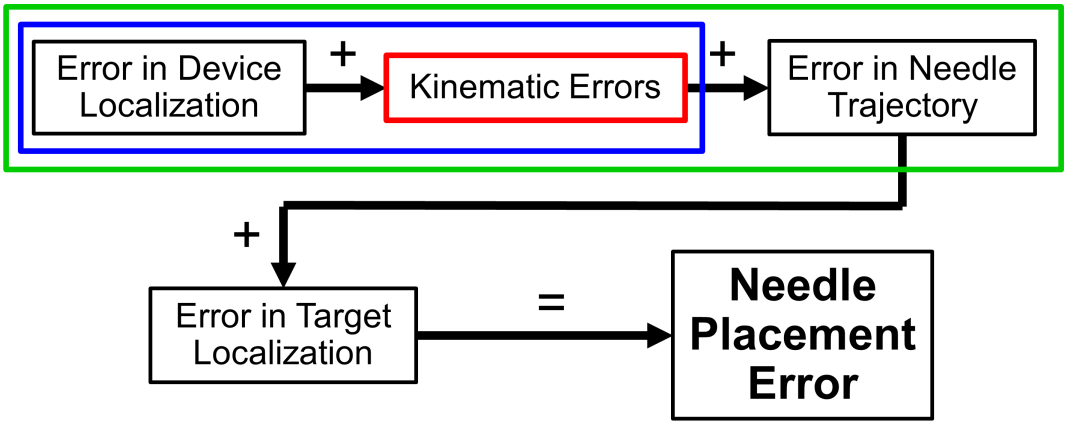

Figure 3.14: Illustration of the components of needle placement error measured in each of the three accuracy tests. Red box: errors measured in the open-air targeting test. Blue box: errors measured in the intra-MR targeting test. Green box: errors measured in the intra-MR phantom needle guidance test. Evaluation of target localization error was not performed, as it was beyond the scope of this chapter.

3.2.9.1 Open-Air Targeting Accuracy

The device's ability to align a needle to a target in free space was determined with the use of a coordinate measuring machine (FX7107, Brown & Sharp, North Kingstown, Rhode Island) with a volumetric accuracy[45] of 5.2 µm. The device's arm was fitted with two steel tooling balls, and their positions were measured with the coordinate measuring machine over 81 different device positions. To reach the full range of needle trajectories, a regular grid of nine points was defined for each set of linear stages. The device was then moved through all combinations of these positions for the front and rear sets of stages. The tooling balls were mounted to the device at depths representative of the farthest typical target and entry point depths. Error in the position of each tooling ball, E_{TB}, was computed as the absolute distance between its expected position as computed from the forward kinematics solution and that measured by the coordinate measuring

www.manaraa.com

machine. Angular error, A_{TB}, was computed as the angle between the expected needle trajectory from forward kinematics, and the line between the furthest and nearest tooling balls, as measured by the coordinate measuring machine.

3.2.9.2 Intra-MR Trajectory Alignment Accuracy

The system was evaluated for its ability to align its needle guides with targets in 3D under MRI guidance. This was done by fitting the device's arm with two MR-visible spheres, coincident with the needle axis, and aligning the device to a set of five target and entry point pairs throughout the range of its workspace. The spheres were then imaged to determine the true trajectory of the needle guides in MR space. The 10 mm diameter spheres were filled with the same gadolinium solution as the registration fiducials. Centroids of the fiducials were localized using three sets of images: two sets of axial images with the phase encode direction swapped, and coronal images for the third coordinate (with phase encoding in the superior-inferior direction). Coordinates were only measured in the phase encode direction in each image. The target points p_i^t and entry points p_i^e are virtual and therefore independent of the device's calibration and tracking errors. Errors were quantified following the methods described by Cool *et al.*[46] The needle axis, n_i, was defined as the line between the two spherical fiducials, and the needle guidance error (NGE) was calculated as the minimum distance between each target point and the needle axis

$$NGE_i^{tr} = M\left(p_i^t, n_i\right). \tag{3.7}$$

where the equation of the needle is defined by

$$n_i = p_i^n + \hat{v}_i^n s, \tag{3.8}$$

www.manaraa.com

and $M(a,b)$ is a function that measures the minimum distance from a point a to a line segment $b = p + \hat{v}s$

$$M(a,b) = \left| (a-p) - \left[(a-p) \bullet \hat{v} \right] \hat{v} \right|. \tag{3.9}$$

NGE represents the total error in using the system to point a needle at p_i^t through p_i^e.

One quantifiable contributor to NGE is needle guidance human error (NGHE). NGHE represents the ability of the user to align the device with the desired needle path using the alignment interface. NGHE was measured by computing the distance between the needle axis from the forward kinematics solution k_i, and p_i^t

$$NGHE_i^{tr} = M\left(p_i^t, k_i\right), \tag{3.10}$$

where the needle axis computed from the kinematics solution is defined as $k_i = p_i^k + \hat{v}_i^k s$.

Needle trajectory error (NTE) evaluates the discrepancy between n_i and the expected needle trajectory from the forward kinematics solution. NTE includes contributions from errors in device-to-MR registration, geometric distortions in images of the spherical fiducials, localization of fiducial centroids, and repeatability of the MR bed positioning. NTE is computed as the minimum distance between n_i and the point ttp_i, defined as the nearest point to p_i^t along k_i

$$ttp_i = p_i^t - \left\{ \left(p_i^t - p_i^k \right) - \left[\left(p_i^t - p_i^k \right) \bullet \hat{v}_i^k \right] \hat{v}_i^k \right\}. \tag{3.11}$$

$$NTE_i^{tr} = M\left(ttp_i^t, n_i\right) \tag{3.12}$$

The experiment was performed five times to quantify targeting repeatability.

www.manaraa.com

3.2.9.3 Needle Placement in Tissue-Mimicking Phantoms

Tissue-mimicking prostate phantoms were developed to quantify the system's potential for delivering needles to tumours under ideal conditions. The phantoms were based on the design presented by Lindner *et al.*[47], with the 10% gelatin prostate substituted for 3% agar (both by mass). Lindner *et al.* showed that the forces required to penetrate the perineum (alginate) and prostate (gelatin) of their phantom were nearly equivalent to those required for human tissue. Agar was used for this work because it has MRI relaxation values (T1 and T2) similar to human prostate tissue, and is stiffer than gelatin, thereby representing a more difficult challenge for needle guidance accuracy than gelatin would.[48, 49] Each phantom consisted of a 72 cm^3 agar prostate, embedded in alginate impression material (Type II – Regular set, 25% by mass) inside a rectangular plexiglass box with an opening on one end to allow for needle insertions. The mold for the prostate was generated from a manually segmented 3D transrectal ultrasound image of a biopsy patient's prostate and was scaled in size (6 cm R-L, 5 cm S-I, 4.5 cm A-P) to allow for a wider range of targets. The agar was prepared using a modified version of the method used by Rickey *et al.*[50], wherein the mixture only consisted of agar and distilled water. The center of the prostate phantom was located ~10 cm from the box opening, which corresponds to the average anatomical distance from a patient's perineum to the center of the prostate. Five such phantoms were prepared and mock needle guidance procedures were performed on each on separate days. Each mock procedure followed the workflow outlined in section 3.2.5, but without thermal ablation, and five virtual points in each prostate were targeted during each session.

www.manaraa.com

Evaluation of system accuracy was performed by computing NGE, NGHE, and NTE in a similar manner to that in the previous section (errors for the phantom experiment are denoted by the superscript *ph*). For NGE^{ph}, the virtual points p_i^t and p_i^e were defined by the user manually selecting targets in the phantom and dragging the desired needle trajectory in the focal laser ablation guidance software, respectively. n_i was defined by the line through the segmented needle, as found in two axial images, one near the target and one near the selected entry point. Localization of the needle in each image was computed using an intensity-weighted centroid, following the method described in section 3.2.3 for the registration fiducials.

3.2.10 Clinical Evaluation

The system was tested clinically on two patients to determine its effect on the accuracy of needle delivery, time to deliver needles, and efficiency of the procedure workflow. The patients gave informed consent, and were enrolled in an ongoing University Health Network Research Ethics Board approved phase I study of MR-guided focal laser thermal therapy for patients with low-risk prostate cancer (ClinicialTrials.gov ID: NCT01094665). The system is only used in Canada, and has been classified as a Class I medical device under Health Canada's regulations. Using the system, a total of nine needles were delivered to the patients' prostates for focal laser ablation. Needle guidance accuracy was defined as in section 3.2.9.3 for the phantom experiment. Gradient echo images of the needles in their final positions were acquired in axial, sagittal, and coronal planes. Needle trajectories were measured in axial images using the method described in section 3.2.3 for registration fiducials.

www.manaraa.com

3.2.11 MR Imaging Parameters

Table 3.1 summarizes the MR imaging parameters used for all acquisitions described in this chapter. The imaging sequence used in each case was a 2D fast spoiled gradient echo. Imaging parameters used for visualizing needles in the clinical cases varied at the MR operator's discretion, and the values included are only a representative example.

Table 3.1: MR imaging parameters used for all images acquired in this chapter.

Parameter	*B0*	*TR*	*TE*	*FA*	*Slice Thickness*	*FOV*	*Acq. Matrix*	*BW*
Distortion Test	3	270	4	25	3	400 x 400	256 x 256	195
SNR Test	3	270	4	25	3	400 x 400	256 x 256	977
Tracking Frame (Accuracy Tests)	3	270	4	30	3	140 x 140	128 x 128	244
Spherical Markers (Accuracy Tests)	3	270	4	30	3	140 x 140	128 x 128	244
Tissue-Mimicking Phantom (Accuracy Tests)	3	100	4	60	3	80 x 80	128 x 128	244
Tracking Frame (Clinical Cases)	1.5	120	1.8	60	4	150 x 150	128 x 128	63
Needle Localization (Clinical Cases)†	1.5	6	1.5	60	4	300 x 300	256 x 256	244
Units	T	ms	ms	deg.	mm	mm	-	Hz/px

†. Varied at MR operator's discretion. This is a representative example.

3.3 Results

3.3.1 MR-Compatibility

3.3.1.1 Image Distortion and Signal-to-Noise Ratio

Figure 3.15 shows the baseline and difference images from the distortion test.

www.manaraa.com

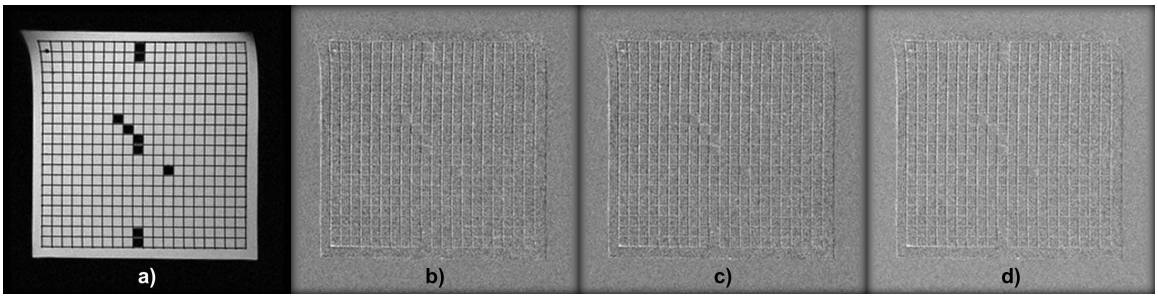

Figure 3.15: Images from distortion test: a) baseline. Difference images: b) device only, c) device connected, d) device powered.

Examination of the difference images indicates that there was no notable distortion produced by the presence or operation of the device. The obvious distortion at the top of the phantom in Figure 3.15 is due to field distortions produced by the rectangular phantom itself, and not the device. It is clear from the difference images that the distortion was not affected by the presence of the device. These distortions are larger than would be typically observed in clinical images because of the low bandwidth used for these measurements.

Table 3.2: Summary of SNR measurements.

	Baseline	**Device Only**	**Device & Cables**	**Device Powered**
SNR	29.4	30.0	28.0	27.9
Change	-	**+ 1.8%**	**- 5.0%**	**- 5.3%**

Table 3.2 summarizes the SNR in each case. SNR was found to decrease by no more than 6% from its value in the baseline image (case 1) in all other cases. It is therefore concluded that the decrease in image SNR due to the device's presence is minimal.

3.3.1.2 Effects of MRI on the Device

Effects of the scanner on the device were minimized by using non-magnetic materials for all major components. Accordingly, the induced force and torque on the device were not

www.manaraa.com

detectable and were judged to be considerably less than the limits imposed in the ASTM standard. rf heating and encoder miscounts were not detected during device testing.

3.3.1.3 ASTM Classification

The ASTM has specified a standard for marking medical devices for safety in the MR environment.[51] Following the results of the MR compatibility tests, this system is classified as MR Conditional. While the system has been demonstrated to not experience rf heating, it has only been tested using a specific set of MRI sequences and parameters. As such, there is potential for this effect to become problematic if the device were used under a different MRI scanning protocol. Please contact the authors for more information regarding the specific scanner parameters and device configurations under which testing for rf heating was performed.

3.3.2 Targeting Accuracy

3.3.2.1 Open-Air Targeting Accuracy

Error in positioning of the furthest tooling ball was $E_{TB} = 0.29 \pm 0.11$ mm, with the angular error in trajectory being $A_{TB} = 0.11 \pm 0.04°$. A one-tailed *t*-test showed that the mean positioning error of the furthest tooling ball was statistically significantly less than 0.32 mm ($p = 0.005$, $n = 81$). The one-sided 95% prediction interval of E_{TB} was found to be 0.48 mm. It is therefore expected that, for any target with a known position relative to the device coordinate system, the device will be capable of placing a needle at that target within 0.48 mm, in 95% of attempts.

www.manaraa.com

3.3.2.2 Intra-MR Accuracy Tests

The quantitative results from the intra-MR alignment and phantom needle guidance experiments are summarized in Table 3.3.

Table 3.3: Summary of device accuracy tests in MR. Needle guidance error, NGE [Eq. (3.7)], needle guidance human error, NGHE [Eq. (3.10)], and needle trajectory error [Eq. (3.12)] quantify the system accuracy for both the intra-MR trajectory alignment, and tissue-mimicking phantom targeting tests. 95% CI is the confidence interval on the mean. 95% PI is the prediction interval for each error. All values are reported as mean ± STD. Values in bold are those mentioned in the discussion.

Experiment	Trajectory Alignment Accuracy in MR			Tissue-Mimicking Phantom Targeting Accuracy in MR		
	NGE (mm)	NGHE (mm)	NTE (mm)	NGE (mm)	NGHE (mm)	NTE (mm)
1	0.96 ± 0.22	0.51 ± 0.19	0.70 ± 0.07	1.25 ± 0.33	0.47 ± 0.08	1.19 ± 0.30
2	1.28 ± 0.48	0.56 ± 0.18	1.14 ± 0.13	1.96 ± 0.67	0.62 ± 0.26	1.77 ± 0.40
3	1.22 ± 0.30	0.40 ± 0.35	0.99 ± 0.05	1.04 ± 0.74	0.51 ± 0.29	0.99 ± 0.46
4	1.03 ± 0.28	0.51 ± 0.12	0.72 ± 0.11	1.52 ± 0.82	0.50 ± 0.19	1.49 ± 0.72
5	1.13 ± 0.44	0.56 ± 0.29	0.85 ± 0.07	1.42 ± 0.69	0.47 ± 0.31	1.13 ± 0.39
Mean	**1.11 ± 0.34***	**0.51 ± 0.22**	**0.86 ± 0.19**	**1.44 ± 0.69**†	0.51 ± 0.23	**1.31 ± 0.52**
95% CI	(0.97, 1.26)	(0.42, 0.60)	(0.78, 0.94)	(1.16, 1.73)	(0.42, 0.61)	(1.10, 1.53)
95% PI‡	**1.71**	0.89	1.19	**2.64**	0.91	2.22

* Statistically significantly less than 1.4 mm using one-sided *t*-test (p = 0.0003, 22 DOF).
† Statistically significantly less than 2.0 mm using one-sided *t*-test (p = 0.0002, 24 DOF).
‡ One-sided prediction interval

To aid in the interpretation of Table 3.3**,** refer to Figure 3.16, which graphically summarizes each component of needle guidance error that was measured.

www.manaraa.com

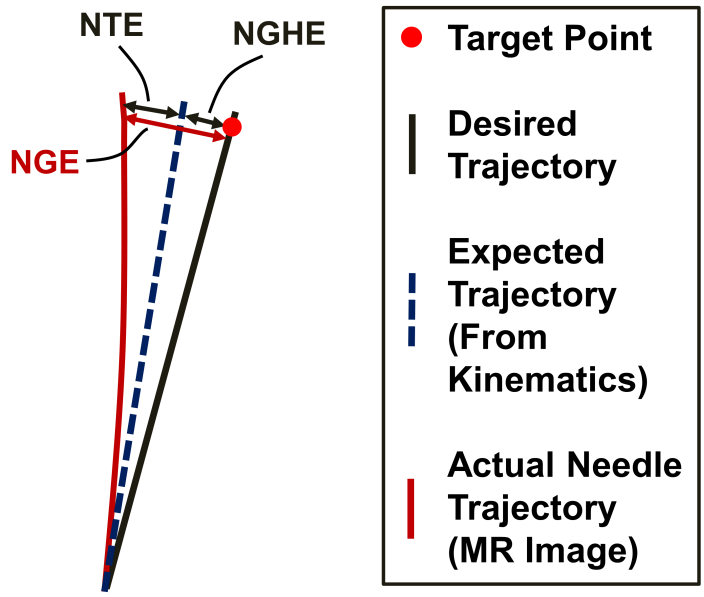

Figure 3.16: Illustration of each of the components of needle guidance error that were measured: needle trajectory error (NTE), which includes errors due to needle deflection and device localization; needle guidance human error (NGHE), which measures the user's ability to align the device with the desired needle trajectory; and needle guidance error (NGE), which includes contributions from NTE and NGHE.

The mean needle guidance error for the trajectory alignment test was found to be $NGE^{tr} = 1.11 \pm 0.34$ mm. The one-sided 95% prediction interval of NGE^{tr} was found to be 1.71 mm. It is therefore expected that, for a target identified in an MRI image, the device will be capable of pointing its needle guides at that target within 1.71 mm, in 95% of trials. This value can be viewed as the expected overall performance of the device in an MR scanner if there were no effects of tissue and needle deflection. The mean needle guidance human error over all trials was found to be $NGHE^{tr} = 0.51 \pm 0.22$ mm. This indicates that approximately half of the error associated with aiming a needle at a target in MR is due to misalignment of the device from its intended trajectory. NGHE can be reduced by proportionately reducing the precision to which the device must be aligned, as dictated by the alignment interface. The precision level used for these tests was 0.25 mm

www.manaraa.com

(for linear stage positions), since it was found that most users could more quickly and easily align the device at this level than at the 0.125 mm precision level.

The mean needle guidance error from the phantom targeting experiment was $NGE^{ph} = 1.44 \pm 0.69$ mm. The one-sided 95% prediction interval of NGE^{ph} was 2.64 mm. From this it is expected that, given a target in a tissue with mechanical properties similar to the phantom used in our experiment and localized in an MR image, the device will be capable of guiding a needle to within 2.64 mm of that target in 95% of attempts.

Analysis of NTE from both experiments provides insight regarding the sources of targeting error. In the trajectory alignment experiment, NTE^{tr} includes contributions from registration errors, MR bed positioning errors, and modeling inaccuracies in the kinematics equations. It does not include effects of needle deflection, whereas NTE^{ph} does. The discrepancy between NTE^{ph} and NTE^{tr} is therefore due to the effects of needle deflection alone. Since the error due to needle deflection, NDE, is independent of the other contributors to NTE^{ph}, it follows that NDE adds to NTE^{tr} in quadrature. It is thus possible to compute the rms NDE, which was found to be $NDE_{rms} = 1.10$ mm for the phantom experiment.

3.3.3 Clinical Evaluation

The system was used to successfully deliver laser fibers to two patients' prostates for focal laser ablation. It was found that needle deflection was greater than in the phantom targeting experiments, with the mean needle guidance error over both patients being $NGE^{pt} = 7.45 \pm 4.56$ mm. The overall rms needle deflection error was found to be $NDE_{rms} = 8.59$ mm. While the needle deflection was much greater than in the phantom experiment, the therapy was successfully delivered in both cases. Much of this success

www.manaraa.com

was owed to the fact that the needle could be clearly visualized in MR images, which were acquired intermittently during insertion. It was also found that needles inserted into adjacent template holes deflected similarly; a characteristic that was exploited to compensate for needle and tissue deflection effects. Table 3.4 summarizes the quantitative performance of the system for these two patients.

Table 3.4: *In vivo* needle targeting errors in two patients. Patient 1 had four needles inserted, while patient 2 had five. Needle deflection error in patient 2 was less than half that in patient 1, demonstrating how much tissue properties can vary between patients.

Patient	NGE (mm)	NGHE (mm)	NTE (mm)	NDE_{rms} (mm)	Time to Reach Target (min)
1	10.79 ± 3.26	0.37 ± 0.09	10.93 ± 3.31	11.27	12 ± 6
2	4.78 ± 3.67	0.39 ± 0.15	4.60 ± 3.71	5.60	6 ± 3
Mean	**7.45 ± 4.56**	**0.38 ± 0.12**	**7.41 ± 4.71**	**8.59**	**9 ± 5**

NDE_{rms} for the second patient was less than half that in the first. This result demonstrates how tissue properties can vary greatly between patients, which can result in vastly different degrees of needle deflection. The average time required to guide needles to their final location was 9 ± 5 min (n = 9), compared to 35 ± 17 min (n = 3) in a case where needles were inserted using a fixed grid template or 21 ± 17 min (n = 3) when they were inserted freehand. Imaging of the device's registration fiducials did not interrupt the procedure workflow, as this was performed before the patient arrived in each case. The device was then removed from the scanner bed, and precisely repositioned on a set of custom-made rails once the patient had been anesthetized.

3.4 Discussion

Results from the MRI compatibility tests showed that the needle guidance system does not cause an appreciable level of image distortion or decrease in SNR in MRI images. In addition, the MRI was found to not impair the device's operation through the introduction

www.manaraa.com

of force, torque, rf heating, or interference with its electrical systems. The system was therefore deemed to be safe to operate within the bore of an MRI scanner with a patient.

Results from the intra-MR trajectory alignment test indicated how well the system can perform its chief function: to align its needle guides with an MRI-identified target. A prediction interval on NGE^{tr} indicated that, in 95% of trials, the device is expected to be capable of aiming its needle guides to within 1.71 mm of a selected target. This is well within the goal of 2.5 mm, indicating that this system has the potential to target the smallest tumours considered clinically significant.[32] The results from MRI-guided needle insertion tests provided quantification of the error associated with using the system to deliver needles to targets in a tissue-mimicking phantom. A prediction interval computed on NGE^{ph} indicated that the system is expected to be capable of delivering a needle to its target within the bore of an MRI scanner to within 2.64 mm, in 95% of trials. This result further suggests that the system has the potential to target prostate tumours of the smallest clinically significant size. A comparison between NTE^{ph} and NTE^{tr} allowed quantification of the effects of needle deflection in the form of root mean squared needle deflection error, NDE_{rms} = 1.10 mm. Despite the fact that the prostate phantom used has a comparable stiffness to that of human tissue, it was not expected that the same performance measured in the phantom experiment could be achieved *in vivo*. The tissue between the perineum and prostate (which makes up the majority of the insertion length) exhibits inhomogeneous, non-isotropic material properties.[52] As such, the results of the phantom needle insertion tests represent the best performance that the system could achieve in placing a needle in a patient with tissue of homogeneous, isotropic material properties, and stiffness on the same order of that of human tissue. Differences in needle

www.manaraa.com

guidance error between the patient trials and the phantom needle guidance test are mainly due to needle deflection. This is the case, as the intra-MR trajectory alignment test has confirmed that the system can accurately and reliably align its needle guides with a target in the bore of a clinical MRI scanner.

The amount of needle deflection, as indicated by NDE_{rms}, was almost an order of magnitude larger in human tissue than in the phantom experiment, yet the system was still used successfully to deliver focal laser ablation to two patients. This was made possible by the system's ability to monitor the trajectories of partially inserted needles in MR images. In this way, the needle deflection at its final depth could be predicted from the initial level of deflection, and the needle could be reinserted from a different angle if indicated. Using the device in 'target only mode' allowed the physician to quickly and easily modify the needle's trajectory during this process. In addition, it was found that needles inserted in adjacent template holes deflected similarly. This allowed the final location of a subsequent needle to be predicted with some certainty. Figure 3.17 shows two needles inserted in a patient through adjacent template holes, demonstrating how both needles deflecting in the same direction. Finally, the time required to deliver needles to targets with sufficient accuracy was observed to be much less when using our system (9 ± 5 min) than with either a fixed grid template (35 ± 17 min) or freehand insertion (21 ± 17 min). While there were not enough trials performed for the timing data to be considered statistically significant, it is expected that this trend would continue based on the fact that the system: a) consistently provides initial needle trajectories that aim within 1.71 mm of the intended target, b) allows simultaneous insertion of multiple needles in the same template, allowing for some prediction of subsequent needle deflection based on

www.manaraa.com

the previous insertion, and c) provides a mechanism for quickly modifying needle angulation when the needle trajectory is deemed unsatisfactory. It was found that both NDE_{rms} and the time required to successfully place needles at their targets were approximately halved for the second patient compared to the first. It is believed that these differences were mostly due to differences in tissue properties between the two patients, but increased experience in using the system in the second case may have also been a factor.

Clinical evaluation of the system is ongoing, and an optimal method of correcting for needle deflection is being sought, as a solution to this problem could considerably reduce procedure time by reducing the number of insertion attempts and needle image acquisitions required.

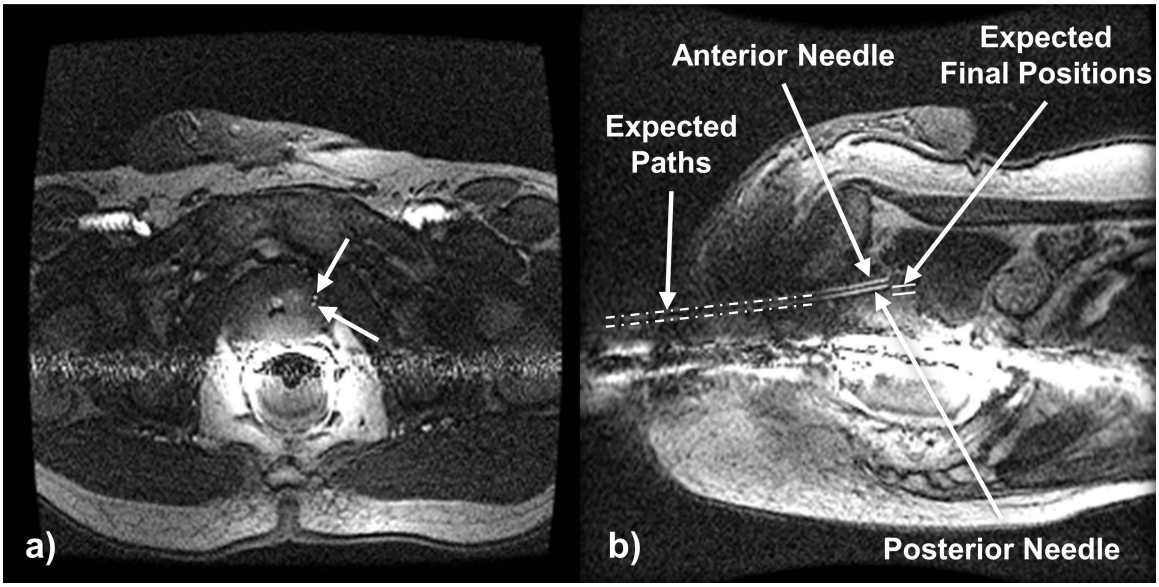

Figure 3.17: MR images of needles in a patient's prostate. a) Axial image showing needles, b) sagittal image of needles showing how inserting a needle into a posterior template hole allowed the physician to reach the original, more anterior target.

www.manaraa.com

3.5 Conclusions

MR compatibility tests showed that the presence of the trajectory alignment device has a negligible effect on MR image distortion and SNR. Effects of the MRI on the operation of the system were also deemed negligible. The system was then shown to be capable of aiming its needle guides to within 1.71 mm of a target within the bore of a clinical MRI scanner, as indicated by a 95% prediction interval. Needle targeting tests in a tissue-mimicking phantom showed the device to be capable of delivering needles to targets in the phantom within 2.64 mm, indicated by a 95% prediction interval. Although needle deflection was much greater than in the phantom experiments, use of the system in two patients for focal laser ablation procedures was successful, owing to effective methods of measuring and compensating for needle deflection. It was also observed that needles could be delivered using this system in less time than using a fixed grid template or a freehand technique. These promising results led to the use of this system for delivering needles for FLA therapy in eight cases, which will be described in Chapter 4.

www.manaraa.com

References

1. A. Jemal, F. Bray, M. M. Center, J. Ferlay, E. Ward and D. Forman, "Global cancer statistics," CA. Cancer J. Clin. **61**, 69-90 (2011).

2. F. Labrie, B. Candas, A. Dupont, L. Cusan, J. L. Gomez, R. E. Suburu, P. Diamond, J. Levesque and A. Belanger, "Screening decreases prostate cancer death: first analysis of the 1988 Quebec prospective randomized controlled trial," Prostate **38**, 83-91 (1999).

3. R. Etzioni, R. Gulati, S. Falcon and D. F. Penson, "Impact of PSA screening on the incidence of advanced stage prostate cancer in the United States: a surveillance modeling approach," Med. Decis. Making **28**, 323-331 (2008).

4. A. Bill-Axelson, L. Holmberg, F. Filén, M. Ruutu, H. Garmo, C. Busch, S. Nordling, M. Häggman, S. O. Andersson and S. Bratell, "Radical prostatectomy versus watchful waiting in localized prostate cancer: the Scandinavian prostate cancer group-4 randomized trial," J. Natl. Cancer Inst. **100**, 1144-1154 (2008).

5. F. H. Schröder, J. Hugosson, M. J. Roobol, T. L. J. Tammela, S. Ciatto, V. Nelen, M. Kwiatkowski, M. Lujan, H. Lilja and M. Zappa, "Screening and prostate-cancer mortality in a randomized European study," N. Engl. J. Med. **360**, 1320-1328 (2009).

6. A. W. Levinson, H. J. Lavery, N. T. Ward, L. M. Su and C. P. Pavlovich, "Is a return to baseline sexual function possible? An analysis of sexual function outcomes following laparoscopic radical prostatectomy," World J. Urol. **29**, 29-34 (2011).

7. W. R. Parker, R. Wang, C. He and D. P. Wood Jr, "Five year expanded prostate cancer index composite-based quality of life outcomes after prostatectomy for localized prostate cancer," Br. J. Urol. **107**, 585-590 (2011).

8. L. Klotz, L. Zhang, A. Lam, R. Nam, A. Mamedov and A. Loblaw, "Clinical results of long-term follow-up of a large, active surveillance cohort with localized prostate cancer," J. Clin. Oncol. **28**, 126-131 (2010).

9. F. Fang, N. L. Keating, L. A. Mucci, H. O. Adami, M. J. Stampfer, U. Valdimarsdóttir and K. Fall, "Immediate risk of suicide and cardiovascular death after a prostate cancer diagnosis: cohort study in the United States," J. Natl. Cancer Inst. **102**, 307-314 (2010).

10. K. L. Greene, P. C. Albertsen, R. J. Babaian, H. B. Carter, P. H. Gann, M. Han, D. A. Kuban, A. O. Sartor, J. L. Stanford, A. Zietman and P. Carroll, "Prostate specific antigen best practice statement: 2009 update," J. Urol. **182**, 2232-2241 (2009).

www.manaraa.com

11. A. Bill-Axelson, L. Holmberg, M. Ruutu, M. Häggman, S. O. Andersson, S. Bratell, A. Spångberg, C. Busch, S. Nordling and H. Garmo, "Radical prostatectomy versus watchful waiting in early prostate cancer," N. Engl. J. Med. **352**, 1977-1984 (2005).

12. I. Thompson, J. B. Thrasher, G. Aus, A. L. Burnett, E. D. Canby-Hagino, M. S. Cookson, A. V. D'Amico, R. R. Dmochowski, D. T. Eton, J. D. Forman, S. L. Goldenberg, J. Hernandez, C. S. Higano, S. R. Kraus, J. W. Moul and C. M. Tangen, "Guideline for the management of clinically localized prostate cancer: 2007 update," J. Urol. **177**, 2106-2131 (2007).

13. H. U. Ahmed, R. G. Hindley, L. Dickinson, A. Freeman, A. P. Kirkham, M. Sahu, R. Scott, C. Allen, J. Van der Meulen and M. Emberton, "Focal therapy for localised unifocal and multifocal prostate cancer: a prospective development study," Lancet Oncol. (2012).

14. H. U. Ahmed, "The index lesion and the origin of prostate cancer," N. Engl. J. Med. **361**, 1704-1706 (2009).

15. U. Lindner, J. Trachtenberg and N. Lawrentschuk, "Focal therapy in prostate cancer: modalities, findings and future considerations," Nat. Rev. Urol. **7**, 562-571 (2010).

16. T. V. Johnson, S. J. Garlow, O. W. Brawley and V. A. Master, "Peak window of suicides occurs within the first month of diagnosis: implications for clinical oncology," Psycho-Oncology (2011).

17. J. Bax, D. Cool, L. Gardi, K. Knight, D. Smith, J. Montreuil, S. Sherebrin, C. Romagnoli and A. Fenster, "Mechanically assisted 3D ultrasound guided prostate biopsy system," Med. Phys. **35**, 5397-5410 (2008).

18. M. R. Engelbrecht, H. J. Huisman, R. J. F. Laheij, G. J. Jager, G. J. L. H. van Leenders, C. A. Hulsbergen-Van De Kaa, J. J. de la Rosette, J. G. Blickman and J. O. Barentsz, "Discrimination of prostate cancer from normal peripheral zone and central gland tissue by using dynamic contrast-enhanced MR imaging," Radiology **229**, 248-254 (2003).

19. M. A. Haider, T. H. van der Kwast, J. Tanguay, A. J. Evans, A. T. Hashmi, G. Lockwood and J. Trachtenberg, "Combined T2-weighted and diffusion-weighted MRI for localization of prostate cancer," Am. J. Roentgenol. **189**, 323-328 (2007).

20. G. Bauman, T. Belhocine, M. Kovacs, A. Ward, M. Beheshti and I. Rachinsky, "18F-fluorocholine for prostate cancer imaging: a systematic review of the literature," Prostate Cancer P. D. (2011).

21. A. Ward, C. Crukley, C. McKenzie, J. Montreuil, E. Gibson, J. Gomez, M. Moussa, G. Bauman and A. Fenster, "Registration of in vivo prostate magnetic resonance

www.manaraa.com

images to digital histopathology images," Prostate Cancer Imaging. Computer-Aided Diagnosis, Prognosis, and Intervention, 66-76 (2010).

22. U. Lindner, N. Lawrentschuk, R. A. Weersink, S. R. H. Davidson, O. Raz, E. Hlasny, D. L. Langer, M. R. Gertner, T. Van der Kwast and M. A. Haider, "Focal laser ablation for prostate cancer followed by radical prostatectomy: validation of focal therapy and imaging accuracy," Eur. Urol. **57**, 1111-1114 (2010).

23. O. Raz, M. A. Haider, S. R. H. Davidson, U. Lindner, E. Hlasny, R. Weersink, M. R. Gertner, W. Kucharcyzk, S. A. McCluskey and J. Trachtenberg, "Real-time magnetic resonance imaging-guided focal laser therapy in patients with low-risk prostate cancer," Eur. Urol. **58**, 173-177 (2010).

24. G. S. Fischer, I. Iordachita, C. Csoma, J. Tokuda, S. P. DiMaio, C. M. Tempany, N. Hata and G. Fichtinger, "MRI-compatible pneumatic robot for transperineal prostate needle placement," IEEE Trans. Mech. **13**, 295-305 (2008).

25. A. A. Goldenberg, J. Trachtenberg, Y. Yi, R. Weersink, M. S. Sussman, M. Haider, L. Ma and W. Kucharczyk, "Robot-assisted MRI-guided prostatic interventions," Robotica **28**, 215 (2010).

26. A. Krieger, C. Csoma, Iordachital, II, P. Guion, A. K. Singh, G. Fichtinger and L. L. Whitcomb, "Design and preliminary accuracy studies of an MRI-guided transrectal prostate intervention system," in *Med. Image Comput. Comput. Assist. Interv.*, *Vol. 10,* edited by N. Ayache, S. Ourselin and A. J. Maeder (2007), pp. 59-67.

27. A. Krieger, I. Iordachita, S. E. Song, N. B. Cho, P. Guion, G. Fichtinger and L. L. Whitcomb, Proc. IEEE International Conference on Robotics and Automation, Anchorage, Alaska, 2010.

28. M. G. Schouten, J. Ansems, W. K. Renema, D. Bosboom, T. W. Scheenen and J. J. Futterer, "The accuracy and safety aspects of a novel robotic needle guide manipulator to perform transrectal prostate biopsies," Med. Phys. **37**, 4744-4750 (2010).

29. D. Stoianovici, D. Song, D. Petrisor, D. Ursu, D. Mazilu, M. Muntener, M. Schar and A. Patriciu, ""MRI Stealth" robot for prostate interventions," Minim. Invasive Ther. Allied Tech. **16**, 241-248 (2007).

30. S. Zangos, C. Herzog, K. Eichler, R. Hammerstingl, A. Lukoschek, S. Guthmann, B. Gutmann, U. J. Schoepf, P. Costello and T. J. Vogl, "MR-compatible assistance system for punction in a high-field system: device and feasibility of transgluteal biopsies of the prostate gland," Eur. Radiol. **17**, 1118-1124 (2007).

31. G. Fischer, A. Krieger, I. Iordachita, C. Csoma, L. Whitcomb and G. Fichtinger, "MRI compatibility of robot actuation techniques – a comparative study," in *Med.*

www.manaraa.com

Image Comput. Comput. Assist. Interv., edited by D. N. Metaxas, L. Axel, G. Fichtinger and G. Szekely (2008), pp. 509-517.

32. J. I. Epstein, H. Sanderson, H. B. Carter and D. O. Scharfstein, "Utility of saturation biopsy to predict insignificant cancer at radical prostatectomy," Urology **66**, 356-360 (2005).

33. J. Cepek, B. Chronik, U. Lindner, J. Trachtenberg and A. Fenster, "Development of an MRI-compatible device for prostate focal therapy," in *Med. Image Comput. Comput. Assist. Interv.*, *Vol. 7510,* edited by N. Ayache, H. Delingette, P. Golland and K. Mori (2012), pp. 455-462.

34. J. Bax and A. Fenster, United States Patent No. US 2010/0319164 A1 (2008).

35. E. M. Haacke, R. Brown, M. Thompson and R. Venkatesan, *Magnetic resonance imaging: physical principles and sequence design*. (Wiley-Liss, 1999).

36. K. Bannan, W. B. Handler, C. Wyenberg, B. A. Chronik and S. P. Salisbury, "Prediction of force and image artifacts under MRI for metals used in medical devices," (2012).

37. Y. Ishihara, A. Calderon, H. Watanabe, K. Okamoto, Y. Suzuki and K. Kuroda, "A precise and fast temperature mapping using water proton chemical shift," Magn. Reson. Med. **34**, 814-823 (1995).

38. A. J. Welch, *Optical-thermal response of laser-irradiated tissue*. (Springer Verlag, 2011).

39. D. Stoianovici, "Multi-imager compatible actuation principles in surgical robotics," Int. J. Med. Robotics Comput. Assist. Surg. **1**, 86-100 (2005).

40. N. Yu, R. Gassert and R. Riener, "Mutual interferences and design principles for mechatronic devices in magnetic resonance imaging," Int. J. Comput. Assist. Radiol. Surg. **6**, 473-488 (2011).

41. American Society for Testing and Materials, "Standard Test Method for Evaluation of MR Image Artifacts from Passive Implants", 2007

42. National Electrical Manufacturers Association, "Determination of Signal-to-Noise Ratio (SNR) in Diagnostic Magnetic Resonance Imaging", 2008

43. American Society for Testing and Materials, "Standard Test Method for Measurement of Magnetically Induced Displacement Force on Medical Devices in the Magnetic Resonance Environment", 2006

www.manaraa.com

44. American Society for Testing and Materials, "Standard Test Method for Measurement of Magnetically Induced Torque on Medical Devices in the Magnetic Resonance Environment", 2006

45. American Society of Mechanical Engineers, "Methods for Performance Evaluation of Coordinate Measuring Machines", 1997

46. D. Cool, S. Sherebrin, J. Izawa, J. Chin and A. Fenster, "Design and evaluation of a 3D transrectal ultrasound prostate biopsy system," Med. Phys. **35**, 4695 (2008).

47. U. Lindner, N. Lawrentschuk, R. A. Weersink, O. Raz, E. Hlasny, M. S. Sussman, S. R. Davidson, M. R. Gertner and J. Trachtenberg, "Construction and evaluation of an anatomically correct multi-image modality compatible phantom for prostate cancer focal ablation," J. Urol. **184**, 352-357 (2010).

48. T. J. Hall, M. Bilgen, M. F. Insana and T. A. Krouskop, "Phantom materials for elastography," IEEE Trans. Ultrason. Ferr. **44**, 1355-1365 (1997).

49. N. Hungr, J. A. Long, V. Beix and J. Troccaz, "A realistic deformable prostate phantom for multimodal imaging and needle-insertion procedures," Med. Phys. **39**, 2031 (2012).

50. D. Rickey, P. Picot, D. Christopher and A. Fenster, "A wall-less vessel phantom for Doppler ultrasound studies," Ultrasound Med. Biol. **21**, 1163-1176 (1995).

51. American Society for Testing and Materials, "Standard Practice for Marking Medical Devices and Other Items for Safety in the Magnetic Resonance Environment", 2008

52. T. Podder, D. Clark, J. Sherman, D. Fuller, E. Messing, D. Rubens, J. Strang, R. Brasacchio, L. Liao and W. S. Ng, "In vivo motion and force measurement of surgical needle intervention during prostate brachytherapy," Med. Phys. **33**, 2915 (2006).

www.manaraa.com

Chapter 4.

A Mechatronic System for In-Bore MR-Guided Insertion of Needles to the Prostate: Experiences Using the System for Prostate Focal Laser Ablation in Eight Patients†

4.1 Introduction

Prostate cancer remains the most common solid organ malignancy diagnosed in North American men.[1] In order to reduce the treatment related morbidity associated with radical therapies and attempt to provide immediate oncologic control, focal therapy has emerged as a novel minimally-invasive approach for prostate cancer treatment. Focal therapies aim to ablate the index lesion while leaving the majority of the gland, including the delicate neurovascular bundles and the urethral sphincters intact.[2] Prudent selection of appropriate candidates for focal therapy and treatment planning necessitates the use of novel imaging and biopsy protocols in order to locate and characterize the prostate cancer foci.[3]

Multi-parametric magnetic resonance imaging (mpMRI) has the highest sensitivity of all prostate imaging modalities for detection and localization of prostate

†. A version of this chapter is in preparation for submission for publication: Cepek, J., Lindner, U., Louis, AS., Ghai, S., Davidson, SRH., Gertner, M., Hlasny, E., Sussman, MS., Trachtenberg, J., Fenster, A., "A Mechatronic System for In-Bore MR-Guided Insertion of Needles to the Prostate: Experiences Using the System for Prostate Focal Laser Ablation in Eight Patients." J. Magn. Reson. Im. (2013, In Preparation).

www.manaraa.com

tumours, and has superior anatomic resolution of the prostate and surrounding structures compared to other imaging modalities.[4, 5] These features make mpMRI an ideal modality for guiding both targeted prostate biopsy and focal therapy to prostate tumours. Also, many emerging focal therapy modalities use thermal energy for tissue ablation, and magnetic resonance (MR) imaging offers temperature mapping for real-time feedback during the procedure to confirm therapeutic temperatures are reached at the target, while ensuring damage to the surrounding tissues is limited.[6] Dynamic contrast-enhanced MR imaging may also be used immediately after treatment to confirm complete ablation of the target.[7]

A number of different strategies have been evaluated to deliver percutaneous needles to prostate tumours under MR-guidance.[8-12] Our group has previously evaluated a brachytherapy-like template approach in the context of our ongoing trial of MR-guided focal laser ablation (FLA). An optimal needle delivery method should feature high targeting accuracy, needle angulation to accommodate large prostates, and demonstrated safety and compatibility with the MR scanner. In addition, the ability to fit within the limited confines of the MR bore and guide needles without removing the patient from the scanner bore is an ideal feature for maintaining an efficient intra-procedural workflow and limiting patient motion, which could lead to inaccuracies in targeting and thermal mapping. In an attempt to satisfy these criteria, we recently developed a mechatronic system for in-bore MR-guided insertion of needles to the prostate, as described in Chapter 3 and in ref. [13]. This system could potentially be applied to transperineal prostate biopsy and focal therapies requiring interstitial delivery of laser fibers, electrodes or cryoprobes. Chapter 3 reported brief preliminary results from

www.manaraa.com

the first two cases of MR-guided prostate FLA using this system. Following these two pilot cases, device and patient positioning was optimized. We now report comprehensive results from clinical evaluation of our system in eight cases of FLA for localized prostate cancer.

4.2 Materials and Methods

4.2.1 System Design

Full details of our design process for the system are described in Chapter 3. Briefly, we constructed a needle guidance device using MR-compatible materials, comprehensively validated its safety and compatibility within the MR environment, and rigorously quantified its needle guidance accuracy in tissue-mimicking phantoms. The device has four degrees-of-freedom for aligning needle trajectories, including vertical and horizontal translation and angulation. The delivery arm is controlled by three handles that are manually manipulated by the operator from outside of the MR scanner bore. Visual feedback for needle guide alignment is provided based on proximity of the arm to the target position in the form of coloured lights displayed on an MR-compatible LED panel. The device's principal function is to precisely align its needle guide with an MR-identified target while remaining in the MR bore. Following this, needles are inserted manually under MR imaging guidance.

The system provides the interventionalist with several advantages over other methods of transperineal prostate needle guidance. In contrast to a grid template approach, this system allows target points in the prostate to be specified at any position in 3D space. This feature allows pre-treatment plans to be generated with complete freedom in the geometric arrangement of the planned needle locations. In addition, angulated

www.manaraa.com

needle trajectories can be used to avoid critical structures, and, in the case of focal therapy, to ensure accurate conformation of the ablation volume to the target region.

4.2.2 Integration with Clinical Workflow

Prior to the beginning of each procedure, the device is mounted on the MR scanner table for localization within the MR image space using an MR-visible fluid-filled tracking frame. The device is then removed from the fixed mounting apparatus on the MR table to facilitate patient positioning, placement of the endorectal (ER) receive coil and administration of anesthesia. The device is then replaced on the mounting apparatus at the precise position where it was imaged and its base is locked in position. All subsequent movements of the device's movable components are then tracked in real-time with MR-compatible linear position encoders. Sterile draping is then applied to the procedural field, including draping of the device with a sterile plastic sheet. All components of the device in direct contact with the patient or interventionalist, including needle guides, guidance arm, and alignment handle, are sterilized using ethylene oxide and installed on the device immediately before use. Figure 4.1 shows the device during setup and its positioning for an MR-guided FLA procedure.

www.manaraa.com

Figure 4.1: Needle guidance device setup and components. a) Device in place on MR table prior to patient positioning. LED grid panel indicates position of the needle guide relative to target position. b) Sterilizable components including (from top to bottom): guidance arm, mounting pin, alignment handle and needle guides. c) Device in operating position before moving the patient into the MR bore. d) Placement of laser fibers with the patient remaining inside the bore.

4.2.3 Intra-Procedure Performance Assessment

The mechatronic system was used to guide needles for prostate FLA as part of an ongoing Phase I/II clinical trial (ClinicalTrials.gov ID: NCT01094665). For this procedure, a custom cannula system (hereafter referred to as a needle) was used to deliver laser fibers for ablation. For each target, a desired needle trajectory was selected using custom 3D visualization software that displays the target and prostate contours on MR images of the prostate. The desired trajectory was then transmitted to the MR-compatible LED grid display in the MR scanner room. Using this display, the interventionalist

www.manaraa.com

precisely aligned the needle guides of the device to the intended trajectory, and then manually advanced needles transperineally without removing the patient from the MR scanner bore. Needles were incrementally inserted and imaged to monitor their insertion path until they reached their final desired depth.

After complete insertion of each needle, the trocar was removed and replaced by a 16-gauge closed-ended catheter (Flexineedle, Best Medical International, Springfield, VA) filled with a 1% solution of Gd-DTPA for high contrast visualization of catheter placement.[14] A series of axial fast spoiled gradient echo (FSPGR) and balanced steady state free precession (bSSFP or FIESTA on GE scanners) MR images were then acquired of each catheter in its final position. The bSSFP images provide high soft tissue contrast, and can be used to confirm accurate placement of catheters relative to anatomical landmarks. The axis of each catheter was then identified in the FSPGR images, and compared to the intended target point for calculation of needle guidance error, defined as the perpendicular distance between the needle axis and the selected target point. Error in positioning of the needle along the insertion direction was not included in this definition because each needle was intentionally inserted beyond its target point, and a "pull-back" technique was used to create an elongated volume of ablated tissue.

The time required to successfully guide each needle to its target was also recorded. Timing began immediately before insertion and ended once images of the needle had been acquired and the needle was confirmed to be in an acceptable location at the proper depth. Needle guidance time using this system in eight cases (29 insertions) was compared to that for nine cases (18 insertions) earlier in this trial in which needles were guided using the "MRI-compatible brachytherapy-like template", as described by

www.manaraa.com

Raz *et al.*[15] Unfortunately, needle guidance error could not be compared between these two approaches, since the template method did not target specified points – needles were inserted into the most favorable template hole available. All procedures were performed in a 1.5 T closed bore GE MR scanner (Signa HDxt 1.5T, GE Healthcare, Milwaukee, WI).

4.2.4 Data analysis

The Mann-Whitney U test was used to compare needle guidance times between the template- and mechatronic device-guided approaches, and the Wilcoxon signed rank test was used to test if the median of components of needle guidance error differed significantly from zero. Statistics were computed using GraphPad Prism version 6.02.

4.3 Results

Needle guidance error was successfully recorded for a total of 29 needle insertions. Figure 4.2 shows images of two catheters in their final position in the prostate on FSPGR and bSSFP images. Optimal visualization of both the needles and prostate anatomy was achieved with bSSFP sequences.

www.manaraa.com

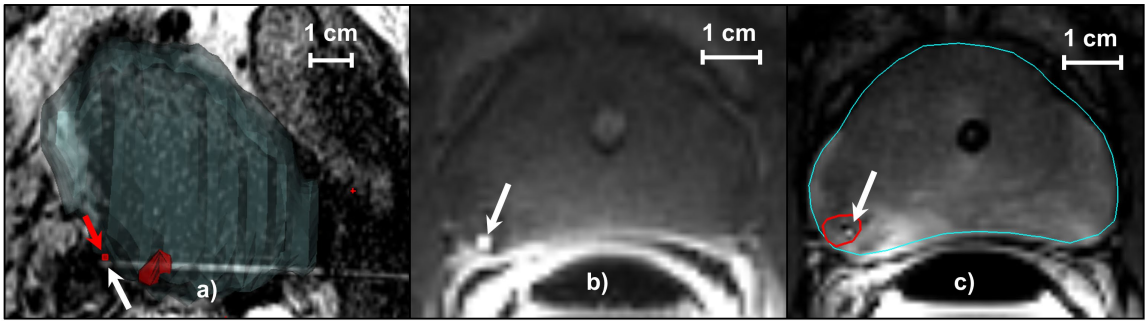

Figure 4.2: Images showing final catheter placement in two different prostates. a) Patient 7, sagittal FSPGR image showing 3D prostate (blue) and target region (red) surfaces, target point (red arrow) and needle at its final position (white arrow) in the left posterior peripheral zone. b) Patient 3, axial FSPGR image showing excellent visualization of the catheter, but poor contrast between prostatic and surrounding tissue. c) Patient 3, bSSFP image showing excellent visualization of the same catheter in *(b)*, clear contrast between prostatic and surrounding tissue, and internal prostate anatomical detail.

Table 4.1 shows the needle guidance error and needle guidance time for each patient. The median number of needles inserted per patient was 4 (range 1 – 4). 90% of the needles were placed within 6 mm of their target in less than 13 minutes each.

Table 4.1: Needle guidance error and needle guidance time for each of six patients. Data are shown as median (interquartile range).

Patient	Prostate Volume (cm^3)	# of Targets	Target Location(s)*	Target Volume(s) (cm^3)	# of Needles Inserted	Needle Guidance Error (mm)	Needle Guidance Time (min)
1	73	1	RPB	4.67	4	3.4 (2.9 – 4.8)	7.5 (5.3 – 9.0)
2	49	1	LPA	1.53	4	3.4 (2.5 – 5.2)	8.5 (7.3 – 9.8)
3	36	1	RPB	0.17	1	1.9	9.0
4	44	1	RPB	0.81	4	2.8 (1.4 – 5.8)	6.5 (3.8 – 10.8)
5	76	1	RPM	0.13	4	2.2 (1.1 – 4.8)	8.0 (5.8 – 9.5)
6	36	1	RPA	3.96	4	2.4 (1.9 – 4.2)	12.0 (11.3 – 12.8)
7	268	2	LPB, MPM	0.64, 0.72	4	5.5 (1.2 – 9.3)	9.0 (5.0 – 11.5)
8	28	1	RAA	0.48	4	5.1 (3.8 – 5.6)	7.5 (6.3 – 11.0)
Median	**47**	**1**	**RPM**	**0.72**	**4**	**3.4 (2.1 – 5.2)**	**8.0 (6.5 – 10.5)**

* Listed in order of lateral (R = right, L = left, M = midgland), anterior-posterior (A = anterior, P = posterior, M = midgland), and superior-inferior (B = base, A = apex, M = midgland) position of the target(s) in the prostate.

Needle guidance error was also decomposed into orthogonal components in the anterior-posterior (AP) and medial-lateral (ML) directions. The components are shown in

www.manaraa.com

Figure 4.3. The median needle guidance errors were 1.8 mm and 0.6 mm in the posterior and lateral directions, respectively. The median of both error components were found to be statistically significantly different from zero ($p < 0.0001$), suggesting that needles tend to deflect posteriorly and laterally in the prostate. Figure 4.3 also shows the empirical cumulative distribution function (CDF) of the measured values of needle guidance error. The figure indicates the fraction of needles inserted that reached their target within a given level of error.

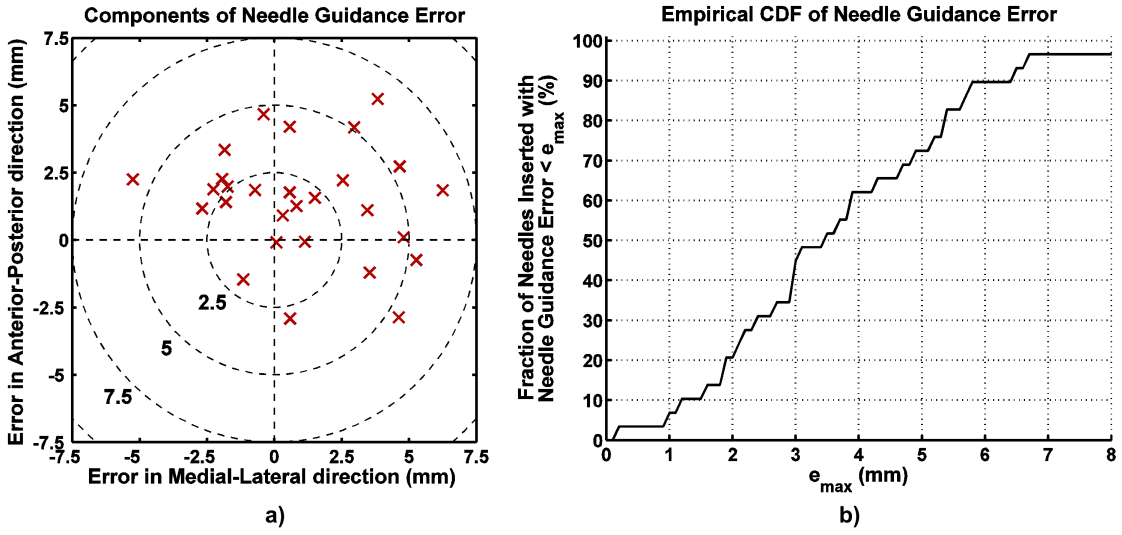

Figure 4.3: Needle guidance error for each of the 29 insertions. a) Components of needle guidance error in the anterior-posterior and medial-lateral directions. Positive values correspond to the posterior and lateral directions. The point (0,0) corresponds to the target point for each insertion. Needles tended to deflect in the lateral and posterior directions. b) Fraction of needles within a given level of error e_{max} using the system described in this chapter.

Needle guidance times for the two sets of patients treated with either template or the mechatronic system are shown in Figure 4.4. A statistically significantly shorter median guidance time was found with the device compared to the template approach: 8 vs. 18 min ($p < 0.0001$, 95% CI of difference: 5 – 13 min). The variance in needle guidance time is also noted to be less when using our system.

www.manaraa.com

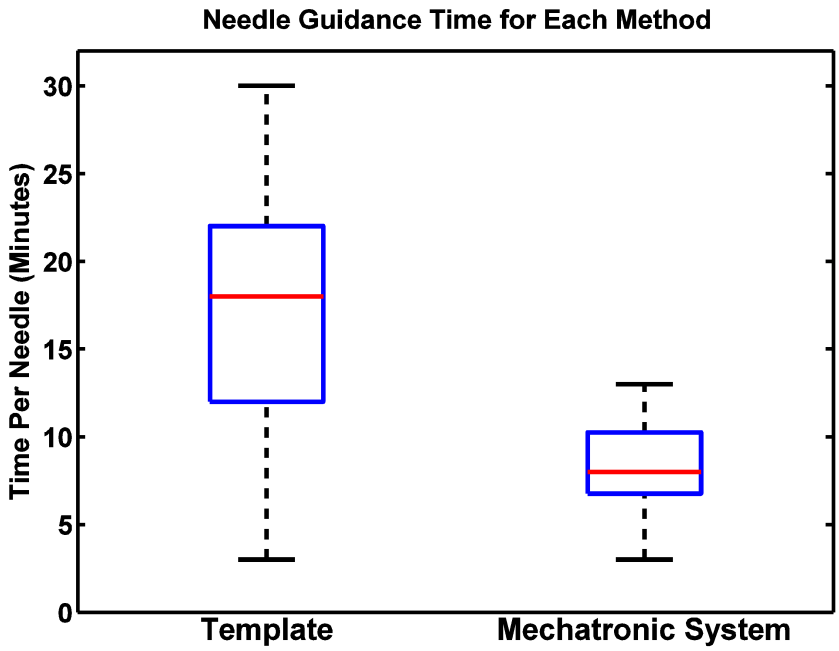

Figure 4.4: Box plot showing the time required to guide each needle to its target using either a brachytherapy-like grid template, or the mechatronic system described in this work. Red line: median, blue box: interquartile range (IQR), black bars: extremum. The median time was statistically significantly different between the two methods ($p < 0.0001$).

4.4 Discussion

In an attempt to take full advantage of the capabilities that MR imaging offers for the delivery of prostate FLA, we developed a fully MR-compatible mechatronic system for the precise in-bore guidance of needles to the prostate.[11, 16-19] Our device has the advantage of being operated by an interventionalist while remaining in the scanner, reducing error introduced by moving the patient in and out of the bore, and decreasing needle guidance time. In using the system to guide 29 needles for prostate FLA in eight patients, the median needle guidance error achieved was 3.4 mm, with a targeting time significantly less than the grid template approach previously used. This difference may be attributed to the fact that our device does not necessitate patient removal from the scanner for advancement of needles, as well as the overall mechanical stability of the system. In

www.manaraa.com

addition, our system has the ability to target any location within the prostate, rather than a fixed set of non-ideal targets based on the location of the template holes. For this reason, the needle guidance error could not be compared to that using the grid template approach.

The potential clinical importance of the accuracy achieved with this system must be highlighted. In the context of targeted biopsy, the goal is to sample tissue from within an MR-identified target region, and a high probability of successfully doing so is desired. A spherical tumour of the smallest size generally considered clinically relevant is 0.5 cm^3 (5 mm radius).[20, 21] Our results suggest that, using this system, the probability of successfully sampling such a target is 72%, since approximately 72% of the data in Figure 4.3 falls within 5 mm of the target. If multiple attempts are made to biopsy the same target, the total probability of success increases to 92%, and 98% if 2 or 3 samples are taken, respectively (assuming the errors are independent). These probabilities would increase as the size of the target increases. In the context of needle-based focal therapy such as FLA, treatment success is defined as completely ablating the focal target region while avoiding damage to surrounding critical structures.[22] If a single laser fiber is used, the target will be successfully ablated if the needle placement error is less than the width of the planned treatment volume margin surrounding the tumour. An increase in tumour size would result in a smaller margin, and therefore a decreased probability of success. Lesions exceeding a threshold size necessitate insertion of multiple fibers per tumour, for which prediction of the probability of successful ablation requires a more complex analysis.[15, 17, 23]

Another notable benefit encountered in using this system was its ability to target tumours in patients who may have been excluded from other whole-gland treatment

www.manaraa.com

modalities. Patient 7 had a prostate with a volume of 268 cm^3, yet we were able to target a tumour in the far lateral posterior peripheral zone using an angulated needle trajectory to avoid pubic arch interference. Patient 8 had an anterior tumour near the prostate apex for which needle access was occluded by the urethra. This patient's tumour was also reached using an angulated needle trajectory. These cases are illustrated in Figure 4.5.

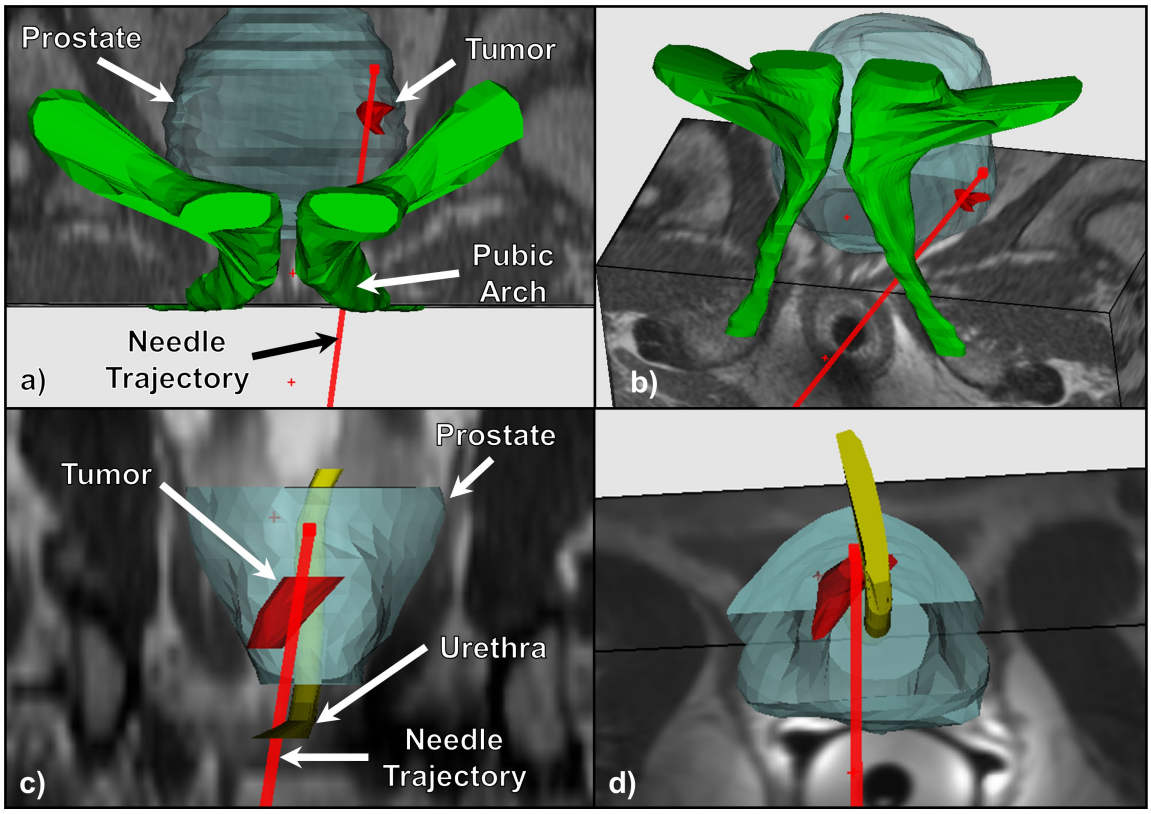

Figure 4.5: Two cases for which the needle guidance system proved extremely valuable. a), b) Patient 7, with a prostate volume of 268 cm^3. The use of an angulated needle trajectory allowed the tumour in the far lateral posterior peripheral zone to be reached while avoiding pubic arch interference. c), d) Patient 8, with an anterior tumour that would have been inaccessible using a parallel needle trajectory due to interference with the urethra. The target was reached while avoiding damage to the urethra using the angulated trajectory shown.

Since error in needle placement is of clinical importance, the cause of it must be discussed. The median error in aligning this system's needle guides to an MR-identified target was quantified in Chapter 3 as 1.1 mm. This number represents the accuracy with which the device can align its needle guides to targets at an insertion depth of 15 cm.

www.manaraa.com

Needle insertion tests in phantoms then quantified the minimum error achievable using this system to insert needles into homogenous tissue with stiffness similar to that of human tissue as median 1.3 mm. Finally, results in this chapter demonstrated a median needle guidance error of 3.4 mm in human tissue. The increased error in human tissue is expected to be due to needle deflection during the initial skin puncture and along the needle's long insertion path through heterogeneous tissue. It is not expected to be caused by other sources such as inaccurate registration of the device to the MR image space or movement of the device during the procedure, since these sources of error have been controlled.

It must be pointed out that the definition of needle guidance error used in this work does not include prostate motion, meaning that the reported values of targeting error are potentially underestimated.[24] However, our use of a Foley catheter and a fully-inflated endorectal MR coil may substantially reduce intra-treatment prostate motion caused by variable rectal and bladder filling and rectal peristalsis, which are generally considered major contributors to prostate motion during radiotherapy.[25] In addition, prostate motion is monitored in each procedure by acquiring T2-weighted whole-gland images when motion is suspected, and the final position of each needle is verified using a bSSFP sequence, which provides excellent soft tissue contrast for confirming the location of needles relative to prostate structures. Finally, while the time to guide each needle to its target was significantly reduced using this system compared to a template approach, there is still room for improvement. The limiting factor preventing a further reduction in needle guidance time is the lack of a readily-available method of controlling needle trajectories in real-time.

www.manaraa.com

4.5 Conclusions

We have developed a mechatronic needle guidance system for MR-guided transperineal biopsy and focal therapies of the prostate, and evaluated its performance in delivering 29 needles in eight cases of MR-guided prostate FLA. The time taken to guide each needle to its target was significantly reduced compared to the fixed grid template approach previously used, and the system provided a reliable method of accurately aligning needle guides for in-bore needle delivery to the prostate. However, despite these successes, we suspect that needle placement error is currently substantially contributing to incomplete target coverage in some cases. To address this issue, we propose to develop a better understanding of the relationship between the uncertainty in needle placement error and target coverage, enabling the generation of treatment plans that will ensure a higher rate of treatment delivery success. This proposal led to the work described in the following chapter.

www.manaraa.com

References

1. R. Siegel, D. Naishadham and A. Jemal, "Cancer statistics, 2013," CA. Cancer J. Clin. **63**, 11-30 (2013).

2. M. R. Abern, M. Tsivian and T. J. Polascik, "Focal therapy of prostate cancer: evidence-based analysis for modern selection criteria," Curr. Urol. Rep. **13**, 160-169 (2012).

3. J. De La Rosette, H. Ahmed, J. Barentsz, T. B. Johansen, M. Brausi, M. Emberton, F. Frauscher, D. Greene, M. Harisinghani and K. Haustermans, "Focal therapy in prostate cancer - report from a consensus panel," J. Endourol. **24**, 775-780 (2010).

4. J. V. Hegde, R. V. Mulkern, L. P. Panych, F. M. Fennessy, A. Fedorov, S. E. Maier and C. Tempany, "Multiparametric MRI of prostate cancer: An update on state-of-the-art techniques and their performance in detecting and localizing prostate cancer," J. Magn. Reson. Imaging **37**, 1035-1054 (2013).

5. C. M. Hoeks, J. O. Barentsz, T. Hambrock, D. Yakar, D. M. Somford, S. W. Heijmink, T. W. Scheenen, P. C. Vos, H. Huisman and I. M. van Oort, "Prostate cancer: multiparametric MR imaging for detection, localization, and staging," Radiology **261**, 46-66 (2011).

6. J. Chen, B. L. Daniel, C. J. Diederich, D. M. Bouley, M. A. van den Bosch, A. M. Kinsey, G. Sommer and K. B. Pauly, "Monitoring prostate thermal therapy with diffusion-weighted MRI," Magn. Reson. Med. **59**, 1365-1372 (2008).

7. H. L. M. Cheng, M. A. Haider, M. J. Dill-Macky, J. M. Sweet, J. Trachtenberg and M. R. Gertner, "MRI and contrast-enhanced ultrasound monitoring of prostate microwave focal thermal therapy: An in vivo canine study," J. Magn. Reson. Imaging **28**, 136-143 (2008).

8. G. S. Fischer, I. Iordachita, C. Csoma, J. Tokuda, S. P. DiMaio, C. M. Tempany, N. Hata and G. Fichtinger, "MRI-compatible pneumatic robot for transperineal prostate needle placement," IEEE Trans. Mech. **13**, 295-305 (2008).

9. A. Krieger, I. Iordachita, S. E. Song, N. B. Cho, P. Guion, G. Fichtinger and L. L. Whitcomb, Proc. IEEE International Conference on Robotics and Automation, Anchorage, Alaska, 2010.

10. U. Lindner, A. Louis, A. Colquhoun, P. Boström, S. Davidson and O. Raz, "First robotic magnetic resonance-guided laser focal therapy for prostate cancer: a case report and review of the literature," Interven. Oncol. Soc. J. **1**, 69-77 (2011).

11. C. Ménard, R. C. Susil, P. Choyke, G. S. Gustafson, W. Kammerer, H. Ning, R. W. Miller, K. L. Ullman, N. Sears Crouse and S. Smith, "MRI-guided HDR prostate

www.manaraa.com

brachytherapy in standard 1.5 T scanner," Int. J. Radiat. Oncol. Biol. Phys. **59**, 1414-1423 (2004).

12. D. Stoianovici, D. Song, D. Petrisor, D. Ursu, D. Mazilu, M. Muntener, M. Schar and A. Patriciu, ""MRI Stealth" robot for prostate interventions," Minim. Invasive Ther. Allied Tech. **16**, 241-248 (2007).

13. J. Cepek, B. Chronik, U. Lindner, J. Trachtenberg, S. Davidson, J. Bax and A. Fenster, "A system for MRI-guided transperineal delivery of needles to the prostate for focal therapy," Med. Phys. **40**, 012304 (2013).

14. M. S. Sussman, U. Lindner, M. Haider, W. Kucharczyk, E. Hlasny and J. Trachtenberg, "Optimizing contrast agent concentration and spoiled gradient echo pulse sequence parameters for catheter visualization in MR-guided interventional procedures: An analytic solution," Magn. Reson. Med. **70**, 333-340 (2013).

15. O. Raz, M. A. Haider, S. R. H. Davidson, U. Lindner, E. Hlasny, R. Weersink, M. R. Gertner, W. Kucharcyzk, S. A. McCluskey and J. Trachtenberg, "Real-time magnetic resonance imaging-guided focal laser therapy in patients with low-risk prostate cancer," Eur. Urol. **58**, 173-177 (2010).

16. M. Roethke, A. Anastasiadis, M. Lichy, M. Werner, P. Wagner, S. Kruck, C. D. Claussen, A. Stenzl, H. Schlemmer and D. Schilling, "MRI-guided prostate biopsy detects clinically significant cancer: analysis of a cohort of 100 patients after previous negative TRUS biopsy," World J. Urol. **30**, 213-218 (2012).

17. A. Oto, I. Sethi, G. Karczmar, R. McNichols, M. K. Ivancevic, W. M. Stadler, S. Watson and S. Eggener, "MR Imaging–guided Focal Laser Ablation for Prostate Cancer: Phase I Trial," Radiology **267**, 932-940 (2013).

18. U. Lindner, N. Lawrentschuk and J. Trachtenberg, "Image guidance for focal therapy of prostate cancer," World J. Urol. **28**, 727-734 (2010).

19. R. C. Susil, K. Camphausen, P. Choyke, E. R. McVeigh, G. S. Gustafson, H. Ning, R. W. Miller, E. Atalar, C. N. Coleman and C. Ménard, "System for prostate brachytherapy and biopsy in a standard 1.5 T MRI scanner," Magn. Reson. Med. **52**, 683-687 (2004).

20. J. I. Epstein, P. C. Walsh, M. Carmichael and C. B. Brendler, "Pathologic and Clinical Findings to Predict Tumor Extent of Nonpalpable (Stage T1c) Prostate Cancer," JAMA: the Journal of the American Medical Association **271**, 368-374 (1994).

21. G. Ploussard, J. I. Epstein, R. Montironi, P. R. Carroll, M. Wirth, M.-O. Grimm, A. S. Bjartell, F. Montorsi, S. J. Freedland and A. Erbersdobler, "The contemporary

www.manaraa.com

concept of significant versus insignificant prostate cancer," Eur. Urol. **60**, 291-303 (2011).

22. G. Bozzini, P. Colin, P. Nevoux, A. Villers, S. Mordon and N. Betrouni, "Focal therapy of prostate cancer: energies and procedures," Urol. Oncol.-Semin. Ori. **31**, 155-167 (2012).

23. U. Lindner, R. Weersink, M. Haider, M. Gertner, S. Davidson, M. Atri, B. Wilson, A. Fenster and J. Trachtenberg, "Image guided photothermal focal therapy for localized prostate cancer: phase I trial," J. Urol. **182**, 1371-1377 (2009).

24. H. Xu, A. Lasso, P. Guion, A. Krieger, A. Kaushal, A. K. Singh, P. A. Pinto, J. Coleman, R. L. Grubb III and J.-B. Lattouf, "Accuracy analysis in MRI-guided robotic prostate biopsy," Int. J. Comput. Assist. Radiol. Surg. **8 (Online)**, 1-8 (2013).

25. R. Jiang, R. Barnett, J. Chow and J. Chen, "The use of spatial dose gradients and probability density function to evaluate the effect of internal organ motion for prostate IMRT treatment planning," Phys. Med. Biol. **52**, 1469 - 1484 (2007).

www.manaraa.com

Chapter 5.

Treatment Planning for Prostate Focal Laser Ablation in the Face of Needle Placement Uncertainty†

5.1 Introduction

The concept of focal therapy for the treatment of patients with clinically localized, low- to intermediate- risk prostate cancer is receiving increased attention, and the safety and efficacy of a variety of focal therapy delivery modalities is being evaluated in a number of trials.[1] One particularly attractive modality is focal laser ablation (FLA). Prostate FLA involves interstitial placement of one or multiple diffusing laser fibers into the "dominant lesion" or "index" tumour.[2] With recent advances in multi-parametric magnetic resonance (MR) imaging and its reported high sensitivity in detecting clinically significant tumours, localization of the tumour selected for FLA is commonly based on an assessment of T2-weighted, diffusion-weighted, and dynamic contrast-enhanced (DCE) MR images.[3, 4] This process provides the interventionalist with a well-delineated 3D target for FLA (hereafter referred to as the *target* or *focal target*).[5-7] Most commonly, diode lasers at 980 nm (infrared) are used for ablation, as this technology is cheaper and more compact than alternatives such as Nd-YAG lasers, and water has good absorption at this wavelength.[8] In addition, systems with FDA approval

†. A version of this chapter has been published: Cepek, J., Lindner, U., Davidson, S., Haider, M., Ghai, S., Trachtenberg, J., Fenster, A., "Treatment Planning for Prostate Focal Laser Ablation in the Face of Needle Placement Uncertainty." Med. Phys. (2014, In Press).

www.manaraa.com

for use in prostate are now available. Once a fiber has been placed within the target region, usually through the perineum via a coaxial cannula system, ablation is performed for a period of ~ 2 – 10 minutes at a laser power of ~ 5 – 15 W. By performing multiple laser fiber insertions, regions of ablated tissue up to ~ 10 cm^3 can be produced.[5, 6, 9, 10] FLA is MR-compatible, allowing for intra-treatment visualization of prostate cancer, clear visualization of optical fiber placement in the prostate, and tissue temperature monitoring using MR thermometry.[1, 11] In addition, FLA allows the possibility of re-treatment or secondary radical surgery, if necessary; has been shown to cause limited treatment-related morbidity in several Phase I clinical trials; and the ability to create confluent regions lacking any remaining viable cells using FLA has been demonstrated.[5-7, 10] As many of the academic centers studying FLA move towards Phase II studies, the level of oncologic control achievable using this technique will need to be proven. It is important at this transition stage to address any flaws identified during the Phase I trials of FLA, and correct them before moving forward. Such a strategy will ensure an accurate evaluation of the true potential that FLA offers for the treatment of prostate cancer.

While the accurate specification of surrogate endpoints for prostate focal therapy are not yet established,[12] one fact regarding the planning of focal therapy remains true: any method of focal therapy should aim to destroy 100% of the tissue in the index tumour. While FLA has shown more promise in terms of preserving urinary, bowel, and erectile function than alternatives such as high intensity focused ultrasound and cryoablation,[1] evidence from the Phase I clinical trials and case studies on prostate FLA completed to date suggest that complete focal target destruction is not consistently being

www.manaraa.com

achieved.[5-7, 13]. In their Phase I trial studying US-guided FLA in 12 patients, Lindner *et al.* reported a median fraction of pre-treatment target volume treated of 53% overall, and 81% in the last four patients treated.[5] In another trial, in which nine men were treated with MR-guided FLA, Oto *et al.* found that the target was not completely overlapped by the ablation zone seen on immediate post-procedure DCE MR images in two cases.[6] Furthermore, in most of these cases, one of the reasons for finding positive biopsy cores in the region previously treated (defined as treatment failure in these studies) was suspected to be poor overlap between the ablated and targeted regions.[5, 6, 13] It has been hypothesized by several clinicians working in this field that a primary reason for insufficient overlap is error in needle placement, and several authors have identified the need for methods of planning prostate focal therapy.[1, 6, 14, 15] These hypotheses are consistent with the findings of several previous studies in which the effects of needle placement errors on the dose delivered in prostate brachytherapy were shown to cause clinically significant deviations from the prescribed dose, and modifications to treatment planning methods were required to compensate for this effect.[16-18] At the time of writing, no systematic methods of planning laser fiber placement for FLA have been published.

In this work, a systematic method of planning target points for the placement of laser fibers for prostate FLA is developed. The method assumes that the shape of the ablated tissue region created by each laser fiber is known to the interventionalist for a given laser power and application time, and assumes that ablated regions created by each fiber are independent. Each target is modeled as an ellipse of minimum area that encloses a projection of the true focal target along the needle insertion direction, and assumes that

www.manaraa.com

FLA can create a cylindrical volume of ablated tissue that is elongated along the direction of needle insertion. This type of geometric planning has been employed for planning various types of ablative therapy including rf ablation of liver tumours,[15, 19, 20] and rf ablation of lung tumours.[21] In these works, each ablation volume was modeled as either a sphere or cylinder, and planning consisted of finding an optimal geometric arrangement of the ablation volumes to completely ablate the tumour. Other authors have identified a combined effect of performing multiple ablations in close proximity, resulting in a larger volume of ablated tissue than would be achieved by performing each of the ablations separately.[22-24] However, as the response of tissue to thermal therapy has been shown to vary greatly depending on the organ,[25] and a method of accurately specifying thermal properties and levels of perfusion in human prostate tissue has yet to be developed, an initial conservative approach of assuming independent ablations is taken in this work.

Following the planning method, a method of estimating the probability of achieving complete target ablation for a given plan is presented, and results are shown for a range of realistic focal target sizes and shapes, and levels of needle placement uncertainty. Finally, a table is provided for estimating the maximum target size that can be confidently ablated over a range of target and FLA geometrical parameters, and the level of needle placement uncertainty expected. This table can be used to estimate patient eligibility for FLA based on a minimum required probability of achieving complete target ablation.

www.manaraa.com

5.2 Methods

5.2.1 Treatment Planning

In this section, a systematic method for specifying the desired placement of laser fibers is developed. The method begins with a simplification of the geometry of the problem, thereby reducing the degrees-of-freedom in treatment planning. Next, the minimum plan required to completely cover a focal target of given shape and size with a fixed size of ablation region is defined, followed by a systematic method of augmenting the minimum plan by increasing the number of laser fibers.

5.2.2 3D Ablation Volume Model

In FLA, laser light is directed into tissue using a diffuser at the end of an optical fiber. Absorption of light energy causes an increase in tissue temperature over time, eventually resulting in irreversible tissue damage. In thermal therapy for cancer treatment, the ablated region is defined as the boundary within which the tissue is definitely irreversibly injured.[26] Estimation of the boundary of irreversible thermal injury is generally performed by monitoring tissue temperature over time, and is defined by thresholding either temperature or an integral parameter (*e.g.* Arrhenius integral or cumulative equivalent minutes at 43°C).[26] For pre-treatment planning, estimation of the boundary of the ablated region can be performed by numerical simulation of the 3D distribution of tissue temperature over time. Most commonly, such a simulation amounts to solving the Pennes bioheat equation using finite element or similar methods.[27]

The most common type of laser diffuser used for FLA is cylindrical. Evidence from numerical simulations and DCE MRI indicate that the resulting volumes of ablated

www.manaraa.com

tissue are approximately ellipsoidal, and elongated in the needle insertion direction.[28, 29] Images of ablation regions, as visualized on immediate post-treatment dynamic contrast enhanced MR imaging, are shown in Figure 5.1. If each region of ablated tissue can be assumed to be independent and tissue properties are uniform, pre-treatment planning can be simplified as a geometric problem, *i.e.* the ablated region resulting from multiple confluent laser applications is equivalent to the superimposition of each individual ablation region. Ablated regions are expected to be independent if:

i. laser fibers in close proximity are not fired simultaneously, and
ii. for fibers that are fired in succession in close proximity, the amount of thermal tissue damage beyond the boundary of definite irreversible damage does not substantially contribute to the thermal damage caused by the next laser application.

5.2.3 2D Approximation

After a single catheter insertion, multiple confluent ablation regions can be created along the catheter's axis by retracting the laser fiber in between or during laser application.[30] In accordance with these observations, and assuming that the extent of all positions of laser application covers the farthest and nearest volume of the target along the catheter axis, an ablation region can be idealized as a cylinder of diameter D_{treat}. This idealized ablation region shape is conservative with respect to ensuring target ablation, since the actual ablation region will always be slightly larger. The idealized cylindrical ablation region concept is shown in Figure 5.2. The amount of healthy tissue damaged beyond the idealized cylindrical model of the ablated region depends on the separation between individual ablations along the axis of the laser fiber. If the laser fiber is retracted at a

www.manaraa.com

constant rate, the resulting ablation region is expected to be cylindrical (in the absence of any heat sink effects).

Using this model of ablation volume shape, planning for FLA only requires consideration of the target shape as projected onto a plane perpendicular to the needle insertion direction (*i.e.,* as seen from the "needle's eye view"). The targets are then idealized as an ellipse of minimum area that completely encloses the projection of the target onto this plane. Moreover, use of this model assumes that all needle trajectories are approximately parallel to each other, and that the depth of laser fibers can be accurately measured and controlled (*e.g.* using imaging).

These simplified models of ablation and target shapes result in a reduction in the dimensionality and computational requirement of the problem (from 3D to 2D), and a reduction in the number of degrees-of-freedom in treatment planning. The resulting idealized problem can be systematically studied with much greater simplicity.

www.manaraa.com

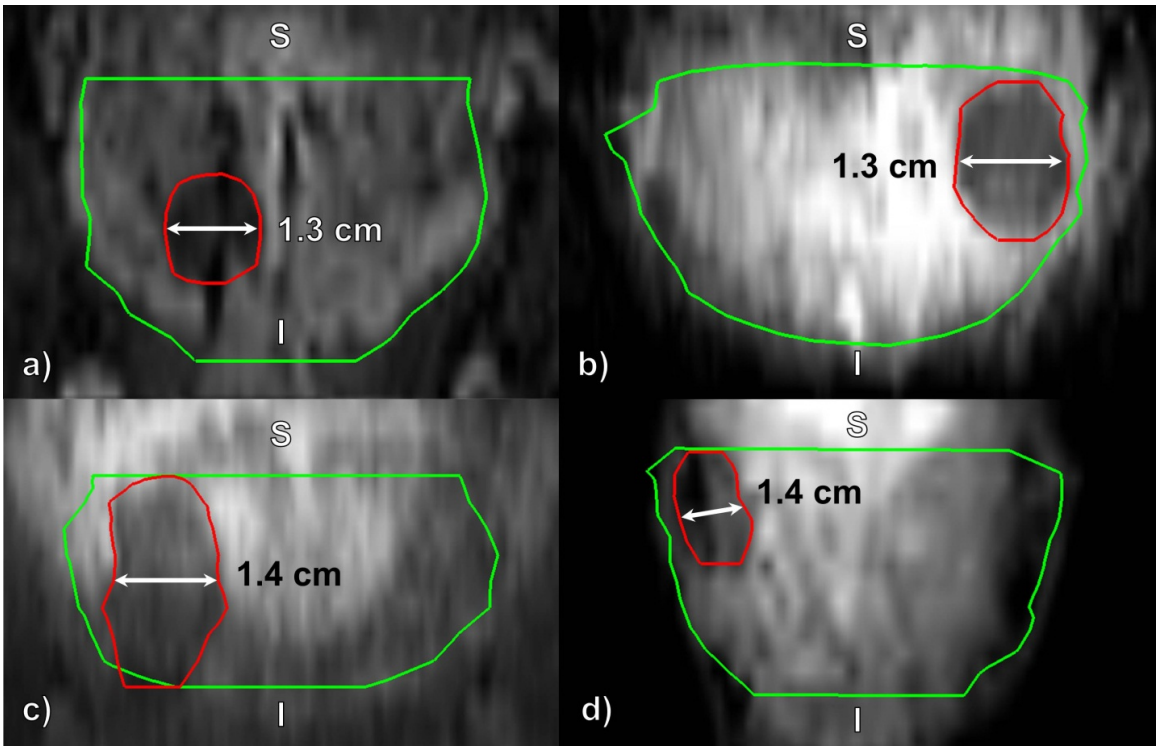

Figure 5.1: Estimated regions of ablated tissue in four patient's prostates, as seen on immediate post-treatment dynamic contrast-enhanced MR images (coronal slices): a), b) single fiber insertion with laser application at only one axial position; c), d) single fiber insertion with multiple laser applications at multiple axial positions, which created a region of ablated tissue that is elongated in the direction of the laser fiber (needle) axis. In all cases the insertion direction was approximately superior-inferior, with case d) showing a slight lateral angulation.

www.manaraa.com

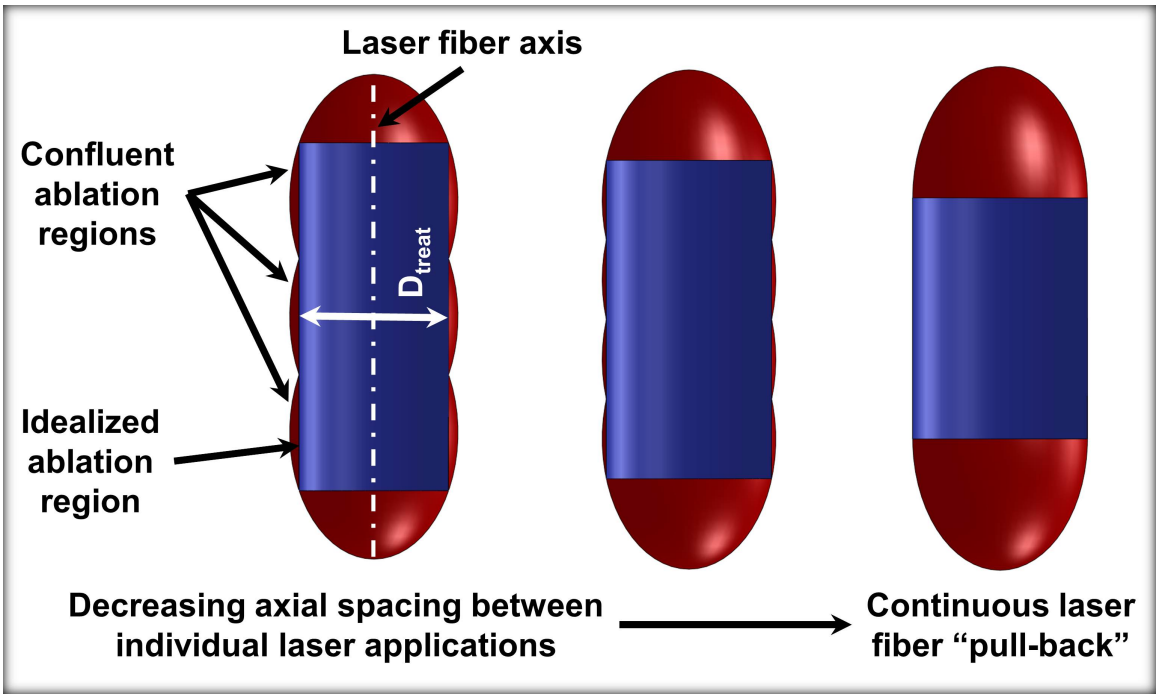

Figure 5.2: Idealized ablation volume. A set of confluent regions of ablated tissue in the direction of the needle insertion is modeled as a cylinder of maximum diameter that can be enclosed by the actual ablated region. As the axial spacing between laser applications is reduced, the amount of under-prediction of ablated tissue around the periphery of the ablation region decreases, and it increases at each end.

Consideration of the planned axial positioning of the laser fibers must also be made in order to avoid strongly violating the cylindrical model of confluent ablation regions. The cylindrical model will be valid if the planned margin m_p, as seen from the needle's eye view, is equal to the minimum distance from the target to the planned ablation volume in the direction perpendicular to the laser fiber's axis m_{min}. This is illustrated in Figure 5.3.

www.manaraa.com

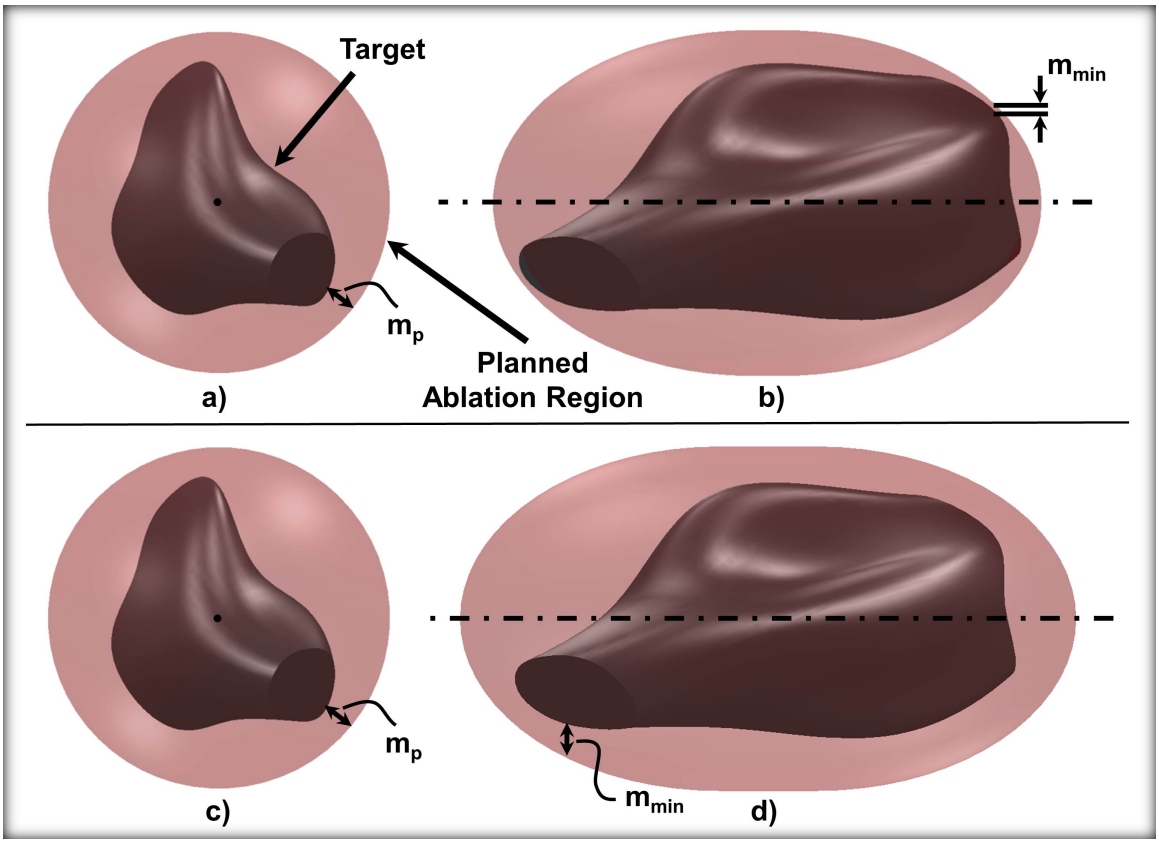

Figure 5.3: Effect of laser fiber axial positioning on the validity of the cylindrical ablation region model. a), c), view from "needle's eye view"; b), d), view perpendicular to needle axis. The cylindrical ablation region model is valid if the axial extent of the planned ablation region is chosen such that $m_p = m_{min}$. In a) & b), the planned ablation region is not long enough ($m_p > m_{min}$), in c) & d), $m_p = m_{min}$ and therefore the 2D model would reliably predict when needle placement error results in untreated target tissue.

5.2.4 Specification of Planned Laser Fiber Locations

A systematic method of planning the placement of laser fibers was designed based on the following constraints and guidelines:

- For a given plan, an increase in the ablation diameter should result in a nearly uniform increase in margin of the treatment plan around the periphery of the target,
- A maximum of eight target points (number of laser fibers) is permitted, and
- All individual ablation regions are of equal diameter.

Following these guidelines, two possible patterns of fiber placement were defined: Pattern A: the placement of laser fibers is equally distributed along the major axis of the ellipse-shaped target (linear pattern), and Pattern B: laser fibers are placed

www.manaraa.com

around an ellipse that is concentric to the idealized target ellipse boundary (concentric ellipse pattern). These two patterns are shown in Figure 5.4.

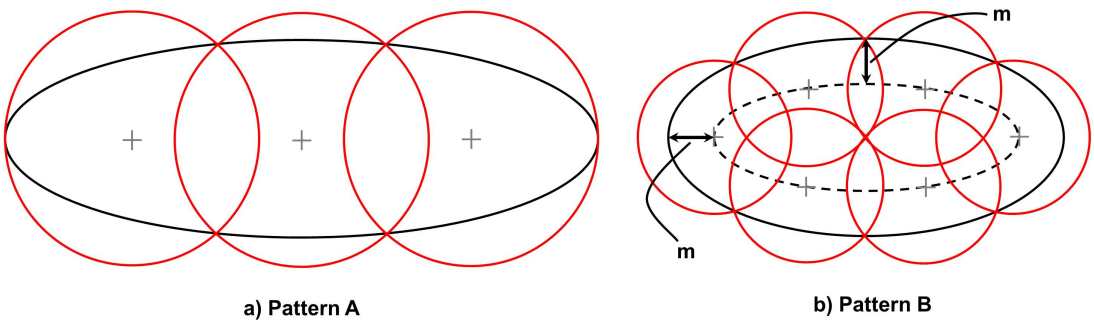

Figure 5.4: The two patterns considered for the ideal placement of laser fibers: a) Pattern A (linear pattern), b) Pattern B (concentric ellipse pattern). Solid black contour: idealized target boundary, red contours: idealized ablation region boundaries, dashed contour: concentric planning ellipse. For a given target width, target aspect ratio, and number of laser fibers, the ideal pattern of the two is that which requires the smallest ablation diameter.

For each combination of target length, target aspect ratio AR (length divided by width), and number of laser fibers, the minimum required ablation radius and corresponding pattern can be defined as that for which the total ablation region completely covers the target with zero margins (*i.e.* the minimum distance from the target boundary to any exterior ablation region boundary is zero). This method defines a family of baseline treatment plans. Each baseline plan can subsequently be augmented by increasing the number of laser fibers; thereby increasing the overlap of ablation regions, and increasing the margins around the periphery of the target. Figure 5.5 describes this planning algorithm graphically. Figure 5.6 shows examples of how the minimum plan is modified by adding laser fibers.

www.manaraa.com

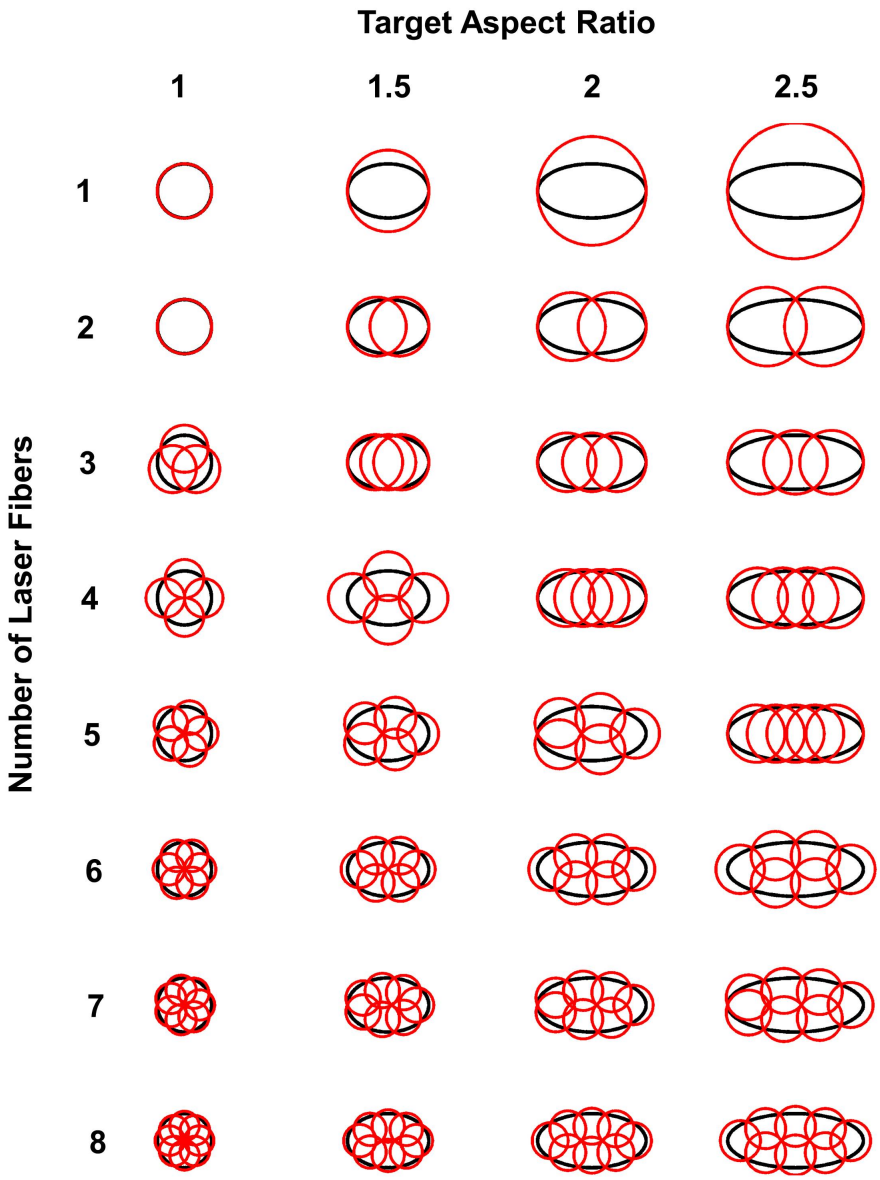

Figure 5.5: Minimum treatment plan required to achieve complete target coverage for varying target aspect ratio and number of laser fibers used. Either Pattern A (fibers equally distributed along the major axis of the target) or Pattern B (fibers distributed around an ellipse concentric to the target boundary) is employed, based on whichever pattern gives the minimum required size of ablation region. Black contour: idealized target boundary, red circle: idealized ablation region boundary.

www.manaraa.com

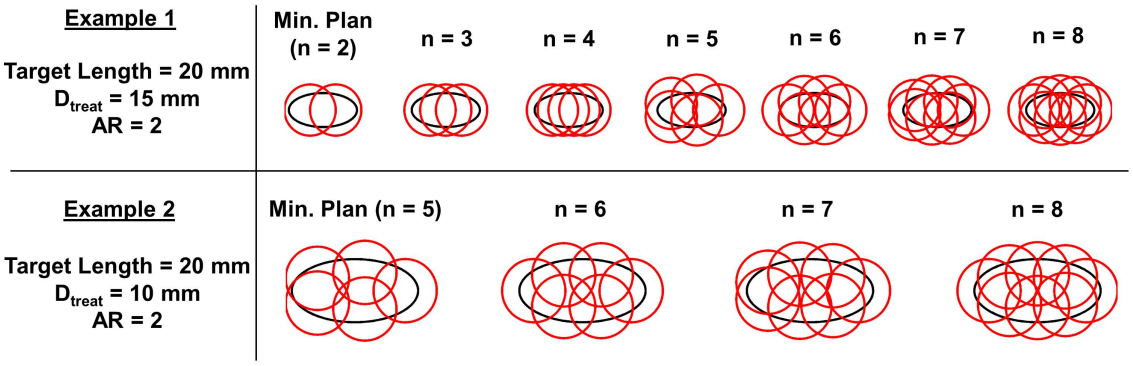

Figure 5.6: Examples showing how the planned number of laser fibers can be increased. Pattern A (the linear pattern) is used when the diameter of the ablation is large relative to the target width. Pattern B (concentric ellipse pattern) is used when the ablation diameter is small relative to the target width, in which case it becomes necessary to distribute laser fibers around the periphery of the target. As the number of laser fibers increases, Pattern B can be employed to increase the treatment margin around the periphery of the target.

Table 5.1 summarizes the minimum required ratio of ablation diameter to target length $R_A = D_{treat} / L$ to completely cover a target with a given number of laser fibers.

Table 5.1: Minimum required ratio of ablation diameter to target length R_A for varying target aspect ratio and number of planned laser fibers.

		Number of Laser Fibers (n)							
		1	**2**	**3**	**4**	**5**	**6**	**7**	**8**
Target Aspect Ratio (AR)	**1**	1.00[A]	1.00[A]	0.87[B]	0.71[B]	0.62[B]	0.58[B]	0.56[B]	0.54[B]
	1.5	1.00[A]	0.72[A]	0.68[A]	0.60[B]	0.50[B]	0.45[B]	0.42[B]	0.40[B]
	2	1.00[A]	0.63[A]	0.54[A]	0.52[A]	0.45[B]	0.39[B]	0.36[B]	0.33[B]
	2.5	1.00[A]	0.58[A]	0.47[A]	0.44[A]	0.42[A]	0.36[B]	0.33[B]	0.29[B]

[A] Fibers placed according to pattern A
[B] Fibers placed according to pattern B.

5.2.5 Estimation of Treatment Overlap

Errors in the final placement of needles relative to their planned locations will be present in all cases, and may result in the fraction of target treated being less than 100%. The actual result will be a function of the planned locations of laser fibers, the size of the ablation regions, and the probability density function (PDF) of needle placement error. In

www.manaraa.com

this section, a mathematical description of treatment overlap in the presence of needle placement uncertainty is presented. Next, the PDF used to model needle placement error is specified.

5.2.6 Mathematical Description of Treatment Overlap

For a given target and corresponding treatment plan, the probability of ablating a specified fraction (or greater) of the target volume is desired to be known. This probability is given by the complementary cumulative distribution function (CCDF) $\bar{F}$ of the fraction of target treated:

$$\bar{F}(y) = P(f_t \geq y),\ 0 \leq y \leq 1 \tag{5.1}$$

where f_t is the fraction of the target volume treated, and $\bar{F}(y)$ is the probability that f_t is greater than or equal to a given value y. Given $\bar{F}(y)$ for a specific target and treatment plan, one could answer questions such as: "what is the probability that at least 90% of the target volume will be ablated?" or "what is the probability that the entire volume of the target will be ablated?"

f_t is defined as the ratio of the volume of target tissue ablated V_{T_A} to the total target volume V_T

$$f_t = \frac{V_{T_A}}{V_T}. \tag{5.2}$$

For a target region T and n planned ablation regions $A_1,...,A_n$ with planned target points $\mathbf{p}_{t_1},...,\mathbf{p}_{t_n}$, the expression for V_{T_A} becomes

$$V_{T_A}(\mathbf{e_1}',...,\mathbf{e_n}',\mathbf{p}_{t_1},...,\mathbf{p}_{t_n}) = \int_T T(\mathbf{x}) \cap \left[A_1(\mathbf{p}_{t_1} + \mathbf{e_1}') \cup ... \cup A_n(\mathbf{p}_{t_n} + \mathbf{e_n}') \right] d\mathbf{x}, \tag{5.3}$$

www.manaraa.com

where $\mathbf{e_1},...,\mathbf{e_n}$ are the needle placement errors for each of the n ablation regions, and T and A_i are defined as

$$T(\mathbf{x}) = \begin{cases} 1, & \mathbf{x} \text{ is within projected target boundary} \\ 0, & \text{elsewhere} \end{cases}, \tag{5.4}$$

and

$$A_i(\mathbf{x}) = \begin{cases} 1, & \mathbf{x} \text{ is within region of ablated tissue} \\ 0, & \text{elsewhere} \end{cases}. \tag{5.5}$$

$\bar{F}$ can be found by solving the integral

$$\bar{F}(y) = \int ... \int_{J(y)} \prod_{i=1}^{n} g_i(\mathbf{e_i}') d^2\mathbf{e_1}', ..., d^2\mathbf{e_n}', \tag{5.6}$$

where $g_i(\mathbf{e_i})$ is the PDF of needle placement error of the i^{th} needle $\mathbf{e_i}$, and $J(y)$ is the set of $\mathbf{e_1},...,\mathbf{e_n}$ for which f_t is greater than or equal to y

$$J(y) = \{\mathbf{e_1},...,\mathbf{e_n} \mid f_t \geq y\}. \tag{5.7}$$

If the integration of Equation (5.6) is performed numerically, the computation time required is proportional to $N_p{}^{2n}$, where N_p is the number of grid points in each direction of a 2D numerical grid. In focal laser ablation of prostate cancer, most targets require multiple laser fibers (target points), making the direct numerical integration of Equation (5.6) impractical in terms of computation time.[5, 6] For example, if four ablation regions are planned, the integration becomes 8-dimensional. Using 100 grid points in each direction, the total time to numerically compute an 8-dimensional integral that takes $1\mu s$ for each 2D component is 278 hours. This is impractical.

Alternatively, Equation (5.6) can be rewritten as

www.manaraa.com

$$\bar{F}(y) = E\left[\mathbf{1}_y\right], \tag{5.8}$$

where $\mathbf{1}_y$ is an indicator function, defined as

$$\mathbf{1}_y = \begin{cases} 1, & (\mathbf{e_1}, \ldots, \mathbf{e_n}) \in J(y) \\ 0, & \text{elsewhere} \end{cases}, \tag{5.9}$$

and $E\left[\mathbf{1}_y\right]$ is its expected value. The function $\mathbf{1}_y$ is equal to one when the final placement of needles, including needle placement error, results in a fraction of target treated that is greater than or equal to y. Using this formulation, estimation of $\bar{F}(y)$ can be obtained using a stochastic Monte Carlo simulation that computes the empirical CCDF

$$\hat{\bar{F}}(y) = \frac{1}{N}\sum_{j=1}^{N}\left(\mathbf{1}_y\right)_j, \tag{5.10}$$

which, by the strong law of large numbers, converges to the true CCDF of f_t as N approaches infinity.[31] Using this approach, N random samples of $\mathbf{1}_y$ are obtained to estimate the CCDF. The probability of achieving complete target ablation is of particular importance, and is defined as $P_{100} = \bar{F}(1)$. This approach requires a model of the PDF of needle placement error $\mathbf{E}$, which is described in the next section.

5.2.7 Statistical Model of Needle Placement Error

In this chapter, needle placement error is defined as the shortest Euclidean distance between a needle's final location in the tissue after insertion and its planned location (target point). Using this definition, errors in the needle depth are ignored; a simplification based on the observation that FLA can create elongated regions of ablated tissue along the direction of needle insertion. Needle placement error includes three

www.manaraa.com

major contributions: 1) error in registration between pre- and intra-treatment images, which results in an error in specification of the planned target point in intra-treatment image space, 2) errors in needle guidance caused predominantly by deflection of the needle during insertion, and 3) tissue motion and deformation during needle insertion. Prediction of a needle's final position in human tissue is a difficult task, and requires *a priori* knowledge of the 3D distribution of tissue properties and structures. Even if real-time imaging is employed during needle insertion, measurement of the current needle position will contain error, and knowledge of the current position cannot be used to predict the future deviations of the needle. For these reasons, needle insertion is considered to be a stochastic process, and the error in final needle placement is modeled with a continuous PDF.[32-34] This approach has been applied in several previous works studying the effects of needle placement error on: the dose distribution in transperineal prostate brachytherapy,[16-18, 35] the ability to detect prostate cancer using biopsy,[36] and trajectory planning for steerable needles.[32, 33] In most of the aforementioned works, either the final placement error, or the error in angulation of the needle is modeled with a 2D normal distribution with mean zero and equal variance σ^2 in all directions. This is the approach used in this work for modeling the needle placement error vector

$$\mathbf{E} \sim N_2\left(0, \sigma^2 \mathbf{I}\right). \tag{5.11}$$

where $\mathbf{I}$ is a 2D identity matrix. Modeling needle placement error in this way assumes that the needle is most likely to reach the point at which it was aimed, and that each orthogonal component of needle placement error is independent. Thus, systematic errors, which may include biases in the system used to guide the needles, asymmetry of the needle tips, and prostate rotation during needle insertion, are assumed to be insubstantial.

www.manaraa.com

Systematic errors of this sort can reasonably be ruled out if: system biases have been detected and corrected (by device calibration), either symmetrically-tipped needles are used or beveled needles are used and the steering effect of the bevel is compensated, and that the physician is anticipating prostate motion and compensating for it.[37] In prostate FLA, symmetrically-tipped needles are most commonly used, so the steering effect of a beveled needle is not likely to be an issue in the context of this work.

If the needle placement error is distributed as in Equation (5.11), then the magnitude of needle placement error follows a Rayleigh distribution with parameter σ [31]

$$\|\mathbf{E}\| \sim Rayleigh(\sigma) \tag{5.12}$$

The value of σ, which is equal to the standard deviation of each orthogonal component of needle placement error, depends on several factors, including: the diameter and material stiffness of the needles used, the imaging modality used for needle guidance, the depth to which needles are inserted, and technique and level of skill.[38, 39] Accordingly, a realistic range of σ for transperineal insertion of needles into the prostate was estimated to be 1 – 4 mm, based on evidence from studies quantifying error in transperineal prostate needle placement.[16, 18, 35, 38, 40, 41]

5.2.8 Numerical Implementation Considerations

Sample Size. A practical value of the number of samples N that gives a reliable estimate of P_{100} is desired. The minimum N required to estimate a proportion within an error of ε with $100(1-\alpha)\%$ confidence is[42]

www.manaraa.com

$$N_\alpha = \left(\frac{Z_{1-\alpha/2}}{\varepsilon} \right)^2 P_{100}\left(1 - P_{100}\right), \tag{5.13}$$

where $Z_{1-\alpha/2}$ is the $\left(1-\alpha/2\right)^{th}$ percentile of the standard normal distribution, and α is the error percentile. Alternatively, since the true value of P_{100} is not known, a conservative estimate of N can be obtained by substituting 0.25 for $P_{100}\left(1-P_{100}\right)$, since this is the maximum value this expression can achieve. For $\alpha = 0.05$ and $\varepsilon = 0.01$, the minimum required number of samples is ~10,000. This value was used for all computations.

Grid Convergence. The method of computing target overlap involves a binary image representation of target and ablation regions, and the accuracy of the solution depends on the pixel size of these images. To ensure that the grid convergence was achieved, the pixel size was successively refined until the estimate of P_{100} (for cases with $P_{100} \geq 0.9$) did not change by more than 0.02 with a decrease in pixel size by a factor of 2. Following this criteria, a final pixel size of 0.125 mm was used for all simulations.

PDF Truncation. Modeling the magnitude of needle placement error $\|\mathbf{E}\|$ with a Rayleigh distribution implies that it can truly take on any value in the range $[0, \infty)$. However, due to the stiffness of the needle and, ultimately, its finite length, $\|\mathbf{E}\|$ will be limited to a finite range in practice. Therefore, to avoid overestimation of the effect of needle placement error, random samples of needle placement error must come from a truncated Rayleigh distribution. Evidence from studies quantifying needle placement error in human prostate suggest that the true truncation point is between 2σ and 3σ, where σ is the parameter of the Rayleigh distribution.[40, 41] The sensitivity of the results to the specification of the truncation point within this range was quantified. It was

www.manaraa.com

found that truncating random samples of needle placement error at 3σ compared to that at 2σ resulted in, at most, an increase in the estimated number of laser fibers required of one. For the results presented, 3σ was used, as this makes the results more conservative.

5.2.9 Treatment Simulation Parameters

Monte Carlo stochastic simulations of treatment coverage were performed over a range of target lengths and aspect ratios, treatment region radii, and levels of needle placement standard deviation. Realistic ranges of each of these parameters were chosen based on evidence found in the clinical literature, and that from an ongoing Phase I/II trial studying FLA of prostate cancer (ClinicalTrials.gov ID: NCT01094665).[9] The ranges of the parameters are summarized in Table 5.2, and the choice of each range is justified in the following sections.

Table 5.2: Ranges of the parameters varied for simulations of the fraction of target treated.

Parameter	Range	Units
Target Aspect Ratio (AR)	1 – 2.5	-
Target Length (L)	5 – 30	mm
Ablation Diameter (D_{treat})	10 – 20	mm
σ	1 – 4	mm

5.2.10 Treatment Target Shapes

A realistic range of focal target shapes was estimated using data from an ongoing phase I/II clinical trial investigating the use of FLA in men with localized prostate cancer.[9] A total of 47 target contours were considered. Each contour was defined by an expert radiologist (either M.A.H. or S.G.) on pre-treatment multi-parametric MR images using T2-weighted, dynamic contrast-enhanced, and diffusion-weighted MR sequences. Each 3D target volume was projected onto a plane along the needle insertion direction

www.manaraa.com

(approximated as the superior-inferior direction since needles are delivered transperineally), and an ellipse of minimum area was found for each. Histograms of the widths and aspect ratios of the fitted ellipses for the 47 targets considered are shown in Figure 5.7. Six examples of projected target volumes (generated from the set of 47 expertly-delineated targets described above) and their corresponding elliptical representations are shown in Figure 5.8.

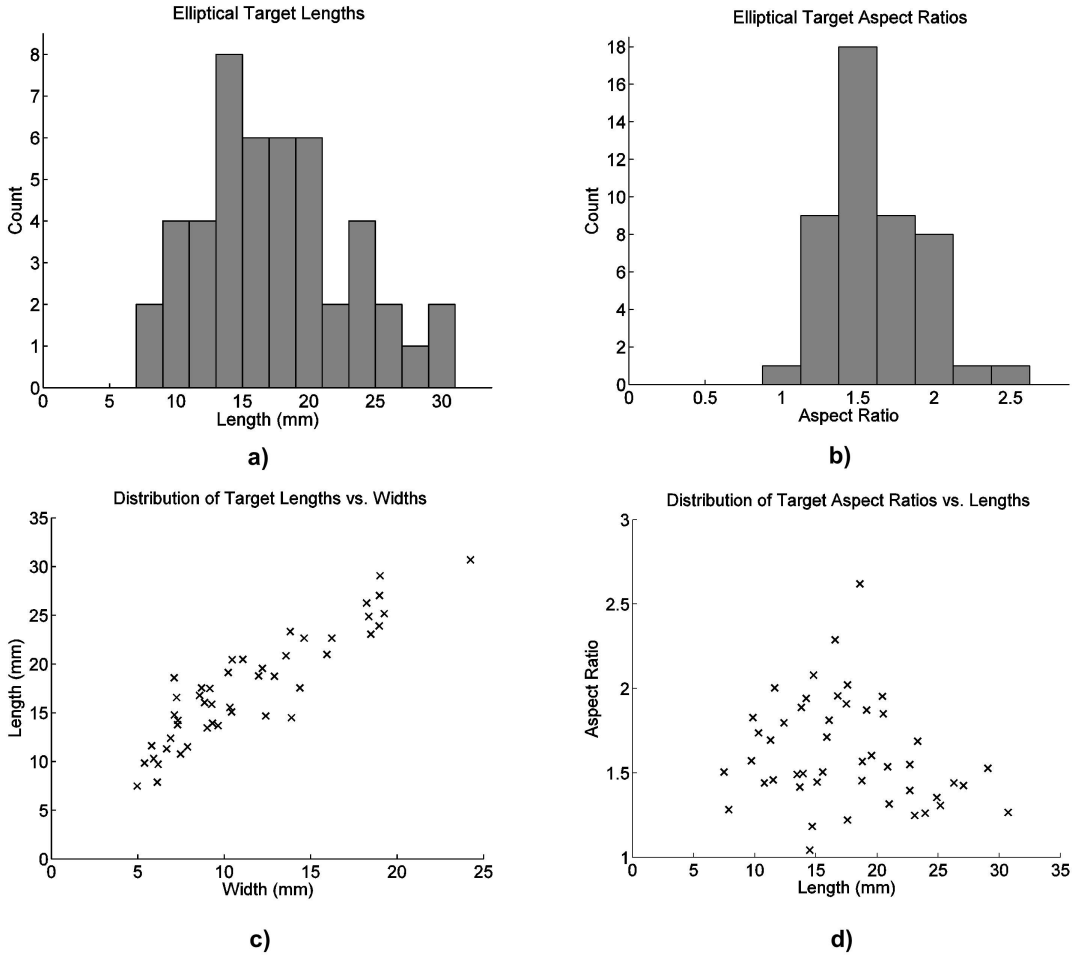

Figure 5.7: Distribution of the sizes and aspect ratios of the ellipses enclosing the MR-identified targets in 47 men included in a Phase I/II clinical trial of FLA for prostate cancer: a) histogram of ellipse lengths, b) histogram of ellipse aspect ratios, c) lengths vs. widths, d) aspect ratios vs. lengths.

www.manaraa.com

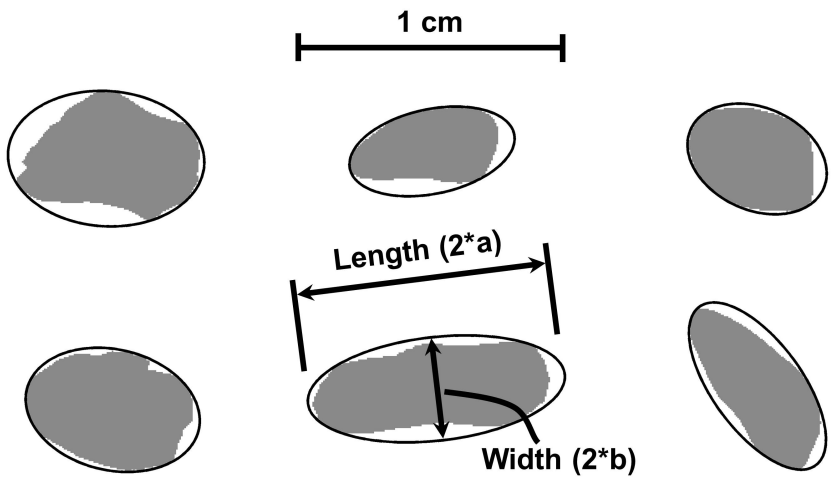

Figure 5.8: Examples of ellipses of minimum area fitted to target shapes, as seen from the "needle's eye view". Gray regions: actual volumes of suspected tumours, as contoured on multi-parametric MR images; black contours: fitted ellipses. The aspect ratio AR is defined as AR = length/width.

Based on the data shown in Figure 5.7, a range of target aspect ratios of 1 – 2.5, and a range of target lengths of 5 – 30 mm were chosen for the simulations.

5.2.11 Ablation Sizes

FLA, using a single 980 nm laser fiber, is capable of producing volumes of ablated tissue up to 50 mm in diameter (in a plane perpendicular to the laser fiber) using a bare fiber, and up to 80 mm in diameter when a cooling sheath is used.[8] The cooling sheath consists of concentric tubes of recirculating fluid (saline) surrounding the laser fiber, and prevents the formation of carbonized tissue near the fiber, allowing the light to penetrate further into the tissue. However, due to the small size of the prostate gland, the range of ablation diameters practically used ranges from ~ 10 – 20 mm;[10, 43] thus this was the range considered in this chapter.

www.manaraa.com

5.3 Results

5.3.1 Idealized Treatment Simulations

Figure 5.9 shows the estimated probability of achieving complete target coverage (P_{100}) over the range of parameters described in Section 5.2.9.

www.manaraa.com

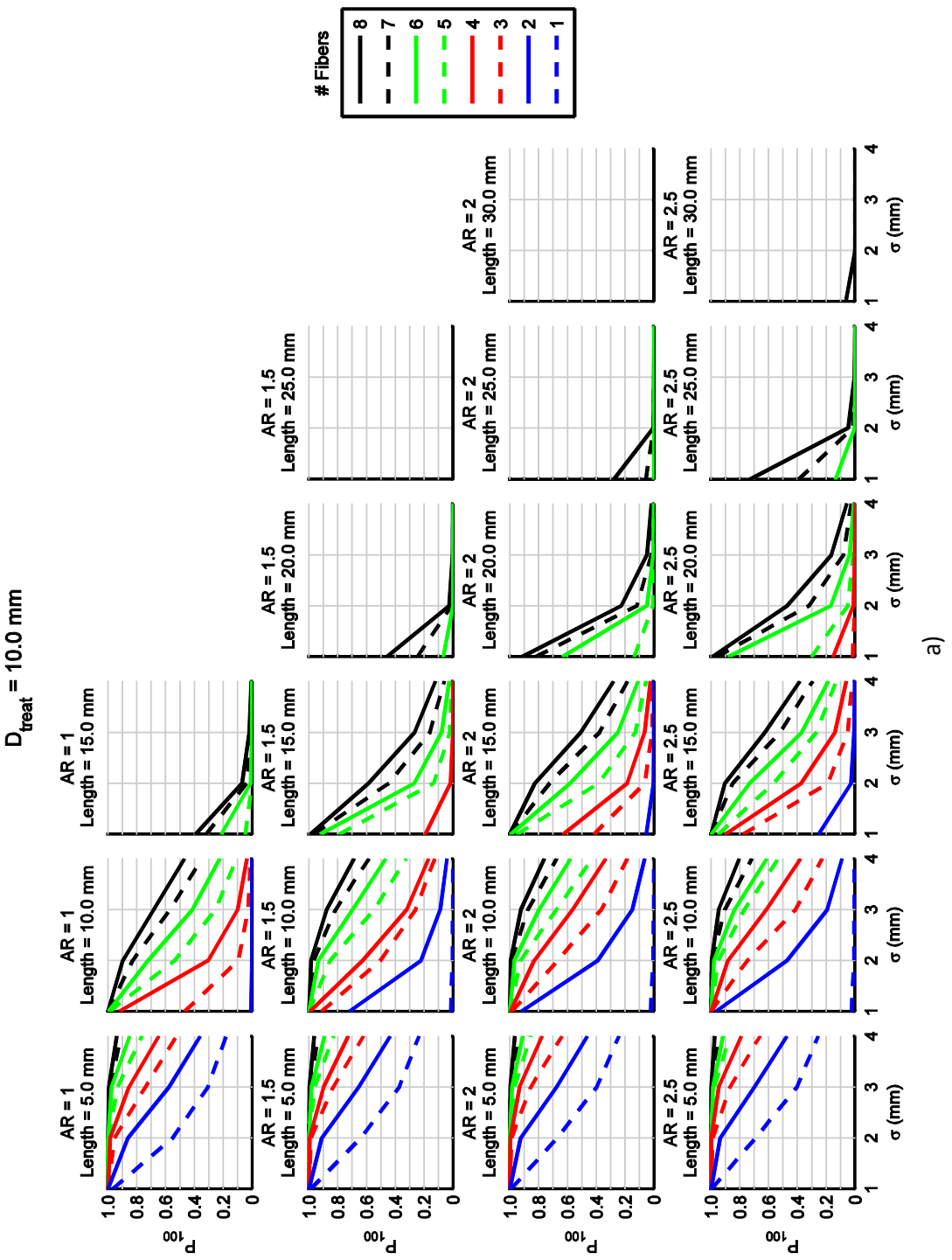

www.manaraa.com

www.manaraa.com

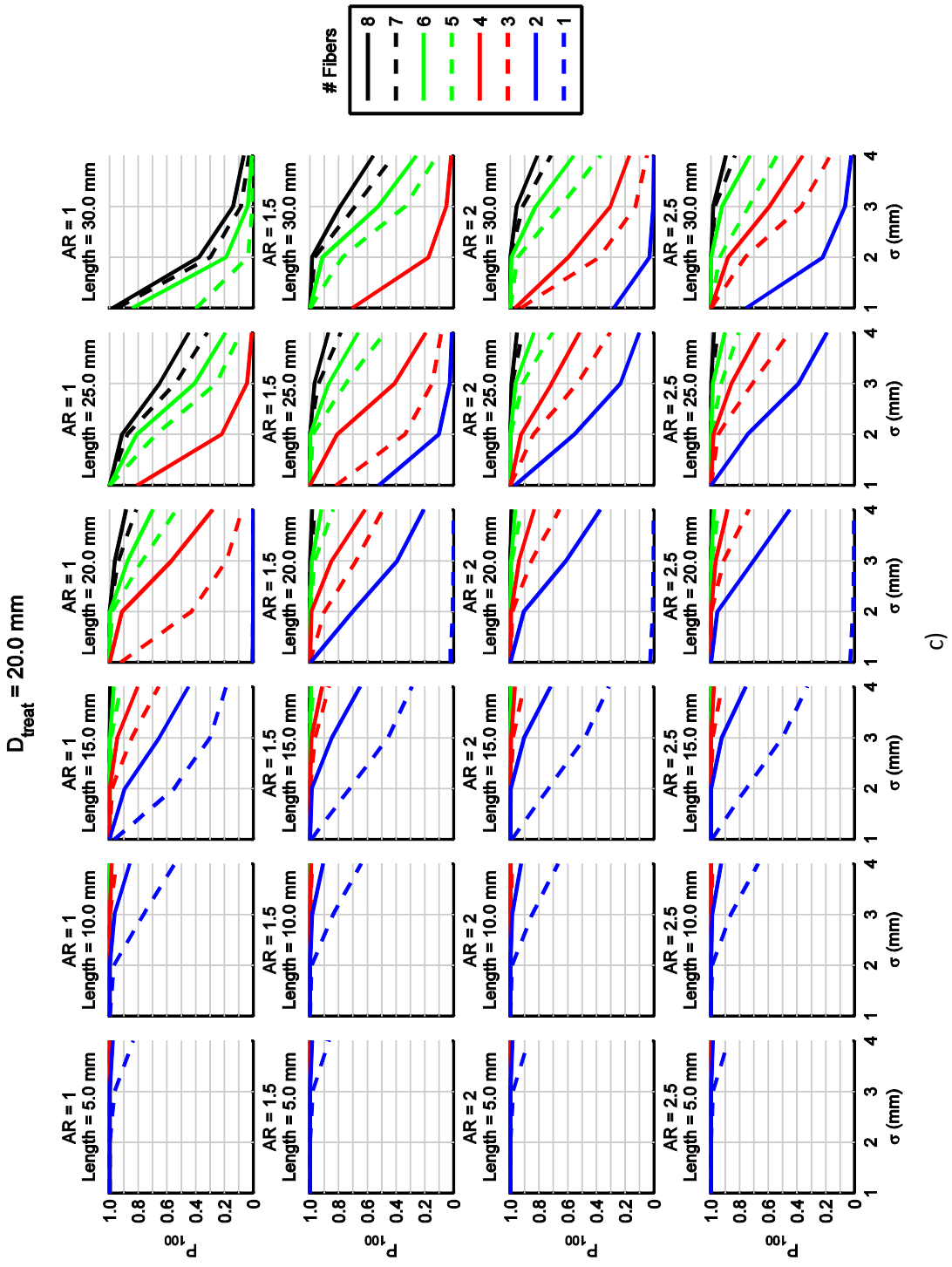

c)

www.manaraa.com

Figure 5.9: Probability of achieving complete focal target ablation (P_{100}) for a given target aspect ratio, target length, standard deviation of needle placement error and various diameters of ablation regions: a) 10 mm, b) 15 mm, c) 20 mm. For a given set of: minimum desired P_{100}, target size and shape, size of ablation achievable, and estimated level of needle placement uncertainty, this figure can be used to estimate the number of laser fibers that should be used for the treatment. Cases for which target coverage cannot be achieved using 8 fibers or less are omitted.

Figure 5.9 illustrates the sensitivity of P_{100} to the standard deviation of needle placement error under various conditions. When the target length is small relative to the ablation diameter, P_{100} is largely insensitive to σ. Specifically, if the ablation diameter is at least 5 mm larger than the target length, nearly all cases achieve $P_{100} \geq 0.9$ using 4 laser fibers or less if $\sigma \leq 3$ mm. However, as the target length approaches the ablation diameter, P_{100} decreases abruptly, and becomes considerably more sensitive to σ and the number of laser fibers used. The effect of increasing aspect ratio (*i.e.* a narrower target) is to increase P_{100}, but this effect is only appreciable for targets that are larger in length than the ablation diameter. The sensitivity of P_{100} to σ is also noted to be higher when a small number of fibers are used (*i.e.* < 4). This observation is intuitive, since an increase in the number of fibers increases treatment overlap between individual ablations, so that a portion of target tissue missed by one fiber is likely to be ablated by an adjacent one. As well, in the limits of treatability with 8 fibers or less (targets with large length), the limiting factor is the uncertainty in needle placement error. It appears that σ of 1 mm vs. 2 mm would allow the size of targets that one could confidently ablate to substantially increase.

While Figure 5.9 is useful for studying the trends in P_{100} as the various target and treatment parameters vary, it is difficult to interpolate between graphs for a particular case. A useful tool for determining eligibility for FLA is Table 5.3, which shows the maximum target length allowable to maintain $P_{100} \geq 0.9$.

www.manaraa.com

Table 5.3: Maximum allowable target length (in mm) to maintain a minimum probability of complete target ablation (P_{100}) of at least 90%.

# Laser Fibers		2	4	6	8	2	4	6	8	2	4	6	8
		Target Aspect Ratio = 1											
		D_{treat} = 10 mm				**D_{treat} = 15 mm**				**D_{treat} = 20 mm**			
	1	7	10	12	12	12	17	20	21	17	24	29	≥ 30
σ	**2**	< 5	6	8	9	9	12	15	17	14	20	23	25
(mm)	**3**	< 5	< 5	6	8	6	10	12	14	12	16	19	21
	4	< 5	< 5	< 5	6	< 5	7	10	13	8	13	17	19
		Target Aspect Ratio = 1.5											
		D_{treat} = 10 mm				**D_{treat} = 15 mm**				**D_{treat} = 20 mm**			
	1	8	11	15	17	15	20	26	29	22	28	≥ 30	≥ 30
σ	**2**	5	7	10	12	11	15	19	22	17	23	≥ 30	≥ 30
(mm)	**3**	< 5	< 5	7	9	7	11	15	18	13	18	24	27
	4	< 5	< 5	< 5	6	< 5	8	12	15	10	15	20	24
		Target Aspect Ratio = 2											
		D_{treat} = 10 mm				**D_{treat} = 15 mm**				**D_{treat} = 20 mm**			
	1	10	12	17	20	18	22	≥ 30	≥ 30	26	30	≥ 30	≥ 30
σ	**2**	5	9	11	13	12	16	22	26	20	25	≥ 30	≥ 30
(mm)	**3**	< 5	6	8	10	8	13	17	20	15	21	28	≥ 30
	4	< 5	< 5	5	7	< 5	10	14	17	10	18	23	27
		Target Aspect Ratio = 2.5											
		D_{treat} = 10 mm				**D_{treat} = 15 mm**				**D_{treat} = 20 mm**			
	1	11	17	19	23	20	25	≥ 30	≥ 30	28	≥ 30	≥ 30	≥ 30
σ	**2**	5	9	12	15	13	18	25	28	22	29	≥ 30	≥ 30
(mm)	**3**	< 5	6	8	11	8	14	18	22	15	23	≥ 30	≥ 30
	4	< 5	< 5	5	7	< 5	11	14	18	11	19	25	≥ 30

The maximum number of fibers used is assumed to be constrained by a limit on the total treatment time and allowable tissue damage due to needle insertions. Ablation diameter is based on the power of the laser used and laser application time, and other considerations such as proximity to critical structures. The level of needle placement uncertainty varies based on the system used to guide needles, the type of needles used, and the modality used for image guidance, among other factors.

In planning FLA for a particular clinical case, one would proceed as follows:

1. Estimate: the target's length (major axis) and aspect ratio (length/width) as seen from the needle's eye view, the diameter of ablation region achievable, and the level of uncertainty in needle placement.
2. Using Table 5.3, find the minimum required number of laser fibers.

www.manaraa.com

3. Using Table 5.1, find the corresponding pattern of laser fibers.

5.4 Discussion

We have developed a simplified method for estimating the fraction of focal target volume treated in prostate focal laser ablation when uncertainty in needle placement is expected. The method involves a 2D idealization of both focal target and ablation region shapes, and a Monte Carlo stochastic simulation of needle placement error to predict the probability of achieving complete target coverage. The result is a set of graphs and tables that can be easily referred to in the pre-treatment planning process for estimating the number of laser fibers required to completely ablate a given target. These results may also be used to determine a patient's eligibility for prostate FLA, since it may not be possible to achieve a high probability of full coverage with a reasonable number of laser fibers. The results also quantify the potential clinical benefit of systems that can place needles in the prostate with high precision in the context of prostate focal laser ablation.

While these results provide a simple method of estimating the level of planning required for prostate FLA, there are several important clinical details that must be considered when interpreting them. The simulations do not consider the fact that the treatment outcome can potentially be predicted as treatment progresses (*i.e.* by measuring the locations of needles already inserted using imaging and/or monitoring tissue temperature using MR thermometry),[7, 19, 20] and dynamically augmented by performing more ablations than planned. For this reason, the results are conservative, in that they attempt to predict the probability of treating the entire target in the absence of any dynamic plan augmentation (*i.e.*, dynamic re-planning). However, there are reasons why dynamic plan augmentation may not be reliably effective. Among them is the fact

www.manaraa.com

that image registration error may not be entirely detectable. In this case, while the needle placement error relative to the intra-treatment prostate image may be measurable, there will likely remain some uncertainty in the true location of the target volume that was delineated on pre-treatment imaging.[44, 45] Another reason is a desire to attain consistent and predictable treatment times, and levels of treatment-related side effects. A plan that is not optimized considering uncertainties in needle placement may result in several non-confluent regions of target tissue left untreated. In this situation, the number of additional needles required to fully treat the target may result in a substantial (unplanned) increase in procedure time and an unnecessary increase in damage to healthy tissue from excessive needle insertions. Another potential deviation from the assumptions made in this work is variation in ablation diameter between laser applications, which may depend on: variations in performance of the equipment used, inhomogeneity of tissue optical and thermal properties, and the amount of local perfusion.[26] To illustrate this effect, Figure 5.10 shows two post-treatment DCE MRI scans acquired immediately after FLA treatments in two separate patients. It should also be noted that the non-perfused volume seen on post-treatment DCE MR imaging may not exactly represent the true volume of definite tissue necrosis.[46, 47]

www.manaraa.com

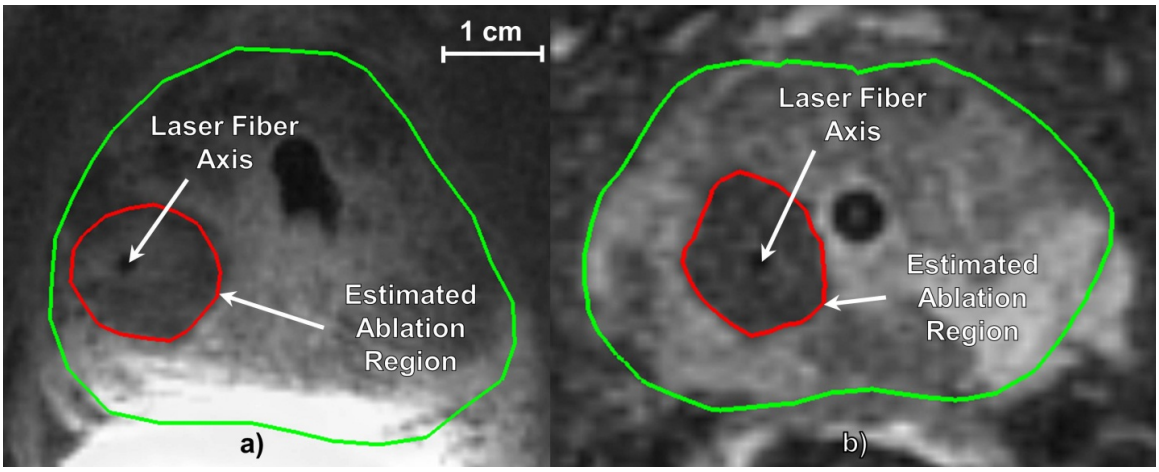

Figure 5.10: Immediate post-treatment axial dynamic contrast-enhanced MR images showing variation in ablation region symmetry: a) more tissue was ablated medial to the laser fiber than lateral, b) the region of ablated tissue was much more axisymmetric about the laser fiber axis.

Ideally, a map of tissue properties and perfusion rate would be used as inputs to a numerical simulation that could predict the volume of ablated tissue at each planned laser fiber location. The planned placement of each laser fiber could then be adjusted, and the damage volume recomputed until the plan was deemed optimal. Such an approach has been taken for planning rf ablation.[27] However, this approach requires knowledge of the level of perfusion and thermal properties of prostatic and surrounding tissue, and an accurate method of determining patient-specific maps of these properties is not currently available.[48] In addition, uncertainty in the values of these properties between the pre- and intra-treatment times is expected, and their effect on the probability of achieving a complete ablation could only be accounted for if statistical models of their uncertainty were available.[15, 49] In the absence of this information, this work aims to develop approximate guidelines for planning the number of laser fibers required for confidently ablating prostate focal targets, and corresponding target size limits to improve selection criteria for ongoing clinical trials.

www.manaraa.com

Another important consideration is the potential for damaging surrounding critical structures (*i.e.* rectal wall, urethra, neurovascular bundles, or urethral sphincters). Increasing the ablation diameter by increasing the laser power or ablation time will always improve the predicted fraction of target treated, but may increase the level of treatment-related morbidity. Such considerations must be made on a case-by-case basis, since the idealized target representation used in this work ignores the target location and orientation relative to the rest of the prostate gland. If the geometry of the critical structure in question was known relative to the target, the techniques used in this work could be applied to estimate the probability of damaging that structure (due to inaccurate needle placement). However, unless a biological heat transfer model was employed, this estimate is not expected to be accurate, since the thermal properties and rates of perfusion in the neurovascular bundles, and rectal and urethral mucosae are expected to differ from that of prostate tissue. In addition, the thermal dose required to damage such structures differs from that of prostate tissue. For these reasons, such results were not included.

Finally, the selection of the minimum desired value of P_{100} is contentious, and depends on the cost of performing a repeat treatment, among other factors. If re-treatment can be performed safely and quickly, then a lower P_{100} (higher rate of re-treatment) may be acceptable.

5.5 Conclusions

Focal laser ablation of prostate cancer is receiving increased attention, as it has shown potential for ablating focal target regions within the prostate with a low rate of treatment-related morbidity. However, the effects of needle placement error on focal target

www.manaraa.com

treatment coverage have been suspected to be substantial, and the literature indicates a general consensus regarding the need for planning methods for prostate FLA. In this work, we used a simplified model of the focal target and ablation region shapes, and Monte Carlo stochastic simulations to quantify the effect of needle placement error on the probability of achieving complete target ablation. It was found that the predicted probability of completely ablating a focal target is sensitive to needle placement uncertainty, especially when the target width is large relative to the ablation size. The results of this work will be useful in planning prostate FLA, and quantify the potential clinical benefit of advanced systems for accurate needle delivery, several of which are currently under development.[50-53]

www.manaraa.com

References

1. G. Bozzini, P. Colin, P. Nevoux, A. Villers, S. Mordon and N. Betrouni, "Focal therapy of prostate cancer: energies and procedures," Urol. Oncol.-Semin. Ori. **31**, 155-167 (2012).

2. U. Lindner, J. Trachtenberg and N. Lawrentschuk, "Focal therapy in prostate cancer: modalities, findings and future considerations," Nat. Rev. Urol. **7**, 562-571 (2010).

3. J. V. Hegde, R. V. Mulkern, L. P. Panych, F. M. Fennessy, A. Fedorov, S. E. Maier and C. Tempany, "Multiparametric MRI of prostate cancer: An update on state-of-the-art techniques and their performance in detecting and localizing prostate cancer," J. Magn. Reson. Imaging **37**, 1035-1054 (2013).

4. M. Moradi, S. E. Salcudean, S. D. Chang, E. C. Jones, N. Buchan, R. G. Casey, S. L. Goldenberg and P. Kozlowski, "Multiparametric MRI maps for detection and grading of dominant prostate tumors," J. Magn. Reson. Imaging **35**, 1403-1413 (2012).

5. U. Lindner, R. Weersink, M. Haider, M. Gertner, S. Davidson, M. Atri, B. Wilson, A. Fenster and J. Trachtenberg, "Image guided photothermal focal therapy for localized prostate cancer: phase I trial," J. Urol. **182**, 1371-1377 (2009).

6. A. Oto, I. Sethi, G. Karczmar, R. McNichols, M. K. Ivancevic, W. M. Stadler, S. Watson and S. Eggener, "MR Imaging–guided Focal Laser Ablation for Prostate Cancer: Phase I Trial," Radiology **267**, 932-940 (2013).

7. O. Raz, M. A. Haider, S. R. H. Davidson, U. Lindner, E. Hlasny, R. Weersink, M. R. Gertner, W. Kucharcyzk, S. A. McCluskey and J. Trachtenberg, "Real-time magnetic resonance imaging-guided focal laser therapy in patients with low-risk prostate cancer," Eur. Urol. **58**, 173-177 (2010).

8. U. Lindner, N. Lawrentschuk and J. Trachtenberg, "Focal laser ablation for localized prostate cancer," J. Endourol. **24**, 791-797 (2010).

9. U. Lindner, S. R. Davidson, N. E. Fleshner, A. Finelli, A. R. Zlotta, M. A. Jewett, T. H. Van der Kwast, M. R. Gertner, E. Hlasny and S. A. McCluskey, "Initial Results of MR Guided Laser Focal Therapy for Prostate Cancer," J. Urol. **189**, e227-e228 (2013).

10. U. Lindner, N. Lawrentschuk, R. A. Weersink, S. R. H. Davidson, O. Raz, E. Hlasny, D. L. Langer, M. R. Gertner, T. Van der Kwast and M. A. Haider, "Focal laser ablation for prostate cancer followed by radical prostatectomy: validation of focal therapy and imaging accuracy," Eur. Urol. **57**, 1111-1114 (2010).

www.manaraa.com

11. J. Cepek, B. Chronik, U. Lindner, J. Trachtenberg, S. Davidson, J. Bax and A. Fenster, "A system for MRI-guided transperineal delivery of needles to the prostate for focal therapy," Med. Phys. **40**, 012304 (2013).

12. H. U. Ahmed, C. Moore, E. Lecornet and M. Emberton, "Focal therapy in prostate cancer: determinants of success and failure," J. Endourol. **24**, 819-825 (2010).

13. Z. Amin, W. Lees and S. Bown, "Interstitial laser photocoagulation for the treatment of prostatic cancer," Br. J. Radiol. **66**, 1044-1047 (1993).

14. D. Fuentes, F. Yusheng, A. Elliott, A. Shetty, R. J. McNichols, J. T. Oden and R. J. Stafford, "Adaptive Real-Time Bioheat Transfer Models for Computer-Driven MR-Guided Laser Induced Thermal Therapy," IEEE Trans. Biomed. Eng. **57**, 1024-1030 (2010).

15. G. D. Dodd, M. S. Frank, M. Aribandi, S. Chopra and K. N. Chintapalli, "Radiofrequency thermal ablation computer analysis of the size of the thermal injury created by overlapping ablations," Am. J. Roentgenol. **177**, 777-782 (2001).

16. R. Taschereau, J. Roy and J. Pouliot, "Monte Carlo simulations of prostate implants to improve dosimetry and compare planning methods," Med. Phys. **26**, 1952-1959 (1999).

17. S. Nath, Z. Chen, N. Yue, S. Trumpore and R. Peschel, "Dosimetric effects of needle divergence in prostate seed implant using ^{125}I and ^{103}Pd radioactive seeds," Med. Phys. **27**, 1058-1066 (2000).

18. M. Bues, E. J. Holupka, P. Meskell and I. D. Kaplan, "Effect of random seed placement error in permanent transperineal prostate seed implant," Radiother. Oncol. **79**, 70-74 (2006).

19. H. Zhang, F. Banovac, S. Munuo, E. Campos-Nanez, H. Abeledo and K. Cleary, Proc. SPIE 6509, Medical Imaging: Visualization and Image-Guided Procedures, 2007.

20. B. J. Wood, J. K. Locklin, A. Viswanathan, J. Kruecker, D. Haemmerich, J. Cebral, A. Sofer, R. Cheng, E. McCreedy and K. Cleary, "Technologies for guidance of radiofrequency ablation in the multimodality interventional suite of the future," J. Vasc. Interv. Radiol. **18**, 9-24 (2007).

21. F. Banovac, P. Cheng, E. Campos-Nanez, B. Kallakury, T. Popa, E. Wilson, H. Abeledo and K. Cleary, "Radiofrequency ablation of lung tumors in swine assisted by a navigation device with preprocedural volumetric planning," J. Vasc. Interv. Radiol. **21**, 122-129 (2010).

www.manaraa.com

22. P. J. Littrup, A. Ahmed, H. D. Aoun, D. L. Noujaim, T. Harb, S. Nakat, K. Abdallah, B. A. Adam, R. Venkatramanamoorthy and W. Sakr, "CT-guided percutaneous cryotherapy of renal masses," J. Vasc. Interv. Radiol. **18**, 383-392 (2007).

23. F. Oshima, K. Yamakado, A. Nakatsuka, H. Takaki, M. Makita and K. Takeda, "Simultaneous microwave ablation using multiple antennas in explanted bovine livers: relationship between ablative zone and antenna," Radiat. Med. **26**, 408-414 (2008).

24. H. Wang, P. J. Littrup, Y. Duan, Y. Zhang, H. Feng and Z. Nie, "Thoracic Masses Treated with Percutaneous Cryotherapy: Initial Experience with More than 200 Procedures," Radiology **235**, 289-298 (2005).

25. S. Permpongkosol, T. L. Nicol, H. Khurana, R. E. Link, Q. J. Zhai, L. R. Kavoussi and S. B. Solomon, "Thermal maps around two adjacent cryoprobes creating overlapping ablations in porcine liver, lung, and kidney," J. Vasc. Interv. Radiol. **18**, 283-287 (2007).

26. S. Thomsen and J. A. Pearce, "Thermal damage and rate processes in biologic tissues," in *Optical-Thermal Response of Laser-Irradiated Tissue,* edited by A. J. Welch and M. J. Van Gemert (Springer, New York, 2011), pp. 487-549.

27. C.-C. Chen, M. I. Miga and R. L. Galloway, "Optimizing electrode placement using finite-element models in radiofrequency ablation treatment planning," IEEE Trans. Biomed. Eng. **56**, 237-245 (2009).

28. P. Colin, P. Nevoux, M. Marqa, F. Auger, X. Leroy, A. Villers, P. Puech, S. Mordon and N. Betrouni, "Focal laser interstitial thermotherapy (LITT) at 980 nm for prostate cancer: treatment feasibility in Dunning R3327-AT2 rat prostate tumour," BJU Int. **109**, 452-458 (2012).

29. M.-F. Marqa, P. Colin, P. Nevoux, S. R. Mordon and N. Betrouni, "Focal laser ablation of prostate cancer: numerical simulation of temperature and damage distribution," Biomed. Eng. Online **10** (2011).

30. T. J. Vogl, R. Straub, K. Eichler, D. Woitaschek and M. G. Mack, "Malignant Liver Tumors Treated with MR Imaging–guided Laser-induced Thermotherapy: Experience with Complications in 899 Patients (2,520 lesions)," Radiology **225**, 367-377 (2002).

31. A. Papoulis and S. U. Pillai, *Probability, random variables and stochastic processes, 3rd ed.* (McGraw-Hill, New York, 2002).

32. R. Alterovitz, M. Branicky and K. Goldberg, "Motion planning under uncertainty for image-guided medical needle steering," Int. J. Rob. Res. **27**, 1361-1374 (2008).

www.manaraa.com

33. R. Alterovitz, T. Siméon and K. Goldberg, Proc. Robotics: Science and Systems, Atlanta, Georgia, 2007.

34. N. J. Cowan, K. Goldberg, G. S. Chirikjian, G. Fichtinger, R. Alterovitz, K. B. Reed, V. Kallem, W. Park, S. Misra and A. M. Okamura, "Robotic needle steering: Design, modeling, planning, and image guidance," in *Surgical Robotics: Systems Applications and Visions,* edited by J. Rosen, B. Hannaford and R. M. Satava (Springer, New York, 2011), pp. 557-582.

35. L. Beaulieu, L. Archambault, S. Aubin, E. Oral, R. Taschereau and J. Pouliot, "The robustness of dose distributions to displacement and migration of ^{125}I permanent seed implants over a wide range of seed number, activity, and designs," Int. J. Radiat. Oncol. Biol. Phys. **58**, 1298-1308 (2004).

36. M. E. Chen, P. Troncoso, D. A. Johnston, K. Tang and J. R. Babaian, "Optimization of prostate biopsy strategy using computer based analysis," J. Urol. **158**, 2168-2175 (1997).

37. G. Wan, Z. Wei, L. Gardi, D. B. Downey and A. Fenster, "Brachytherapy needle deflection evaluation and correction," Med. Phys. **32**, 902-909 (2005).

38. P. Blumenfeld, N. Hata, S. DiMaio, K. Zou, S. Haker, G. Fichtinger and C. Tempany, "Transperineal prostate biopsy under magnetic resonance image guidance: a needle placement accuracy study," J. Magn. Reson. Imaging **26**, 688-694 (2007).

39. G. Wan, Z. Wei, L. Gardi, D. B. Downey and A. Fenster, "Brachytherapy needle deflection evaluation and correction," Med. Phys. **32**, 902 (2005).

40. P. L. Roberson, V. Narayana, D. L. McShan, R. J. Winfield and P. W. McLaughlin, "Source placement error for permanent implant of the prostate," Med. Phys. **24**, 251-257 (1997).

41. R. C. Susil, K. Camphausen, P. Choyke, E. R. McVeigh, G. S. Gustafson, H. Ning, R. W. Miller, E. Atalar, C. N. Coleman and C. Ménard, "System for prostate brachytherapy and biopsy in a standard 1.5 T MRI scanner," Magn. Reson. Med. **52**, 683-687 (2004).

42. A. J. Hayter, *Probability and statistics for engineers and scientists, 4th ed.* (Brooks/Cole, Boston, 2012).

43. M. Atri, M. R. Gertner, M. A. Haider, R. A. Weersink and J. Trachtenberg, "Contrast-enhanced ultrasonography for real-time monitoring of interstitial laser thermal therapy in the focal treatment of prostate cancer," Can. Urol. Assoc. J. **3**, 125-130 (2009).

www.manaraa.com

44. N. Makni, P. Puech, P. Colin, A. Azzouzi, S. Mordon and N. Betrouni, "Elastic image registration for guiding focal laser ablation of prostate cancer: Preliminary results," Comput. Methods Programs Biomed. **108**, 213-223 (2012).

45. U. Lindner, N. Lawrentschuk and J. Trachtenberg, "Image guidance for focal therapy of prostate cancer," World J. Urol. **28**, 727-734 (2010).

46. H. L. M. Cheng, M. A. Haider, M. J. Dill-Macky, J. M. Sweet, J. Trachtenberg and M. R. Gertner, "MRI and contrast-enhanced ultrasound monitoring of prostate microwave focal thermal therapy: An in vivo canine study," J. Magn. Reson. Imaging **28**, 136-143 (2008).

47. A. Boyes, K. Tang, M. Yaffe, L. Sugar, R. Chopra and M. Bronskill, "Prostate tissue analysis immediately following magnetic resonance imaging guided transurethral ultrasound thermal therapy," J. Urol. **178**, 1080-1085 (2007).

48. D. Fuentes, R. Cardan, R. J. Stafford, J. Yung, G. D. Dodd III and Y. Feng, "High-fidelity computer models for prospective treatment planning of radiofrequency ablation with in vitro experimental correlation," J. Vasc. Interv. Radiol. **21**, 1725-1732 (2010).

49. R. S. Montgomery, A. Rahal, G. D. Dodd III, J. R. Leyendecker and L. G. Hubbard, "Radiofrequency ablation of hepatic tumors: variability of lesion size using a single ablation device," Am. J. Roentgenol. **182**, 657-661 (2004).

50. G. S. Fischer, I. Iordachita, C. Csoma, J. Tokuda, S. P. DiMaio, C. M. Tempany, N. Hata and G. Fichtinger, "MRI-compatible pneumatic robot for transperineal prostate needle placement," IEEE Trans. Mech. **13**, 295-305 (2008).

51. A. Krieger, I. Iordachita, S. E. Song, N. B. Cho, P. Guion, G. Fichtinger and L. L. Whitcomb, Proc. IEEE International Conference on Robotics and Automation, Anchorage, Alaska, 2010.

52. S. E. Song, N. Hata, I. Iordachita, G. Fichtinger, C. Tempany and J. Tokuda, "A workspace-orientated needle-guiding robot for 3T MRI-guided transperineal prostate intervention: evaluation of in-bore workspace and MRI compatibility," Int. J. Med. Robotics Comput. Assist. Surg. **9**, 67-74 (2012).

53. M. Muntener, A. Patriciu, D. Petrisor, D. Mazilu, H. Bagga, L. Kavoussi, K. Cleary and D. Stoianovici, "Magnetic resonance imaging compatible robotic system for fully automated brachytherapy seed placement," Urology **68**, 1313-1317 (2006).

www.manaraa.com

Chapter 6.

Conclusions and Suggestions for Future Work

6.1 Conclusions

The work in this thesis represents several steps towards achieving the goal of enabling complete ablation of prostate focal targets with high confidence using MRI-guided focal laser ablation therapy. This work was divided into four logical chapters, each summarized as follows.

In Chapter 2, the effects of MR image distortion on the accuracy of tracking interventional devices was studied and quantified. Results from the work described in Chapter 2 guided the development of the MRI-compatible needle-guidance system described in Chapter 3, ensuring that the accuracy of the system was independent of the level of magnetic field distortion encountered in the interventional MRI environment.

The system described in Chapter 3 represents the foundation of the rest of the work in this thesis, and consists of an MRI-compatible mechatronic needle guidance device, MRI-compatible trajectory alignment interface, and software for integration of the device with the MRI scanner. The system was rigorously tested for its MRI safety and compatibility, open-air targeting accuracy, intra-MRI targeting accuracy, and potential needle guidance accuracy and repeatability. It was found that the system caused minimal distortion and reduction in SNR in MR images, and had the potential to deliver needles with sufficient accuracy for prostate FLA therapy. The system was also classified as a

www.manaraa.com

Class I medical device under Health Canada regulations, the application for which can be found in Appendix C. The unique approach taken to guiding needles in the bore of an MRI scanner was incorporated into a patent that has been filed in the United States, and is included in Appendix D.

Once safety, MRI-compatibility, and accuracy were proven, the system was used to guide needles to patient's prostates in a Phase I/II clinical trial. Results from the patient trials were presented in Chapter 4, and include a comparison of the time required to deliver needles to targets in the prostate using the previously-employed fixed grid template approach, the needle guidance accuracy achieved *in vivo*, and qualitative experience in using the system for the MRI-guided procedure. The time taken to deliver each needle using this system was found to be statistically significantly shorter than that of the grid template approach (median 8 vs. 18 minutes), and needles were delivered within 5 mm of their target in 72% of attempts. Following this case series, methods of improving the probability of completely ablating focal prostate targets were sought, leading to the work presented in Chapter 5.

In Chapter 5, the effects of needle placement uncertainty on the probability of achieving complete focal target ablation were quantified. This work has resulted in a modification of the selection criteria for patients entering the clinical trial, limiting the maximum target size to ~15 mm, and has quantified the clinical benefit that may be obtained by employing more accurate methods of needle guidance. Results in this chapter may also aid in planning cases of prostate FLA therapy for which the target size, maximum number of laser fibers to be used, size of ablation region created by each laser fiber, and uncertainty in needle placement error are known.

www.manaraa.com

6.2 Suggestions for Future Work

The techniques developed and the knowledge gained throughout this thesis have led to the identification of several areas of future work that could substantially further improve the technique of MRI-guided FLA therapy. Such improvements have the potential to impact the management of men diagnosed with localized prostate cancer, and will be described in the following sections.

6.2.1 Procedure Time

A major problem with the current technique of MRI-guided FLA therapy is the overall procedure time, which can last from ~ 3 - 6 hours, and is highly variable. In an attempt to identify which components of the procedure contribute most, the time required to complete various steps of the procedure was recorded over seven cases of MRI-guided FLA therapy. The data are summarized in Figure 6.1.

www.manaraa.com

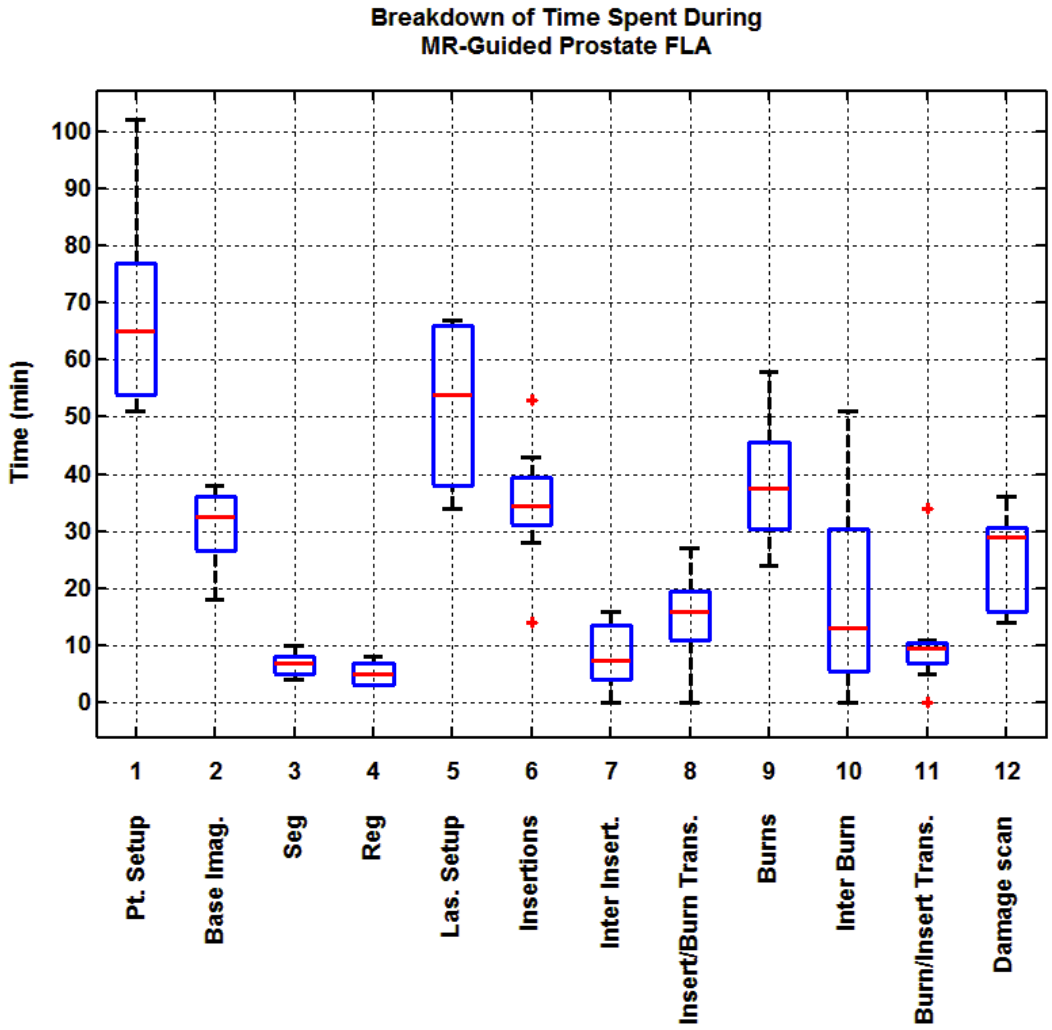

Figure 6.1: Time taken to complete various components of the MRI-guided prostate FLA procedure, as recorded over seven cases. Red line = median, blue box = IQR, black T's = extrema, red crosses = outliers.

As seen in Figure 6.1**,** patient setup time is currently the largest contributor to procedure time. While patient setup time is affected by the design of the needle guidance device and its integration into the clinical workflow, it is currently dominated by the time required to administer general anesthetic, insert an ER coil and confirm its position is acceptable on imaging, and preparation of a sterile field. The effect of device setup on patient setup time is limited, since the device is registered to the MRI coordinate system prior to patient arrival.

www.manaraa.com

Baseline imaging includes acquisition of T2-weighted and DW images, and prostate segmentation and registration. The image acquisition time is relatively fixed; however, implementation of automated segmentation method could reduce procedure time. In addition, the current method of pre- to intra-treatment prostate registration requires a substantial amount of user interaction. Implementation of a reliable automated registration method could not only reduce procedure time, but would also increase the accuracy of the procedure, since appreciable changes in prostate shape may occur between pre- and intra-treatment imaging sessions, resulting in errors in localization of the target region in intra-treatment image space.

Laser setup time is not dependent on the techniques relevant to the work described in this thesis, and will not be discussed.

Major improvements in procedure time could be attained by modifying the workflow of needle insertions and laser power applications. Currently, laser applications are performed in multiple "sessions", with each session consisting of two needle insertions followed by the concurrent application of two lasers. Each procedure consists of ~ 2 - 3 laser application sessions, resulting in a mean laser application time (AKA "burn time" in Figure 6.1) of 36 ± 9 minutes per procedure. Therefore, by performing all laser applications simultaneously, the burn time could be reduced by a factor of 2 - 3 x. In addition, the time required to transition from applying laser power to performing the next set of insertions consumes 11 ± 11 minutes, and the time transitioning from an insertion to a burn consumes 15 ± 9 minutes. Both of these components could potentially be eliminated if all burns were performed in one concurrent session. Implementation of this strategy is currently limited by the number of laser channels available, and the lack of a

www.manaraa.com

treatment planning method that is compatible with this approach. In addition, the time to guide each needle to its target is also substantial, totaling 35 ± 12 minutes per procedure. Potential improvements in treatment planning and needle guidance will be discussed in the following sections.

6.2.2 Improved Treatment Planning

In Chapter 5, there were several simplifications made in the modeling of focal target and ablation volume shapes that may render the method unreliable in some cases. Relaxation of some of these assumptions requires more complex modeling. In addition, each treatment plan should be optimized to ensure an ideal balance between treatment coverage and damage to healthy tissue is achieved. These proposed improvements are described as follows.

I. *Finite-element modeling of thermal dose delivery.* Heterogeneous rates of perfusion within the prostate and surrounding tissue may result in unexpected variations in the spatiotemporal distribution of temperature over the course of FLA therapy delivery. The treatment planning process should therefore include consideration of perfusion effects, preferably by performing 3D finite-element simulations of temperature and predicted tissue damage using patient-specific models of anatomy and maps of perfusion. Such simulations are especially important when treating tumours at the posterior boundary of the prostate, where the cooling effect of the Denonvillier's space and rectal wall are purported to be substantial, thereby presenting the potential for leaving untreated cancerous tissue at the posterior prostate boundary.[1] Such an approach would also quantify the effect of performing multiple ablations simultaneously, whereas the current

www.manaraa.com

method assumes that each ablated region is independent. Challenges in realizing this solution include obtaining accurate quantitative perfusion maps of the prostate and accurately modeling the distribution of laser light and its absorption in tissue.

II. *Treatment plan optimization.* Given the potential for interference between needle trajectories and anatomical structures such as the urethra and pubic arch, as well as the inherent trade-off between the improvement in the probability of treating a focal target (*e.g.* by increasing the size of the planned treatment volume) and that of damaging surrounding healthy tissues, each FLA treatment plan should be optimized. The optimal treatment plan depends on the required probability of completely ablating the focal target, the size and shape of the target relative to the prostate and surrounding anatomy, the level of uncertainty in the localization of target contours on pre-treatment imaging, and the threshold of thermal dose tolerable by healthy surrounding tissues. Such an approach, employed in the pre-treatment phase, would ensure that patients who were predicted to not receive a net benefit from this type of therapy would be diverted to the appropriate alternate management pathway, and those who would benefit would do so with an expected (minimal) level of treatment-related side effects, and a high expected probability of having their focal lesion completely ablated.

6.2.3 Real-Time Control of Needle Trajectories

Compensation of uncertainty in needle placement by increasing the planned ablation volume is not ideal, as this will increase the volume of healthy tissue that is ablated. This issue is particularly concerning in the prostate, for which the sensitive structures and

www.manaraa.com

surrounding organs are in very close proximity. In addition, the size of focal prostate lesions treatable using MRI-guided FLA therapy is currently limited by the uncertainty in needle placement. For these reasons, it is hypothesized that an optimal FLA delivery system should incorporate real-time tracking and control of needle trajectories, and prostate motion tracking and compensation. Doing so will ensure complete ablation of focal targets in a higher proportion of patients, and will allow patients with larger tumours, who may otherwise be good candidates for prostate focal therapy, to be treated using this technique. Potential techniques for achieving these improvements in the future are outlined as follows.

I. *Needle steering.* Much work has been reported on the topic of steering needles in soft tissue, including methods for steering beveled and symmetric needles, and optimization of planning steerable needle paths to avoid obstacles.[2, 3] Novel steerable needle devices have also seen recent development, and are promising in terms of providing the necessary control of the needle trajectory during insertion.[4]

II. *Real-time needle tracking.* While the intra-treatment use of MRI has several advantages in terms of soft tissue contrast and functional imaging capabilities, there are issues in using MRI to track needles in real-time. Due to the small required needle diameter for prostate interventions, non-magnetic metals are still often the material of choice for needles. MR imaging of such needles results in a signal void of generally low contrast relative to surrounding tissue, often with an associated susceptibility artifact that reduces the precision to which needles can be localized. Alternative methods of tracking needle trajectories in real-time

www.manaraa.com

should therefore be employed. While the instrumentation of needles for real-time tracking presents many engineering challenges, new methods, employing the use of fiber Bragg grating strain sensors, have been demonstrated to perform well in the MRI environment.[5, 6] Such methods, combined with a needle guidance device that can provide an accurate reference trajectory, could substantially reduce the uncertainty in final needle placement error, and therefore allow more patients to be confidently treated with FLA therapy.

III. *Prostate motion compensation.* The current method of guiding needles to the prostate assumes that prostate motion during needle insertion is minimal. However, this effect may be appreciable and therefore real-time MR imaging should be employed to compensate for any prostate motion throughout the procedure. Such an issue has been previously identified when performing fusion TRUS-guided prostate biopsy and a method has been developed in our lab for performing 2D-3D registration between a real-time 2D image and a baseline 3D image to compensate this effect.[7, 8] A similar approach could provide a solution to reducing errors in needle placement in MRI-guided FLA, especially if needle steering was employed.

www.manaraa.com

References

1. H. Beisland and E. Stranden, "Rectal temperature monitoring during neodymion-YAG laser irradiation for prostatic carcinoma," Urol. Res. **12**, 257-259 (1984).

2. S. P. DiMaio and S. Salcudean, "Needle steering and model-based trajectory planning," in *Med. Image Comput. Comput. Assist. Interv.,* edited by R. Ellis and T. Peters (Springer, 2003), pp. 33-40.

3. N. J. Cowan, K. Goldberg, G. S. Chirikjian, G. Fichtinger, R. Alterovitz, K. B. Reed, V. Kallem, W. Park, S. Misra and A. M. Okamura, "Robotic needle steering: Design, modeling, planning, and image guidance," in *Surgical Robotics,* (Springer, 2011), pp. 557-582.

4. S. Okazawa, R. Ebrahimi, J. Chuang, S. E. Salcudean and R. Rohling, "Hand-held steerable needle device," IEEE Trans. Mech. **10**, 285-296 (2005).

5. Y.-L. Park, S. Elayaperumal, B. Daniel, S. C. Ryu, M. Shin, J. Savall, R. J. Black, B. Moslehi and M. R. Cutkosky, "Real-time estimation of 3-D needle shape and deflection for MRI-guided interventions," IEEE Trans. Mech. **15**, 906-915 (2010).

6. M. Abayazid, M. Kemp and S. Misra, "3D flexible needle steering in soft-tissue phantoms using Fiber Bragg Grating sensors," IEEE Int. Conf. Rob. Autom., 5843-5849 (2013).

7. T. De Silva, D. W. Cool, J. Yuan, C. Romognoli, A. Fenster and A. D. Ward, "Improving 2D-3D Registration Optimization Using Learned Prostate Motion Data," in *Med. Image Comput. Comput. Assist. Interv.,* edited by K. Mori, I. Sakuma, Y. Sato, C. Barillot and N. Navab (Springer, 2013), pp. 124-131.

8. T. De Silva, A. Fenster, J. Bax, L. Gardi, C. Romagnoli, J. Samarabandu and A. D. Ward, "2D-3D rigid registration to compensate for prostate motion during 3D TRUS-guided biopsy," Proc. SPIE Med. Imag., 83160O-83160O-83166 (2012).

www.manaraa.com

Appendix A. 2D Gradient Echo Imaging of Ellipsoids

A.1 Cylinder

A cylinder with its axis at an angle α to a static, uniform magnetic field, will experience a uniform internal magnetic field shift equal to

$$\Delta B_{z_{cyl}} = \frac{\Delta\chi}{6}\left(3\cos^2\alpha - 1\right)B_0 + \frac{1}{3}\chi_e B_0, \tag{A.1}$$

where $\Delta B_{z_{cyl}} = B_{i_{cyl}} - B_0$ is the difference between the field inside the cylinder and the static field, and $\Delta\chi = \chi_i - \chi_e$ is the difference in magnetic susceptibility between the material inside the cylinder and that outside. Equation (A.1) quantifies the Lorentz-corrected magnetic field shift; the field experienced by protons in MR, and is valid for $|\chi_i| \ll 1$.

For a cylinder with its axis described by the parametric equation

$$\mathbf{l} = \mathbf{s} + \mathbf{v}t, \tag{A.2}$$

the angle α that it makes with the z-component of the static magnetic field is given by

$$\alpha = \cos^{-1}\left(\frac{v_z}{|\mathbf{v}|}\right). \tag{A.3}$$

Given a desired slice location $\mathbf{r_{ss}}$, the rf excitation pulse will excite spins with a magnetic field equal to

$$B_{ss} = \frac{\omega_c}{\gamma} + \mathbf{g_{ss}} \cdot \mathbf{r_{ss}}, \tag{A.4}$$

www.manaraa.com

where ω_c is the center frequency, and $\mathbf{g}_{ss}$ is the slice-select gradient for a slice of arbitrary orientation. During the rf excitation pulse, the slice-select gradient is on, and the magnetic field within the cylinder is

$$B_z = B_0 + \Delta B_{z_{cyl}} + \Delta B_d + \mathbf{g}_{ss} \cdot \mathbf{r}\,, \tag{A.5}$$

where $\Delta B_d(x, y, z)$ is the local distortion in the magnetic field, and is approximated as the sum of uniform and gradient distortion components:

$$\Delta B_d = B_{d_0} + G_x' x + G_y' y + G_z' z\,, \tag{A.6}$$

where B_{d_0} is the uniform component of the static magnetic field distortion and G_x', G_y', and G_z' are components of a static magnetic field distortion gradient in the x, y and z directions, respectively. Equation (A.6) models bulk magnetic field distortions experienced by the entire frame, as well as spatial variation in the distortion across the frame. The purpose of this simplified model is to permit the effects of static field distortion to be studied systematically, and it is expected to yield an estimate of the order of magnitude of localization error. Figure A.1 illustrates this concept. This model also allows the theoretical analysis to be validated by imaging each frame in an MR scanner, since the uniform and gradient components can be simulated by manually applying center frequency and gradient shim offsets.

www.manaraa.com

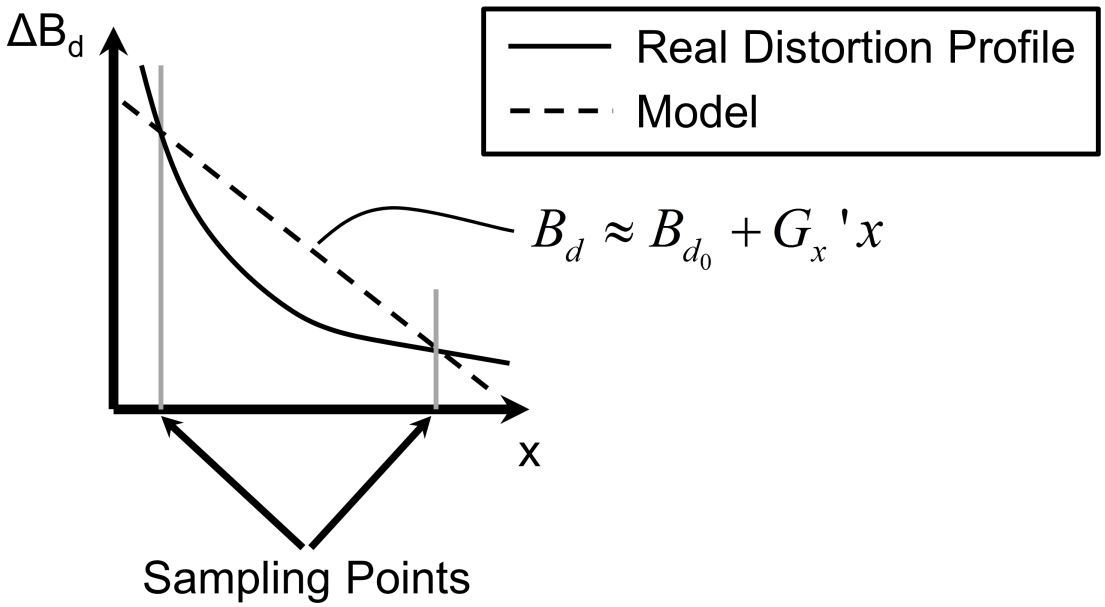

Figure A.1: Illustration of the simplified model of a magnetic field distortion profile in one dimension. If the frame is only imaged (i.e. sampled) at discrete points, then the effect of the distortion profile on localization accuracy may be reasonably captured using a linear model.

For simplicity, it is now assumed that slices are oriented axially (in the x-y plane). Equating (A.4) with (A.5) gives the location z_s at which spins in the selected slice will be excited

$$z_s = \frac{z_{ss} - \frac{1}{g_{ss}}\left(B_0 + \Delta B_{z_{cyl}} + B_{d_0} + s_x G_x' + s_y G_y' - \frac{\omega_c}{\gamma}\right)}{1 + \frac{1}{g_{ss}}\left(v_x G_x' + v_y G_y' + G_z'\right)}, \tag{A.7}$$

where z_{ss} is the desired axial slice location along the z-axis. Deviation of z_s from z_{ss} quantifies the out-of-plane image distortion.

Using (A.2), the x and y positions at which the spins in the cylinder are excited are

$$x_s = s_x + \frac{v_x}{v_z}\left(z_s - s_z\right), \text{ and} \tag{A.8}$$

$$y_s = s_y + \frac{v_y}{v_z}\left(z_s - s_z\right). \tag{A.9}$$

www.manaraa.com

These spins will be encoded in the MR image at the location

$$x_{cyl_{im}} = \begin{cases} x_s + \dfrac{1}{g_{fe}}\left(B_0 - \dfrac{\omega_c}{\gamma} + \Delta B_{z_{cyl}} + \Delta B_d \right) & \text{, frequency encoding in } x \\ x_s & \text{, frequency encoding in } y \end{cases}, \quad \text{(A.10)}$$

$$y_{cyl_{im}} = \begin{cases} y_s & \text{, frequency encoding in } x \\ y_s + \dfrac{1}{g_{fe}}\left(B_0 - \dfrac{\omega_c}{\gamma} + \Delta B_{z_{cyl}} + \Delta B_d \right) & \text{, frequency encoding in } y \end{cases}, \quad \text{(A.11)}$$

$$z_{i_{cyl}} = z_{ss}, \quad \text{(A.12)}$$

where g_{fe} is the gradient strength in the frequency-encoded direction. Note the additional term $\dfrac{1}{g_{fe}}\left(B_0 - \dfrac{\omega_c}{\gamma} \right)$ that represents a shift in the entire field-of-view due to center frequency tuning.

A.2 Sphere

As in the case of a cylinder, a sphere will experience a uniform internal magnetic field shift, in this case equal to

$$\Delta B_{z_{sph}} = \frac{1}{3}\chi_e B_0, \quad \text{(A.13)}$$

the magnitude of which is only dependent on the magnetic susceptibility of the surrounding fluid, assuming $|\chi_i| \ll 1$. It is assumed that slice-select error is small compared to the sphere's radius; ensuring that some spins within the sphere will be excited, and a circle will appear in the image. This circle will appear in an axial image at the location

www.manaraa.com

$$x_{sph_{im}} = \begin{cases} x_{sph_{MR}} + \dfrac{1}{g_{fe}}\left(B_0 - \dfrac{\omega_c}{\gamma} + \Delta B_{d_{sph}} + \Delta B_d \right) & \text{, frequency encoding in } x \\ x_{sph_{MR}} & \text{, frequency encoding in } y \end{cases}, \quad \text{(A.14)}$$

$$y_{sph_{im}} = \begin{cases} y_{sph_{MR}} & \text{, frequency encoding in } x \\ y_{sph_{MR}} + \dfrac{1}{g_{fe}}\left(B_0 - \dfrac{\omega_c}{\gamma} + \Delta B_{d_{sph}} + \Delta B_d \right) & \text{, frequency encoding in } y \end{cases}, \quad \text{(A.15)}$$

where $\left(x_{sph}, y_{sph}, z_{sph}\right)_{MR}$ is the true location of the sphere in the MR coordinate system.

www.manaraa.com

Appendix B. Trajectory Alignment Device Kinematics Solutions

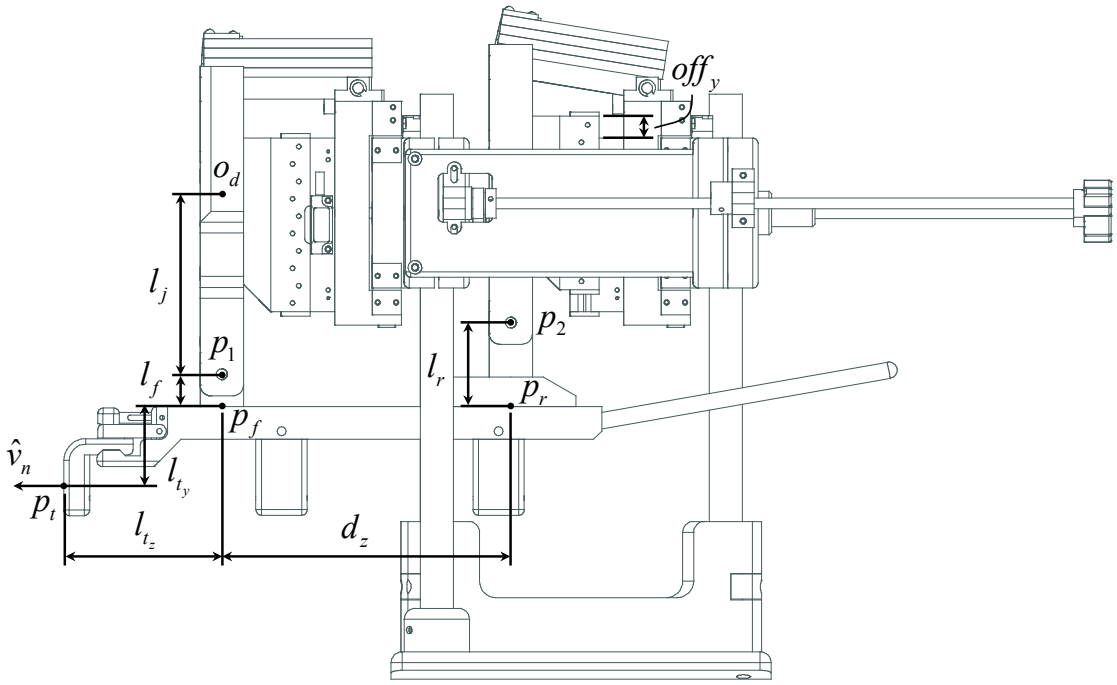

Figure B.1: Device kinematics diagram showing device link constants used in the kinematics solutions, the device origin, and needle point and vector.

www.manaraa.com

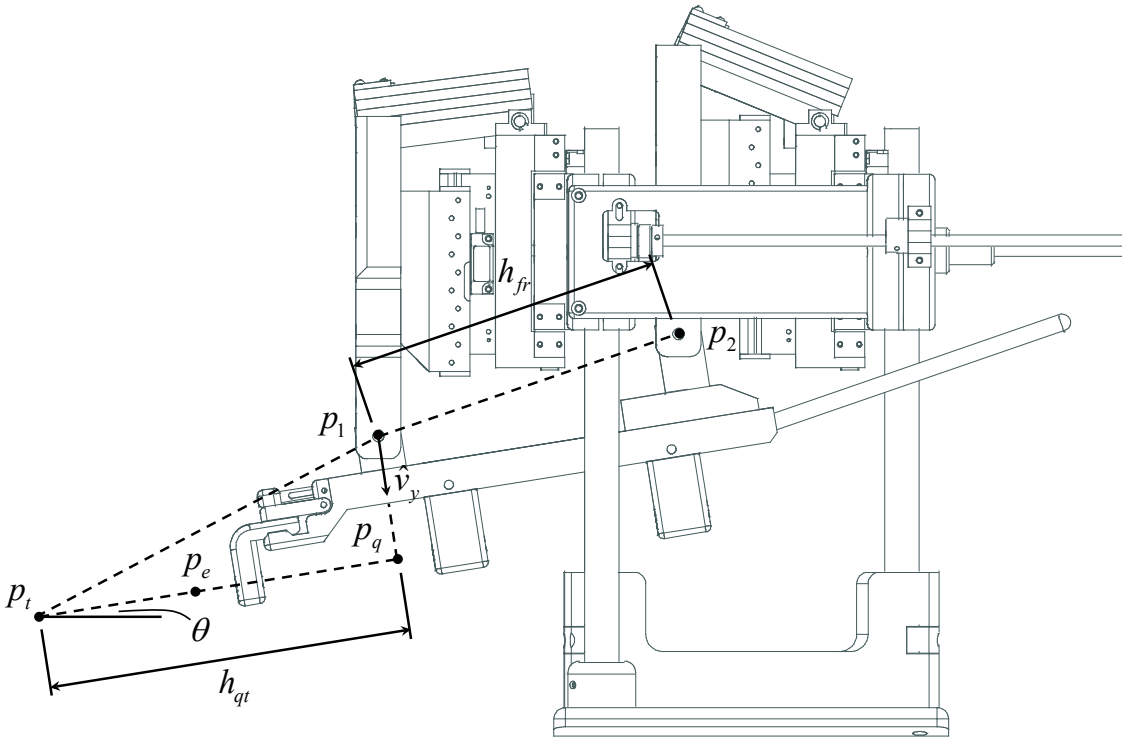

Figure B.2: Device kinematics diagram showing intermediate variables used in the kinematics solutions.

B.1 Forward Kinematics

Given: e_{1x}, e_{1y}, e_{2x}, and e_{2y}, define intermediate variables

$$\delta_y = e_{2y} - e_{1y} + off_y, \tag{B.1}$$

where δ_y is the position of the rear linear stages relative to the front in the y-direction,

$$\delta_{fr} = l_r - l_f, \tag{B.2}$$

where δ_{fr} is a link constant, equal to the difference in length of the front and rear pivot joints,

$$h_{yz} = \sqrt{d_z^2 + \left(\delta_{fr} - \delta_y\right)^2}, \tag{B.3}$$

where h_{fr} is the direct distance between points p_1 and p_2,

$$\theta = \tan^{-1}\left(\frac{\delta_{fr} - \delta_y}{d_z}\right) - \sin^{-1}\left(\frac{\delta_{fr}}{h_{yz}}\right), \tag{B.4}$$

www.manaraa.com

where θ is the angle the needle trajectory makes with the horizontal, and

$$\hat{v}_y = \begin{bmatrix} 0 \\ \cos(\theta) \\ -\sin(\theta) \end{bmatrix}. \tag{B.5}$$

where $\hat{v}_y$ is a unit vector in the direction of the front pivot joint. Define the points p_r and p_f as:

$$p_r = \begin{bmatrix} -e_{2x} \\ e_{2y} - \delta_{fr} + l_r \cos(\theta) + off_y + l_j \\ -l_r \sin(\theta) - d_z \end{bmatrix}, \tag{B.6}$$

and

$$p_f = \begin{bmatrix} -e_{1x} \\ e_{1y} + l_f \cos(\theta) + l_j \\ -l_f \sin(\theta) \end{bmatrix}. \tag{B.7}$$

The needle point p_t and needle vector $\hat{v}_n$ are calculated as:

$$\hat{v}_n = \frac{p_f - p_r}{|p_f - p_r|}, \tag{B.8}$$

and

$$p_t = p_f + l_{t_y} \hat{v}_y + l_{t_z} \hat{v}_n. \tag{B.9}$$

www.manaraa.com

B.2 Reverse Kinematics

Given: p_t and p_e, define intermediate variables

$$\hat{v}_n = \frac{p_t - p_e}{|p_t - p_e|}, \tag{B.10}$$

where $\hat{v}_n$ is the needle vector,

$$\theta = \sin^{-1}\left(\hat{v}_{n_y} \Big/ \sqrt{\hat{v}_{n_y}^2 + \hat{v}_{n_z}^2}\right), \tag{B.11}$$

and

$$h_{qt} = \frac{p_{t_z}}{\cos(\theta)} + l_{ty}\tan(\theta), \tag{B.12}$$

where h_{qt} is the base of the triangle connecting p_t and p_1 in Figure B.2.

Next, p_1 can be defined:

$$p_1 = p_t - \begin{bmatrix} h_{qt}\cos(\theta) i_{z_x}/i_{z_z} \\ h_{qt}\sin(\theta) + l_{ty}\cos(\theta) \\ h_{qt}\cos(\theta) - l_{ty}\sin(\theta) \end{bmatrix}, \tag{B.13}$$

and the linear stage offsets

$$\delta_y = \delta_{fr}\left[1 - 1/\cos(\theta)\right] - d_z\tan(\theta), \tag{B.14}$$

and

$$\delta_x = \hat{v}_{n_x}\left[d_z + \delta_{fr}\sin(\theta)\right]/\hat{v}_{n_z}. \tag{B.15}$$

Finally, the required positions of the linear stages are calculated as:

$$e_{1x} = -p_{1_x}, \tag{B.16}$$

$$e_{1y} = p_{1_y} - l_j, \tag{B.17}$$

$$e_{2x} = e_{1x} + \delta_x, \tag{B.18}$$

and

$$e_{2y} = e_{1y} + \delta_y - off_y. \tag{B.19}$$

www.manaraa.com

Appendix C. Health Canada Application

Dr. Aaron Fenster, Ph.D., Scientist/Professor

30 September 2011

Information Dissemination Unit
Medical Devices Bureau

Dear Reviewers:

The following document "ITA_appliication_Prostate_Abl_Guidance_CLASSI_V3.doc" contains information for Investigational Testing on Human Subjects for the following medical device: **3D Template Positioning Device for Needle Guidance (Model No: TPD – 1000)**. This device has been manufactured by the Robarts Research Institute (University of Western Ontario) for investigational purposes. According to the Medical Regulations Document the TPD-1000 is a *Class I* device. Upon receiving approval from Health Canada, we will submit any further outstanding documentation for this application.

If there are any comments, questions, or concerns, please contact me at

T:
F:
E:

Sincerely

Aaron Fenster, PhD

Imaging Research Laboratories, Robarts Research Institute,

www.manaraa.com

Health Canada - Prostate Ablation Needle Guidance

2 messages

David Tessier Tue, Nov 8, 2011 at 2:23 PM
To: Jeremy Cepek
Cc: Aaron Fenster

Hello, we have received confirmation from Health Canada that the Needle Positioning Device for Prostate Ablation that was developed at Robarts Research Institute is indeed a Class I device. What this means is that we can go ahead and use it in clinical trials. Class I devices do not receive an application confirmation number or evaluation report from Health Canada, so there will not be one on record. We only have the email that was sent to Aaron and myself (attached below).

With regard to the comments in the following email from Health Canada, we have copies of the records that they require, including the protocol and all of the labeling here at Robarts.

Please let me know if you have any questions or concerns.

David Tessier, PhD

-------- Original Message --------
Subject: Re: Fw: ITA - Classification Request
Date: Mon, 7 Nov 2011 15:29:20 -0500
From: Daniel Yoon
To:
Cc:

Dear Dr. Tessier:

Thank you for the attachments. Based on the information provided, the Template Positioning Device for Needle Guidance is a Class I device by Rule 7(1). Please note that although an Investigational Testing Authorization (ITA) is not required, you must possess the records listed in section 81 and comply with the relevant sections of Part 3 of the Medical Devices Regulations.

If you have any questions please feel free to contact me.

Regards,

Daniel Yoon
Regulatory Information Officer
Medical Devices Bureau
Health Canada
Tel:
Fax:

www.manaraa.com

Health Canada Application for Investigational Testing on Human Subjects

(Device Class I)

Template Positioning Device for Needle Guidance (TPD – 1000)

Manufacturer:

Dr. Aaron Fenster, Ph.D., Scientist/Professor

Correspondence:

Dr. Aaron Fenster, Ph.D., Scientist/Professor

www.manaraa.com

Executive Summary

The Template Positioning Device for Needle Guidance (Model no.TPD-1000) acts as a tracking system for insertion of needles by a physician into predetermined locations within prostate cancer patients. The TPD – 1000 is a stand alone device that functions as an enhancement to the present methods for needle guidance within ablation procedures. The device is made to reside within the bore of a MRI machine as an mechanical guided aid to the procedure, operating in conjunction with image guidance. The Template Positioning Device for Needle Guidance has been manufactured by the Robarts Research Institute (University of Western Ontario) for investigational purposes. This device is not an automated needle insertion device; all invasive treatments are performed by a certified physician through manual control of the device, which is used for aligning needle trajectories.

The Template Positioning Device for Needle Guidance has been determined by Health Canada to be Class-I according to Rule 7(2). Used in conjunction with research ethics board (REB)-approved study protocols, this device is only intended to guide the needle during the course of standard clinically approved focal tumor ablation prostate cancer procedures. It is not intended to automatically perform the procedure or diagnose disease; and as such, the physician will not make any clinical decisions using this device exclusively. This device will be transferred to clinical sites of the London Health Sciences Centre (LHSC), London, Canada, and University Health Network, Toronto, Canada, detailed in the Institutional Information section of the application, for investigational testing on human subjects.

The Template Positioning Device for Needle Guidance is a real-time, mechatronic system to be used to guide a needle into the targeted regions, which enables optimal delivery of prostate focal thermal therapies by providing direct correlation of tumor sites and needle trajectories intra-operatively. Registration between the device and MRI coordinate systems will ensure that the needle is aimed directly at its intended target. The device will allow the selection of desired coordinates of the needle point (tumour) through the use of a graphical user interface, and software controlled encoders will allow the physician to align the needle trajectory through this point. Calibration of the device will be performed by a trained technologist over an appropriate regular period, to ensure that the device is reporting a coordinates of the needle point within a tolerance of 1.0 millimeter.

The Template Positioning Device for Needle Guidance will be used as part of a pilot study development trial that involves the application of advanced technologies used to calibrate and define the position of a needle target point for local prostate tumor ablation procedures (using laser ablation techniques during the clinical procedure). The needle Guidance technology will be used in this program at one site of the Toronto district. Within this study about 20 patients will be participating in these trials. The objective of the study is to determine if the use of the Template Positioning Device for Needle Guidance will increase the accuracy and safety of the local ablation procedure by providing more details of the treated region and thus the location of ablated tissue. The Template Positioning Device for Needle Guidance will only be used in addition to the

www.manaraa.com

other standard guidance approach; in this case MRI real time imaging. A qualified physician (interventional radiologist at LHSC or UHN in Toronto) will conduct this procedure at the three participating sites, in accordance with standard clinical procedures.

Each case will be recorded at the clinical sites, while tabulating the correlation with the MRI needle tracked images. This will be used as an aid in verifying the improved accuracy of the Template Positioning Device for Needle Guidance.

The risks to each patient will be no more than the risks encountered by the patient during a standard laser ablation procedure. Qualified personnel from Dr. Fenster's research group will perform an analysis of the data, which will compare the ability of various image processing techniques including overlaying MRI images from the procedures with previous studies to assess the accuracy of the ablated tissue and an overall reduction of needle insertions.

www.manaraa.com

Table of Contents

Executive Summary.....2
Table of Contents.....4

1. Introduction 5
    1.1 Manufacturer Identification..... 5
    1.2 Device Identification..... 5
    1.3 Device Description 6
    1.4 Design Philosophy 6
    1.5 Marketing History..... 6
2. Risk Assessment 7
    2.1 Risk Analysis and Evaluation 7
    2.2 Previous Studies 7
    2.3 Alternative Treatments 7
    2.4 Precautions
    2.5 List of Standards
3. Institutional Information 8
    3.1 Name of Institution 8
4. Protocol 8
    4.1 Inclusion / Exclusion Criteria 9
5. Device Labels 10
    5.1 Device Labeling 10
6. Investigational Agreement 10

www.manaraa.com

1. INTRODUCTION

1.1 MANUFACTURER IDENTIFICATION

Manufacturer: Dr. Aaron Fenster, Ph.D., Scientist and Professor

Correspondence: Dr. Aaron Fenster, Ph.D., Scientist and Professor

1.2 DEVICE IDENTIFICATION

For investigational purposes, the following Name, Model Number, and Serial Numbers identify this device.

- Device Name: Template Positioning Device for Needle Guidance
- Model No.: TPD – 1000
- Serial No.: AA – 001

Table 1 lists the components of a single system, and Figure 1 illustrates its block diagram

Device Components	Status
Template Needle Guidance Device	Experimental/Investigational Use
Encoder Electronics Box	Experimental/Investigational Use
OEM CPU workstation	Licensed Medical Device
MRI machine	Licensed Medical Device

Table 1: List of Components for 3D Ultrasound Abdominal Imaging System

The template positioning device for needle guidance, used in conjunction with the protocols of the study outlined in section 4 of this application, is a **Class-I** medical device according to *Rule 7 - Subject to subrule (1)* of the Medical Devices Regulations :

Rule 7:

(1) Subject to subrule (2), all other non-invasive devices are classified as Class I.

(2) A device described in subrule (1) is classified as Class II if it is intended

(a) to act as a calibrator, tester or quality control support to another medical device; or

www.manaraa.com

(b) to be connected to an active device that is classified as Class II, III or IV.

The TPD – 1000 does not come in contact with skin, eye or any other part of the subject's body, nor does it enter an orifice; therefore, the following rules do not apply:

Rule 4: N / A (TPD – 1000 does not come in contact with injured skin)

Rule 5: N / A (TPD – 1000 does not channel or store gases, liquids, tissues or body fluids)

Rule 6: N / A (TPD – 1000 has no effect on chemical or biological composition of blood or other body fluids)

The TPD – 1000 is not an active device as it does not interact with supplying or withdrawing energy or substances to / from a living subject; thus, rules 8 – 12 do not apply.

Similarly the Special rules do not apply:

Rule 13: N / A (TPD – 1000 does not disinfect or sterilize)

Rule 14: N / A (TPD – 1000 is not composed from or incorporates animal or human cells)

Rule 15: N / A

Rule 16: N / A

1.3 DEVICE DESCRIPTION

Not Applicable (N/A) for Class-I applications.

1.4 DESIGN PHILOSOPHY

Not Applicable (N/A) for Class-I applications.

1.5 MARKETING HISTORY

Not Applicable (N/A) for Class-I applications

www.manaraa.com

2. RISK ASSESSMENT

2.1 RISK ANALYSIS AND EVALUATION

Not Applicable (N/A) for Class-I applications.

2.2 PREVIOUS STUDIES

Not Applicable (N/A) for Class-I applications.

2.3 ALTERNATIVE TREATMENTS

Not Applicable (N/A) for Class-I applications.

2.4 PRECAUTIONS

Not Applicable (N/A) for Class-I applications

2.5 LIST OF STANDARDS

Not Applicable (N/A) for Class-I applications.

www.manaraa.com

3. INSTITUTIONAL INFORMATION

3.1 NAME OF INSTITUTION

The following research study will be conducted at the following institutions:

University Health Network

4. PROTOCOL

This is a single center study to evaluate the safety and feasibility of MRI guided focal prostate cancer laser ablation in patients with a low risk of prostate cancer who have not yet received treatment for their cancer. Patients fulfilling the inclusion criteria and having none of the clinical exclusion criteria will be enrolled into the study after they (or their legal representative) have signed the informed consent form. No control group will be utilized and all patients will receive MRI guided focal laser ablation (FLA) for their focal prostate cancer. As part of the screening process, patients will provide a medical history, blood and urine samples, and undergo a physical examination, including a digital rectal examination (DRE). The MR guided FLA procedure is similar to MR guided brachytherapy, with initial fibers and probes inserted trans-perineally outside the bore of the MR and then the patient is moved inside the bore to verify position before deploying the laser. The treatment is expected to last 1-2 hours, and patients are not expected to experience any pain during the procedure. Laser ablation will be monitored using MR thermometry. An MRI scan will be done immediately after the ablation, as initial assessment for ensuring complete treatment of the target volume, as well as ensuring that treatment does not extend to critical structures.

The current method of delivering prostate focal therapy within the bore of an MR scanner involves the use of a fixed-grid template, and manual needle insertion. This approach suffers from many problems such as: a limited number of possible needle trajectories, increased trauma due to repeated incorrect needle insertions, and a long procedure time since the physician must repeatedly move the patient in and out of the MR bore. By integrating mechatronics and computer visualization techniques, the procedure will be dramatically improved. Registration between the robot and MRI coordinate systems will ensure that the needle is aimed directly at its intended target. The compact, semi-automated device will allow repositioning and insertion of the needle within the MR bore without the need to remove the patient; decreasing procedure time greatly. Image registration and segmentation techniques will ensure that the target is not missed due to tissue deflection, and allow the physician to guide the needle to the target in real-time. The result will be a procedure that is more accurate, less operator-dependent and more reproducible than the current techniques.

www.manaraa.com

We have developed a system (Template Positioning Device for Needle Guidance) as a facilitator for prostate ablation procedures to be integrated with the current standard ablation protocols practiced by the interventional radiologists that can increase the accuracy of probe placement, reduce side effects and overall recurrence rates without introducing a large financial burden on the hospitals to buy expensive equipment.

4.1 Inclusion/Exclusion Criteria

In general inclusion and exclusion criteria for our intra-procedural protocol are the same as those imposed by the prostate ablation procedure itself. However, one of the future directions upon successful accomplishment of this pilot study is to expand the research to be able to include more patients that are not candidates for the prostate ablation procedures due to various reasons (e.g. proximity to sensitive regions, such as the bladder or bowel) into our research. Current protocols followed in University Health Network (UHN) generally indicate non-surgical candidates for the percutaneous ablation procedures. The eligibility criteria are:

Inclusion Criteria

- Men 40-80 years of age;
- Histologically-proven prostate carcinoma;
- Prostate cancer clinical stage T1c and T2a
- Prostate MRI must confirm area suspicious for cancer in the sector of the positive biopsy;
- A minimum of six (6) weeks between the prostate biopsy and the Inclusion Visit;
- Prostate specific antigen (PSA) level 15 ng/mL.

Exclusion Criteria:

- Medically unfit for Radical Retropubic Prostectomy (RRP) surgery
- Patients who are unwilling or unable to give informed consent;
- Patients with foci location in the apex of the prostate or isolated transition zone cancers
- Patients who have received androgen suppression therapy
- Patients who have received or are receiving chemotherapy for prostate carcinoma;
- Patients previously treated with surgery to the prostate (traditional, endoscopic or minimally invasive including HIFU, TUNA, RITA, microwave, TURP, cryotherapy or any curative treatment
- Patients who have undergone radiation therapy for prostate cancer or to the pelvis
- Any condition, or history of illness or surgery that, in the opinion of the Investigator, might confound the results of the study or pose additional risks to the patient (e.g. significant cardiovascular conditions or allergies);

Patients with a history of non compliance with medical therapy and/or medical recommendations;

www.manaraa.com

5. DEVICE LABELS

5.1 LABELING

As required by sections 86(c) and 86(d) of the Medical Device Regulations, Figures 5 and 6 illustrate the labeling that is provided for the Template Positioning Device for Needle Guidance instrument as an investigational device for the institution outlined in Section 3.2.

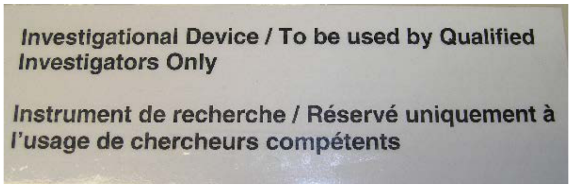

Figure 1: Investigational Labeling adhering to Sections 86(c) and 86(d) Requirements

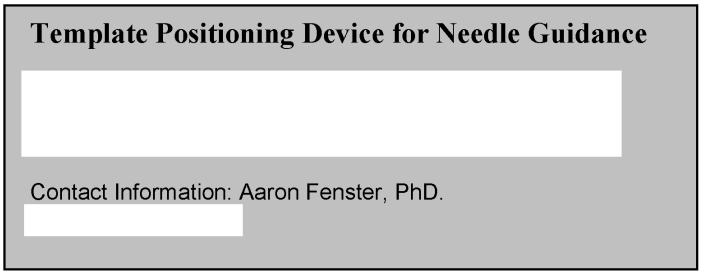

Figure 2: Device Name and Manufacturing Information Label

6. INVESTIGATORS AGREEMENTS

Not Applicable (N/A) for Class-I applications

www.manaraa.com

Appendix D. Patent Application: System and Method for Guiding a Medical Device to a Target Region

Office de la propriété intellectuelle du Canada
Un organisme d'Industrie Canada
www.opic.gc.ca

Canadian Intellectual Property Office
An Agency of Industry Canada
www.cipo.gc.ca

SIM & MCBURNEY

RECEIVED
OCT 16 2013
SIM & McBURNEY
SIM, LOWMAN, ASHTON & McKAY LLP

Date : 2013/10/09

FILING CERTIFICATE

Application No.	: **2,829,084**	**Filing Date**	: 2013/10/01
Expected Open-to-Public Inspection Date	: 2014/04/01	**Your Reference**	:
Priority Date	: United States of America (61/708,636) 2012/10/01		
Title of Invention	: SYSTEM AND METHOD FOR GUIDING A MEDICAL DEVICE TO A TARGET REGION		
Applicant(s)	: FENSTER, AARON; CEPEK, JEREMY; BAX, JEFFREY; LINDNER, URI; TRACHTENBERG, JOHN		
Inventor(s)	: FENSTER, AARON; CEPEK, JEREMY; BAX, JEFFREY; LINDNER, URI; TRACHTENBERG, JOHN		

Special Notice

You are reminded that annual fees to maintain your application are needed for each one-year period between the 2nd and 20th anniversaries and must be paid on or before each anniversary. Failure to pay within the prescribed time limit will lead to abandonment of your application.

Commissioner of Patents

Canada

OPIC CIPO

www.manaraa.com

SYSTEM AND METHOD FOR GUIDING A MEDICAL DEVICE TO A TARGET REGION

Field of the Invention

[0001] The present invention relates to a system and method for guiding a medical device to a target region.

Background of the Invention

[0002] Magnetic resonance (MR) imaging has been recognized as an extremely versatile medical imaging modality that has many applications. For example, MR imaging can be used to visualize prostate cancer, to visualize needles during insertion, and to visualize temperature during thermal therapies. As such, several researchers and clinicians have investigated the feasibility of using MR imaging for delivering focal therapy to patients with prostate cancer. For therapies requiring guidance of a needle, methods have been developed, such as focal therapy, focus laser ablation (FLA), etc. which require the insertion of needles through the patient's perineum. These methods are typically performed with the patient positioned in the semi-prone position within the bore of an MR imaging scanner. As will be appreciated, this position minimizes patient motion during imaging while maximizing patient comfort, both of which are important factors in a procedure that can last for several hours.

[0003] FLA is performed by inserting an open-ended or translucent catheter into the prostate through the patient's perineum. An optical fiber with a diffusing tip is inserted through the catheter to the tumor site, and is attached to a laser for thermal ablation (1).

[0004] MR imaging-guided FLA of prostate cancer has been tested. It was found that MR imaging provided excellent visualization of the needle for guidance, thermal monitoring and damage estimation during the ablation using MR thermometry, and intraoperative visualization of the ablated region.

[0005] While MR imaging provides a full suite of tools for MR imaging-guided FLA, a method and system for accurately guiding the therapy to the tumor site are desired. Further, the accuracy of FLA methods must be evaluated *in vivo* to enable evaluation of the potential clinical efficacy of prostate cancer focal therapies.

www.manaraa.com

[0006] The use of MR imaging for guiding therapy or biopsies has resulted in the development of various systems (2 to 8). While these systems have shown promise with respect to targeting accuracy, issues remain regarding reductions in image signal-to-noise ratio (SNR), procedure workflow, and patient safety.

[0007] SNR reduction is caused by the use of electromechanical actuators that increase the noise in the MR imaging scanners' radio frequency (RF) receive coils, especially if the actuators are moved during imaging (3, 5, 9).

[0008] The main obstacle with respect to procedure workflow is due to the limited workspace around the patient when the patient is positioned within the bore of the MR imaging scanner, and due to the fact that the patient's prostate is generally one (1) meter into the MR imaging scanner bore. The general solution to this problem has been to remove the patient from the MR imaging scanner bore for needle insertion, and then move the patient back into the MR imaging scanner bore for verification of needle depth with MR imaging (4 to 6, 8). As will be appreciated, since the needle cannot be visualized while it is being inserted, this method requires incremental insertions, with multiple translations of the patient into and out of the MR imaging scanner bore. Moving the patient into and out of the MR imaging scanner bore results in excessive movement, reducing potential accuracy and increasing procedure time.

[0009] Systems (3, 5) have been developed that are fully automated, however patient safety may be compromised since there is no haptic feedback or safety system in place.

[0010] As will be appreciated, improvements are generally desired. It is therefore an object at least to provide a novel system and method for guiding a medical device to a target region.

Summary of the Invention

[0011] Accordingly, in one aspect there is provided a device guiding apparatus, comprising support framework, a counterbalance supported by the support framework at a position above a surface on which the support framework rests, and a manipulation assembly supported by the counterbalance, the manipulation assembly comprising at least one support assembly for supporting a medical device at a position intermediate the

www.manaraa.com

counterbalance and the surface such that a user has a direct line-of-site of the at least one support assembly.

[0012] In an embodiment, the support framework, the manipulation assembly, the at least one support assembly and the counterbalance are made of non-magnetic materials. In an embodiment, the device guiding apparatus is positionable within a bore of an MR imaging scanner. In an embodiment, the device guiding apparatus comprises a sensor arrangement for determining the trajectory of the medical device. In an embodiment, the device guiding apparatus comprises an alignment interface providing feedback to the user for adjusting the orientation of the medical device.

[0013] According to another aspect there is provided a device guiding apparatus, comprising support framework, a counterbalance supported by the support framework at a position above a surface on which the support framework rests, and a manipulation assembly supported by the counterbalance, the manipulation assembly comprising at least one support assembly for supporting a medical device at a position intermediate the counterbalance and the surface such that a user has a direct line-of-site of the at least one support assembly, a sensor arrangement configured to obtain sensor data, and processing structure configured to receive sensor data from the sensor arrangement, process the received sensor data to determine the trajectory of the medical device, calculate a point of intersection with a target region based on the trajectory of the medical device, calculate a difference between the point of intersection and a target point associated with the target region, and provide feedback to the user to guide the medical device to the target point based on said calculated difference.

[0014] According to another aspect there is provided a method for providing feedback to a user guiding a medical device to a target region, the method comprising receiving sensor data from a sensor arrangement, processing the received sensor data to determine the trajectory of the medical device, calculating a point of intersection with a target region based on the trajectory of the medical device, calculating a difference between the point of intersection and a target point associated with the target region, and providing feedback to the user based on the calculated difference between the point of intersection and the target point.

[0015] According to another aspect there is provided a non-transitory computer readable medium having stored thereon a computer program comprising computer

www.manaraa.com

readable instructions for execution by a computer to perform a method of providing feedback to a user guiding a medical device to a target region, the method comprising receiving sensor data from a sensor arrangement, processing the received sensor data to determine the trajectory of the medical device, calculating a point of intersection with a target region based on the trajectory of the medical device, calculating a difference between the point of intersection and an actual target point associated with the target region, and providing feedback to the user based on the calculated difference between the estimated target point and the actual target point.

Brief Description of the Drawings

[0016] Embodiments will now be described more fully with reference to the accompanying drawings in which:

[0017] Figure 1 is schematic block diagram of a system for guiding a medical device to a target region;

[0018] Figure 2 is an isometric view of a device guiding apparatus forming part of the system of Figure 1;

[0019] Figure 3 is an isometric view of a frame forming part of the device guiding apparatus of Figure 2;

[0020] Figures 4a to 4c are isometric, bottom and side views, respectively, of a linear motion assembly forming part of the device guiding apparatus of Figure 2;

[0021] Figure 5 is a side view of an extension assembly forming part of the device guiding apparatus of Figure 2;

[0022] Figure 6 is a side view of a manipulation assembly forming part of the device guiding apparatus of Figure 2;

[0023] Figure 7 is an isometric view of a counterbalance assembly forming part of the device guiding apparatus of Figure 2;

[0024] Figure 8 is a cross-sectional view of a locking assembly forming part of the device guiding apparatus of Figure 2;

[0025] Figure 9 is an isometric view of a sensor arrangement forming part of the device guiding apparatus of Figure 2;

[0026] Figures 10a to 10c show views of an alignment interface forming part of the system of Figure 1;

www.manaraa.com

[0027] Figures 11 and 12 show the coordinates associated with the device guiding apparatus of Figure 2;

[0028] Figure 13 shows a detachable fiducial MR-visible component; and

[0029] Figures 14a and 14b show exemplary MR images of the fiducial MR-visible components of Figure 13.

Detailed Description of the Embodiments

[0030] Turning to Figure 1, a system for guiding a medical device to a target region is shown and is generally identified by reference numeral 1000. In this example, the medical device is a needle and the target region is a patient's prostate. The system 1000 comprises a general purpose computing device 2000 that is communicatively coupled to a device guiding apparatus 3000, an alignment interface 4000, and a magnetic resonance (MR) imaging scanner 5000. In this embodiment, the device guiding apparatus 3000 is positioned within the bore of the MR imaging scanner 5000. The device guiding apparatus 3000 is operable in two modes: target only mode and target and entry mode, as will be described below. The general purpose computing device 2000 communicates with the MR imaging scanner 5000 via a file transfer protocol and receives MR images of a target region therefrom. The MR images are processed to register the orientation of a medical device, such as for example a needle, supported by the device guiding apparatus 3000, to select a target point associated with the target region, and to monitor the medical device during use. The general purpose computing device 2000 communicates with the device guiding apparatus 3000 to determine the precise location and orientation of the medical device. The general purpose computing device 2000 compares the location and orientation of the medical device to that required to reach the target point. The general purpose computing device 2000 in turn provides output to the alignment interface 4000 to provide feedback to the physician to enable the physician to adjust the location and orientation of the medical device using the device guiding apparatus 3000, if required.

[0031] The general purpose computing device 2000 in this embodiment is a personal computer or other suitable processing device comprising, for example, a processing unit, system memory (volatile and/or non-volatile memory), other non-removable or removable memory (e.g., a hard disk drive, RAM, ROM, EEPROM, CD-

www.manaraa.com

ROM, DVD, flash memory, etc.) and a system bus coupling the various computing device components to the processing unit. The general purpose computing device 2000 may also comprise networking capability using Ethernet, WiFi, and/or other network formats, to access shared or remote drives, one or more networked computers, or other networked devices.

[0032] Figures 2 to 9 illustrate the device guiding apparatus 3000. In this embodiment, as the device guiding apparatus 3000 is positioned within the bore of the MR imaging scanner 5000, all components of the device guiding apparatus 3000 are made of non-magnetic material. As can be seen, the device guiding apparatus 3000 comprises a frame 3100, a pair of linear motion assemblies 3200a and 3200b, an extension assembly 3300, a manipulation assembly 3400, a counterbalance comprising a pair of counterbalance assemblies 3500a and 3500b, each of which is associated with a respective one of the linear motion assemblies 3200a and 3200b, a locking assembly 3600 and a sensor arrangement 3700, the specifics of which will now be described.

[0033] Figure 3 better illustrates the frame 3100. As can be seen, the frame 3100 comprises a base 3110 made of a generally flat sheet of plastic material, such as for example Delrin®, having a U-shaped cut out 3120 therein. The cut out 3120 increases the amount of clearance available for a physician's hand while manipulating a medical device supported by the device guiding apparatus 3000. Lower brackets 3130a and 3130b are connected to the base 3110. Each of the lower brackets 3130a and 3130b is made of plastic material, such as for example Delrin®. Lower bracket 3130a is connected to an upwardly extending pillar 3140 via a shaft clamp assembly (not shown). Lower bracket 3130b is connected to a pair of upwardly extending pillars 3150a and 3150b via shaft clamp assemblies (not shown). Each of the pillars 3140, 3150a and 3150b is made of a non-metallic fiberglass material. As will be further described below, the pillars 3140, 3150a and 3150b provide elevation to components of the device guiding apparatus 3000 to increase the amount of space available for the physician. An upper bracket 3160a is connected to pillars 3140 and 3150a via shaft clamp assemblies (not shown) adjacent its opposite ends and an upper bracket 3160b is connected adjacent one of its ends to the pillar 3150b via a clamp shaft assembly (not shown). Each of the upper brackets 3160a and 3160b is made of a plastic material, such as for example Delrin®. A support brace 3170 extends between the upper brackets 3160a and 3160b and is made of

www.manaraa.com

a plastic material, such as for example Delrin®. The support brace 3170 is used to reduce the number of pillars required to support the components of the device guiding apparatus 3000 and thereby further increases the amount of space available to the physician. The upper brackets 3160a and 3160b and support brace 3170 are dimensioned to receive the linear motion assemblies 3200a and 3200b, as will now be described.

[0034] Figures 4a to 4c illustrate the linear motion assembly 3200a. As the linear motion assemblies 3200a and 3200b are similar, only linear motion assembly 3200a will be described. Linear motion assembly 3200a is dual-axis and comprises two stages, an x-stage and a y-stage, connected to one another at an angle of ninety (90) degrees. Each stage comprises a carriage 3210 having four (4) mounting holes 3220 and two (2) locating holes 3230 therein. The carriage 3210 is made of a plastic material, such as for example Delrin®. The carriage 3210 is connected to a rail 3240 made of a plastic material, such as for example Delrin®. The rail 3240 is connected to bearing races 3250a and 3250b such that each bearing race 3250a and 3250b extends along one side of the rail 3240. Ball bearing assemblies 3260a and 3260b are fixably connected to the carriage 3210 and each receives one of the bearing races 3250a and 3250b such that the carriage 3210 can move along a single axis with respect to the rail 3240. In this embodiment, the ball bearing assemblies 3260a and 3260b are made of a non-magnetic material. As mentioned previously, the linear motion assembly 3200a is connected to the upper brackets 3160a and 3160b and support brace 3170 of the frame 3100.

[0035] Turning now to Figures 5 and 6, the extension assembly 3300 and the manipulation assembly 3400 are better shown. The extension assembly 3300 comprises a front extension arm 3310 and a rear extension arm 3320. A first end of the front extension arm 3310 is connected to a spring balance arm of the counterbalance assembly 3500a. The body of the front extension arm 3310 is connected to the carriage of the y-stage linear motion assembly 3200a. A second end of the front extension arm 3310 is connected to a manipulator arm 3410 of the manipulation assembly 3400 (described below) via a spherical joint 3330. A first end of the rear extension arm 3320 is connected to a spring balance arm of the counterbalance assembly 3500b. The body of the rear extension arm 3320 is connected to the y-stage of the linear motion assembly 3200b. A second end of the rear extension arm 3320 is connected to the manipulator

www.manaraa.com

arm 3410 of the manipulation assembly 3400 via a spherical joint 3340. Each spherical joint 3330 and 3340 provides the manipulation assembly 3400 with two rotational degrees-of-freedom. As will be appreciated, the extension assembly 3300 allows manipulation assembly 3400 to follow the motion of each linear motion assembly 3200a and 3200b.

[0036] In this embodiment the manipulator arm 3410 is made of a plastic material, such as for example Delrin®. The manipulator arm 3410 has one or more support assemblies for supporting the medical device thereon. In this embodiment, the support assemblies are three (3) needle templates 3420a, 3420b and 3420c mounted on the manipulator arm 3410 at spaced locations. Each of the needle templates 3420a to 3420c is made of a plastic material, such as for example polyether ether ketone (PEEK). An alignment handle 3430 is connected to the rearward end of the manipulator arm 3410 and extends therefrom. The alignment handle 3430 allows the physician to manually manipulate the position and orientation of the manipulator arm 3410 thereby adjusting the position and orientation of the medical device supported by the needle templates 3420a, 3420b and 3420c. In this embodiment the alignment handle 3430 is made of a plastic material, such as for example PEEK. The rear needle template 3420c is used as an extension of the middle needle template 3420b and front needle template 3420a. In this embodiment, the rear needle template 3420c allows the physician to guide a needle into the patient from outside the MR imaging scanner bore. Thus, a direct line-of-site of the rear needle template 3420c is provided allowing the physician to guide the needle through the rear needle template 3420c, middle needle template 3420b and front needle template 3420a, towards the patient.

[0037] Turning now to Figure 7, the counterbalance assembly 3500a is shown. As the counterbalance assemblies 3500a and 3500b are similar, only counterbalance assembly 3500a will be described. In this embodiment, the counterbalance assembly 3500a is similar to that described in U.S. Patent Application Publication No. 2010/0319164 to Bax et al. The counterbalance assembly 3500a is used to allow components of the device guiding apparatus 3000 coupled thereto and having a vertical degree-of-freedom to remain in the position placed by the physician without the force of gravity moving them downward. As will be appreciated, this allows the physician to adjust each degree-of-freedom of the device guiding apparatus 3000 using one hand on

www.manaraa.com

the alignment handle 3430. In this embodiment, the counterbalance assembly 3500a comprises two sets of four (4) biasing elements in the form of leaf springs 3510, or other suitable spring-like arrangements. Each of the leaf springs is made of a plastic material such as for example PEEK. A first end of each set of the leaf springs 3510 is connected to a support arm 3515. A second end of each of the set of leaf springs 3510 is connected to a U-shaped spring balance arm 3520. The spring balance arm 3520 provides mounting for the leaf springs 3510 and ensures that the counterbalance assembly 3500a has a single degree-of-freedom and transfers the vertical force of the counterbalance assembly 3500a to the extension arm connected thereto. As will be appreciated, the spring balance arm 3520 must be able to support the torque of the leaf springs 3510, and thus is made of a stiffer material than the leaf springs 3510. In this embodiment, the spring balance arm 3520 is made of aluminum, which is generally stiffer than PEEK.

[0038] The counterbalance assembly 3500a also comprises two (2) cam bearings 3530. The cam bearings 3530 are offset from the rotational axis of the spring balance arm 3520, and are offset ninety (90) degrees from one another. As a result, the counterbalance assembly 3500a provides the force for offsetting the force of gravity, and compensates for the component of the force that varies with the position of the medical device. The arrangement of the cam bearings 3530 provides a constant force independent of the position of the medical device. In this embodiment, the cam bearings 3530 are made of a ceramic material.

[0039] An adjustment screw (not shown) may be used with adjustment screw hole 3540 to adjust the tension of the leaf springs 3510.

[0040] Referring back to Figure 2, the locking assembly 3600 comprises a front locking assembly 3610a and a rear locking assembly 3610b. The front locking assembly 3610a is shown in Figure 8 and comprises a locking handle 3620a connected to a locking shaft 3630a. The locking shaft 3630a has a large diameter section 3640a that is received through an opening in the frame 3100 via a threaded connection. The locking shaft 3630a has a small diameter section 3650a that extends through linear motion assembly 3200a and is moveable relative to the carriage 3210. When in an unlocked position, the locking shaft 3630a is not in contact with the carriage 3210. When the locking handle 3620a is turned clockwise, the locking shaft 3630a advances into contact with the carriage 3210 of the y-stage so that it assumes the locked position. In the locked

www.manaraa.com

position, the locking assembly 3610a prevents motion of the linear motion assembly 3200a due to the frictional force between the locking shaft 3630a and the carriage 3210. A pair of mechanical stops (not shown) inhibits over-tightening or over-loosening of the locking assembly 3600. The rear locking assembly 3610b is similar to the front locking assembly 3610a and contacts the carriage 3210 associated with y-stage of the linear motion assembly 3200b when in the locked position to inhibit it from moving.

[0041] When both locking assemblies 3610a and 3610b are unlocked, both the linear motion assemblies 3200a and 3200b are allowed to move in response to manipulation of the manipulator arm 3410 via the alignment handle 3420. As such, the needle templates 3420a, 3420b and 3420c may be rotated and/or translated about all four rotational degrees-of-freedom (defined by spherical joints 3330 and 3340) via the manipulator arm 3410 thereby adjusting the orientation of the medical device.

[0042] When locking assembly 3610a is locked and locking assembly 3610b is unlocked, only the linear motion assembly 3200b is allowed to move in response to manipulation of the manipulator arm 3410 via the alignment handle 3420. As such, the angle of the needle templates 3420a, 3420b and 3420c may be manipulated about the spherical joint 3340 via the manipulator arm 3410 thereby adjusting the angle of the medical device.

[0043] When locking assembly 3610a is unlocked and locking assembly 3610b is locked, only the linear motion assembly 3200a is allowed to move in response to manipulation of the manipulator arm 3410 via the alignment handle 3420. As such, the angle of the needle template 3420a may be manipulated about the spherical joint 3330 via the manipulator arm 3410 thereby adjusting the angle of the medical device.

[0044] When both locking assemblies 3610a and 3610b are locked, neither of the linear motion assemblies 3200a and 3200b are allowed to move in response to manipulation of the manipulator arm 3410 via the alignment handle 3420. As such, the needle templates 3420a, 3420b and 3420c are unable to move and the medical device remains stationary.

[0045] Turning now to Figure 9, the sensor arrangement 3700 is better shown. As can be seen, the sensor arrangement 3700 comprises four (4) encoders S1 to S4. In this embodiment, the encoders S1 to S4 are magnetic rotary encoders, such as the MR-compatible linear optical encoders LIA-20 manufactured by Numerik Jena, and used to

www.manaraa.com

measure the angle between the encoder body (identified as S1 to S4) and an associated encoder magnet (not shown). Each of the encoders S1 to S4 is connected to the general purpose computing device 2000 via a wired connection (not shown). An RF filter (not shown) is used to remove noise introduced into the wired connections. The encoders S1 to S4 are constructed of non-magnetic materials and output a sine-cosine signal in the kHz range. Encoder S1 is positioned to measure the x-component (e_{1x}) of the linear motion assembly 3200a. Encoder S2 is positioned to measure the y-component (e_{1y}) of the linear motion assembly 3200a. Encoder S3 is positioned to measure the x-component (e_{2x}) of the linear motion assembly 3200b. Encoder S4 is positioned to measure the y-component (e_{2y}) of the linear motion assembly 3200b.

[0046] The device guiding apparatus 3000 coordinate system is also shown in Figure 9 and is defined as (X_d, Y_d, Z_d) at origin O_d. The needle trajectory, represented by point p_t and needle vector $\hat{v}_n$, is calculated by the general purpose computing device 2000 using the (x, y) coordinates of linear motion assemblies 3200a and 3200b. The (x,y) coordinates of linear motion assemblies 3200a and 3200b are measured by encoders S1 to S4 as coordinates (e_{1x}, e_{1y}) and (e_{2x}, e_{2y}), respectively.

[0047] Turning now to Figures 10a to 10c, the alignment interface 4000 is shown. The alignment interface 4000 allows the physician to align the medical device with the target point associated with the target region, which in this embodiment is selected in an MR image. The alignment interface 4000 permits manual control of the device guiding apparatus 3000 while providing immediate haptic feedback and ensuring patient safety. In this embodiment, the alignment interface 4000 is MR compatible and thus can be placed adjacent to the device guiding apparatus 3000 either inside or outside of the bore of the MR imaging scanner 5000. As will be described, the alignment interface 4000 helps the physician guide the medical device to the target point associated with the target region by representing varying levels of accuracy.

[0048] As can be seen, the alignment interface 4000 comprises a left grid 4010a and a right grid 4010b, each of which comprises a matrix 4020 of twenty-five (25) light panels. An outer square 4030 comprises sixteen (16) of the light panels 4020. Each of the light panels 4020 of the outer square 4030 is backlit by a red colored light emitting diode (LED) 4035, shown in Figure 10b. One of the light panels 4020 of the outer square 4030 is illuminated if the medical device is positioned greater than 3mm from the

www.manaraa.com

target point associated with the target region. An inner square 4040 comprises eight (8) of the light panels 4020. Each of the light panels 4020 of the inner square 4040 is backlit by a yellow colored LED 4045, shown in Figure 10b. One of light panels 4020 of the inner square 4040 is illuminated if the medical device is positioned greater than 0.25mm from the target point associated with the target region, but less than 3mm. A center light panel 4050 is backlight by a green colored LED 4055, shown in Figure 10b, and is illuminated if the medical device is positioned within 0.25mm from the target point associated with the target region.

[0049] Figure 10b shows the circuit components of the alignment interface 4000. As can be seen, the LEDs 4035, 4045 and 4055 are surface mounted and are connected to a microcontroller 4060 and a voltage regulator 4070. A single shielded cable 4080 couples the alignment interface 4000 to the general purpose computing device 2000.

[0050] As shown in Figure 10c, mesh copper shielding 4090 is used to back the LEDs 4035, 4045 and 4055 and a translucent lens 4100 is positioned adjacent to each of the LEDs 4035, 4045 and 4055. Solid copper shielding 4110 is used to back the microcontroller 4060 and voltage regulator 4070. As will be appreciated, copper shielding 4090 and 4110 is used to prevent the alignment interface 4000 from introducing noise into the MR imaging scanner 5000 and to prevent the coils of the MR imaging scanner 5000 from interfering with the operation of the alignment interface 4000. All components of the alignment interface 4000 are non-magnetic.

[0051] During operation, the device guiding apparatus 3000 is positioned within the bore of the MR imaging scanner 5000 and adjacent to a target region. For example, in the event the target region is a patient's prostate, the device guiding apparatus 3000 is positioned in between the patient's legs. The configuration of the device guiding apparatus 3000 allows for the bulk of the components of the device guiding apparatus 3000 to be positioned above the patient's legs, allowing the physician to have a direct line-of-site of the rear needle template 3420c from outside of the bore of the MR imaging scanner 5000.

[0052] As mentioned previously, the device guiding apparatus 3000 is operable in two modes: target only mode and target and entry mode.

www.manaraa.com

[0053] During operation in the target only mode, the physician selects a target point associated with the target region and the alignment interface 4000 instructs the physician how to adjust the needle trajectory such that it will contact the target point. A forward kinematics solution is used to compare the target point with the intersection of the needle with an axial plane that contains the target point.

[0054] Figures 11 and 12 illustrate the device guiding apparatus 3000 showing constants, the device guiding apparatus 3000 origin O_d, and the needle trajectory defined by point p_t and vector $\hat{v}_n$ used to solve the forward kinematics solution.

[0055] To solve the forward kinematics solution, the (x,y) coordinates of linear motion assemblies 3200a and 3200b are measured by encoders S1 to S4 as coordinates (e_{1x}, e_{1y}) and (e_{2x}, e_{2y}). Intermediate variables are defined, as shown in Figures 11 and 12, and are calculated according to the following equations:

$$\delta_y = e_{2y} - e_{1y} + off_y, \tag{1}$$

where δ_y is the position of the linear motion assembly 3200b relative to the front in the y-direction,

$$\delta_{fr} = l_r - l_f, \tag{2}$$

where δ_{fr} is a link constant that is equal to the difference between lengths of the spherical joints 3330 and 3340,

$$h_{fr} = \sqrt{d_z^2 + \left(\delta_{fr} - \delta_y\right)^2}, \tag{3}$$

where h_{fr} is the direct distance between points p_1 and p_2,

$$\theta = \tan^{-1}\left(\frac{\delta_{fr} - \delta_y}{d_z}\right) - \sin^{-1}\left(\frac{\delta_{fr}}{h_{yz}}\right), \tag{4}$$

where θ is the angle the needle trajectory makes with the horizontal, and

$$\hat{v}_y = \begin{bmatrix} 0 \\ \cos(\theta) \\ -\sin(\theta) \end{bmatrix}. \tag{5}$$

where $\hat{v}_y$ is a unit vector that represents the orientation of the front gimbal.

Points p_r and p_f are defined as:

www.manaraa.com

$$p_r = \begin{bmatrix} -e_{2x} \\ e_{2y} - \delta_{fr} + l_r \cos(\theta) + off_y + l_j \\ -l_r \sin(\theta) - d_z \end{bmatrix}, \quad (6)$$

and

$$p_f = \begin{bmatrix} -e_{1x} \\ e_{1y} + l_f \cos(\theta) + l_j \\ -l_f \sin(\theta) \end{bmatrix}. \quad (7)$$

The needle trajectory (point p_t and needle vector $\hat{v}_n$) is calculated as:

$$\hat{v}_n = \frac{p_f - p_r}{|p_f - p_r|}, \quad (8)$$

and

$$p_t = p_f + l_{t_y} \hat{v}_y + l_{t_z} \hat{v}_n. \quad (9)$$

[0056] Only the left grid 4010a of the alignment interface 4000 is used and helps the physician align the medical device (which in this embodiment is a needle) with the target point. To determine which one of the light panels 4020 is to be illuminated, the target point is compared to the intersection of the needle trajectory with an axial plane that contains the target point, as determined using the forward kinematics equations. If the x-component of the difference is greater than 3mm, one of the light panels 4020 associated with one of the exterior columns of the outer square 4030 is illuminated. If the x-component of the difference is between 0.25mm and 3mm, one of the light panels 4020 associated with one of the exterior columns of the inner square 4040 is illuminated. If the x-component of the difference is less than 0.25mm, the center light panel 4050 is illuminated. Similarly, if the y-component of the difference is greater than 3mm, one of the light panels 4020 associated with one of the exterior rows of the outer square 4030 is illuminated. If the y-component of the difference is between 0.25mm and 3mm, one of the light panels 4020 associated with one of the exterior rows of the inner square 4040 is illuminated. If the y-component of the difference is less than 0.25mm, the center light panel 4050 is illuminated.

[0057] During operation in the target and entry mode, the physician selects a target point and entry point and the alignment interface 4000 instructs the physician how

www.manaraa.com

to adjust the needle trajectory using all four degrees-of-freedom such that it will enter the patient at the entry point and will contact the target point. A reverse kinematics solution is used to calculate the position of each linear motion assembly 3200a and 3200b required for the device guiding apparatus 3000 to be aligned with a particular needle orientation.

[0058] Figures 11 and 12 illustrate the device guiding apparatus 3000 showing constants, the device guiding apparatus 3000 origin O_d, and the needle trajectory defined by point p_t and vector $\hat{v}_n$ used to solve the reverse kinematics solution. Points p_t and p_e are defined using the MR imaging scanner 5000. Point p_t is the target point associated with the target region that the needle is to contact. Point p_e is the entry point on the patients' skin that ensures the needle trajectory will not contact any critical structures within the patient's body while moving towards point p_t. Intermediate variables are defined and are calculated according to the following equations:

$$\hat{v}_n = \frac{p_t - p_e}{|p_t - p_e|}, \tag{10}$$

where $\hat{v}_n$ is the needle vector,

$$\theta = \sin^{-1}\left(\hat{v}_{n_y} \Big/ \sqrt{\hat{v}_{n_y}^2 + \hat{v}_{n_z}^2}\right), \tag{11}$$

and

$$h_{qt} = \frac{p_{t_z}}{\cos(\theta)} + l_{ty}\tan(\theta), \tag{12}$$

where h_{qt} is the base of the triangle connecting p_t and p_1 in Figure 12. Next, p_1 is defined as:

$$p_1 = p_t - \begin{bmatrix} h_{qt}\cos(\theta) i_{z_x}/i_{z_z} \\ h_{qt}\sin(\theta) + l_{ty}\cos(\theta) \\ h_{qt}\cos(\theta) - l_{ty}\sin(\theta) \end{bmatrix},$$

and the linear motion offsets:

$$\delta_y = \delta_{fr}\left[1 - 1/\cos(\theta)\right] - d_z\tan(\theta),$$

and

www.manaraa.com

$$\delta_x = \hat{v}_{n_x}\left[d_z + \delta_{fr}\sin(\theta)\right]/\hat{v}_{n_z}.$$

[0059] The desired (x,y) coordinates of linear motion assemblies 3200a and 3200b set as coordinates (e_{1x}, e_{1y}) and (e_{2x}, e_{2y}) are calculated as:

$$e_{1x} = -p_{1_x}, \tag{13}$$

$$e_{1y} = p_{1_y} - l_j, \tag{14}$$

$$e_{2x} = e_{1x} + \delta_x, \tag{15}$$

and

$$e_{2y} = e_{1y} + \delta_y - off_y. \tag{16}$$

[0060] Both the left grid 4010a and right grid 4010b of the alignment interface 4000 are used. The left grid 4010a is used to help the physician align the linear motion assembly 3200a and the right grid is used to help the physician align the linear motion assembly 3200b. To determine which one of the light panels 4020 is to be illuminated, the difference between the position of each linear motion assembly 3200a and 3200b and the target position as determined using the reverse kinematics equations is used. The same x-component and y-component rules used during operation in the target only mode are used during operation in the target and entry mode to determine which one of the light panels 4020 is illuminated.

[0061] As will be appreciated, each time the device guiding apparatus 3000 is used, it is placed within the bore of the MR imaging scanner 5000. Thus, the device guiding apparatus 3000 coordinate system must be determined with respect to the MR imaging scanner 5000 at the beginning of each procedure to ensure accurate guidance. In this embodiment, a detachable fiducial MR-visible component 5100 is used and is shown in Figure 13. The detachable component 5100 comprises two perpendicular drilled holes in the shape of a plus-sign "+". The drilled holes are filled with an aqueous solution of 1% gadolinium by volume (Magnevist, 469 mg/ml). The detachable component 5100 is embedded within a plastic component and is mounted to the device guiding apparatus 3000. An exemplary sagittal MR image 5100' of the detachable component 5100 is also shown in Figure 13. Four points (p_0, p_1, p_2 and p_3) are identified on the MR image 5100' and must be localized for registration. Dashed lines have been superimposed on the MR image 5100' and indicate the image planes in which each point

www.manaraa.com

is localized. The points p_0 and p_1 are localized in axial images, and points p_2 and p_3 are localized in coronal images.

[0062] The captured MR images are filtered to reduce noise using a circular averaging filter having a radius of 2 pixels, and then thresholded. An exemplary fiducial image is shown in Figure 14a. Figure 14b shows the fiducial image of Figure 14a once it has been filtered and thresholded. Since the size of each fiducial tube is known, the threshold value is chosen such that the total area of the thresholded image is equal to the known area of a section of a fiducial tube. Fiducial localization is then performed by the general purpose computing device 2000 to compute an intensity-weighted centroid of the filtered, thresholded image according to the following equation:

$$\bar{x}_i = \frac{\sum_{j=1}^{m}\sum_{k=1}^{n} I(j,k)\, x_i(j,k)}{\sum_{j=1}^{m}\sum_{k=1}^{n} I(j,k)} \tag{20}$$

where $x_i(j, k)$ is the i^{th} coordinate of the pixel at index (j, k), $I(j,k)$ is the corresponding pixel intensity, and $\bar{x}_i$ is the i^{th} coordinate of the centroid of the image of size m x n.

[0063] Sensitivity of fiducial localization to main field inhomogeneity is reduced by measuring coordinates in the phase encode direction of each image. Accordingly, two sets of images of each fiducial are acquired, with the phase encoder direction swapped in each acquisition. Since the axes of the device guiding apparatus 3000 are generally aligned with those of the MR imaging scanner 5000, error in pose estimation of the fiducial arrangement due to slice-select error is minimal. The four points are used to compute the unit vectors in the direction of each of the device guiding apparatus' axes, in MR coordinates, as:

$$\hat{z}_d = \frac{p_1 - p_0}{|p_1 - p_0|},\ \hat{x}_d = \frac{-(p_1 - p_0)\times(p_3 - p_2)}{|(p_1 - p_0)\times(p_3 - p_2)|},\ \text{and}\ \hat{y}_d = \hat{z}_d \times \hat{x}_d, \tag{21}$$

and the origin as the closes point to the line that passes through p_0 and p_1, and that which passes through p_2 and p_3. As such, points in the device guiding apparatus 3000 are converted to the MR imaging scanner's 5000 coordinate system using:

$$(p_{mr})_i = (p_d)_1(\hat{x}_d)_i + (p_d)_2(\hat{y}_d)_i + (p_d)_3(\hat{z}_d)_i + (o_d)_i \tag{22}$$

www.manaraa.com

where p_d is a point in the device guiding apparatus 3000, and p_{mr} is the point in the coordinate system of the MR imaging scanner 5000. Points in the coordinate system of the MR imaging scanner 5000 can be converted to coordinates in the device guiding apparatus 3000 by solving the linear system:

$$\begin{bmatrix} (\hat{x}_d)_1 & (\hat{y}_d)_1 & (\hat{z}_d)_1 \\ (\hat{x}_d)_2 & (\hat{y}_d)_2 & (\hat{z}_d)_2 \\ (\hat{x}_d)_3 & (\hat{y}_d)_3 & (\hat{z}_d)_3 \end{bmatrix} \begin{bmatrix} (p_d)_1 \\ (p_d)_2 \\ (p_d)_3 \end{bmatrix} = \begin{bmatrix} (p_{mr})_1 - (o_d)_1 \\ (p_{mr})_2 - (o_d)_2 \\ (p_{mr})_3 - (o_d)_3 \end{bmatrix}. \quad (23)$$

[0064] The registration fiducials are placed at the MR imaging scanner's 5000 isocenter, scanned before the patient is positioned, and removed from the device guiding apparatus 3000 before the patient arrives, thereby reducing the amount of time the patient must be anesthetized.

[0065] Although in embodiments described above the user is described as being a physician, those skilled in the art will appreciate that other types of users may use the system.

[0066] Although in embodiments described above the orientation of the medical device is adjusted manually via a manipulator arm connected to an adjustment handle, those skilled in the art will appreciate that the orientation of the medical device may be adjusted automatically. In this embodiment, the linear motion assemblies are adjusted through a motor assembly comprising one or more motors.

[0067] Although in embodiments described above the medical device is described as being a needle, those skilled in the art will appreciate that other medical devices may be used such as for example a catheter.

[0068] Although in embodiments described above the target region is described as being the prostate, those skilled in the art will appreciate that other target regions may be targeted with the system such as for example the brain, the cervix, etc.

[0069] Although in embodiments described above the device guiding apparatus is described as utilizing sensors in the form of magnetic rotary encoders, those skilled in the art will appreciate that other instruments may be used to determine position such as for example optical encoders, incremental or absolute encoders, linear encoders, optical tracking systems using a set of stereo cameras a reflective markers, mechanical scales (Vernier scales, etc.), a tracking system using one or more imaging sensors by imaging registration fiducials in real-time as the device is being moved, a stepper motor system

www.manaraa.com

wherein, assuming no slip, the number of steps a motor has been directed are used to determine the position of the medical device, etc.

[0070] Although in embodiments described above the device guiding apparatus is used in conjunction with a MR imaging scanner, it will be appreciate that device guiding apparatus may be used in conjunction with other types of imaging scanners. For example, imaging scanners such as for example a computed tomography (CT) scanning system, a positron emission tomography (PET) scanning system, a single-photon emission computed tomography (SPECT) scanning system, an ultrasound scanning system, etc.

[0071] Although in embodiments described above the various components of the device guiding apparatus are made of plastic materials, those skilled in the art will appreciate that the types of materials used for the various components of the system is dependent on the type of imaging scanner used in conjunction with the system.

[0072] One skilled in the art will appreciate that the device guiding apparatus may be used for imaging humans and/or animals.

[0073] Although embodiments are described above with reference to the accompanying drawings, those skilled in the art will appreciate that variations and modifications may be made without departing from the scope thereof as defined by the appended claims.

[0074] References

1. O. Raz, M. A. Haider, S. R. H. Davidson, U. Lindner, E. Hlasny, R. Weersink, M. R. Gertner, W. Kucharcyzk, S. A. McCluskey and J. Trachtenberg, "Real-time magnetic resonance imaging-guided focal laser therapy in patients with low-risk prostate cancer," Eur. Urol. **58**, 173-177 (2010).

2. G. S. Fischer, I. Iordachita, C. Csoma, J. Tokuda, S. P. DiMaio, C. M. Tempany, N. Hata and G. Fichtinger, "MRI-compatible pneumatic robot for transperineal prostate needle placement," IEEE Transactions on Mechatronics **13**, 295-305 (2008).

3. A. A. Goldenberg, J. Trachtenberg, Y. Yi, R. Weersink, M. S. Sussman, M. Haider, L. Ma and W. Kucharczyk, "Robot-assisted MRI-guided prostatic interventions," Robotica **28**, 215 (2010).

www.manaraa.com

4. A. Krieger, C. Csoma, Iordachital, II, P. Guion, A. K. Singh, G. Fichtinger and L. L. Whitcomb, "Design and preliminary accuracy studies of an MRI-guided transrectal prostate intervention system," Med Image Comput Comput Assist Interv **10**, 59-67 (2007).

5. A. Krieger, I. Iordachita, S. E. Song, N. B. Cho, P. Guion, G. Fichtinger and L. L. Whitcomb, "Development and Preliminary Evaluation of an Actuated MRI-Compatible Robotic Device for MRI-Guided Prostate Intervention," IEEE Int. Conf. Robot., 1066-1073 (2010).

6. M. G. Schouten, J. Ansems, W. K. Renema, D. Bosboom, T. W. Scheenen and J. J. Futterer, "The accuracy and safety aspects of a novel robotic needle guide manipulator to perform transrectal prostate biopsies," Med. Phys. **37**, 4744-4750 (2010).

7. D. Stoianovici, D. Song, D. Petrisor, D. Ursu, D. Mazilu, M. Muntener, M. Schar and A. Patriciu, ""MRI Stealth" robot for prostate interventions," Minimally Invasive Therapy & Allied Technologies **16**, 241-248 (2007).

8. S. Zangos, C. Herzog, K. Eichler, R. Hammerstingl, A. Lukoschek, S. Guthmann, B. Gutmann, U. J. Schoepf, P. Costello and T. J. Vogl, "MR-compatible assistance system for punction in a high-field system: device and feasibility of transgluteal biopsies of the prostate gland," Eur. Radiol. **17**, 1118-1124 (2007).

9. G. Fischer, A. Krieger, I. Iordachita, C. Csoma, L. Whitcomb and G. Fichtinger, "MRI compatibility of robot actuation techniques – a comparative study," Medical Image Computing and Computer-Assisted Intervention–MICCAI 2008, 509-517 (2008).

www.manaraa.com

What is claimed is:

1. A device guiding apparatus, comprising:

support framework;

a counterbalance supported by the support framework at a position above a surface on which the support framework rests; and

a manipulation assembly supported by the counterbalance, the manipulation assembly comprising at least one support assembly for supporting a medical device at a position intermediate the counterbalance and the surface such that a user has a direct line-of-site of the at least one support assembly.

2. The device guiding apparatus of claim 1, wherein the support framework, the manipulation assembly, the at least one support assembly and the counterbalance are made of non-magnetic materials.

3. The device guiding apparatus of claim 2, wherein the device guiding apparatus is positionable within a bore of a magnetic resonance (MR) imaging scanner.

4. The device guiding apparatus of any one of claims 1 to 3, wherein the medical device is a needle.

5. The device guiding apparatus of any one of claims 1 to 4, comprising a sensor arrangement configured to obtain sensor data and processing structure for processing the sensor data to determine the trajectory of the medical device.

6. The device guiding apparatus of claim 5, comprising an alignment interface providing feedback to the user for adjusting the trajectory of the medical device.

7. The device guiding apparatus of any one of claims 1 to 6, wherein the support framework is configured to provide working space for the user.

www.manaraa.com

8. The device guiding apparatus of any one of claims 1 to 7, comprising:

at least one extension arm connected at a first end to the counterbalance and at a second end to the manipulation assembly; and

at least one linear motion assembly connected to the at least one extension arm at a position intermediate the first and second end, the at least one linear motion assembly allowing for manipulation of the trajectory of the medical device.

9. The device guiding apparatus of claim 8, comprising at least one locking mechanism supported by the support framework, the at least one locking mechanism configured to prevent movement of the at least one linear motion assembly when in a first position and configured to permit movement of the at least one linear motion assembly when in a second position.

10. A device guiding apparatus, comprising:

support framework;

a counterbalance supported by the support framework at a position above a surface on which the support framework rests; and

a manipulation assembly supported by the counterbalance, the manipulation assembly comprising at least one support assembly for supporting a medical device at a position intermediate the counterbalance and the surface such that a user has a direct line-of-site of the at least one support assembly;

a sensor arrangement configured to obtain sensor data; and

processing structure configured to:

receive sensor data from the sensor arrangement;

process the received sensor data to determine the trajectory of the medical device;

calculate a point of intersection with a target region based on the trajectory of the medical device;

calculate a difference between the point of intersection and a target point associated with the target region; and

www.manaraa.com

provide feedback to the user to guide the medical device to the target point based on said calculated difference.

11. The device guiding apparatus of claim 10, wherein the support framework, the manipulation assembly, the at least one support assembly, the counterbalance and the sensor arrangement are made of non-magnetic materials.

12. The device guiding apparatus of claim 11, wherein the device guiding apparatus is positionable within a bore of a magnetic resonance (MR) imaging scanner.

13. The device guiding apparatus of any one of claims 10 to 12, wherein the medical device is a needle.

14 The device guiding apparatus of any one of claims 10 to 13, wherein the sensor arrangement comprises a plurality of magnetic rotary encoders.

15. The device guiding apparatus of any one of claims 10 to 14, wherein the processing structure provides feedback to the user via an alignment interface.

16. A method for providing feedback to a user guiding a medical device to a target region, the method comprising:

receiving sensor data from a sensor arrangement;

processing the received sensor data to determine the trajectory of the medical device;

calculating a point of intersection with a target region based on the trajectory of the medical device;

calculating a difference between the point of intersection and a target point associated with the target region; and

providing feedback to the user based on the calculated difference between the point of intersection and the target point.

www.manaraa.com

17. The method of claim 16, further comprising:

adjusting the trajectory of the medical device based on the calculated difference between the point of intersection and the target point.

18. The method of claim 16 or 17, further comprising:

calculating a difference between the point of intersection and an entry point associated with the target point; and

providing feedback to the user based on the calculated difference between the point of intersection and the entry point.

19. The method of claim 18, further comprising:

adjusting the trajectory of the medical device based on the calculated difference between the point of intersection and the target point and based on the calculated difference between the point of intersection and the entry point.

20. A non-transitory computer readable medium having stored thereon a computer program comprising computer readable instructions for execution by a computer to perform a method of providing feedback to a user guiding a medical device to a target region, the method comprising:

receiving sensor data from a sensor arrangement;

processing the received sensor data to determine the trajectory of the medical device;

calculating a point of intersection with a target region based on the trajectory of the medical device;

calculating a difference between the point of intersection and an actual target point associated with the target region; and

providing feedback to the user based on the calculated difference between the estimated target point and the actual target point.

www.manaraa.com

ABSTRACT

A device guiding apparatus comprises support framework, a counterbalance supported by the support framework at a position above a surface on which the support framework rests, and a manipulation assembly supported by the counterbalance. The manipulation assembly comprises at least one support assembly for supporting a medical device at a position intermediate the counterbalance and the surface such that a user has a direct line-of-site of the at least one support assembly.

www.manaraa.com

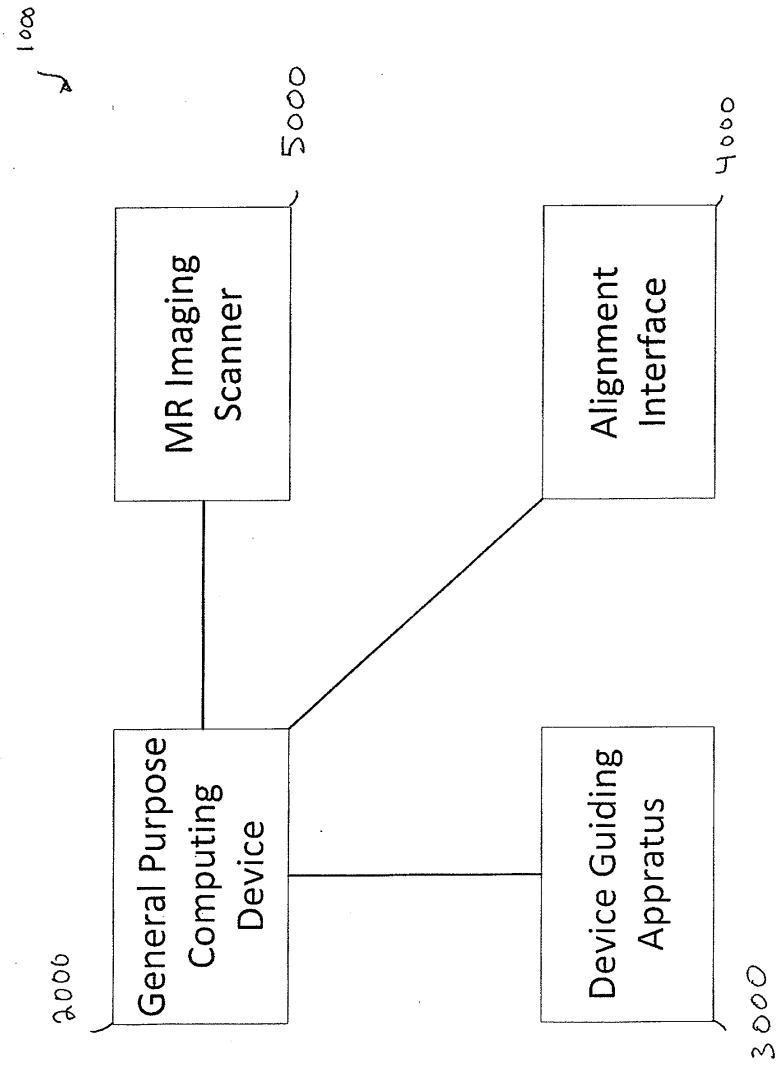

Fig. 1

www.manaraa.com

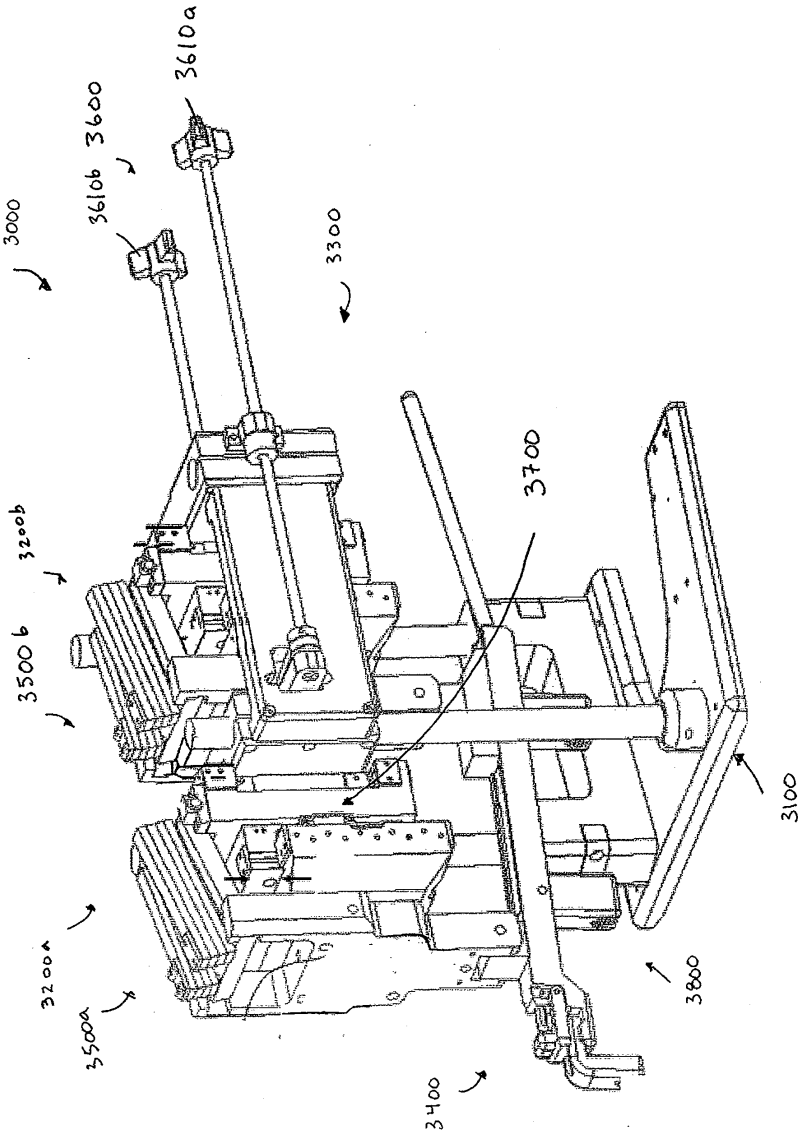

Fig. 2

www.manaraa.com

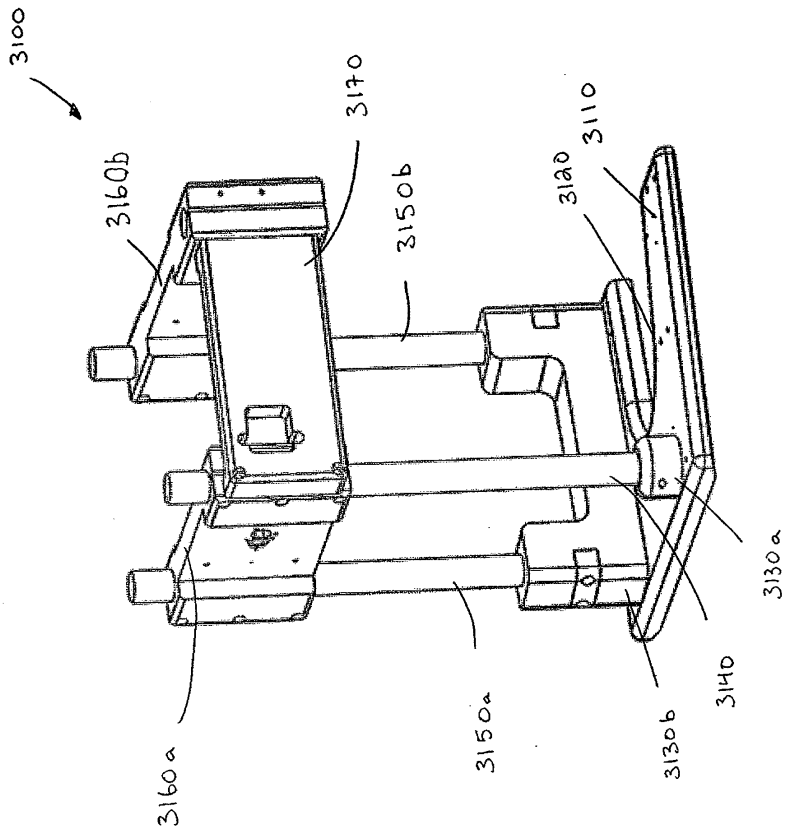

Fig. 3

www.manaraa.com

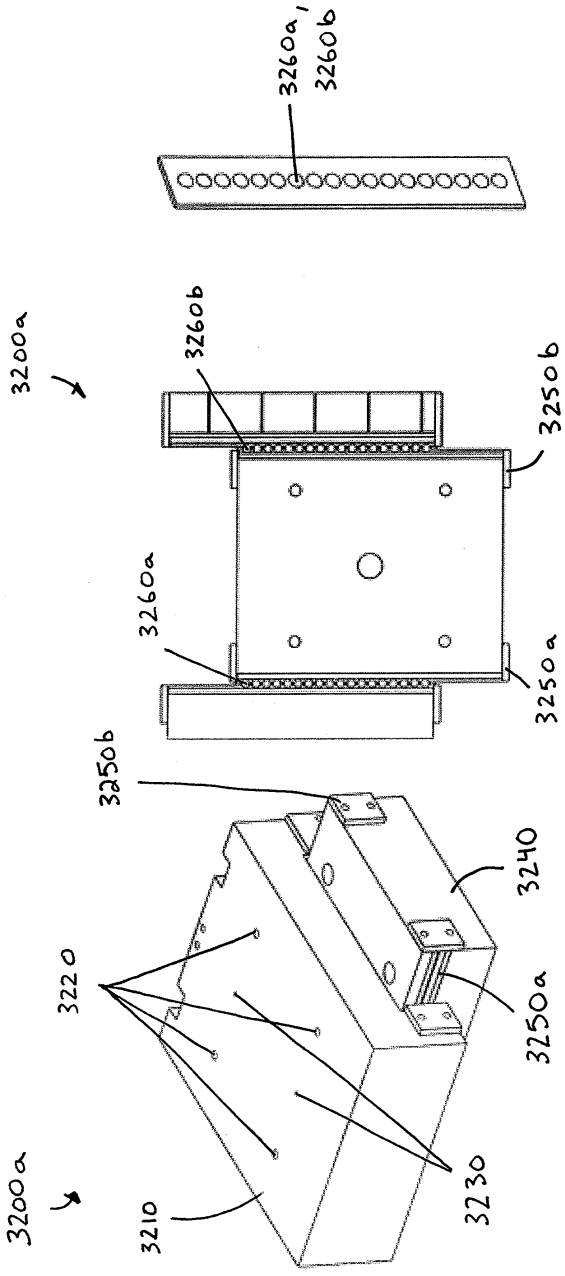

Fig. 4c

Fig. 4b

Fig. 4a

www.manaraa.com

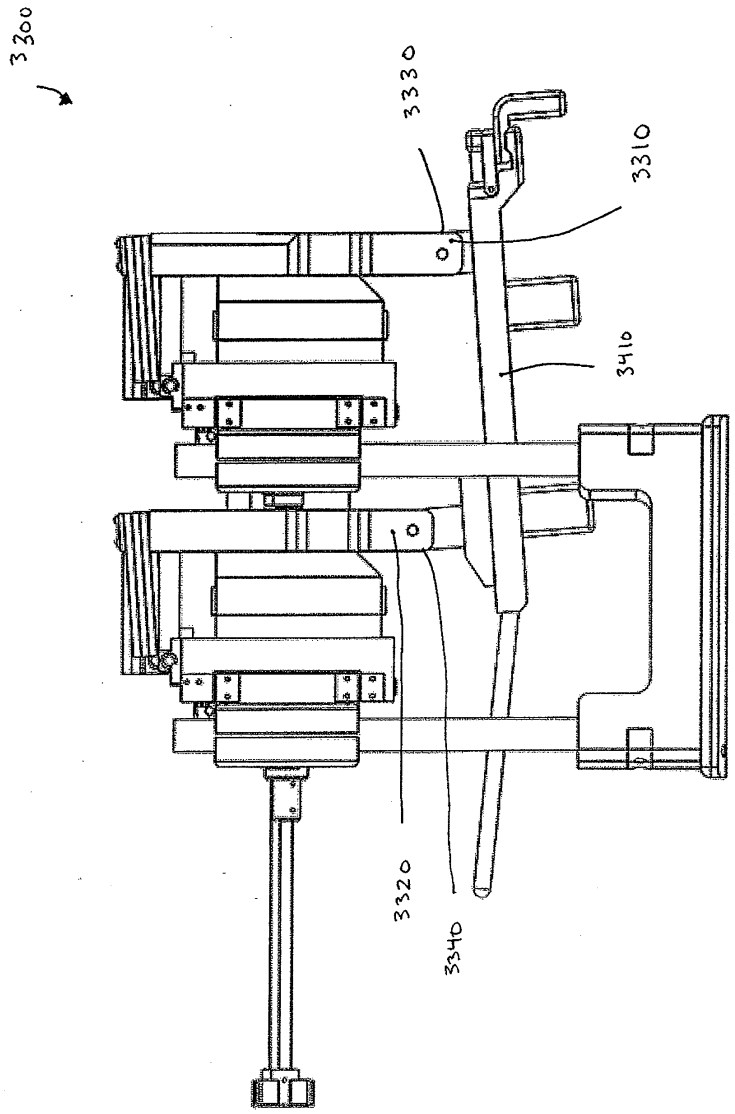

Fig. 5

www.manaraa.com

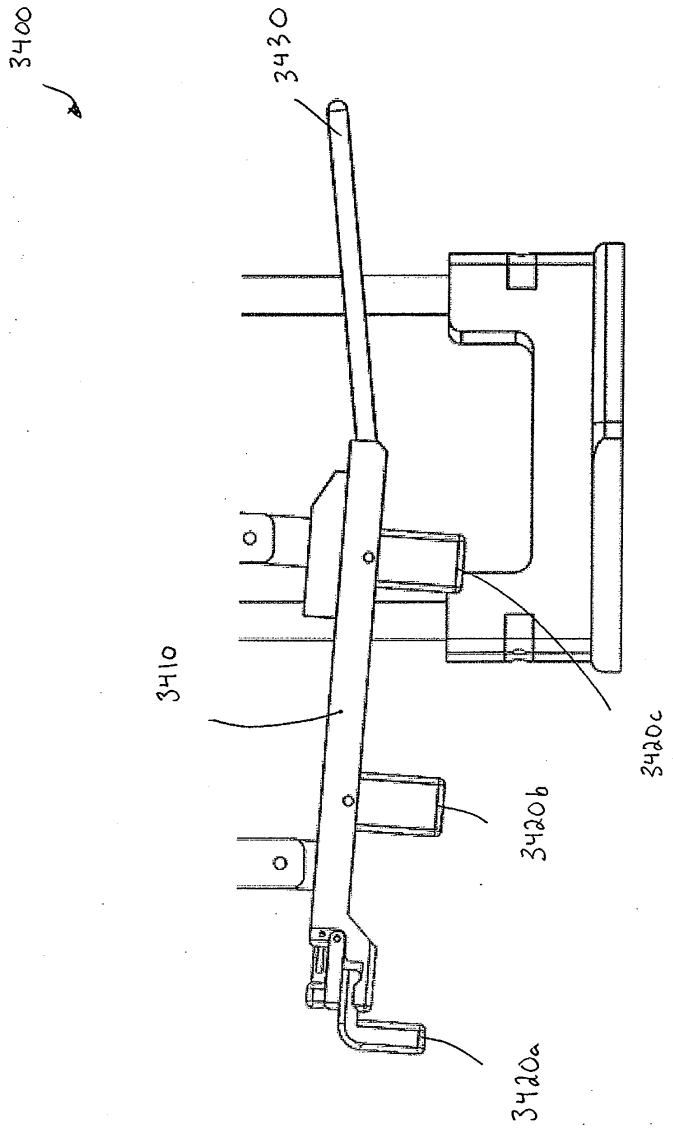

Fig. 6

www.manaraa.com

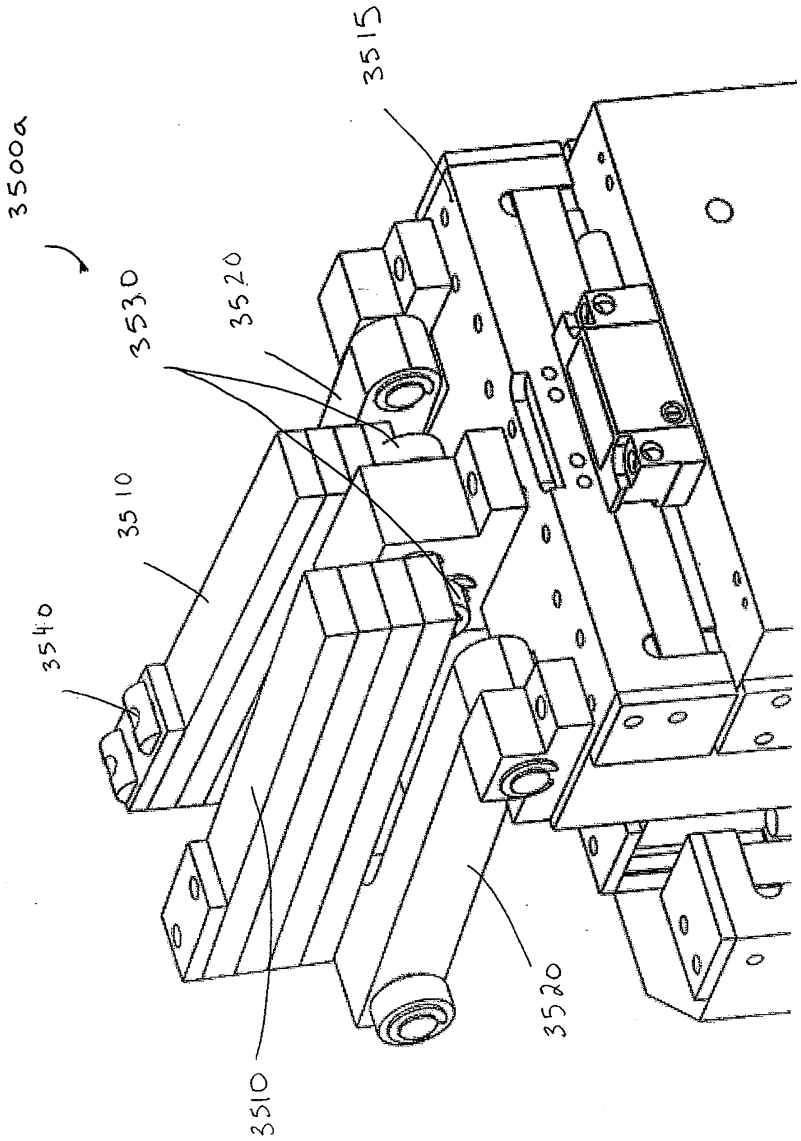

Fig. 7

www.manaraa.com

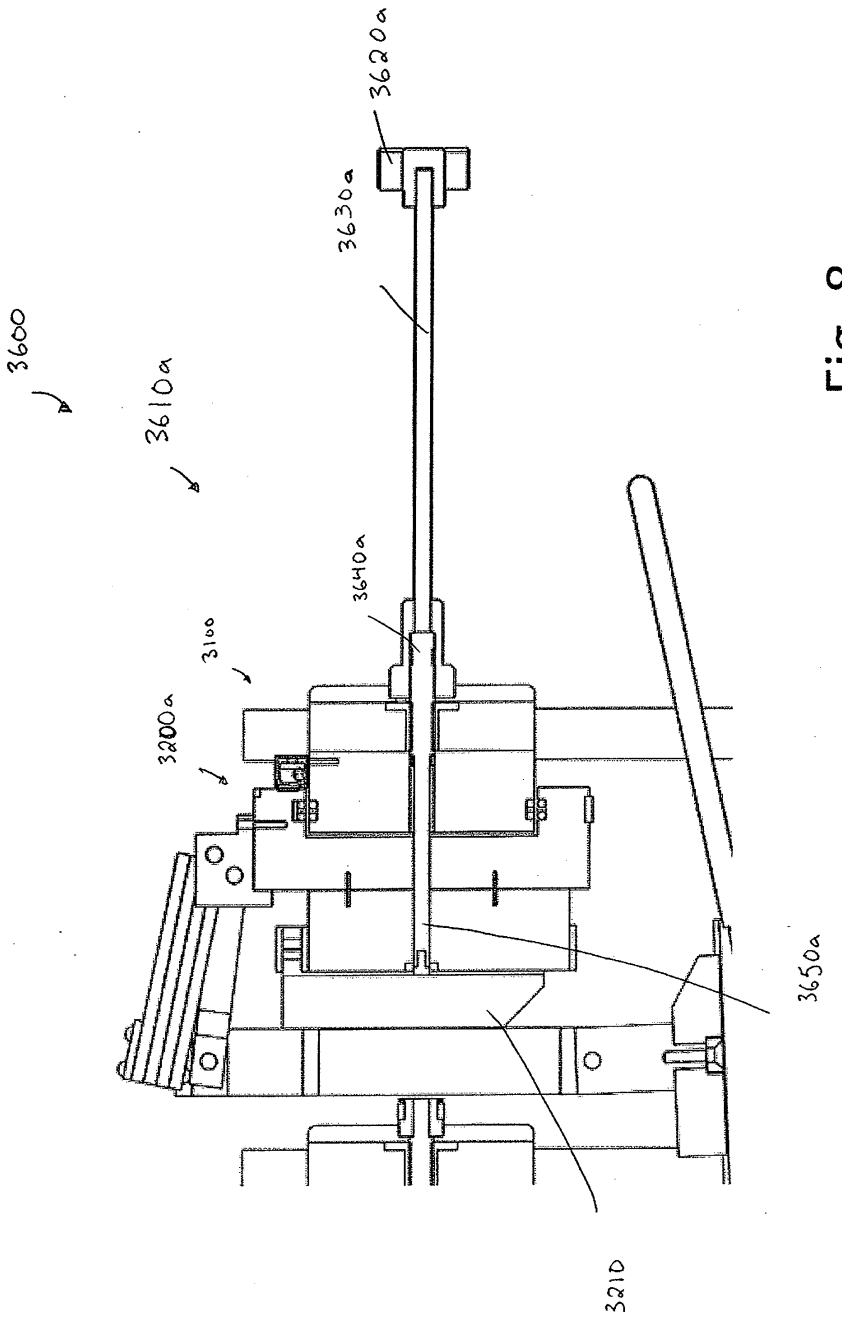

Fig. 8

www.manaraa.com

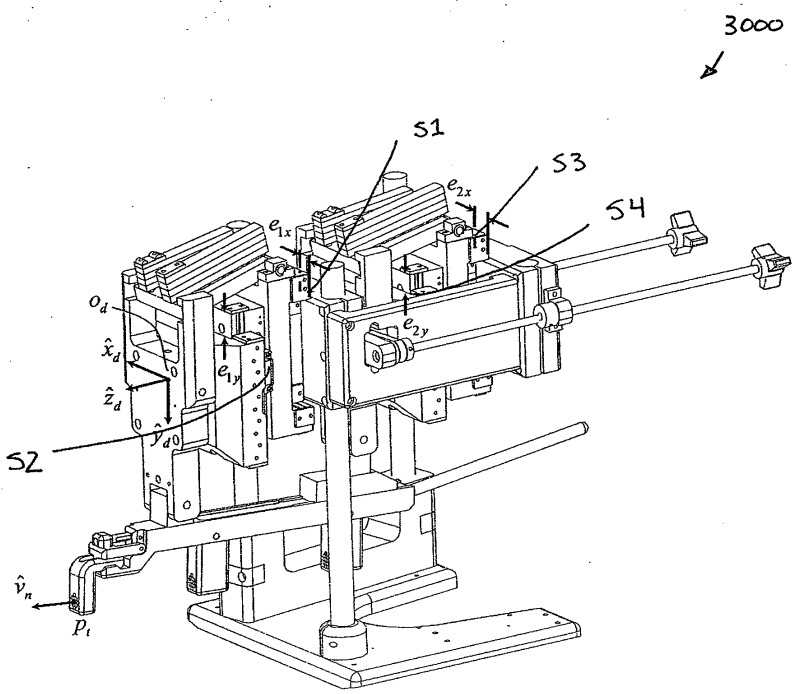

Fig. 9

www.manaraa.com

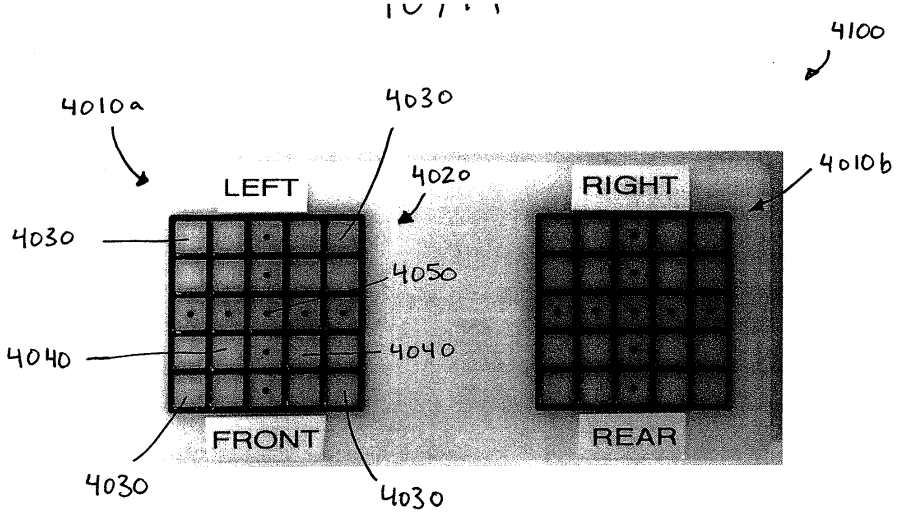

Fig. 10a

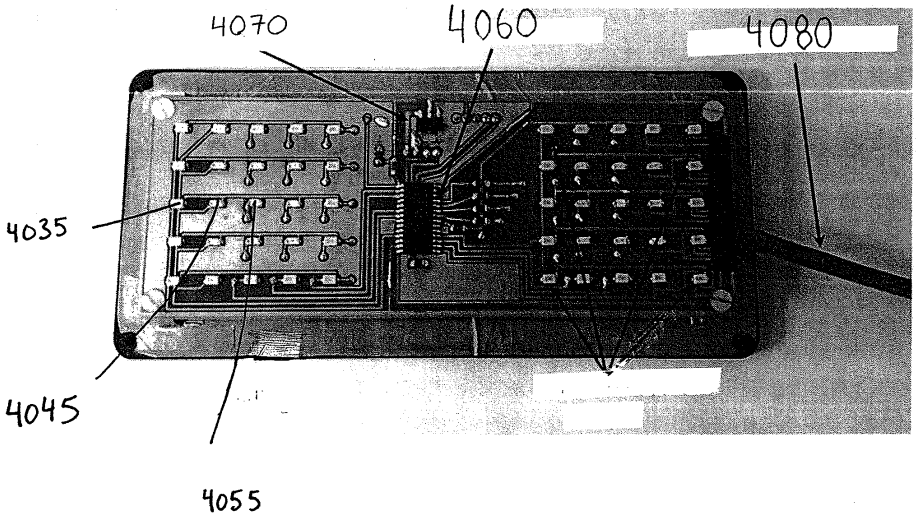

Fig. 10b

www.manaraa.com

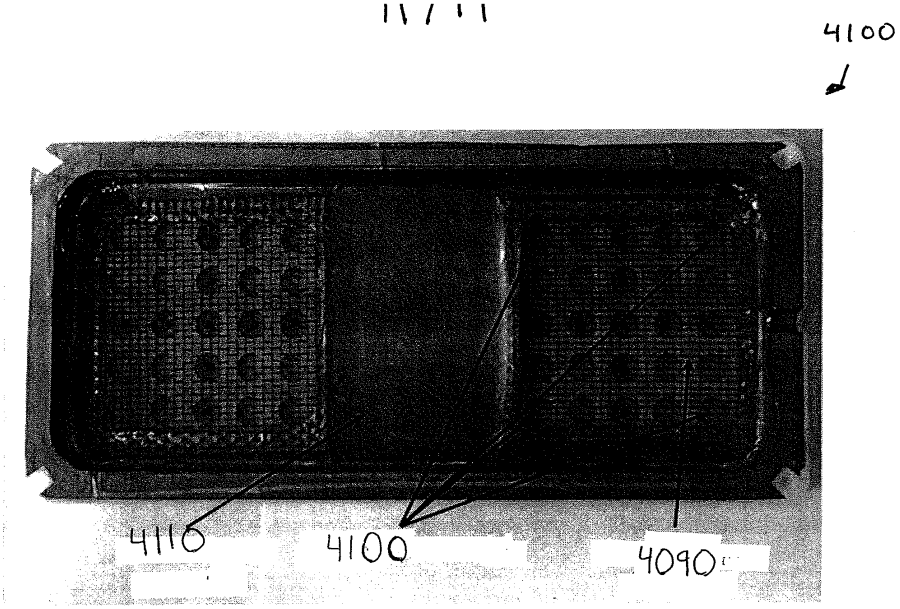

Fig. 10c

www.manaraa.com

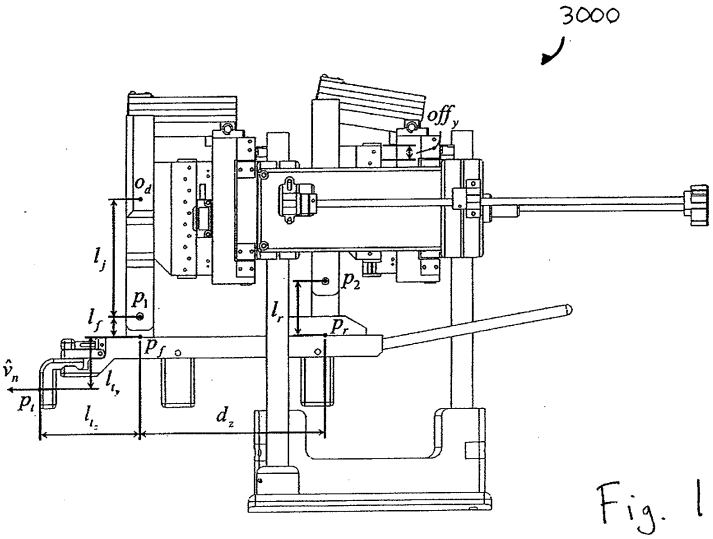

Fig. 11

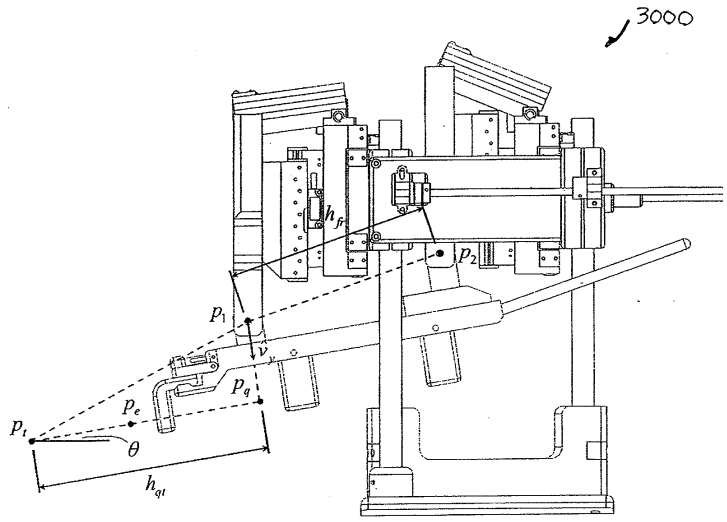

Fig. 12

www.manaraa.com

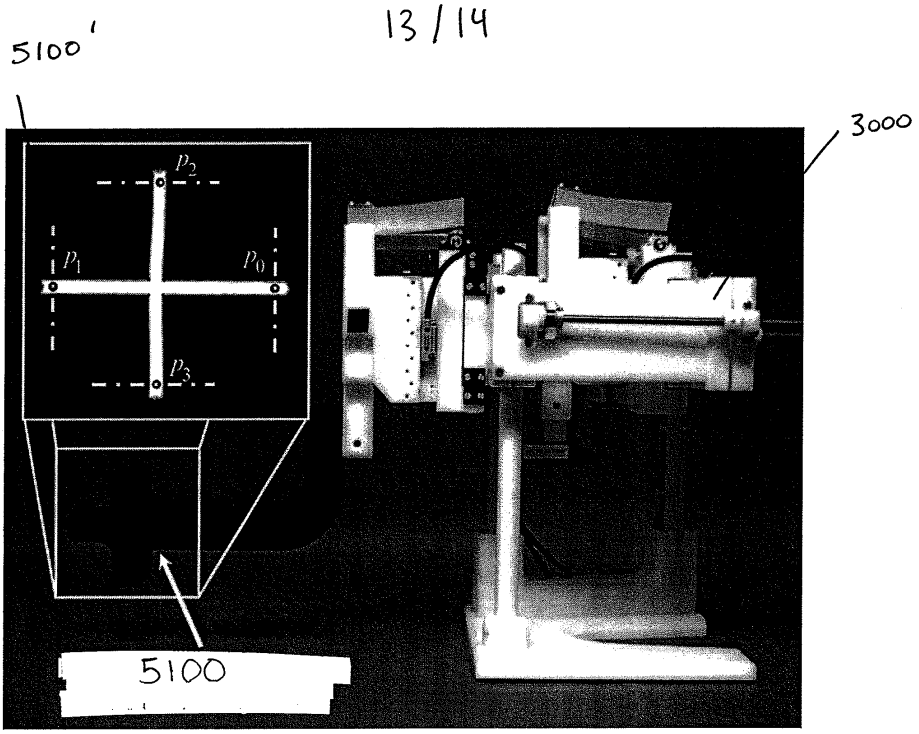

Fig. 13

www.manaraa.com

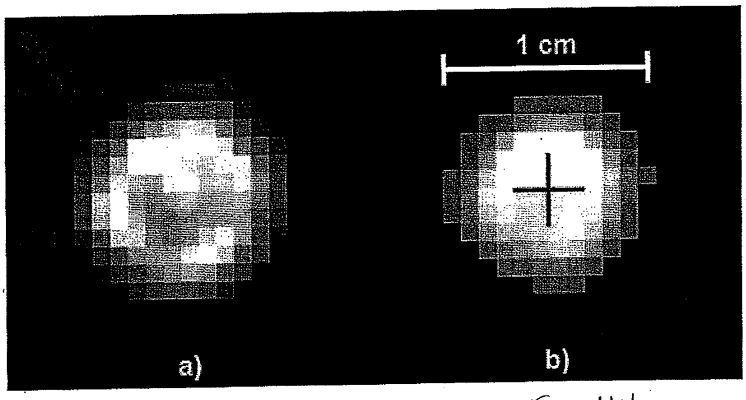

Fig 14a

Fig 14b

www.manaraa.com

Appendix E. Permissions

E.1 Permission to reproduce previously published material in Chapters 2, 3, and 5

American Association of Physicists in Medicine
One Physics Ellipse
College Park, MD 20740-3846
(301) 209-3350
Fax (301) 209-0862
http://www.aapm.org

Office of the Executive Director
Angela R. Keyser

DATE OF REQUEST: October 15, 2013

FROM:
Jeremy Cepek

EMAIL ADDRESS:

1. **Permission is granted to:**

   Jeremy Cepek

2. **Permission is requested to use the following material:**

   J. Cepek, B. Chronik, U. Lindner, J. Trachtenberg, S. Davidson, J. Bax and A. Fenster, "A system for MRI-guided transperineal delivery of needles to the prostate for focal therapy," Med. Phys. 40, 012304-012301-012315 (2013)

   J. Cepek, U. Lindner, S.R.H Davidson, M.A. Haider, S. Ghai, J. Trachtenberg, A. Fenster, "Treatment Planning for Prostate Focal Laser Ablation in the Face of Needle Placement Uncertainty," Med. Phys (Accepted August 12, 2013, Tracking #)

   J. Cepek, B. Chronik, A. Fenster, "The Effects of Magnetic Field Inhomogeneity on the Accuracy of Passive Device Tracking Frames in MR," Med. Phys. (Submitted September 5, 2013, Tracking #)

3. **For what purpose:**

   As chapters in my PhD thesis

Authors seeking permission must also notify the first author of the article from which permission is being sought.

Permission is hereby granted: October 16, 2013
Date

The Association's Journals are *Medical Physics* and *Journal of Applied Clinical Medical Physics*
Member Society of the American Institute of Physics and the International Organization of Medical Physics

www.manaraa.com

E.2 Permission to reproduce Figure 1.3

ELSEVIER LICENSE
TERMS AND CONDITIONS

Nov 05, 2013

This is a License Agreement between Jeremy Cepek ("You") and Elsevier ("Elsevier") provided by Copyright Clearance Center ("CCC"). The license consists of your order details, the terms and conditions provided by Elsevier, and the payment terms and conditions.

All payments must be made in full to CCC. For payment instructions, please see information listed at the bottom of this form.

Supplier	Elsevier Limited The Boulevard,Langford Lane Kidlington,Oxford,OX5 1GB,UK
Registered Company Number	1982084
Customer name	Jeremy Cepek
Customer address	
License number	3260241336956
License date	Nov 01, 2013
Licensed content publisher	Elsevier
Licensed content publication	International Journal of Radiation Oncology*Biology*Physics
Licensed content title	Functional anatomy of the prostate: Implications for treatment planning
Licensed content author	Patrick W. McLaughlin,Sara Troyer,Sally Berri,Vrinda Narayana,Amichay Meirowitz,Peter L. Roberson,James Montie
Licensed content date	1 October 2005
Licensed content volume number	63
Licensed content issue number	2
Number of pages	13
Start Page	479
End Page	491
Type of Use	reuse in a thesis/dissertation
Portion	figures/tables/illustrations
Number of figures/tables/illustrations	1
Format	both print and electronic
Are you the author of this	No

www.manaraa.com

Elsevier article?	
Will you be translating?	No
Order reference number	0001
Title of your thesis/dissertation	New Technology and Techniques for Needle-Based Magnetic Resonance Image-Guided Prostate Focal Therapy
Expected completion date	Dec 2013
Estimated size (number of pages)	250
Elsevier VAT number	GB 494 6272 12
Permissions price	0.00 USD
VAT/Local Sales Tax	0.0 USD / 0.0 GBP
Total	0.00 USD
Terms and Conditions	

www.manaraa.com

E.3 Permission to reproduce Figure 1.4.

November 4, 2013

Jeremy Cepek

Dear Jeremy Cepek:

The Radiological Society of North America (RSNA®) is pleased to grant you permission to reproduce the following figures in print and electronic formats for use in your dissertation/thesis, provided you give full credit to the authors of the original publication.

> Figures 10a, 10b, 10c, 10d
> Hoeks C MA, Barentsz J O, Hambrock T, et al. Prostate cancer: multiparametric MR imaging for detection, localization, and staging. *Radiology* 2011;261:46-66.

This permission is a one-time, non-exclusive grant for English-language use and is exclusively limited to the usage stated and underlined above. The requestor guarantees to reproduce the material as originally published. Permission is granted under the condition that a full credit line is prominently placed (i.e. author name(s), journal name, copyright year, volume #, inclusive pages and copyright holder).

This permission becomes effective upon receipt of this signed contract. Please sign a copy of this agreement, return a signed copy to me and retain a copy for your files. Thank you for your interest in our publication.

[Print Name]: Jeremy Cepek

SIGNATURE: _____ Date: Nov. 4. 2013

Sincerely,

Ashley E. Daly
Senior Manager, Journal Rights & Communications
Publications

www.manaraa.com

Curriculum Vitae

University Education

2010 – Present **PhD Candidate, Medical Imaging, Biomedical Engineering, The University of Western Ontario**
Supervisor: Dr. Aaron Fenster

2008 – 2009 **Master of Engineering Science, Computational Fluid Dynamics, Mechanical & Materials Engineering, The University of Western Ontario**
Supervisor: Dr. Anthony Straatman

2004 – 2008 **Bachelor of Engineering Science, Mechanical Engineering, The University of Western Ontario**
Graduated with distinction

Undergraduate Honours, Scholarships and Awards

2008 **UWO Faculty Association Scholarship**
2008 **Ontario Professional Engineers Scholarship**
2008 **Dr. L. Stuart Lauchland Scholarship**
2008 **UWO In-Course Scholarship**
2007 **Shaw Family Foundation Scholarship**
2005 **UWO In-Course Scholarship**

Research-Specific Honours, Scholarships and Awards

2012 – 2013 **Queen Elizabeth II Graduate Scholarship in Science and Technology**
Awarded based on academic achievement and research merit.
Total Amount: $15,000 CAD

2011 – 2013 **Computer Assisted Medical Interventions CREATE Award**
Awarded to graduate students involved in trans-disciplinary research.
Total Amount: $25,500 CAD

2010 – 2012 **NSERC Doctoral Canada Graduate Scholarship**
Awarded to the top-ranked postgraduate scholarship applicants based on academic excellence, research potential, communication, interpersonal and leadership abilities.
Total Amount: $70,000 CAD

2010 **Ontario Graduate Scholarship (declined)**
Awarded based on academic merit and research potential.
Total Amount: $15,000 CAD

2008 – 2009 **NSERC Master's Postgraduate Scholarship**
Awarded to masters' students based on academic excellence, research potential & interpersonal skills.
Total Amount: $34,600 CAD

2008 **Ontario Graduate Scholarship (declined)**
Awarded based on academic merit and research potential.
Total Amount: $15,000 CAD

www.manaraa.com

2007 **NSERC Undergraduate Student Research Award**
Awarded based on academic achievement and research potential.
Total Amount: $4,500 CAD

Research Experience

2010 – Present **PhD Candidate, Medical Imaging, Biomedical Engineering, The University of Western Ontario**
Supervisor: Dr. Aaron Fenster
- Developed a magnetic resonance imaging (MRI)-guided device for delivering prostate focal laser ablation therapy.
- Studied the effects of needle placement uncertainty on the probability of completely ablating focal prostate lesions and developed guidelines for patient selection for this treatment modality.
- Studied the effects of distortion in MRI on the accuracy of localizing interventional devices.
- Developing methods of monitoring and controlling needle deflection for interventional procedures.

2008 – 2009 **Master of Engineering Science, Computational Fluid Dynamics, Department of Mechanical & Materials Engineering, The University of Western Ontario**
Supervisor: Dr. Anthony Straatman
- Developed custom software for simulating turbulent fluid flow and heat transfer on a large-scale parallel computing network.
- Performed validation experiments and used the software to quantify the pressure drop required and amount of heat transfer achievable using turbulent flow through highly porous graphitic foams.

2007 **Summer Research Position (NSERC Undergraduate Student Research Award), The University of Western Ontario**
Supervisor: Dr. Anthony Straatman
- Learned to solve fluid dynamics problems using numerical methods, studied methods of simulating fluid flow in porous materials, and researched methods of turbulent flow simulation.

Publications, Presentations and Abstracts

Articles in Refereed Journals

Cepek, J., Lindner, U., Davidson, S., Haider, M., Ghai, S., Trachtenberg, J., Fenster, A.: Treatment Planning for Prostate Focal Laser Ablation in the Face of Needle Placement Uncertainty. Med. Phys. (2014, In Press)
Analysis of the effect of needle placement error on treatment outcome, development of selection guidelines for prostate focal laser ablation.

Cepek, J., Chronik, B., Lindner, U., Trachtenberg, J., Davidson, S., Bax, J., Fenster, A.: A system for MRI-guided transperineal delivery of needles to the prostate for focal therapy. Med. Phys. 40, 012304-1-15 (2013)
Development, testing, and initial experiences using a novel system for guiding needles to the prostate within the bore of an MRI scanner.

www.manaraa.com

Cepek, J., Chronik, B., Fenster, A.: The Effects of Magnetic Field Distortion on the Accuracy of Passive Device Localization Frames in MR. Med. Phys. (2013, In Revision)
Quantification of the effects of image distortion in MRI on the accuracy of localizing interventional tools.

Cepek, J., Straatman, A.G.: Modeling of Turbulent Flow and Heat Transfer in Graphitic Foams. Defect and Diffusion Forum 297, 739-744 (2010)
A numerical study of the pressure drop and heat transfer through porous graphitic foams using custom software implemented in a parallel computing framework.

Refereed Conference Proceedings

Cepek, J., Chronik, B.A., Fenster, A.: Errors in Device Localization in MRI using Z-Frames. Medical Image Computing and Computer-Assisted Intervention - MICCAI 8149, 348-355 (2013)
Quantification of errors in using a common device to localize interventional tools in MRI.

Cepek, J., Chronik, B., Lindner, U., Trachtenberg, J., Fenster, A.: Development of an MRI-compatible device for prostate focal therapy. Medical Image Computing and Computer-Assisted Intervention - MICCAI 7510, 455-462 (2012)
Development and preliminary accuracy tests of a novel device for delivery of needles to the prostate in MRI.

Oral Presentations

Cepek, J., Lindner, U., Ghai, S., Haider, M., Davidson, S.R.H., Hlasny, E., Trachtenberg, J., and Kucharczyk, W., MRI-guided focal laser ablation of prostate cancer using a mechatronic needle guidance system: Experience in eight patients. 6th International Symposium on Focal Therapy and Imaging in Prostate & Kidney Cancer. Noordwijk, The Netherlands, May 29th, 2013
Presented qualitative experience and needle guidance error achieved in a case series of patients in a Phase I/II clinical trial using a mechatronic system to guide needles.

Cepek, J., and Straatman, A.G., Modeling of Turbulent Flow and Heat Transfer in Graphitic Foams. Canadian Applied and Industrial Mathematics Society. London, Canada. June 11th, 2009.
Presented the numerical method and results of turbulent flow simulation in graphitic foams.

www.manaraa.com

Selected Poster Presentations

Cepek, J., Lindner, U., Ghai, S., Davidson, S.R.H., Trachtenberg, J., Fenster, A. Toward accurate delivery of prostate focal therapy: the effects of needle placement uncertainty, and the development of guidelines for patient-specific treatment plans for focal laser ablation. Canadian Cancer Research Conference. Toronto, Canada, November 3 – 6, 2013.
Technical challenges in accurately delivering focal therapy, and how they limit patient selection.

Cepek, J., Chronik, B., Fenster, A., Errors in Device Localization in MRI using Z-Frames. Medical Image Computing and Computer Assisted Intervention – MICCAI. September 22 – 26, 2013.
Effects of imaging distortion in MRI on the accuracy of interventional tool localization.

Cepek, J., Lindner, U., Chronik, B., Davidson, S.R.H., Trachtenberg, J., Fenster, A.: MRI-Guided Focal Therapy of Prostate Cancer. OICR Scientific Meeting. Toronto, Canada, March 7 – 8, 2013.
Technical advances in MRI-guided focal laser ablation therapy of prostate cancer.

Cepek, J., Rajchl, M., Lindner, U., Trachtenberg, J., Fenster, A.: Evaluation of Tissue Thermal Damage Models in *in vivo* Human Prostate Tissue. Imaging Network Ontario Symposium. Toronto, Canada, February 4 – 5, 2013.
Preliminary analysis of the variation in predicted ablated tissue volume using different models.

Intellectual Property

System and Method for Guiding a Medical Device to a Target Region. US Patent. Application Number 2,829,084, United States Patent and Trademark Office. Inventors: Jeremy Cepek, Aaron Fenster, Jeffrey Bax, Uri Lindner, John Trachtenberg (2013)
A novel method of guiding needles to the prostate gland within the bore of an MRI scanner.

Relevant Teaching and Work Experience

2008 – Present **Graduate Teaching Assistant, The University of Western Ontario**
Prepared lectures and tutorials, marked assignments and tutored students for eleven undergraduate courses in the departments of mechanical engineering and medical biophysics.

2012 – Present **Engineering Services, Nugrowth Designs Inc.**
Designed and built a motion controller for the accurate placement of neural electrodes in animal brain studies.

2010 – 2011 **Western Engineering Summer Academy Instructor, The University of Western Ontario**
Developed and delivered a summer program for high school students to learn about mechanical engineering through lectures, demonstrations, hands-on activities and tours.

www.manaraa.com

2009 **Engineering Consulting, AGS Scientific Inc.**
Provided engineering consulting services for KMW Energy Inc. in collaboration with a professional engineer.

www.manaraa.com